GEOPHYSICAL STUDY OF THE KRIBI-CAMPO SEDIMENTARY SUB-BASIN BY THE MODELLING OF GRAVITY DATA

ETUDE GEOPHYSIQUE DU SOUS BASSIN SEDIMENTAIRE DE KRIBI-CAMPO PAR LA MODELISATION DES DONNEES GRAVIMETRIQUES

by

KUE PETOU Rokis Malquaire

Msc. The University of Yaounde I

Mle: 09W0599

A THESIS SUBMITTED IN FULFILLMENT
OF THE REQUIREMENTS FOR THE DEGREE OF

Doctor of Philosophy

In

THE FACULTY OF SCIENCES
(Geophysics and Geo-exploration)

June 2020

UNIVERSITÉ DE YAOUNDÉ I
UNIVERSITY OF YAOUNDE I

FACULTÉ DES SCIENCES
FACULTY OF SCIENCE

DÉPARTEMENT DE PHYSIQUE
DEPARTMENT OF PHYSICS

ATTESTATION DE CORRECTION DE LA THÈSE DE DOCTORAT/Ph.D.

Nous, Professeur **OWONO OWNO Luc Calvin** et Professeur **VONDOU Derbetini Appolinaire,** respectivement Président du Jury et Examinateur de la thèse de Doctorat/Ph.D de Monsieur **KUE PETOU Rokis Malquaire,** Matricule **09W0599**, préparée sous la direction des Professeurs **MANGUELLE-DICOUM Eliezer et OWONA ANGUE Marie Louise,** intitulée : « **Geophysical Study Of The Kribi Campo Sedimentary Sub-Basin By The Modelling Of Gravity Data** », soutenue le **Vendredi 05 Juin 2020,** en vue de l'obtention du grade de **Docteur/Ph.D en Physique,** Spécialité **Physique de l'Environnement Terrestre,** Option **Géophysique et Géoexploration,** attestons que toutes les corrections demandées par le Jury de soutenance ont été effectuées.

En foi de quoi, la présente attestation lui est délivrée pour servir et valoir ce que de droit.

Fait à Yaoundé le 23 SEPT 2020

L'Examinateur	Le Chef de Département de Physique	Le Président du jury
Prof. VONDOU Derbetini Appolinaire	Prof. NDJAKA Jean-Marie Bienvenu	Prof. OWONO OWONO Luc Calvin

Dedication

This work is dedicated to my family

ACKNOWLEDGEMENTS

A lot of people have contributed in many ways to the success of this work and as part of my appreciation to the contribution of these people I would want to express my profound gratitude to each of them;

Firstly, I would like to thank Professor Emeritus **Manguelle-Dicoum Eliezer**, the supervisor of this thesis who accepted to have a watchful eye on the overall preparation of this thesis. I always remember and cherish his valuable contributions and suggestions during this work.

I would like to thank Professor **Owona Angue Marie Louise**, director of this thesis who initiated and followed up this work, for providing me the opportunity of taking part in a data acquisition campaign. I am so deeply grateful for her help, valuable guidance and financial support throughout this thesis that I do not have enough words to express my deep and sincere appreciation.

My acknowledgement goes to the Vice-rector in charge of Education, Professionalization and Development of Information and Communication Technologies, Professor **Owono Owono Luc Calvin**, the chief of department of Physics of the Faculty of Science of the University of Yaounde 1, Professor **Ndjaka Jean-Marie Bienvenu** and all the lecturers of the department.

I express my gratitude to the jury for all the precious time they will be willing to sacrifice in order to examine this work.

I would like to thank the Geophysics' Lab Teachers: Professor **Nouayou Robert, Professors Njandjock Nouck Philippe, Tabod Charles Tabod, Ndougsa Mbarga Theophile**, **Vondou Derbetini** for precious edification.

My acknowledgments go to Doctors **Njingti-Nfor, Abate Marcel, Ngatchou Evariste**, for their help and support brought for the realization of this work.

My completion of this project could not have been possible without the support of my classmates, they are equally acknowledged.

Finally, I must express my very profound gratitude to my parents for providing me with unfailing support and continuous encouragement throughout my years of study and through the process of researching and writing this thesis. This accomplishment would not have been possible without them. Thank you Mr and Mrs **KUE**.

TABLE OF CONTENTS

LIST OF SYMBOLS

- $\int$: Integration
- ∂ : partial derivative
- d/dx: derivation with respect to x
- ∇ ou grad: nabla operator or gradient
- Δ : variation
- $\sum$: summation
- Pn: Legendre polynomial
- R : average earth's radius (m)
- a : equatorial radius of reference ellipsoid (m)
- B : Bouguer anomaly (gal)
- c : polar radius of reference ellipsoid (m)
- C : Universal gravitational constant ($m^3.kg^{-1}.s^{-2}$)
- G : gravity potential ($m^2.s^{-2}$)
- g : theoretical value of gravity on the reference ellipsoid (m/s^{-2})
- δ or ρ : density ($g.cm^{-3}$)
- λ : wavelength (m)
- k : wave number (m^{-1})
- φ : geocentric latitude (degree)
- ω : earth's rotation velocity ($rad.s^{-1}$)

ABBREVIATIONS

- CAPAB: Central Africa Pan-African Belt
- CC: Congo Craton
- CCSZ: Central Cameroonian Shear Zone
- GPS: Global Positioning System
- N: North
- NE: North-East
- NW: North-West
- ORSTOM : Office de la recherche scientifique et technique Outre-Mer (Became IRD)
- PAB: Pan-African Belt
- S: South
- SE: South-East
- SW: South-West
- TTG: tonalite–trondhjemite–granodiorite
- W: West
- WSW: West South-West

LIST OF FIGURES AND TABLES

- **FIGURES**

- **TABLES**

ABSTRACT

A new gravity survey is carried out in the Kribi-Campo sub-basin in South Cameroon located between latitudes 2˚20’ N - 3˚20’ N and longitudes 9˚15’ E - 10˚00’ E. The data are incorporated to the existing ones, analyzed and modeled in order to elucidate the subsurface structure of the area. The area is characterized in its north-western, southwestern and southeastern parts by considerably high positive anomalies indicative of the presence of dense intrusive bodies. The observed high and low gradient zones are indicative of major and minor faults. We find that, 1) from the analysis of the gravity residual anomaly map, the high positive anomalies observed in the Kribi and Lolabe-Campo areas are the signature of a shallow dense intrusions; 2) the results obtained from the 2D spectral analysis on anomaly grids give a depth to the basement rocks of the basin from 0.60 km to 3.93 km. This represents the thickness of the sedimentary formations overlying the basement; 3) from the multi-scale analysis of the maxima of the horizontal gradient, the Kribi intrusion is confined between depths of 0.5 km and 5.2 km with a density contrast of 0.07 $g.cm^{-3}$ and the Lolabe-Campo intrusion between 0.5 and 2.8 km with a density contrast of 0.13 $g.cm^{-3}$. 4) the results of the application of the ideal body solution and the 2.5D modelling to the Lolabe-Campo intrusion suggest that the emplacement, breaking up and separation of the intrusive igneous body was the outcome of two tectonic events corresponding to an upward vertical translational tectonic movement followed by an anticlockwise rotational faulting tectonic movement. 5) The 3D model the Kribi dense intrusive igneous block is surrounded by sedimentary formations to the south-west and metamorphic formations to the north-east.

The interpretation of the structural map, the 2.5D and 3D models could serve as a guide in the investigation and exploitation of oil, gas and mineral sources in the study area, facilitating the location of points favorable to their existence. These results could also serve as a guide in the identification of risk areas, help in identifying the direction of fluid flow in the subsurface. The interpretation of the sedimentary thickness values can serve to identify areas with the highest mineral and hydrocarbon production potentials which correspond to areas with the highest sedimentary thickness

Keywords: Kribi-Campo, gravity data, modelling, Intrusion, structural map, sedimentary basin.

RESUME

Une nouvelle campagne gravimétrique est effectuée dans le sous bassin sédimentaire de Kribi-Campo, au sud du Cameroun, entre les latitudes 2˚20 'N - 3˚20' N et les longitudes 9˚15 'E - 10˚00' E. Les données sont incorporées aux existantes, analysées et modélisées afin d'élucider la structure souterraine de la zone. La zone est caractérisée dans ses parties nord-ouest, sud-ouest et sud-est par des anomalies positives considérablement élevées, révélatrices de la présence de corps intrusifs denses. Les zones à gradient élevé et faibles observées indiquent des discontinuités majeures et mineures. Nous constatons que, 1) d'après l'analyse de la carte des anomalies, les anomalies fortement positives observées dans les régions de Kribi et de Lolabe-Campo sont la signature d'intrusions denses et peu profondes ; 2) les résultats obtenus à partir de l'analyse spectrale 2D sur des grilles d'anomalie donnent une profondeur aux roches du bassin de 0,60 km à 3,93 km. Ceci représente l'épaisseur des formations sédimentaires recouvrant le sous-sol ; 3) de l'analyse multi-échelle des maxima du gradient horizontal, l'intrusion de Kribi est confinée entre des profondeurs de 0,5 km et 5,2 km avec un contraste de densité de 0,07 $g.cm^{-3}$ et l'intrusion de Lolabe-Campo entre 0,5 et 2,8 km avec un contraste de densité de 0,13 $g.cm^{-3}$. 4) les résultats de l'application de la solution du corps idéal et de la modélisation 2.5D à l'intrusion de Lolabe-Campo suggèrent que, la rupture et la séparation du corps igné intrusif résultaient de deux événements tectoniques correspondant à un mouvement tectonique translationnel vertical ascendant suivi d'un mouvement tectonique rotationnel dans le sens inverse des aiguilles d'une montre. 5) Le modèle 3D du bloc igné dense et intrusif de Kribi est entouré de formations sédimentaires au Sud-Ouest et de formations métamorphiques au Nord-Est.

L'interprétation de la carte structurale, des modèles 2.5D et 3D pourrait servir de guide pour la recherche et l'exploitation des sources de pétrole, de gaz et de minéraux dans la zone d'étude, facilitant ainsi la localisation des points propices à leur existence. Ces résultats pourraient également servir de guide pour l'identification des zones à risque, aider à identifier la direction de l'écoulement du fluide dans le sous-sol. L'interprétation des valeurs d'épaisseur sédimentaire peut servir à identifier les zones à potentiels de production de minerais et d'hydrocarbures les plus élevés correspondant aux zones avec les épaisseurs sédimentaires les plus élevées

Mots-clés : Kribi-Campo, données gravimétriques, modélisation, intrusion, carte structurale, bassin sédimentaire.

1. GENERAL INTRODUCTION

The science of geophysics applies the principles of physics to the study of the Earth. Geophysical investigations of the interior of the Earth involve taking measurements at or near the Earth's surface that are influenced by the internal distribution of physical properties. Analysis of these measurements can reveal how the physical properties of the Earth's interior vary vertically and laterally. Thus, Geophysics can be defined as the study of the body Earth material through physical principles and laws. Such a study is enhanced by observing the behavior of given physical parameters such as density, resistivity, elasticity, magnetic susceptibility, electrical conductivity and radioactivity leading to applied Geophysics.

The success of any geophysical method relies on there being a measurable contrast between the physical properties of the target and the surrounding medium. The properties utilized are, typically, density, elasticity, magnetic susceptibility, electrical conductivity and radioactivity.

Geophysical prospecting therefore helps to decipher information on the nature and the in-situ state of different structure of the earth and propose related geophysical models, to describe internal movement of the earth and to identify their causes.

1.1 Problem statement

Geophysical modelling seeks to determine models of the Earth's physical properties (e.g. density, conductivity) that can adequately reproduce anomalies in geophysical survey data (e.g. gravity, DC resistivity) while being consistent with geologic information. The physical properties are related to mineral structure and, hence, the models are an important source of information for understanding subsurface geology as it applies to mineral exploration. To be reliable, Earth models used for mineral exploration and natural disaster prevention should be consistent with all available geologic and geophysical information. The absence of a model of the earth's structure makes it difficult to understand its geodynamics, to identify and characterize its formations and to evaluate their potential in term of natural resources. Carrying out a geophysical prospecting with the aim of collecting gravity data and geological information, correcting, processing and deriving gravity models which are in return interpreted and correlated with other geophysical results can be a great mean of deciphering the basement, understanding its geodynamics and evaluating its potential in mineral resources. These are two aspects that are important to help achieve the goal of gravity modeling: 1) collect more reliable

gravity data, and 2) increase the kinds of geologic and geophysical information that can be incorporated.

The research of this thesis is aimed at developing subsurface gravity models from land collected gravity data. Considering the absence of gravity data in the Kribi-Campo corridor and the resulting absence of geophysical information specific to this sub-basin, gravity data collection campaign is required which will allow reliable models regarding the subsurface. Once these data have been collected following looping technique, several filters should be applied to remove all effects of non-geological sources. Model appraisal approaches are discussed in more details in sections 3 and 4 of chapter 3, but before models can be quantified and evaluated via those approaches, an important step is to develop methods to incorporate constraining geological information into geophysical gravity modelling. The research in this thesis deals primarily with those steps.

Gravity modelling technology has generally provided some basic functionality for incorporating geologic and other geophysical information into geophysical modelling. The gravity data modelling approach has shown a great importance as it serves as a guide to show where and how the boundaries of the 1D, 2D and 3D geologic model may need to be adjusted to address density excesses and deficiencies. Another aspect of the models is that they can reveal the existence of mineral resource patterns and potential accumulation area which can serve as a guide for mineral exploration. It can also highlight low surface magmatic accumulation which are necessary to the development of geothermal reservoirs which is a great source of energy. Gravity modelling is equally a great tool for deciphering faults, lineaments and tectonic accidents that are usually at the origin of tectonic activities.

1.2 Thesis Objectives

Geological, tectonic and geophysical information available in the study area have helped to an extent to understand the major tectonic movements occurring in the zone rendering it tectonically active. The same information highlighted that the subsurface of south Cameroon is occupied by numerous intrusive bodies which are mainly made of magmatic elements. The lack of gravity data in the Kribi-Campo area has led to few specific information on the nature and characteristics of formations underlying this coastal basin corridor. The main objectives of this thesis are:

- To carry out a gravity survey in the Kribi-Campo corridor in order to provide gravity data that can be utilized for better understanding of this basin structure

- Correct the data in order to eliminate the effects of non-geological sources.
- Apply some gravity filters on the data and help to understand the anomalies evolution within the area. Several two-dimensional gravity anomaly maps will be derived and interpreted.
- Carry out a structural study of the zone with the aim of delineating the lineaments underlying its basement
- Calculating the 2.5 and 3D gravity models to determine the geological and geometrical characteristics of the targeted formations. Structural and mineral implications will equally be discussed.

A specific goal of this research is to develop the best gravity model of the Kribi-Campo sedimentary sub-basin that will not just help to understand its geological and tectonic layout but also contribute in evaluating its mineral potential. Enhancing therefore the geodynamics knowledge of this coastal basin.

1.3 Thesis Overview

This is a manuscript-based thesis and the main part (chapter 3) consists of four research articles. Versions of sections 1 to 4 have been published in peer-reviewed journals at the time of submission of this thesis.

Chapter 1 provides an overall view of the study area from the geological perspective to the tectonic setting through the geographical overview. Previous geophysical studies are equally perused. It is meant to present the existing literature in the studied zone and it functions as an introductory reading before moving to the development of methods and theory provided in the subsequent chapters. Chapter 2 has two main focuses; the first is to present the gravity modelling concept which is anchored on the gravity theory. The second is to describe the gravity surveying techniques that we used to collect the data which we analyzed in this research and to present the methodological approaches that served in their processing and interpretations. Chapter III is divided into four major sections. Section 1 deals with an approach to the collection and correction of gravity data, specifically, the impact of some major gravity corrections on the raw data and their accuracy. Section 2 deals with the determination of structural and geometrical parameters of the Kribi-Campo sedimentary sub-basin. Section 3 is involved in the 2.5D modelling of a high-density formation located in the Lolabe-Campo locality. Section 4 follows with the elaboration and interpretation of the 3D gravity model of the Kribi-Campo intrusive body. The general conclusion closes the thesis by summarizing the

results, discussing their significance, providing a critical assessment of the approaches developed, and mentioning future related research.

To reduce the manuscript length, some mathematical and theoretical details were left out. However, that content is not crucial to the understanding of the results developed herein.

CHAPTER I: TECTONIC AND GEOLOGICAL OVERVIEW

INTRODUCTION

The main issue of any geophysical survey is the mapping of the subsurface of the Earth. Thus, carrying a geophysical survey in any region will help to precise the information over the Earth's subsurface patterns by proposing a geological model according to the physical parameter studied; meanwhile, the results obtained are theoretical and evidences of their relevance can be given if this theoretical model fits with the geology which may be known. In other words, good knowledge of geology is prior to the settlement of any geophysical survey in a given area. Hence geology remains at the centre of any geo-environmental exploration no matter the fabulous progresses of geophysics.

According to the statement above, the current chapter will present

Firstly, the tectonic and geological fundamentals through the Central Africa Pan-African Belt (CAPAB) and Cameroon's geology summary;

Then, a presentation of the study area will be made, regarding especially geological, geographical and geophysical information obtained through previous studies.

1. Tectonic and geological settings

Africa is known as a stable unit which is composed of four main shields or cratons namely: the Cratons of Congo, Kalahari, West-African and Sahara Metacraton. Unlike America or Europe, the African geological history is not very well known due to the lack of researches carried out. Therefore, the available information shows that most of the important deformations caused by tectonic forces occurred at the beginning of the South Atlantic Ocean expansion in the late 500 Ma (approximate age of the South Atlantic Ocean). This geodynamic event caused the breakup of the African shield into actual known shields separated by features called Mobile Zones. One of the interesting features resulting of these tectonic events is the Pan-African Belt (PAB).

1.1. The Pan-African Belt in Central Africa

1.1.1. The Pan-African orogeny

The 'Pan-African' is a system of orogenic belts in Africa, Brazil and Eastern Antarctica. It Pan-African was interpreted as a thermo-tectonic event, some 500 Ma ago, during which a

number of mobile belts formed, surrounding older cratons. The concept was then extended to describe tectonic, magmatic, and metamorphic activities from Neoproterozoic to earliest Paleozoic age, especially for the crust that was once part of Gondwana (Kröner, 1979). The Pan-African orogenic cycle was the result of ocean closure, arc and micro continent accretion and final suturing of continental fragments to form the supercontinent Gondwana. This seems to suggest that the opening of large Neoproterozoic oceans between the Brazilian and African cratons, the West African and Sahara-Congo Cratons; and the African cratons and India/Antarctica resulted from breakup of the Rodinia supercontinent some 800 - 850 Ma (Kröner, 1979).

Within the Pan-African orogeny concept, two broad types are distinguished. One type consisted of predominantly Neoproterozoic supracrustal and magmatic assemblages, many of juvenile origin, with structural and metamorphic geneses that are similar to those in the Phanerozoic collision and accretion belts. Another type consisted of poly-deformed high-grade metamorphic assemblages, exposing middle to lower crustal levels, whose origin, environment of formation and structural evolution are more difficult to reconstruct. Kröner, 1979) provide more highlights on the orogenic mobile belts. Among the Pan-African orogeny, there exist many systems such as the Arabian-Nubian Shield, Mozambique and Zambezi Belt, Lufilian Arc, Damara Belt, Gariep and Saldania Belts, Kaoko Belt, Trans-Saharan Belt among others. We do not extend on them because we will emphasise on the Central Africa Pan-African system.

1.1.2. The Pan-African Belt in Central Africa

The Pan-African system in Central Africa covers three countries (and a part of south western Nigeria that is the Ife–Ilesha schist belt (Caby and Boessé, 2001)): Cameroon, Chad and the Central African Republic where it is known as the Oubanguides Belt. It is sometimes referred to as North Equatorial Fold Belt (Poidevin, 1983; Nzenti et al., 1988). The Pan-African episode in Central Africa and especially in Cameroon is described as rejuvenated magmatic and metamorphic rocks belonging to several Precambrian epochs (Cornachia and Dars, 1983; Ngako et al., 1991; Penaye et al., 1993). These rocks are essentially migmatites and granites.

Within the Pan-African concept, Ngako et al. (2008) describe three main geotectonic units:

The Poli Group represented by an early Neoproterozoic back-arc basin formed between 830 and 665 Ma (Ngako, 1999; Penaye et al., 1993), that includes: detrital and volcanoclastic deposits, metavolcanics (tholeitic basalts and calk-alkaline rhyolites), and pre-, syn- to late-

tectonic calk-alkaline intrusions (diorites, granodiorites and granites) emplaced between 660 and 580 Ma (Toteu et al., 1987 and 2001).

- The Adamawa domain including huge Pan-African batholiths and large-scale Paleoproterozoic remnants that were metamorphosed during the Pan-African history (Toteu et al., 2001).
- The Yaoundé Group represented by a syntectonic basin and a Neoproterozoic belt. The Yaoundé Group comprises the Mbalmayo-Bengbis series, the Ayos series and the Yaoundé series.

1.2. Overview of Cameroon's geology

Cameroon's geological history starts in the Precambrian Era, but the main significant events are 800 Ma post related especially with the South Atlantic's opening in the Tertiary.

1.2.1. Geological data

Cameroon is constituted of a basement complex and superficial structures including volcanic formations and a sedimentary overburden.

- **The basement or basal complex**

The basal complex is essentially made up of Precambrian magmatic and metamorphic rocks rejuvenated during the Pan-African orogeny (Ngako et al., 1991; Penaye et al., 1993). It is composed of metamorphosed and granitised rocks that form the metamorphic complex (gneisses, quartzites, migmatites and charnockites), and platforms formations. Oldest units represent the Cameroonian part of the Congo Craton (CC) in the South (Bessoles and Lasserre, 1977; Regnoult, 1986). The basal complex is correlated with the Dahomeyan of West Africa.

- **The sedimentary overburden**

In the South and the North Cameroon respectively, the sedimentary overburden is represented by Cenozoic and Mesozoic rocks, and recent sedimentary layers. Lower Cretaceous sedimentary formations cover the Bénoué trough, the Mamfé Gulf and Bida. The sedimentary overburden lies on the Precambrian basement.

- **The volcanic formations**

They are represented by volcanic structures related to the tectonic passageway corresponding to the Cameroon Volcanic Line. Volcanic formations also include plutonic formations; some are cambro-ordovician (550 to 500 Ma) hence their relationship with "younger granites" from Nigeria (Regnoult, 1986); others, younger than the previous, belong to the Adamaoua basement like characteristic granites of hossérés (Nyoré, Gouna, Peské, etc.). The volcanic activity which started in the late Eocene is still continuing with the trachybasaltic volcanism of Mount Cameroon (Bessoles and Lasserre, 1977).

Structural geology divides South-Cameroon into two sets (fig.1):

- The CC in the Southern part, represented by the Ntem complex which has not been affected by the Pan-African thermo-tectonic event;
- The central and northern parts, that corresponds to the Central Africa mobile zone, where the Pan-African orogeny occurs. This E-W orogenic zone, the CAPAB, is sited at the Northern edge of the CC and crosses Cameroon, the CAR and reaches Sudan (Penaye et al., 1993; Nzenti et al., 1994; Poidevin, 1983). It may continue to the N-E of Brazil.

1.2.2. Tectonic data

While the Craton part is assumed to be steady, deformations occur in the Mobile Zones that include the Pan-African Chain.

According to tectonic investigations, Mobile Zones have known two main deformation stages termed D1 and D2. These stages are not identical in the Northern as well as in the Southern edge of the Pan-African domain.

- The D1 stage is associated to a W and SW complex over thrust affecting the Eburnean bedrock in the north, while it occurs in the southern edge without any tangential deformation with an indefinite regional significance;
- The D_2 stage occurs in the south with tangential tectonics marked by the setting up of the Yaoundé nappe oriented south towards the Congo Craton. Meanwhile, this stage in north is marked by N-S to E-W echelon or right folds and overfolds related to senestrial strike-slip and sometimes associated to a late D_2 stage marked by N70° to N110° dextral strike-slip faults which is mainly represented by the CCSZ (Ngako et al., 1991)

2. Presentation of the study area

2.1. Geographical setting

The Kribi-Campo sub-basin is located between 2˚20'N and 3˚20'N, and extends over 6150 km^2 offshore and 45 km^2 in a triangular onshore area. It is limited to the South by the Campo high, to the east by the Precambrian basement, and to the North by a possible Aptian salt and/or the northern end of the Kribi Fracture Zone noted Kribi FZ (Figure 1). The western limit of the sub-basin seems to be broadly defined by the Kribi Fracture Zone (Ntamack-Nida et al. 2010)

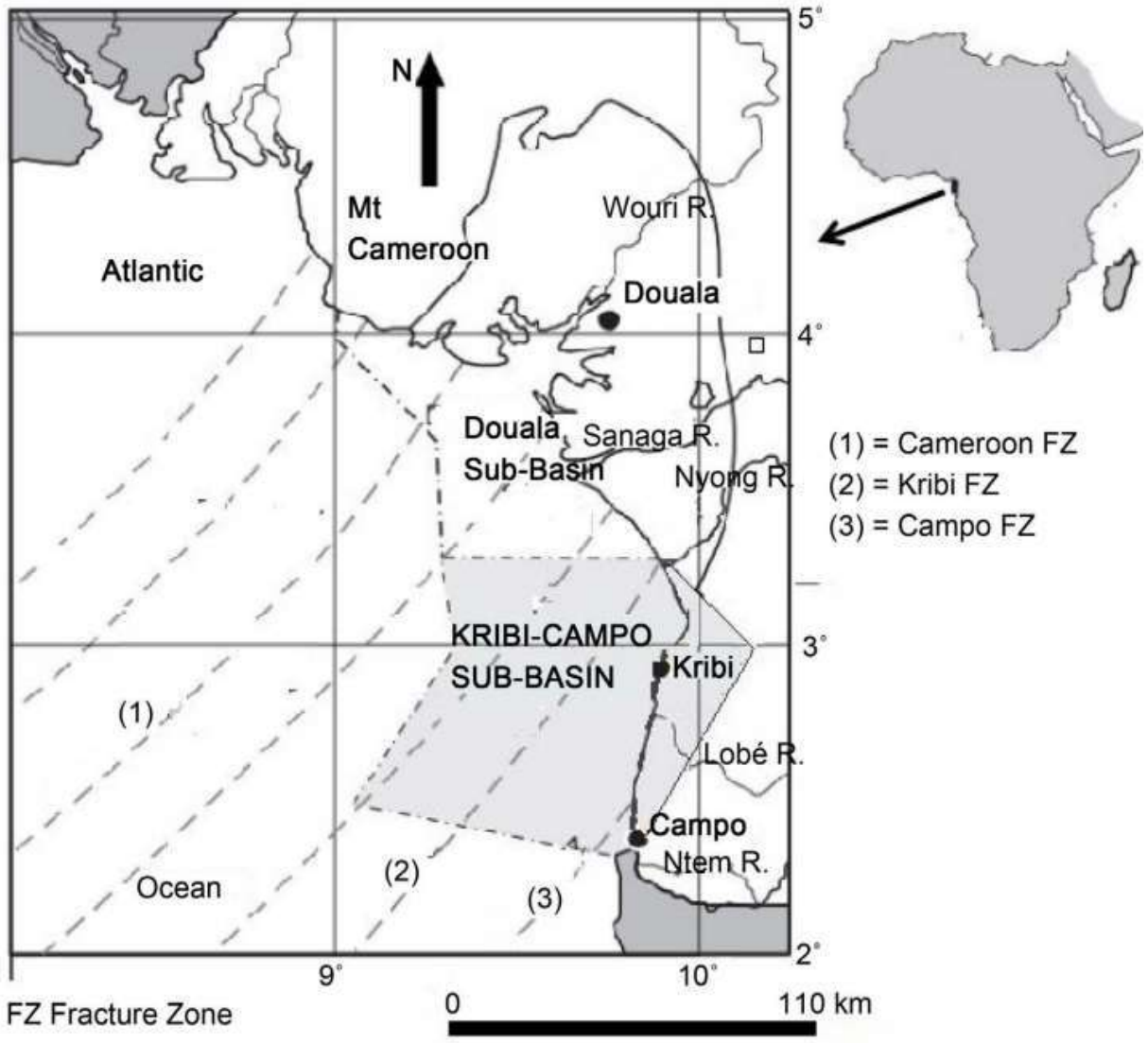

Figure 1: Location of The Kribi-Campo Sub-Basin In Cameroon (West Africa) Between The Main Fractures of The Cameroon Margin (Modified After Ntamack-Nida Et Al. 2010).

a) The climate

The general climate of this region is the equatorial climate characterized by two rainy seasons (from April to June and from September to November) and two dry seasons (from December to March and from July to August). The Kribi-Campo area is located at the coastal area of the region where there are only two seasons: one dry season from December to March and one rainy season from April to November. This area can receive up to 5000 mm of precipitations per year.

b) The relief

The average altitude in south Cameroon is about 700 m. In some areas, we have mountains that can rise up to 1000m.This altitude decreases towards the south close to the Ntem River. For the south-western part, the altitude gets lower as we move from the continent towards the coast and average 100m. The valleys are often very swampy

c) The hydrography

The sanaga, the Kienke, la lobe, lakoundje and the Ntem are the main rivers traversing this area. They flow towards the west in the direction of the Atlantic Ocean. It is to be noted that the main affluent of this hydrographic network are controlled by the substratum fractures. At some areas, geological features can be observed at the aplomb of hydrographic flow, helping thus to correlate hydrology, geologic and geophysical interpretations.

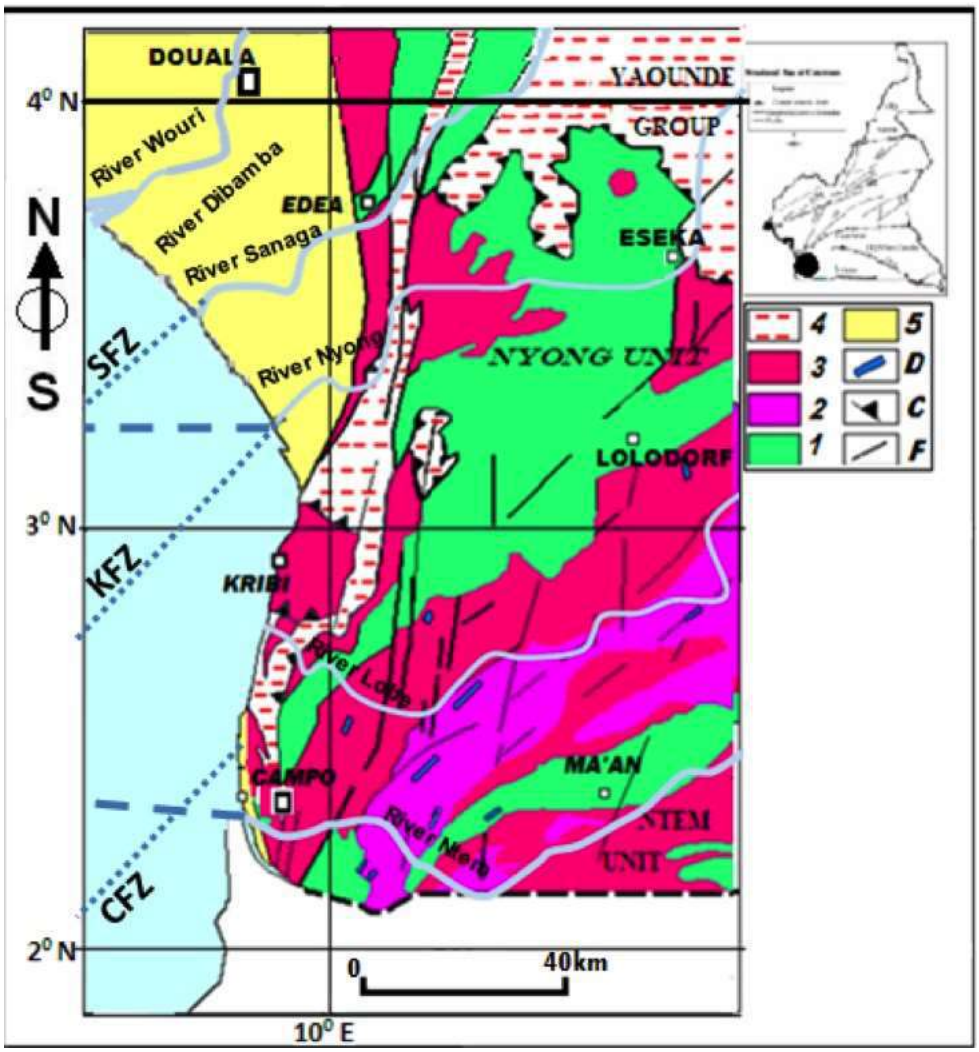

Figure 2a: Structural Map showing the Douala and Kribi-Campo sub-basins of Cameroon (modified from Kue Petou et al. 2017) 1. Archean and paleoproterozoic green rocks belts; 2. Archean charnockites and granitoïds; 3. Gneiss; 4. Granitic mobile zone; 5. Sedimentary basin; C. overlapping; D. Dolerites; F. Faults (SFZ: Sanaga Fault Zone; KFZ: Kribi Fault Zone; CFZ: Campo Fault Zone).

2.2. Geology and tectonic framework

2.2.1. The Congo Craton (Ntem Group)

a) Ntem Complex

The Ntem Complex represents the north-western part of the Archaean Congo craton in Central Africa (Clifford and Gass, 1970; Bessoles and Trompette, 1980) and is very well exposed in southern Cameroon (Rocci, 1965; Maurizot et al., 1986). It is limited to the north by a major thrust (figures 2a and 2b) that marks the contact with the Pan-African orogenic belt (Yaounde group) and is composed of various rock types, with rocks of the TTG (tonalite–trondhjemite–granodiorite) suite constituting the greater part (Nédélec et al., 1990). Three main rock types, the charnockitic suite, granodioritic suite and the tonalitic suite make up this TTG

unit. The tonalitic suite (known as ‘‘Soo granite’’ in Champetier de Ribes, 1957; and as ‘‘Soo tonalite’’ in Nédélec et al., 1990) is essentially exposed to the north and is strongly mylonitized and retrogressed along the fault boundary with the Pan-African orogenic belt, while granodioritic suite massifs form distinct bodies within the dominantly charnockitic southern zone.

Exposures of supracrustal rocks (banded iron formations and sillimanite-bearing paragneisses) that represent remnants of greenstone belts form xenoliths in TTG suite rocks. Late- to post-tectonic granitoids and syenites with alkaline affinity intrude the TTG (Nédélec, 1990; Tchameni, 1997; Tchameni et al., 2000) and clearly postdate the major crustal forming episode. Eburnean (2.1Ga) doleritic dykes (Toteu et al., 1994; Vicat et al., 1996) represent the last magmatic activity in the Ntem complex. Petro-structural studies suggest two major episodes of deformation in this geological domain. The first deformation episode is characterized by vertical foliation, stretching and vertical lineation and isoclinal folds. These structural elements could mark the diapiric emplacement of the granitoids (Tchameni et al., 2001). The second major tectonothermal event is marked by the development of sinistral shear planes trending north–south to N45E, and partial melting of charnockitic and tonalitic members of the TTG suite and the greenstone belt country rocks, described as post-Archaean and post-charnockitic migmatisation by Nsifa (2005).

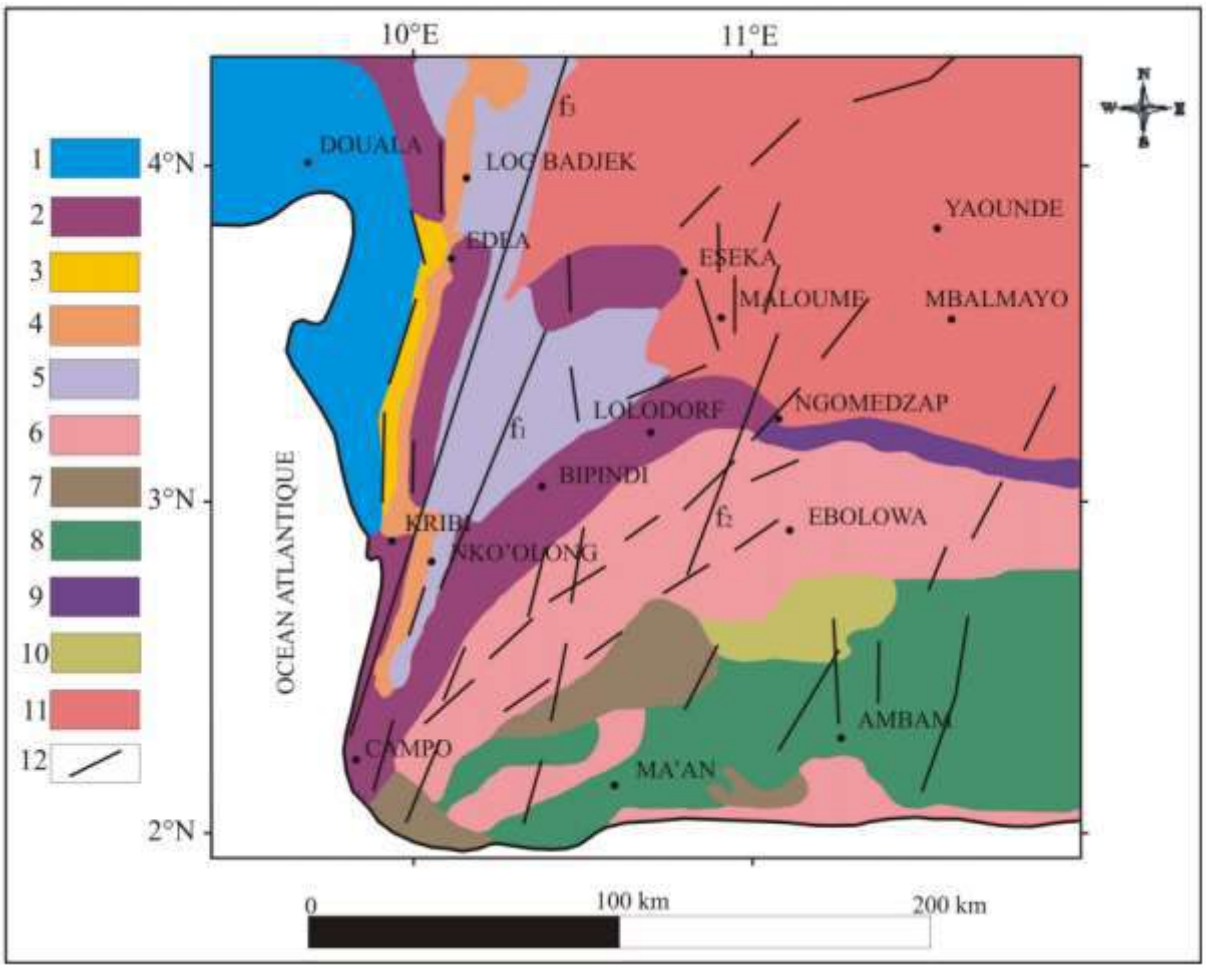

Figure 2b: Geological Map of South-West Cameroon From Nsifa, 2005 (Modified). ***Cameroon Atlantic Coast Basins: 1: Sediments. Nyong Unit: 2: Gneiss; 3: Metagranodiorite; 4: Metamorphic Rocks of The Yaoundé Group; 5: Green Rock Belt. Ntem Unit: 6: Charnockites; 7: Green Rock Belt; 8: Striped Series; 9: Tonalites; 10: Potassic Granitoïdes. Yaoundé Group: 11: Undifferentiated Metamorphic Unit of The North Equatorial Panafrican Belt. 12: Faults. F1 And F2 : Deep Gravimetric Faults (Koumetio, 2004) ; F3 : Kribi-Campo Fault.***

b) Lower Nyong Unit

This series consists of metasedimentary and metavolcanic rocks, as well as syn-to late-tectonic D_2 granitoids and syenites (Pouclet et al. 2007); and displays three groups of a ges (Toteu et al. 1994, Lassere and Soba, 1976, Toteu et al. 2001, Lerouge et al. 2006): (1) Archaean U-Pb ages (2500–2900 Ma) were obtained from detrital zircons in metasedimentary rocks, and presumably magmatic zircons in charnockites and migmatitic gneisses; (2) Palaeoproterozoic U-Pb zircon ages of ca. 2050 Ma corresponding to a thermometamorphic event associated with an important crustal melting and emplacement of some granite and syenite massifs, and (3) a Neoproterozoic U-Pb zircon age of 626 ± 26 Ma corresponding to

the metamorphic effect of Pan-African thrusting. This unit includes some Archaean parts of the Ntem Complex that were reworked during a Palaeoproterozoic event, and new Palaeoproterozoic material that was accreted to the Archaean craton.

2.2.2. Yaounde Group

The Yaounde Group is located at the North of the CC and stretches from West to East. It is represented by the Yaoundé series and the Mbalmayo-Bengbis series.

The Yaounde series is made up of gneisses and migmatites garnets coming from old granitised and metamorphosed sediments in the high-pressure granulite facies. It constitutes the heart of the Pan African thrust (Nzenti et al, 1984 and 1988; Nédelec et al, 1986). Metasedimental granulitic gneisses are found around parallel 4°N (Yaoundé) but we can also find synmetamorphic igneous rocks at the vicinity (Nzenti et al, 1988).

The Precambrian basement of the area, as that of the whole Yaoundé series (figure 2), comprises two geological facies: gneisses associated with micaschists (ectinites), and migmatitic garnetiferous gneisses (migmatites). These rocks somehow contain rutile and opaque minerals (graphite and titanium iron oxides). The Yaoundé Group comprises the low-grade Mbalmayo schists, interpreted as the sole of the nappe (Nédelec et al., 1986), the medium-grade micaschists and the Yaoundé high-grade gneisses. In the Lomié region, the Yaoundé nappe overthrusts the Dja Group composed of schists and dolerites of assumed Paleoproterozoic age (Poidevin, 1983). Two main tectonic phases affect the Yaoundé Group (Nzenti et al., 1988): a layering resulting from tectonic transposition marks D1; D2 corresponds to tangential tectonics with isoclinal folds and flat-laying shear zones associated with S2 schistosity and N0–N20 stretching lineation. Low-temperature mylonitic shear zones developed in the same stress field than D2 mark a late-D2 phase. D3 is marked by the development of N70 dextral shear zones indicating a later E–W compression. The D1–D2 transition is characterized by the emplacement of plutonic rocks and corresponds to the peak of HP granulite facies metamorphism (T = 750–800 C and P = 1000–1200 MPa), which triggered a widespread migmatization (Nzenti et al., 1988). The nappe tectonics was initiated under high-grade conditions and ended under medium to low-grade conditions. From recent geochemical and isotopic data, the metasediments of the Yaoundé Group are considered as post-626 Ma orogenic-related deposits (Toteu et al., 2001).

3. Previous geophysical studies

Previous geophysical studies in this area include gravity, magnetotelluric, seismic and others. Gravity studies include those from Koumetio (2017); Koumetio et al. (2014, 2012); Owona Angue et al. (2011, 2013); Owona Angue (2012); Tadjou et al. (2009, 2008); Mbom Abane (1997); Poudjom et al. (1995); Dumont (1986); Collignon (1968) Magnetotelluric studies include those Manguelle-Dicoum et al. (1992) and Njingti et al. (2017)

Seismic studies include those from Tabod et al. (1992); Tokam Kamga (2010); Ntepe et al. (2004) and Ateba et al. (1992).

In 1968, Collignon proposed one of the first gravity anomaly maps of Cameroon highlighting the very first boundaries of the craton of Congo. The main directions defining the putting in place of volcanic and tectonic activities were also underlined in his studies. In the following interpretations, the author suggests that the lithology of the region is more influenced by old and deeper units.

Tabod (1991) from seismic data along the Cameroon Volcanic line, established the first seismicity map of Cameroon (figure 3). This map highlights the depths of the earthquake focal points over the territory. As observed on figure 3 the focal points for the earthquakes that occurred around the Kribi Campo area are located at depth superior or equal to 30 km. This is an evidence of the fact that, this region is still active. Several following studies have confirmed these results namely Ateba et al., (1992), Ntepe et al. (2004) and Tokam Kamga et al., (2010).

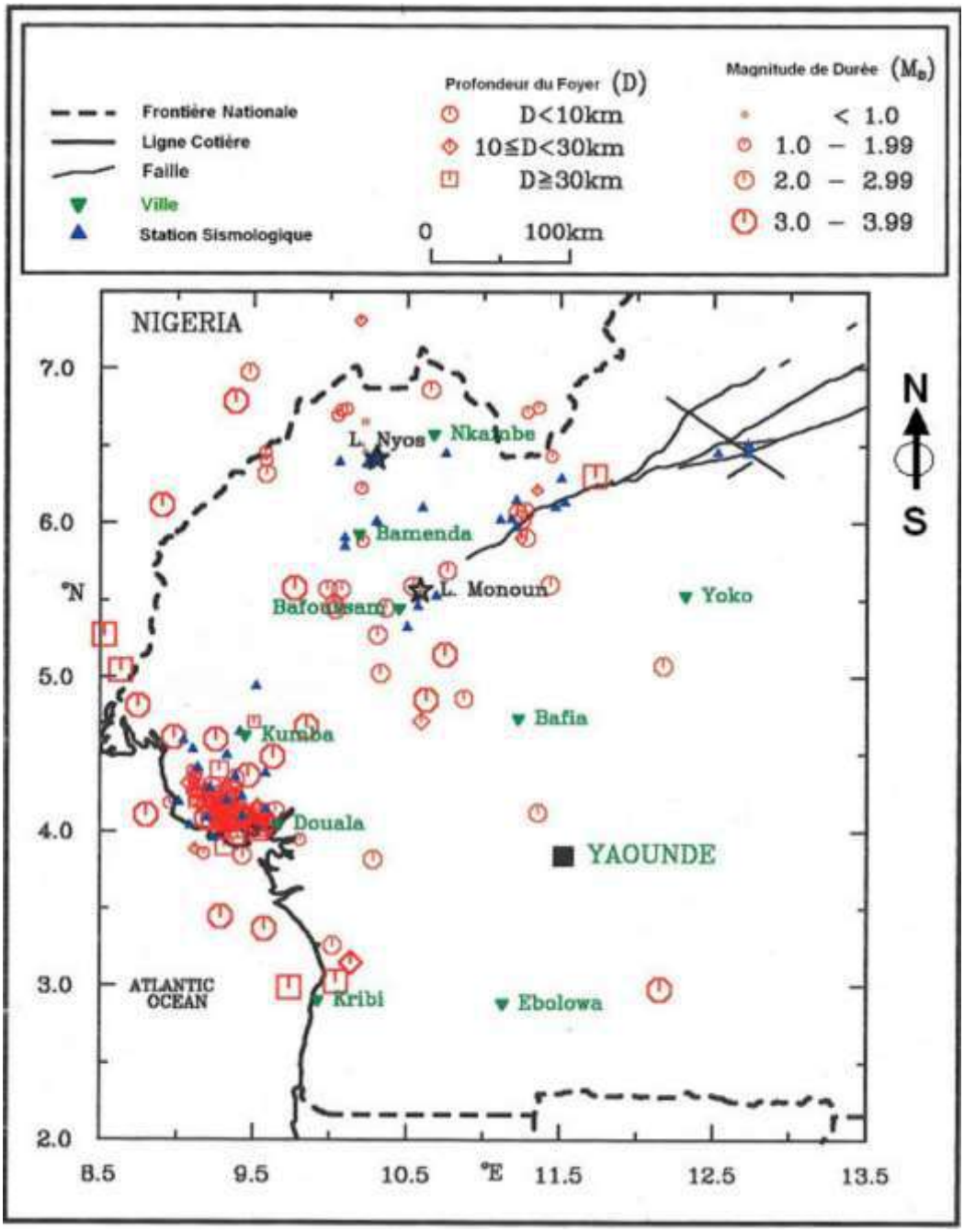

Figure 3: Seismicity map of the west Cameroon (Tabod, 1991).

Manguelle-Dicoum, 1988 and Manguelle-Dicoum et al., 1992 studied the structure of the basement of the septentrional boundaries of the craton of Congo. They indicate that there is outpouring of the formations of the panafrican unit over the formations of the craton of Congo.

Poudjom et al. (1995), four years later in their estimations of the depth of the crust from gravity data, carried out a first evaluation in the Kribi Campo and craton of Congo areas. Their conclusions indicate that, the crust is thin beneath the basin and thicker beneath the craton.

Ntepe et al. (2004) investigate the seismicity of the Kribi region following an earthquake that occurred in the region two years earlier. Their analysis coupled with previous events that happened in the region suggests the existence in the area, of a tectonic activity caused by a fault system known as the Kribi-Campo fault. This fault is said to be an extension of the Sanaga fault (Ngako et al. 2003). In the same study, the authors evaluate the risks potential of the area and find that, over a 25 km radius around Kribi is the most exposed zone to tectonic activities.

Tadjou et al. (2008, 2009) propose a gravity model of the transition zone between the craton of Congo and the Panafrican belt. Their results agree quite well with those of Poudjom et al. 1995 and Tokam Kamga et al. 2010 on the thinning of the crust beneath the basin and its thickening beneath the craton. The gravity model proposed by these authors suggests a collision between the basin and the craton followed by an inverse fault with an outpouring of the formations of the craton over the Panafrican. Their model obtained in 2009 is shown on figure 4

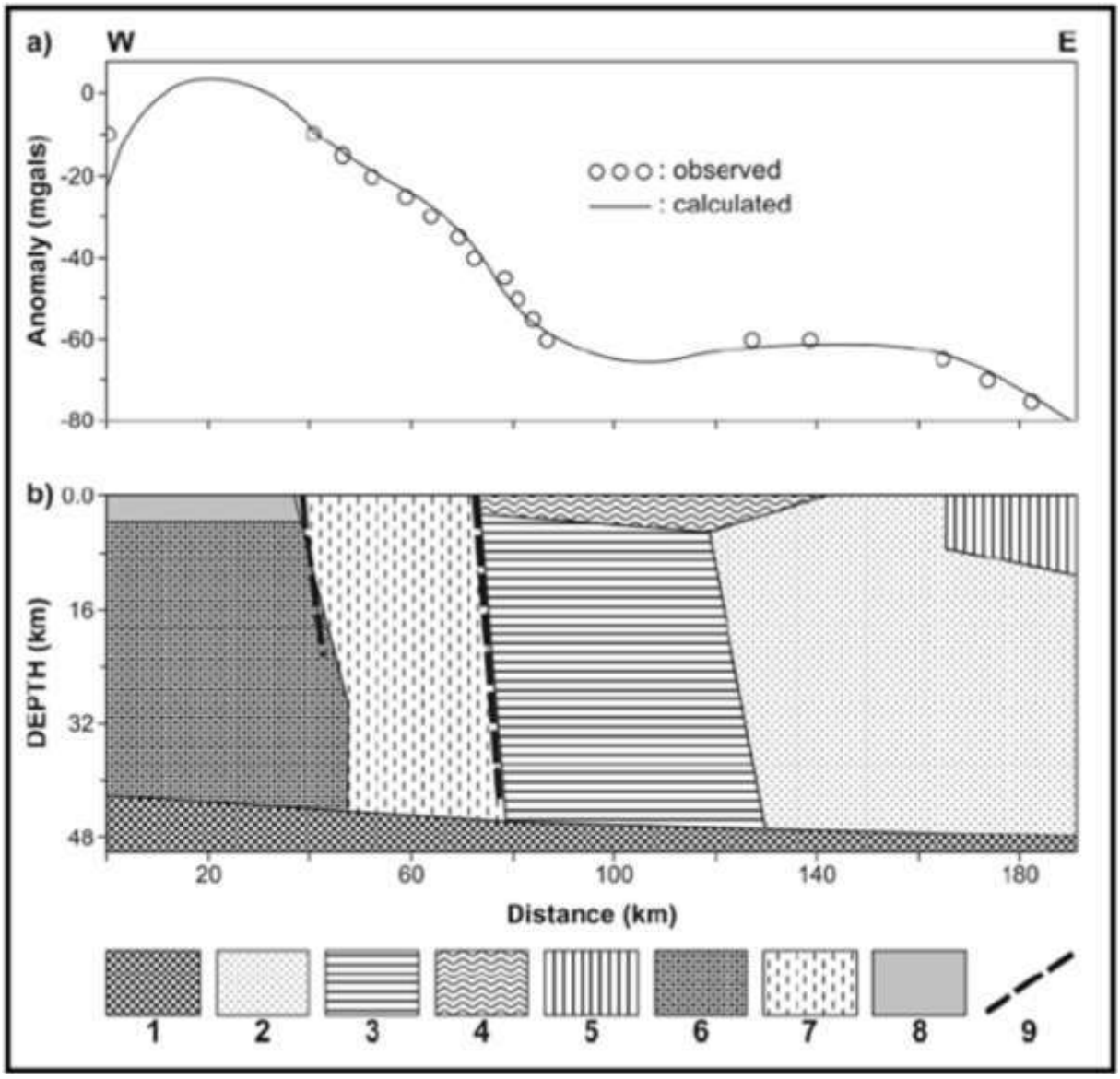

Figure 4: Gravity Model of the E-W Profile as Proposed by Tadjou et al. (2009). A) Theoretical Curves of Observed Anomalies. B) Proposed Model of Structures: 1) Upper Mantle; 2) Ntem Unit (Craton of Congo); Nyong Unit (Eburnean); 4) Green Rock Belt (Craton); 5) Gneiss (Craton) 6) Syenite (Panafrican Deep Structures); 7) Granilites; 8) Phanerozoic Cover; 9) Faults.

Tokam Kamga (2010) proposed a model of the crust over Cameroon from the interpretation of seismological data collected between 2005 and 2007. The velocity models obtained suggest on one hand that the average depth of the Moho under the craton is 45 km and 28 km under the Kribi-Campo domain (figure 5). On the other hand, these models suggest the presence a mafic type of rocks occupying the lower crust

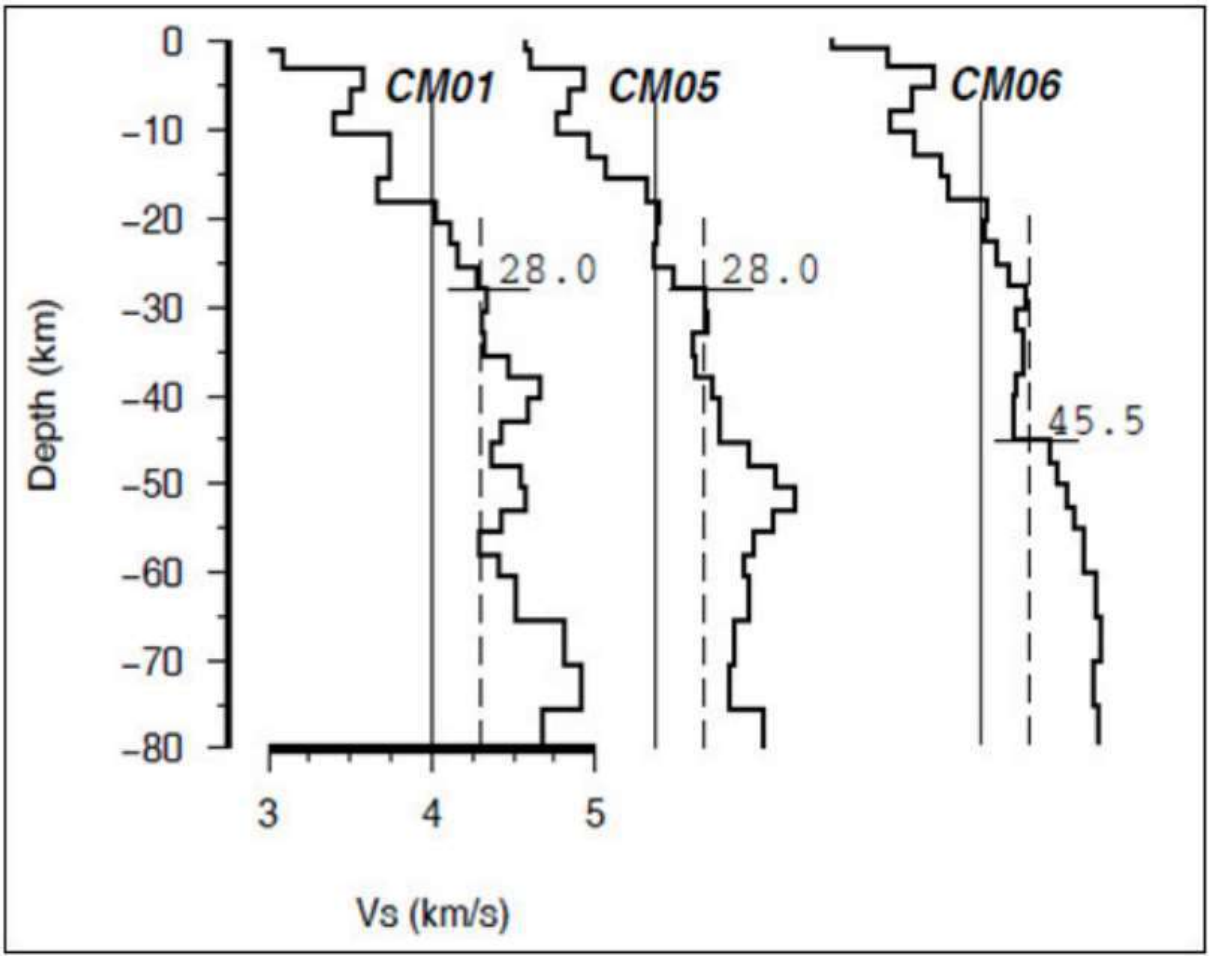

Figure 5: Velocity Models for the Crust and Upper Mantle for the Seismological Stations Collected Between 2005 And 2007 In South-West Cameroon (Tokam Kamga et al., 2010).

In order to ameliorate the gravity model proposed by Tadjou et al. (2009) Owona Angue et al. (2011) and Owona Angue (2012) propose a gravity model from a profile extending from Kribi to Lolodorf. The model (figure 6) shows that the granulites resulting from the intrusion of magmatic and metamorphic rocks represent the East border the Kribi-Campo sedimentary basin and are located on the West borders between the craton of Congo and the panafrican belt. The authors indicate that these boundaries belong to Kribi-Campo fault, which is supposed to be the continuation of the Sanaga faults. However, the model proposed by Owona Angue et al., (2011) differs from the one proposed by in that, the orientations of the panafrican structures and the fault system agree with the notion of the outpouring of the panafrican structures over the craton formations. The same author proposes a 2D resistivity model of a profile in the study area. This model (figure 8) presents two resistant blocks of rocks separated by a less resistant block. This model will be subject to further characterization by Koumetio et al. (2014).

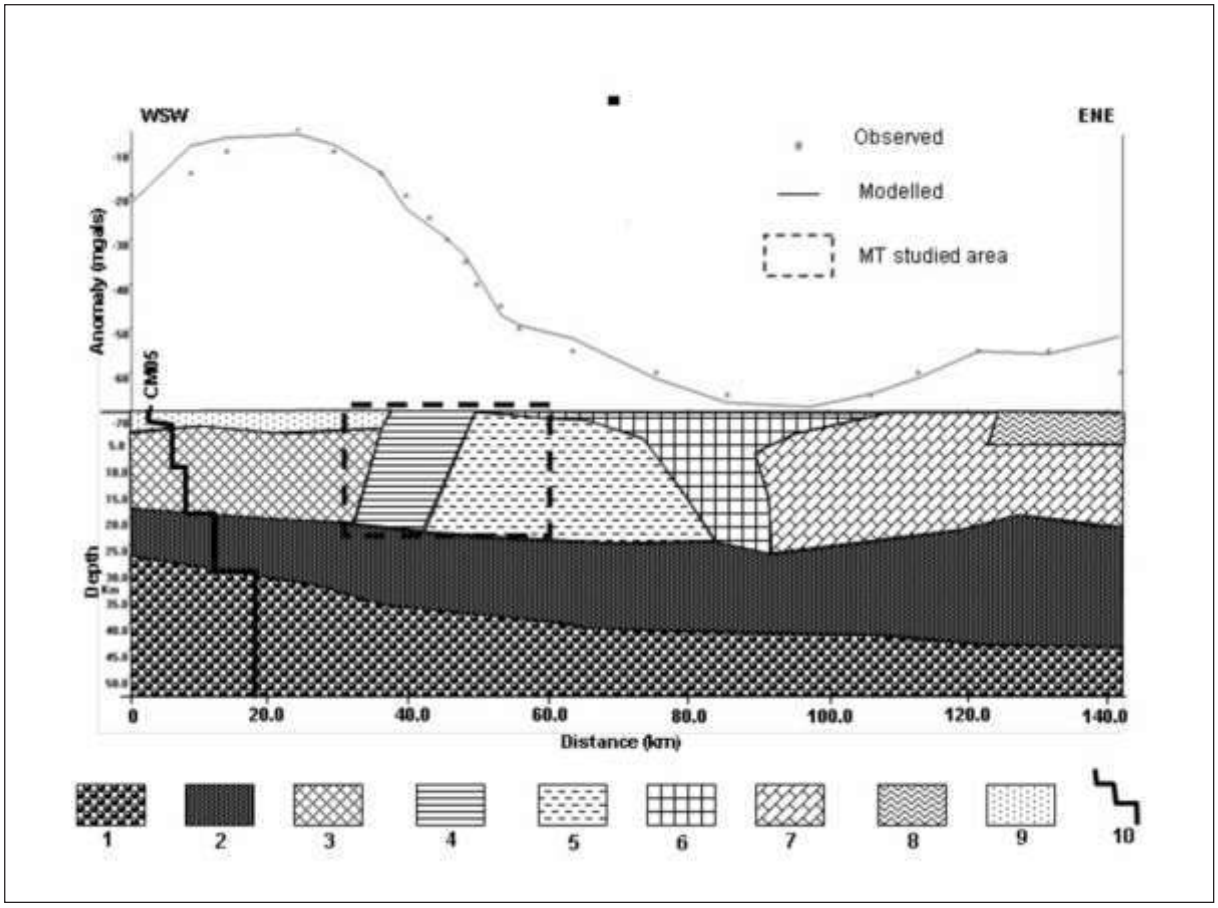

Figure 6: Gravity Model Proposed by Owona et al. (2011). 1. Uppermost Mantle D^1= 3.22 G/Cm^3; 2. Lower Crust Mafic Layer D_2= 3.04 G/Cm^3; 3. Syenite (Panafrican Belt) D_3= 2.93 G/Cm^3; 4. Granulites (Panafrican Belt) D_4= 2.86 G/Cm^3; 5. Nyong Unit (Erbunean) D_5= 2.78 G/Cm^3; 6. Granite Of Ntem Units (Congo Craton) D_6=2.64 G/Cm^3; 7. Greenstone Granitoids D_7= 2.69 G/Cm^3; 8. Gneiss (Congo Craton) D_8= 2.76 G/Cm^3; 9. Phanerozoic Cover D_9= 2.43 G/Cm^3; 10. Average Velocity Model For The Kribi-Campo Tectonic Province Shown At The Approximate Location Of The Station CM05.

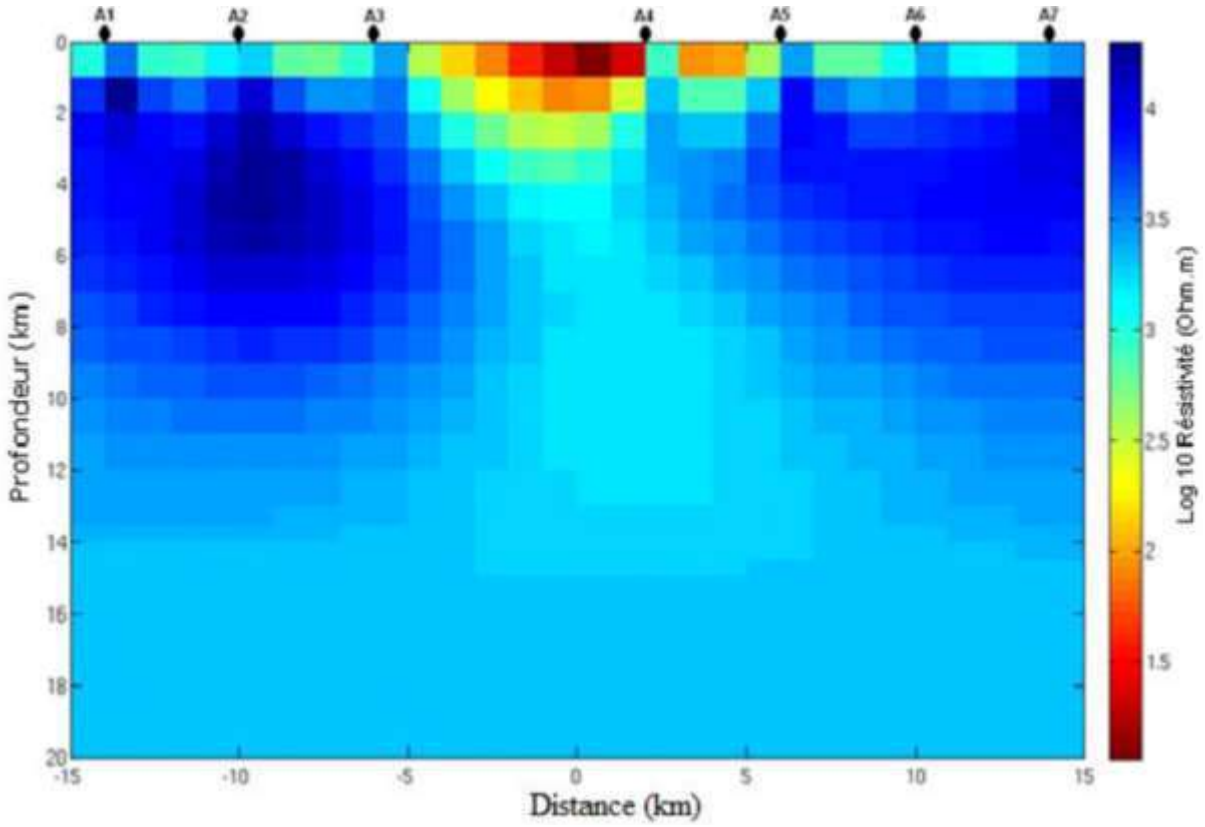

Figure 7: 2D Inverted Resistivity Model Proposed by Owona et al. (2012).

Koumetio et al. (2012, 2014) and Koumetio, 2017 carried out an investigation using the gravity method of the South-West region of Cameroon with structural and tectonic implications. From the processing of old gravity data (collected in 1965 during the reconnaissance campaign in Cameroon by Collignon) through the choice and interpretation of filtered regional and residual gravity anomaly maps, among other results obtained from his study are the following:

- The substratum of the Douala sedimentary basin is denser than that of the Nyong Unit;
- The low-density intrusive bodies which are deeper than the others are predominant in Bipindi and Pouma;
- The predominant high-density intrusive bodies are found in the regions of Lolodorf; Matomb-Gog Mapubi and Kribi-Edea;
- The south region of Cameroon is afftected by distensive and multidirectional tectonics
- The Bipindi intrusive body could be composed of syenites nepheline while the Kribi-Edea intrusions are composed of dolerites, tonalities and syenites alcalines.

In 2012, they presented a 2.5 model of a profile along the Kribi-Edea Zone (figure 8). The model shows two blocks of the same type of igneous rock with a density contrast of 0.167 g

cm^{-3} in comparison with the density of the surrounding metamorphic rocks confined between 0.9 and 9.3 km.

In 2014, just two years after, the same authors presented a 3D model of the Bipindi low density intrusive rock (figure 9). The 3D model of Bipindi zone shows two dissymmetrical blocks of the same type of rock with a density contrast of − 0.095 $g \cdot cm^{-3}$ in comparison with the density of the surrounding metamorphic rocks. Confined between 1 and 14 km depth and situated in the senestral shear zone they are said to be composed of nepheline syenites

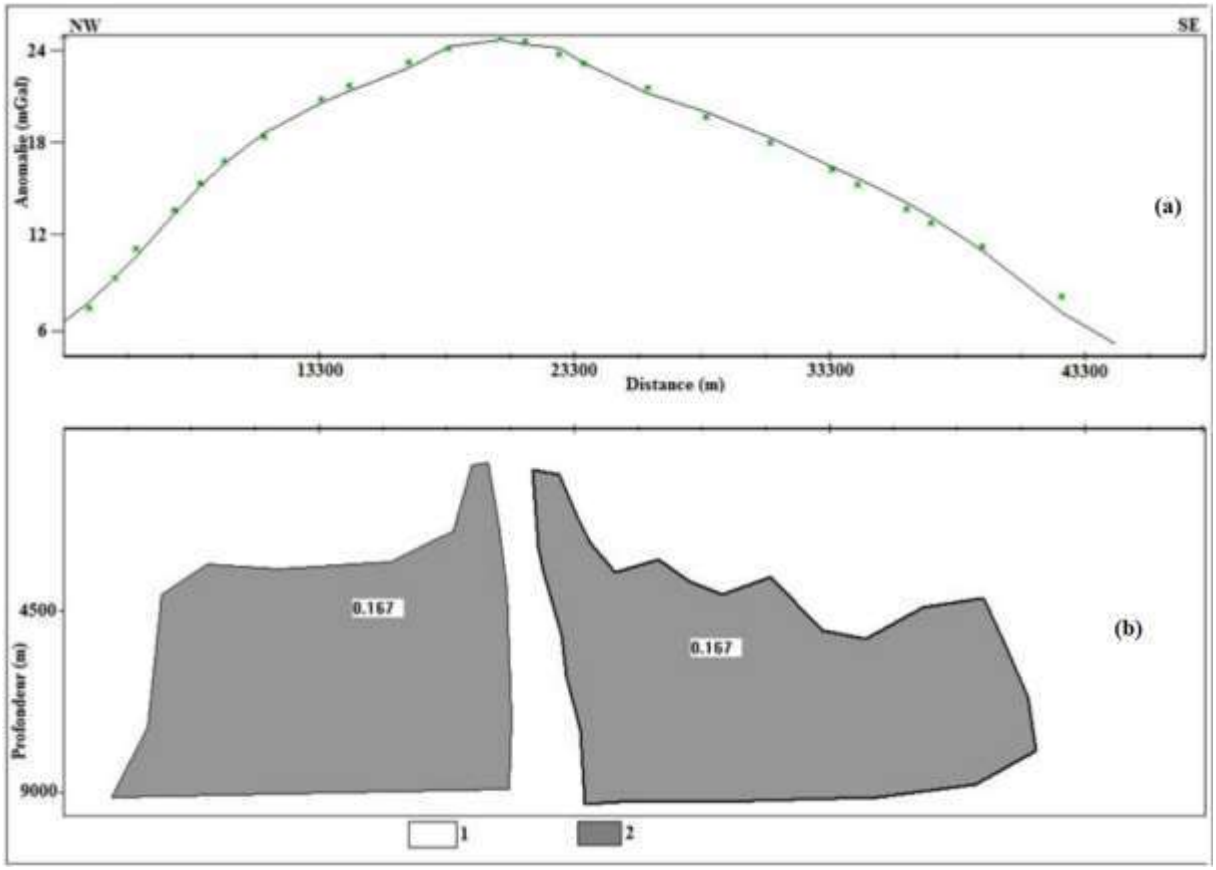

Figure 8: A 2.5D Model of Profile AB. (*A*) Experimental Residual Anomaly and Theoretical Curve. Asterisks: Observed Anomaly; Solid Curve: Calculated Anomaly. (*B*) Interpretative Structure Model: 1, Metamorphic Rocks; 2, Igneous Rocks. (Koumetio et al. 2012).

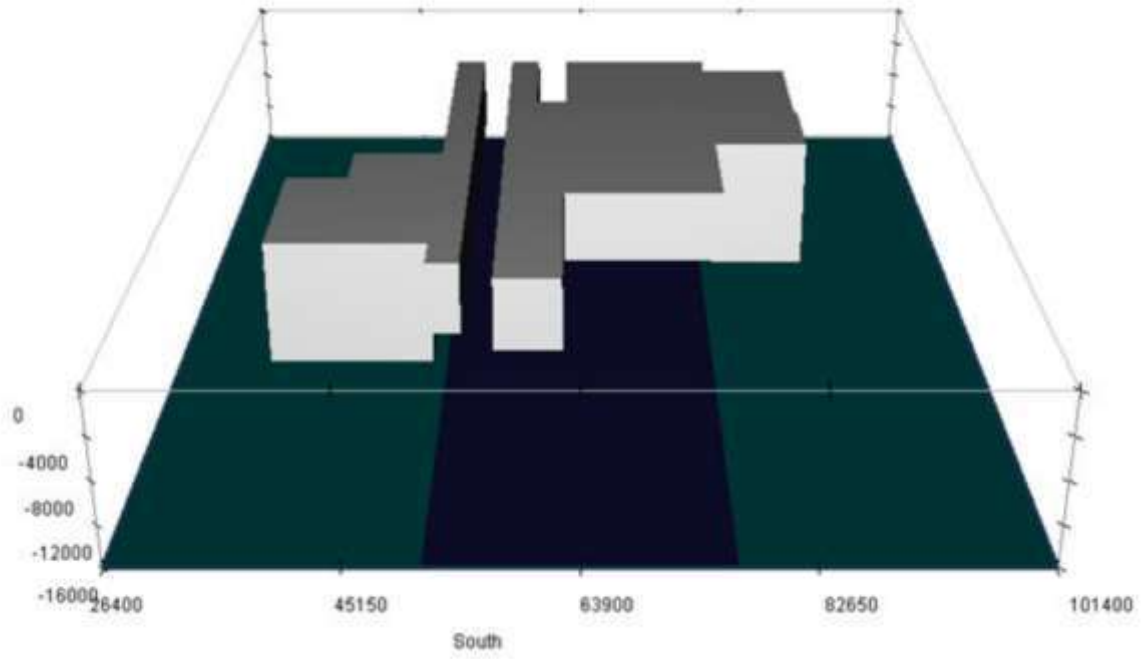

Figure 9: 3D Model of The Intrusive Body of Bipindi (Kometio et al. 2014).

4. Conclusion

The previous studies presented in this chapter have contributed extensively to the understanding of the south-west Cameroon subsurface structural layout. Some of the main conclusions that can be outlined from this review are:

- The subsurface of south-west Cameroon is traversed by many faults, the main one being the Kribi-Campo fault which is the continuation of the Sanaga fault. This region is tectonically active.
- Geophysical and geological data have led to the interpretation of a continent to continent type of collision followed by an overlapping of the craton of congo by the north equatorial panafrican belt. In this transition zone between these two massive continental blocks, a succession of compression and distention movements is observed giving birth to the numerous faults delineated.
- The region's subsurface also presents numerous intrusive bodies, some of which have detailly been characterized in the works of Koumetio 2017.
- Most of the results presented in these studies are of a regional scale and highlight the subsurface features on a broader extend of south Cameroon. The main results in the works of Koumetio, 2017 are focused mostly on the central portion of south-Cameroon. The western portion of the subsurface, which constitutes the Kribi-Campo sedimentary

sub-basin have less been deciphered. This can obviously be explained by a couple of reasons; until the initiation of this research, this area had not been subject to a land gravity survey. Part of this area is found in a dense equatorial forest into which access was difficult except for open fields and roads and also because of the presence of the Campo-Ma'an national park that covers a portion of the area and the Ntem river flood plains which are very swampy, woody and extremely inaccessible by foot. The Kribi-Campo corridor, given the impracticability of most of its roads and its position in the edge of the equatorial forest coupled with the swampy nature of the soil, was not covered during the 1965 reconnaissance gravity campaign carried out by Collignon. Less information is therefore known in this section of south Cameroon with an immense potential in natural resources. This lack of data in the basin area has resulted to the lack of focused geophysical information in the zone making all the known information to derive either from other geophysical methods or from satellite data which provide less precise results. Insights on the Kribi-Campo sub-basin area have therefore not been highlighted so far. This will constitute the main focus of this thesis.

- The data that have led to these conclusions derived from the 1965's geophysical survey carried out by Collignon which on their own are too sparse making it difficult to derive results in the area.

We can therefore mention an insufficiency in terms of the knowledge of the structure of the crust in the Kribi-Campo sedimentary sub-basin, also in terms of the nature and the geometrical proportion of the formations constituting it. The gravity model of the sub-basin subsurface structure is still unknown.

CHAPTER II: MATERIALS AND METHODS, FROM GRAVITY THEORY TO GRAVITY MODELLING: UNDERSTANDING THE CONCEPT AND THE METHODS

2.1. Introduction

Gravity prospecting involves measurements of variations in the field of the earth. One hopes to locate local masses of greater or lesser density than the surrounding formations and learn something about them from the irregularities in the earth's field. It is not possible however to determine a unique source for an observed anomaly. Observations normally are made at the earth's surface. Like magnetics, radioactivity, and some electrical techniques, gravity is a natural-source method. Local variations in the densities of the rocks near the surface cause little changes in the gravity field. Gravity and magnetics techniques often are grouped together as the potential methods.

A successful interpretation of gravity data requires a methodic approach. This is achieved through a very good data acquisition, followed by data corrections in other to eliminate the effects of non-geological sources and the interpretation to provide with physical models that best represent the structure of the studied basement.

2.2. The gravity theory

2.2.1. Gravity field and shape of the earth

Gravity prospecting was developed from the study of the earth's gravitational field. This subject is of great interest to geodesists to determine the shape of the earth. Given that the earth is not a perfect homogeneous sphere, gravitational acceleration is not constant over the earth's surface. The gravity magnitude depends on five main factors: latitude, elevation, topography of the surrounding terrain, earth tides and density variation in the surface. Gravity studies are more concerned with the changes due to the last factor. These changes called gravity anomalies are often smaller than the changes due to latitude and altitude

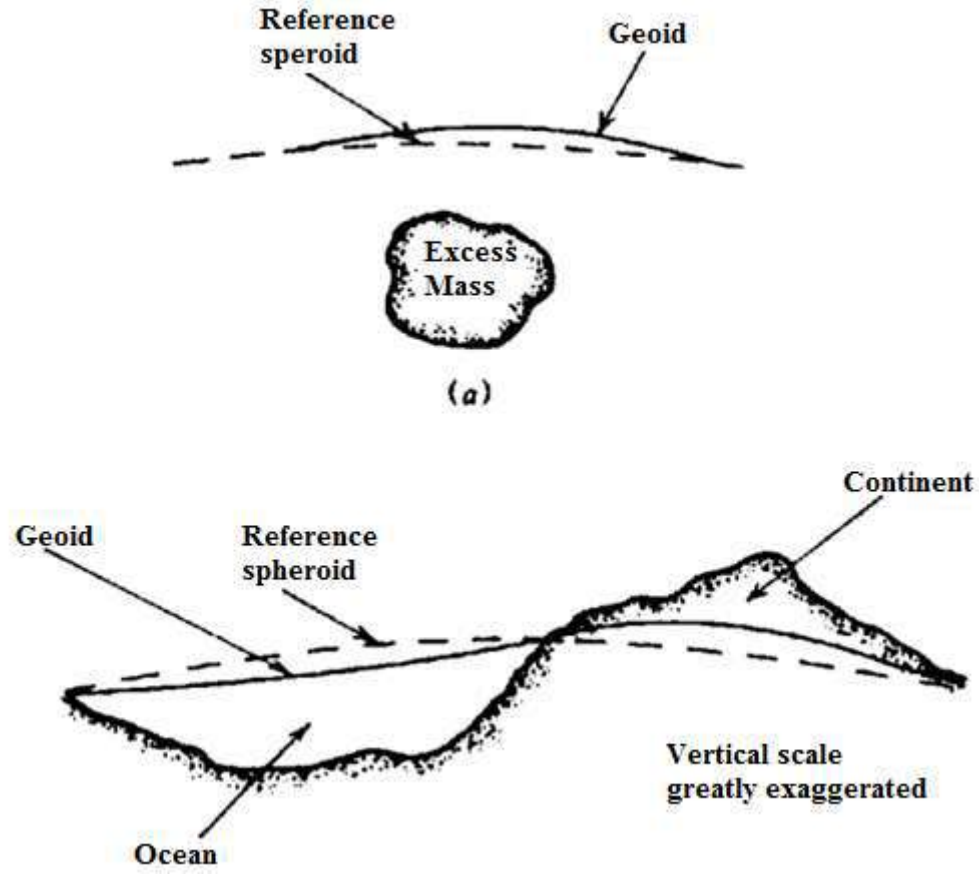

Figure 10: Comparison of Reference Spheroid and Geoid.

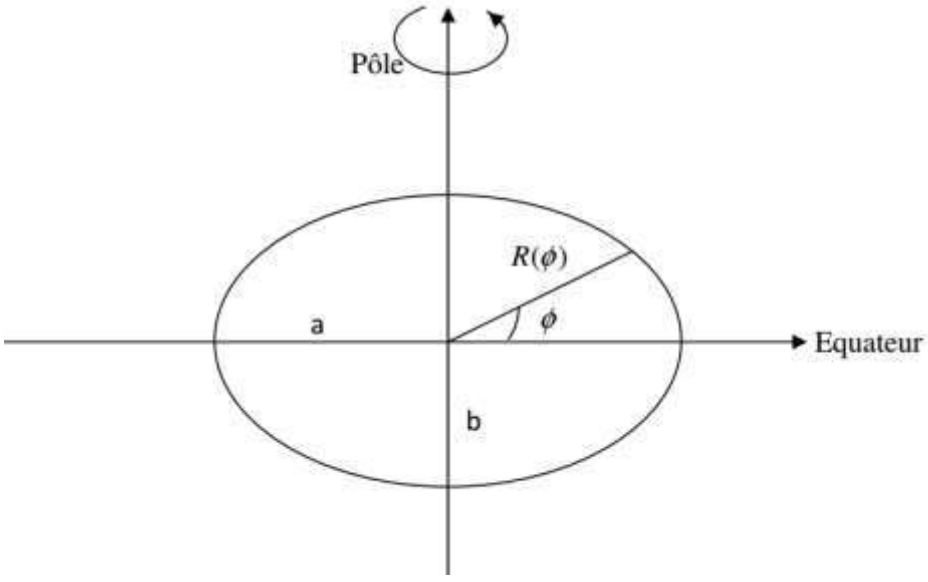

Figure 11: A Simplified Model of The Earth: Ellipsoid of Reference.

In the simplified model of the earth, the disturbing masses located in the upper part of the crust can induce changes of the order 5.10^{-5} g which is about 0.5 Gal. The effect due to tidal force

can reach 3.10^{-7} g which is about 0.3 Gal (Balmino, 1986). The difference between the radius at the equator (a) and at the poles (b) divided by the former ($f = \frac{a-b}{a}$) is called flattening (figure 11).

Theoretically, it is possible to calculate this shape assuming that the earth has a fluid shape rotating around an axis and with a density that increases with depth, even though this variation is not uniform. This density values vary from about $3g/cm^3$ at the crust level up to 12 g/cm^3 at the center of the earth. The surface of this theoretical earth is the gravity equipotential surface. This surface is called ellipsoid of reference (figure 10). The gravitational field vector is normal to this surface at all points. It's relative to this ellipsoid that gravity anomalies are calculated. The reference ellipsoid can be defined as a mathematical surface which is function of the gravity at each point of the surface. We obtain the value of g at every point of the reference ellipsoid from a formula adopted by the International Union of Geodesy and Geophysics. This formula, called International Gravity Formula (IGF), is written as:

$$g = 978032,7(1 + 0,0053024 \sin^2 \Phi - 0,0000058 \sin^2 2\Phi)\ mGal. \quad (2.1)$$

where g is the theoretical gravity and Φ *the latitude*

The equatorial radius of the corresponding ellipsoid is a = 6 378,137 km and its flattening f = 1 / 298.257. Note that formula (2.1) was adopted in 1980 to replace an older version dating back to 1967, which replaced the first formula dating back to 1930.

However, the expression of the gravity formula (2.1), despite its good accuracy, is also only a rough approximation. It assumes that there is no undulation on the surface of the earth, when in fact there are medium altitudes of 500 m, altitudes and depths of the order of ± 9000 m above sea level (Telford et al., 1976). The true level of the sea is influenced by these variations; the observer must therefore take this into account when measuring elevations. The geodesist defines an experimental middle level of the seas to do these measures. This average level, obtained in the absence of the Ocean current and by calculating the averages in time in order to cancel the effect of ocean tides, is called geoid. It is a physical surface, a real equipotential of the earth. It is obvious that the geoid and the reference ellipsoid do not coincide in all their points since the geoid is deformed up under the continents by the attraction of the masses above, and down on ocean basins. However, the difference between the two surfaces does not exceed 50 m (Telford et al., 1976).

2.3. The gravity surveying

2.3.1. Field operations

The absolute measurement of gravity is usually carried out at a fixed installation by the accurate timing of a swinging pendulum or of a falling weight. Relative gravity measurements may be made in various ways. Three types of instruments have been used: the torsion balance, the pendulum and the gravimeter (or gravity meter). The latter is the sole instrument now used for prospecting. The others having only historical interest (Telford, 1976).

Gravity data acquisition procedure is based on two main techniques:

The first consist of considering all measurement stations as base stations. After measuring the relative gravity value at the first station S_1, we move to station S_2 to measure and come back to station S_1 and move again to station S_2. Station S_2 becomes at this point the base station from which S_3 can be measured. This procedure is repeated until the last station Sn. This technique means that 4 shuttles have to be done at one station which makes this technique costly in time consuming. Nevertheless, this approach is more accurate.

The second technique, as illustrated on figure 12, consist of defining a base station S_1 where measurements are taken, moving to station S_2, S_3, ……Sn and coming back to station S_1 at the end to close the measurement loop. It is required to close the measurement loop before 24 hours in other to avoid the influence of the rotation of the Earth, the position of the sun and the moon. Two values taken at the same station in different periods are never the same. The difference is called drift.

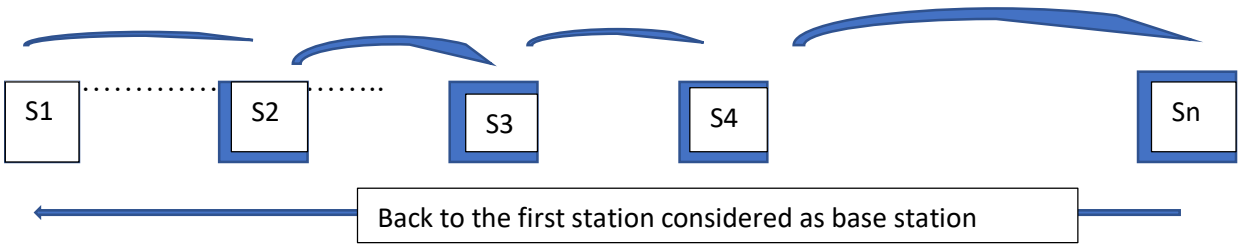

Figure 12: Illustration of The Measuring Loops.

Readings are taken by placing the instrument on the ground and levelling it. This is call calibration. Theoretically, calibration can be carried out by tilting because a precise geometrical system is involved, but this is not the usual procedure. Generally, readings are taken at two or more stations where the value of g is already known. If the value of δg between the stations is large enough to cover a reasonable fraction of the instrument range. A linear response is usually assumed between them. However, one should occupy several additional stations if possible. This calibration can be automatic with the latest instruments. Another aspect of reading a gravity meter concerns seismic activity or cultural movement such as those of vehicles or people. These will disrupt the readings (the meter is actually a low frequency seismometer). If this occurs, all operations should be stopped.

a) A step by step measurement procedure using the Lacoste-Romberg gravimeter

- Identify the measuring station and place the gravimeter support plate, then check the horizontality of the station using the water level of the base.
- Record the geographical coordinates (latitude, longitude, altitude) at the station.
- Remove the gravimeter from its box (this is done twice to avoid any shock) and put it on the station.
- Check that the temperature is at 50^0C
- Adjust the horizontality of the gravimeter by using the circular knobs of black colors for the centralization of the water level. The left knob adjusts the water level on the right and the right knob adjusts the water level on the left.
- When horizontality is assured, open the mass. The pointer of the frame begins to oscillate immediately.
- Stabilize and centralize the dial hand using the graduated metal knob located in the center of the gravimeter. This wheel also reads the decimal part of the displayed value.
- Once the pointer is stabilized and centered, close the mass and read the displayed value.
- This gravimeter gives us the variation of gravity in mGal.

NB: Proper handling of the gravimeter requires softness and finesse in the fingering. For a good reading, we must stand in front of the screen; we use a parasol for better readability.

This gravimeter is powered by a 9V battery and should be used with the following precautions:

- 9V power source.
- The gravimeter battery must always be powered to maintain the temperature at 50^0C because if the battery is fully discharged, it recovers the energy inside the gravimeter which becomes inefficient.
- Always close the mass to prevent the filament from cutting, because it is very sensitive, even to the slightest movement.
- Be assured of the horizontality of the measuring platform and the gravimeter before any measurement.

b) Principle of Lacoste-Rombert gravimeter

The flail OM turns around O by changing the length of the spring of stiffness k. This spring is said to be zero length because its tension is proportional to its length, that is, if all external forces were removed, the length of the spring would tend to zero (such a thing is physically impossible because of the thickness each turn and the weight of the spring). The tension of the spring is given by the relation T = k. (S-z) where z is a small correction which takes into account that the spring does not have exactly the zero length (Figure 13). By matching the moments with respect to the axis of rotation passing through the point O, we have:

$$mgz\cos\theta = \mathrm{k(s-z)bsin}\,\alpha \qquad (2.2)$$

According to the law of sinuses in any triangle, we have

$$\sin\alpha = \frac{y\cos\theta}{s} \qquad (2.3)$$

We therefore obtain:

$$\mathrm{g}= \frac{kb}{ma}\left(1-\frac{z}{s}\right) \qquad (2.4)$$

When g increases by dg, the spring lengthens ds such that:

$$\frac{dg}{ds} = \frac{kb}{ma} zy\ \frac{1}{s^2} \qquad (2.5)$$

We then obtain:

$$dg = \left(\frac{k}{m}\right)\left(\frac{b}{a}\right)\left(\frac{z}{s}\right)\left(\frac{y}{s}\right) ds \tag{2.6}$$

The equation (2.5) shows that we can have the smallest variations of g by decreasing the factor $\left(\frac{k}{m}\right)\left(\frac{b}{a}\right)\left(\frac{z}{s}\right)\left(\frac{y}{s}\right)$.

However, it should be noted that the closer the spring is to the length zero, the smaller z is and the higher ds becomes.

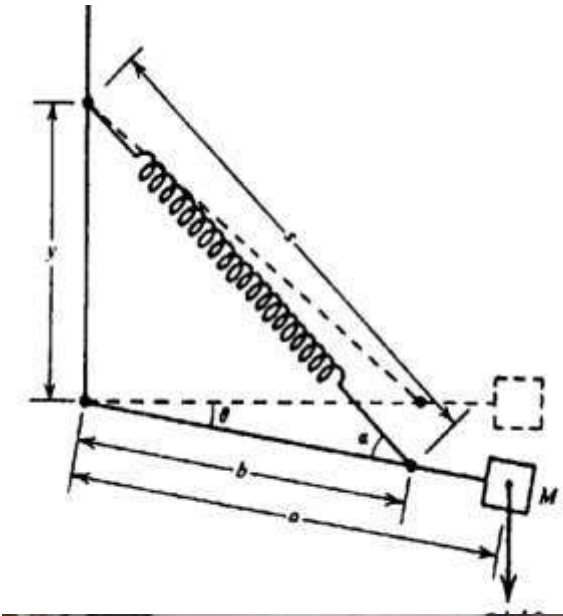

(A)

(B)

Figure 13: A) Principle of Operation of The Lacoste-Romberg Gravimeter; B) A Photo of The Lacoste-Romberg-Gravimeter Used During Our Survey.

a)

b)

c)

Figure 14: Some Field Images: A) Gravimeter Setting At The Ecole Publique Station In Kribi; B) Data Measurement At The Kribi Station 100m From The Deep Water Port Of Kribi Entrance; C) Data Measurement at Kribi Station 1km From The Deep Water Port Of Kribi; D) Data Collection In The Heart Of The Forest In The Locality Of Lokoundje; E) Departure For The Next Measuring Station.

Fieldwork is done by performing gravimetric readings on stations which constitute a canvas of points covering the concerned region. These readings are, in general, influenced by factors such as altitude, the surrounding topography, the earth tides, and the drift rate of the gravity meter. It is then necessary to make corrections on these measurements to reduce them to the values that they would have on an equipotential surface reference, the reference ellipsoid.

2.3.2. Data processing

The gravity data collected in our study zone are presented on the following figure **15**

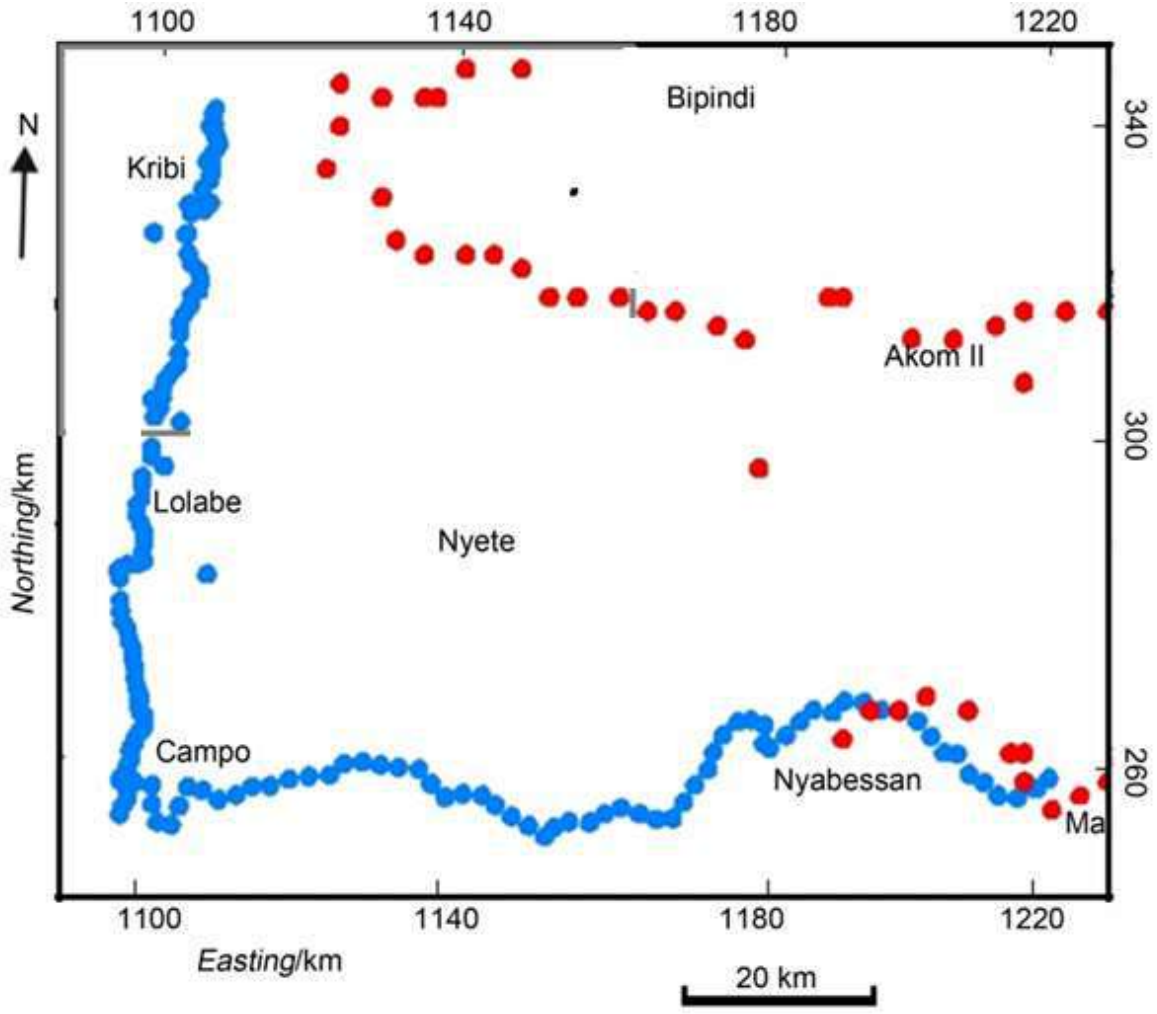

Figure 15: Gravity Data Distribution Map. The red dots represent the data from the ORSTOM Geophysical Survey (1968) while the blue dots represent the data points we collected.

This part is concerned with the various corrections that need to be applied to the raw data in order to eliminate the effect of non-geological sources. In the specific case of our data collected for the research studies, four main gravity data correction were applied to the data namely: the free air correction; the terrain correction, the plateau correction and the luni-solar correction. For further details on these corrections, see chapter 3 on *"*corrections of raw gravity data and impact evaluation*"*

2.4. The work methodology

2.4.1. Gravity operators

a) The continuation operator

The continuation is an operation that consists of artificially displacing the observation plan and calculate the field that would be observed in these new points from the data collected in the field. The continuation can be upward or downward. The upward continuation moves the anomaly's altitude from z = 0 to an altitude z> 0. This operator acts as a low-pass electronic filter attenuating the short wavelengths; highlighting the anomalies of deeper structures and deeper, depending on the altitude of the continuation.

Assuming g (x, y, z) to be a function defined in the 3-dimensional spatial domain, its 2-dimensional Fourier transform denoted G (kx, ky, z) or F[g] breaks down the function g (x, y, z) in terms of the wavelengths it contains, and is expressed by the relation:

$$F(g) = G(k_x, k_y, z) = \int_{-\infty}^{+\infty} \int_{-\infty}^{+\infty} g(x,y,z) e^{i(k_x x + k_y y)} dxdy \quad (2.7)$$

The inverse transform makes it possible to recover the function g:

$$F^{-1}[G] = g(x,y,z) = \frac{1}{4\pi^2} \int_{-\infty}^{+\infty} \int_{-\infty}^{+\infty} G(k_x, k_{y,} z) e^{i(k_x x + k_y y)} dxdy \quad (2.8)$$

kx and ky are the wave numbers along the x and y axes respectively, given by:

$$k_x = \frac{2\pi}{\lambda_x};\ k_y = \frac{2\pi}{\lambda_y} \quad (2.9)$$

λx and λy are the wavelengths along the x and y axes, respectively. The radial wave number

k is the norm of the wave vector $\vec{k} = k_x \vec{i} + k_y \vec{j}$:

$$k = \sqrt{k_x^{\ 2} + k_y^2} \quad (2.10)$$

Potential fields satisfy the Laplace equation outside the sources; and if we are interested in a map at altitude z1, we will have:

$$\frac{\partial^2}{\partial y^2} g(x,y,z_1) + \frac{\partial^2}{\partial y^2} g(x,y,z_1) + \frac{\partial^2}{\partial z^2} g(x,y,z_1) = 0 \quad (2.11)$$

Which corresponds in the spectral domain to the equation:

$$-(k_x{}^2 + k_y^2)G(k_x, k_y, z_1) + \frac{\partial^2}{\partial z^2} G(k_x, k_y, z_1) = 0 \quad (2.12)$$

If we know the value of the spectrum for z = 0 then a solution to this second order differential equation is:

$$G(k_x, k_y, z_1) = G(k_x, k_y, 0)e^{-z_1\sqrt{k_x{}^2 + k_y^2}} \quad (2.13)$$

The upward continuation operator for a map is therefore:

$$O_P = e^{-kx} \quad (2.14)$$

The downward continuation has the same expression as the upward extension, but the sign of the change of altitude is opposite (z < 0). It is a high-pass filter that has the disadvantage of amplifying the noise (measurement errors) contained in the signal, thus reducing the reliability of the interpretation. This is why its use is very limited.

b) The vertical derivative operator

When several structures are close enough and located at approximate depths, the measured signal generally shows the existence of a single anomaly. The vertical derivation makes it possible to better distinguish (separate) the different anomalies.

According to the expression (2.13), the extension of the function g to the altitude z is written in the spectral domain:

$$G(k_x, k_y, z_1) = G(k_x, k_y, 0)e^{-z\sqrt{k_x{}^2 + k_y^2}} \quad (2.15)$$

Deriving this expression with respect to z, we obtain:

$$\frac{\partial G(k_x, k_y, z)}{\partial z} = -\sqrt{k_x{}^2 + k_y^2}\,G(k_x, k_y, 0)e^{-z\sqrt{k_x{}^2 + k_y^2}} = -\sqrt{k_x{}^2 + k_y^2}\,G(k_x, k_y, z) \quad (2.16)$$

The vertical derivation operator is therefore:

$$(O_{DV}) = -\sqrt{k_x{}^2 + k_y^2} \tag{2.17}$$

For a derivation of order n, the operator is:

$$(O_{DV})_n = (-\sqrt{k_x{}^2 + k_y^2})^n \tag{2.18}$$

c) The horizontal derivative operator

The horizontal derivatives along x and following y can be estimated in the spatial domain by the finite difference method. Assuming $g_{i,j}$ (i = 1, 2, ..., Nx; j = 1, 2, ..., Ny) the values of the field of anomalies g in a grid of measurements contained in the horizontal plane, sampled according to a step Δx and Δy along the directions x and y respectively, the directional derivatives of the field g at index points i, j are approximated by the relations (Blakely, 1995):

$$\frac{\partial g(x,y)}{\partial x} \approx \frac{g_{i+1,j} - g_{i-1,j}}{2\Delta x} \tag{2.19}$$

$$\frac{\partial g(x,y)}{\partial y} \approx \frac{g_{i,j+1} - g_{i,j-1}}{2\Delta y} \tag{2.20}$$

In the Fourier domain, the directional derivatives of the order n following x and y are respectively:

$$F\left[\frac{\partial^n g}{\partial x^n}\right] = (ik_x)^n F[g] = (ik_x)^n G \tag{2.21}$$

$$F\left[\frac{\partial^n g}{\partial y^n}\right] = (ik_y)^n F[g] = (ik_y)^n G \tag{2.22}$$

The horizontal derivative in a given direction makes it possible to highlight on the map anomalies, the geological contacts quasi perpendicular to the direction of derivation.

d) The regional-residual separation operator

Gravity anomaly maps generally superimpose the effects of deep, shallow, widespread and local density contrasts. The effect of a local or shallow structure that is to be interpreted is sometimes hidden in the geophysical signature of larger regional structures. The regional-residual separation thus makes it possible to isolate the anomalies due to the deep and extended

sources (long wavelength anomalies) from those resulting from the contrasts of reduced and less deep extension density (short wavelength anomalies). It is important to mention, in describing the regional as coming from deep and extensive structures, that this is related to the scale of the region and the positions of structures studied; it is the same for the residual. There are several methods that can be used to make a regional-residual separation:

- graphic methods;
- analytical methods that can be divided into two groups: the grid method, and the polynomial method.

In this study, we used the polynomial method to carry out the separation. Given that the graphic method is subjective and the data were not collected in grid with regular spacing, the grid method and graphic method could not be used without interpolation beforehand.

e) The polynomial method

This method consists of constructing a polynomial of a suitable degree, which generates an analytical surface that is fitted to an experimental surface by the least squares' method (Abdelrahman et al., 1985). This analytical surface represents the regional one, and the differences in the importance of the variable compared to this regional one makes it possible to separate the masses which can correspond to more or less buried sources. In practice, the so-called regional order n is assimilated to a polynomial of degree n. At a point of coordinates (x, y) on the chosen surface, the regional order n can be written as (Radhakrishhna and Krishnamacharyulu, 1990):

$$F_n(x,y) = \sum_{p=0}^{n}\sum_{q=0}^{p} C_m A_m(x,y) \tag{2.23}$$

where C_m is a real coefficient, $A_m(x,y) = x^q y^{p-q}$ and for every couple (p, q), we have $m = \frac{1}{2}\left[p(p+3)\right] - q + 1$, the maximum value of m being $\frac{1}{2}(n+1)(n+2)$. Let G (x, y) be the value of the anomaly at the point of coordinates (x, y) on the chosen surface, the least squares method allows to write:

$$\sum_{i=1}^{n} G(x_i,y_j).A_k(x_i,y_j) = \sum_{m=1}^{\frac{1}{2}(n+1)(n+2)} C_m \sum_{i=1}^{n} A_k(x_i,y_j).A_m(x_i,y_j) \tag{2.24}$$

Where $k = 1,..., \frac{1}{2}(n+1)(n+2)$

By developing the relation (2.23), one obtains ½ (n + 1) (n + 2) equations which make it possible to determine ½ (n + 1) (n + 2) coefficients Cm. We can then calculate Fn (x, y) using the relation (2.22) and deduce the residual of order n by:

$$R_n(x,y) = G(x,y) - F_n(x,y) \tag{2.25}$$

When n is small, the regional anomaly has values with a deviation relatively large compared to those of the Bouguer anomaly. As we increase the order of the polynomial, the regional anomaly approaches the Bouguer, which makes it possible to highlight the structures more and more close to the surface with the corresponding residual anomalies.

f) The calculation maxima of gradient of the gravity field

The procedure for determining the maximum of the horizontal gradient of the vertical derivative of Bouguer's anomalies is as follows:

- Determination of the upward continued field at different altitudes by using the continuation operator of formula (2.14);
- Calculation of the vertical derivative at different altitudes. To avoid amplification of the noise from data errors to the detriment of the actual signal, as it is usually the case when calculating the vertical derivative of the field by the method where the operation takes place in the frequency domain (Gunn, 1975), the vertical derivation will take place in the space domain by the method of finite differences proposed by Florio et al. (2006). This method has the advantage that it uses the upward continuation which is a stable operator that smooths the noise and also allows to calculate the vertical derivative at different altitudes. Let g_v be vertical derivative of potential field g at altitude h,

$$g_v = \left(\frac{\partial g}{\partial z}\right)_h = \frac{g^{up}_{h+\Delta h} - g^{up}_h}{\Delta h} \tag{2.26}$$

Where g^{up}_h is the upward continuation at the altitude h and $g^{up}_{h+\Delta h}$ the upward continuation at the altitude $h+\Delta h$. If g_{HV} is the horizontal gradient of the vertical derivative of the field at an altitude h; its value is calculated in the spatial domain from the following formula:

$$g_{HV} = \sqrt{\left(\frac{\partial g_v}{\partial x}\right)^2 + \left(\frac{\partial g_v}{\partial y}\right)^2} \tag{2.27}$$

Where g_v is the vertical derivative at altitude h of the gravity field g as defined in equation (2.26);

2.4.2. Quantitative gravity methods

a) Spectral analysis equations

As define by Spector and Grant in 1970, the spectral analysis is based on the properties of the energy spectrum of Gravimetric anomalies. It makes it possible to locate the major density contrasts and consequently to estimate the mean depths of the disturbing masses. Actually, a small anomaly with an amplitude that decreases rapidly will be characterized by high frequencies. On the other hand, a large anomaly whose amplitude decreases weakly will be characterized by more or less concentrated spectra towards the low frequencies. These two types of anomalies can be separated from their respective energy spectra.

A non-periodic function f (x) representing the variation of the field along a given profile can be decomposed into infinite sinusoidal terms such as:

$$f(x) = \int_{-\infty}^{+\infty} F(\omega) e^{-i\omega x} dx \tag{2.28}$$

where F (w) is the Fourier transform of f(x). F (w) is given by the relation:

$$F(\omega) = \frac{1}{2\pi} \int_{-\infty}^{+\infty} f(x) e^{-i\omega x} dx \tag{2.29}$$

In practice, since the anomaly profiles consist of a finite number of points, it is preferable to use the discrete Fourier transform. Spector and Grant (1970) showed that if fn is a series of N measurement points sampled with a constant pitch on the profile, the discrete Fourier transform of this series is given by:

$$F_k = \frac{1}{N} \sum_{n=0}^{N-1} f_n e^{\frac{2\pi kn}{N}} \tag{2.30}$$

where k is the wave number, and F_k the Fourier wave at the frequency k. The energy contained in each frequency of the field created by the disturbing sources (or spectral energy) is given by (Bhattacharyya, 1966):

$$E_k = |F_k|^2 \tag{2.31}$$

The mean depth of the source is estimated from the values of the spectral energy given by the relation (Dimitriadis et al., 1987):

$$E_k = e^{-4\pi kh} \tag{2.32}$$

This last relation shows that the logarithm of the energy contained in each frequency of the field created by the disturbing sources varies linearly as a function of the frequency considered. Thus, if Δ (LogE) is the variation of the logarithm of the energy in the frequency interval Δk, the depth h of the roof of the source is given by:

$$h = \frac{\Delta(LogE)}{4\pi\Delta k} \tag{2.33}$$

b) The ideal body solution equation

As pointed out by Parker (1974), ideal body theory is used to delineate bounds on the spatial extent of the anomaly source with an approximate model. It is important to have an idea of the suspected anomaly source in order to give a good approximation of it. The inverse method developed by Parker allows, when the anomalies are well individualized, to choose amongst all possible solutions, those that best fit the data. The linear programming technique is used to carry out the calculations. This technique consists of considering a model where the density value ρ is known at certain given positions (X_0, Z_0). The domain under the profile is subdivided into quadrangular cells with dimensions dx and dz (dx is the dimension of a cell following the profile direction and dz is the dimension following the vertical axis) centered in (X_0, Z_0) and for which the value of ρ is assumed to be constant (figure 16). The gravity field at each point denoted i is the sum of the effects of all the cells. It is given by the following formula:

$$g_i = \sum_{j=1}^{N} \sum_{k=1}^{K} G_{ijk}\rho_{jk} + \varepsilon_i \tag{2.34}$$

where N is the number of cells in the profile direction, K the number of cells in the vertical direction. G_{ijk} is the Green's function associated with the gravimetric effect of the elementary prism (j, k) observed at the point i, ρ_{jk} is the density of prism centered in (x_j, z_k) and ε_i is the error on the value of field observed at the point i.

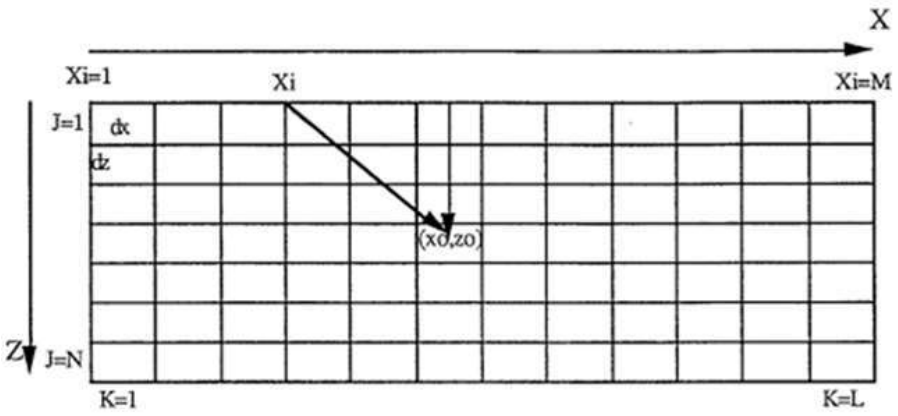

Figure 16: Representation of The Prisms in The Linear Programming Technique.

CHAPTER III: RESULTS AND DISCUSSIONS

SECTION 1: CORRECTIONS OF RAW GRAVITY DATA AND IMPACT EVALUATION

1.1. Introduction

The purpose of gravity field reduction and correction is to eliminate from the observed gravity data any element that would be observed if we were studying a simple and essentially uniform earth. The remaining components are considered to be anomalous. In other words, anything that is left over is the result of density variation due to local the repartition of geological structures and eventually of local exploration interest. The diagram below is a conceptual flow chart for the gravity correction process, adapted from Chapin (1996). In land surveys, gravity data are measured above sea level; In order to calculate gravity anomalies, measured values have to be reduced to the sea-level. Anomalies result from subtracting a value for normal gravity on the spheroid.

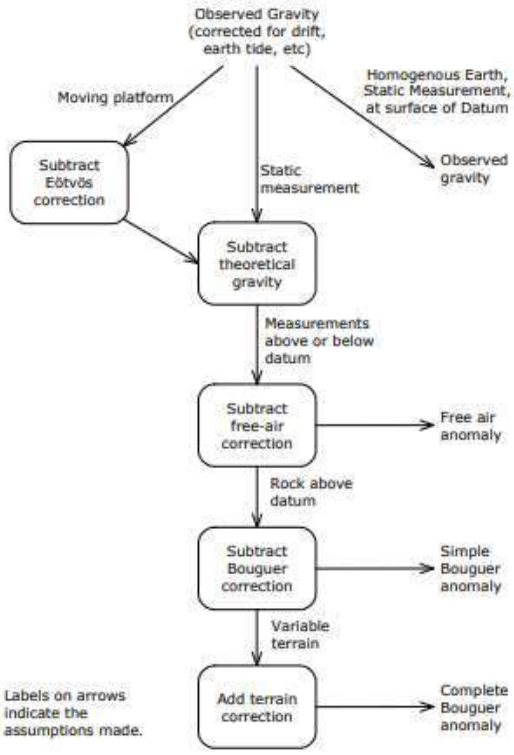

Diagram 1: Conceptual flow chart of gravity correction process

1.1. Area and Gravity reductions

1.1.1. Data collection approaches

Two main techniques are generally used in a gravity data acquisition field. There are done in loop were measurements begin at a station and end at the same station. The first approach consists of considering all measurement stations as base stations. Measurements of the relative gravity value are collected at the first station S_1, from S_1 moving to station S_2 to measure and come back to station S_1 and move again to station S_2. Station S_2 becomes at this point the base station from which S_3 can be measured (figure 17). This procedure is repeated until the last station Sn. This technique means that 3 measurements have to be done at one station which makes this procedure costly and time consuming. Nevertheless, this approach is accurate as it reduces substantially the tidal influence on measurements and instrument fatigue.

The second approach, which is the one we used in this study consists of taking measurements at the base station S_1 , moving to S2, then S3 until Sn and coming back to S1 to close the measurement loop.

In general, the values measured at the beginning and end at the base station are not similar. This difference, called drift, is due partly to the gravity-meter, partly to the lunar tide (Mathew et al. 1997)

The measured values are thus hampered by errors since one of their components is derived from the drift and does not reflect a change in the g values due to subsurface heterogeneities.

The Correction is made on the assumption that the drift is linear in time. In our survey in South Cameroon, we used these step by step handling of the Lacoste-Romberg gravimeter to take the measurements at every station:

Using the Gravimeter:

1. Level the stool using the bubble in the center. Measure and record the height from the ground to the lip of the stool.

2. Take out instrument and level using the two bubbles. This is done using the three knobs on the legs at the bottom of the meter and the 2 "bubble" levels at the top. The bubbles of both levels must be at the center of the level for the gravimeter to be level. This is best done by one

person adjusting 2 of the legs while watching both levels simultaneously. After the gravimeter is level, turn it on.

3. The meter is read by looking in the eyepiece and turning the "turns indicating" dial until the beam is coincident with the center line of the reticle (cross-hairs). Always approach the center line from the same direction (from the left). To do so, turn the dial clockwise until the beam is on the left. Then turn (slowly) counter-clockwise until you approach the center line. If you overshoot, restart by moving the beam all the way to the left again. The beam takes a second to adjust, so go slowly and wait for the beam to adjust before continuing to turn the dial.

4. Once the beam is aligned with the center line, the dial can be read. The largest two digits of the dial reading (hundreds) are determined from the small number showing through the window indicating how many turns of the dial have been made, the next two digits (ones) are read from the dial with the "0" of the vernier as the reference, and the tenths are read from the vernier. Estimate the errors of the gravity measurements. The number is converted to milligals by multiplying by the dial constant shown on the side of the gravimeter. Note these are relative measurements of gravity. To obtain actual gravity measurements we would have to go to a place where the gravity is known and calibrate the meter.

5. Record the measurement, the time, the geographical coordinate of the station and it's elevation.

6. Make sure to return to the base station before the end of the day!

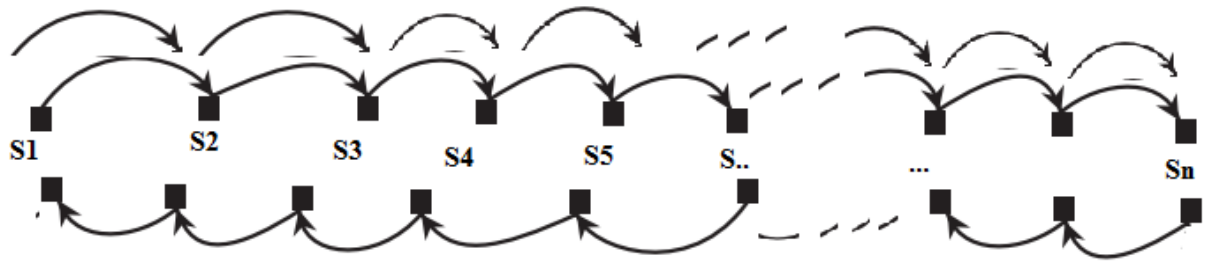

Figure 17: First approach loop representation: every station is entitled to 3 measurements.

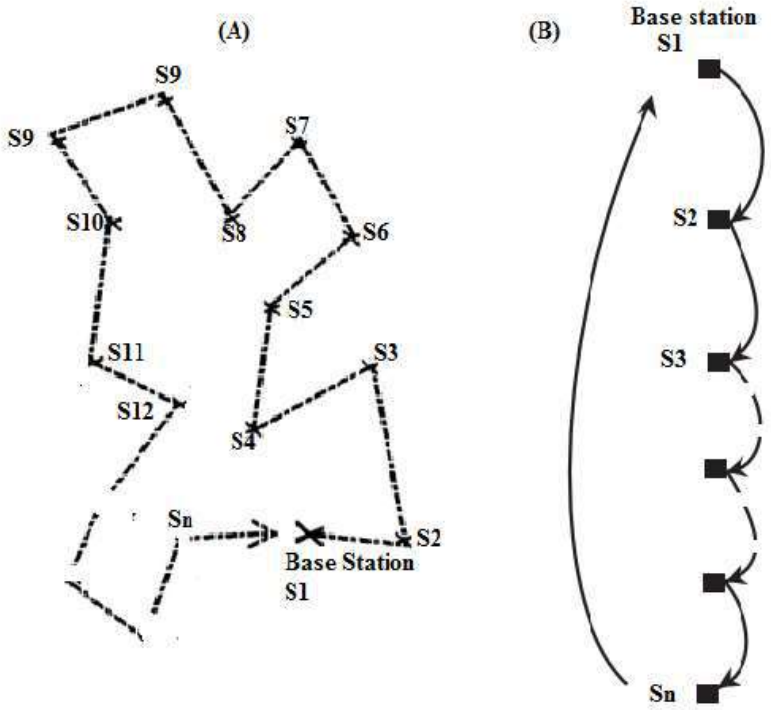

Figure 18: Second approach loop representation: (A) measurements are taken around the base station which is the beginning and the ending point of the loop. (B) Measurements are taken along a path, return to base station to close the loop.

1.1.1. Correction for instrumental drift

This correction attempts to eliminate the influences of tides on the measurements and the fatigue of the instrument. For this purpose, it is necessary to follow a certain path between reading stations. In practice, a series of measurements is made by following a loop path: the series usually starts at a given point and ends at the same point (Figure 18). The starting point of the loop is normally connected to a base station.

1.1.2. Free air correction or altitude correction

The measured values of g have variations which are only due to the position of the measuring station and not to the subsurface heterogeneities or the effect for mass between observed point and the datum. In order to eliminate these variations, the altitude or free air correction is applied on the data. The free-air correction accounts for gravity variations caused by elevation differences in the observation locations. For a displacement of h with respect to the reference level, we have

$$g_h = \frac{Gm}{(r+h)^2} = \frac{Gm}{r^2(1+2(h/r)+(h/r)^2)} \quad (3.1)$$

Given that, $r>>h$, r is the earth radius, g_h is the value of g at the elevation h, G is the gravitational constant; m the mass of the earth.

The free-air correction is given as

$$C_F = g_h - g_r = -2hg_r / r \quad (3.2)$$

For stations above the reference level ($h \succ 0$, in meters), C_F is positive and is described by the formula

$$C_F = 0.3086h \ \ (mgal) \quad (3.3)$$

1.1.3. Latitude Correction

This correction considers the variations of g with the latitude caused by to the rotation and the flattening of the earth. From world geodesic measurements, we know that the earth is an ellipsoid of almost perfect revolution. On this surface, the gravitational field can be described by the following equation (WGS-84)

$$g_{th}(\phi) = 9.7803253359 \frac{1+0.00193185265241\sin^2\phi}{\sqrt{1-000669437999014\sin^2\phi}} \quad (3.4)$$

Where $g_{th}(\phi)$ is the field value the at the point of geodesic latitude φ. The correction C_ϕ for a displacement l following a meridian is given by

$$C_\phi = \frac{\partial g_{th}}{\partial l}.l \quad \text{with} \quad dl = R(\phi)d\phi \approx R_e d\phi \quad (3.5)$$

Where R_e is the equatorial radius of the earth (6378, 136 km). For smaller scale studies the expression (with l in meters) can simplified to (Bernard Giroux and Michel Chouteau, 2008)

$$C_\phi = 8.1669\times10^{-4}.l.\sin 2\phi \quad [mgal] \quad (N \to S) \quad (3.6)$$

For the calculations of the latitude correction in this study, given the local nature of the study area and also, the data were taken in an approximate profile line, the distance from the meridian is considered to be constant

1.1.4. Plateau Correction or Bouguer Slab Correction

The plateau correction is very important as it accounts for the thickness of rocks between the elevation at the current station and the elevation at the base station thus accounts for the excess mass underlying observation points located at altitude higher than the reference elevation (sea level or the geoid). Inversely, it accounts for a mass deficit at points of observation located under the elevation datum (figure 19).

In this paper, we calculated the plateau correction assuming a constant slide value between the observation point and the reference altitude for all the stations.

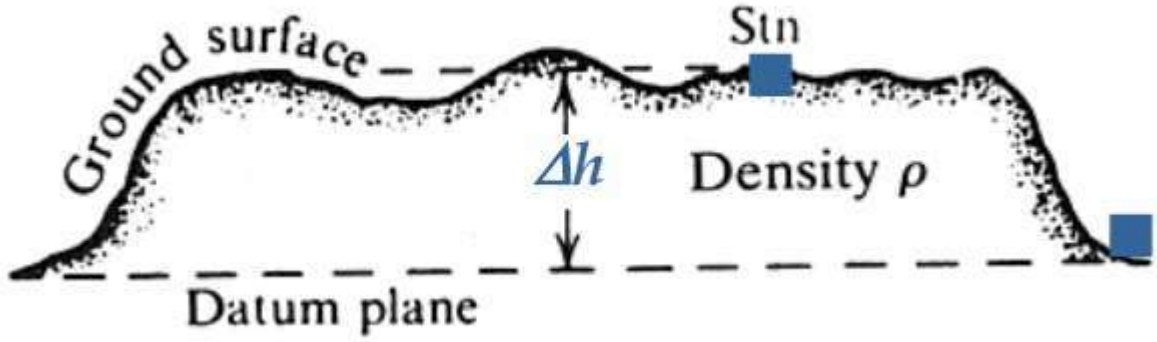

Figure 19: Bouguer slab representation.

For a slice of height h, the attraction is given by

$$C_p = -0.04191\rho_B h \quad mgal \quad (h \succ 0) \tag{3.7}$$

ρ_B is the presumed density of the mass of the slice (ρ_B = 2.67 g / cm^3 on average). As C_p increases with h, it is subtracted when $h \succ 0$ and therefore

Usually, we the free-air correction and the plateau correction are combined to obtain what is called the Bouguer correction.

$$C_B = (0.3086 - 0.04191\rho_B)h \quad mgal \quad (h \succ 0) \tag{3.8}$$

For the value of ρ_B = 2.67 g / cm^3

$$C_B = 0.1966h \quad mgal \quad (h \succ 0) \tag{3.9}$$

1.1.5. Terrain Correction

The application of the Bouguer correction removes the attraction of a slice of land of thickness h. If the topographical variations are such that the field cannot be approximated by a

uniform slice, it is necessary to integrate numerically on one hand the parts which exceed it and on the other hand the parts which are missing to the slice of Bouguer. Thus the bouguer correction refers to the gravity effect of the intervening plate mass between stations S and the base level B while the terrain correction takes into account the effects of topographic elevations and deficits (Figure 20)

Several approaches have been developed to calculate the terrain correction, amongst which the Hammer approach which uses a reticle that is superposed to topographic maps and tables prepared by Hammer. We also have the of Nettleton approach which consists of representing, on the same figure, a topographic profile and the profiles of the Bouguer anomaly corresponding to it, calculated for several densities. For the terrain correction C_T applied in this paper, we have elaborated a robust matlab code.

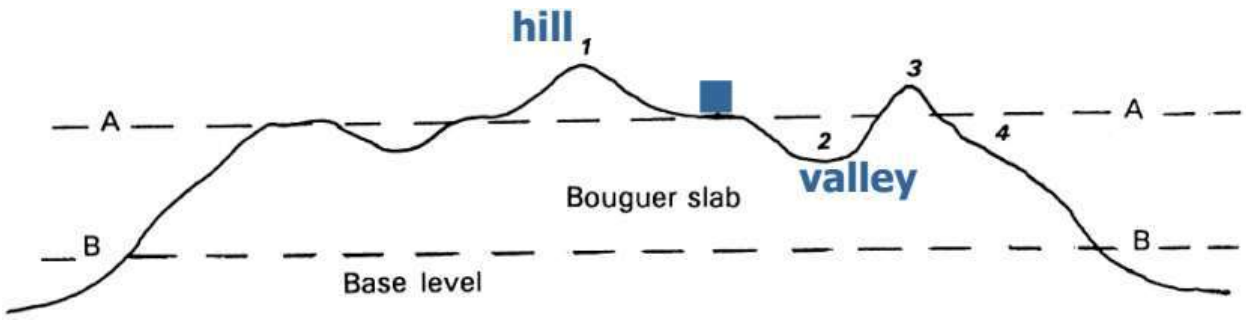

Figure 20 : Illustration of the Bouguer correction and Terrain correction Indiscrepancies.

1.1.6. Luni-solar correction

The biggest recurring gravity variations are due to effect of nearest to Earth celestial bodies Moon and Sun. Magnitude direction of gravity field vector i.e. vertical direction is varying by changing gravity field. These changes should be taken into account during precise geodetic observations. The influence of the celestial body can be expressed by tide potential. Tide generating potential for non-deformable (rigid) Earth could be defined as spherical function series (Petroškevičius, 2008):

$$V_T = \frac{Gm}{r}\sum_{n=2}^{\infty}\left(\frac{R}{r}\right)^n P_n(\cos z), \tag{3.10}$$

where G is the gravitational constant; m the mass of the celestial body; r the geocentric distance to the celestial body; R the geocentric distance of point on Earth surface; z is the geocentric zenith distance of celestial body; $P_n(\cos z)$ −Legendre polynomials.

Darius Popovas (2011) described an algorithm which can be used to analyze the effect of the Moon and the Sun to the levelled height difference, he used the Love numbers h_n and k_n from (Varga, 1989) which values depends on the elasticity of the earth.

Therefore, the height difference correction for real Earth could be expressed by formulas:

$$\delta h = \sum_{n=2}^{\infty} \gamma_n \delta h_n^{'} \quad \text{With } \gamma_n = 1 + k_n - h_n \tag{3.11}$$

Using the Vargas love numbers (h_2 = 0.6053, h_3 = 0.2890; h_4 = 0.1758; k_2 = 0.2993; k_3 = 0.0925; k_4 = 0.0414 (Vargas 1989) the expression was approximated to:

$$C_L = \delta h = \gamma_2 \frac{3GmR}{2gr^3} d \sin 2z \cos(A-a) + \gamma_3 \frac{3GmR^2}{2gr^4} d(4-5\sin^2 z)\sin z \cos(A-a) + \gamma_4 \frac{5GmR^3}{4gr^5} d(4-7\sin^2 z)\sin 2z \cos(A-a) \tag{3.12}$$

d is the distance between points, A is the azimuth of the deflection of the vertical, a refers to the azimuth of the levelling line.

The change ratio of lunisolar correction is rapidly unstable and uneven. Research has proven that lunisolar corrections in precise levelling can be calculated with more accuracy, considering azimuth changes and levelling rate deficiency. During our data collection survey, we recorded the time and the position at each levelling station which are necessary to accurately assess the impact of celestial bodies. Those values have used in this study to calculate lunisolar correction for each levelling station.The works of Darius Popovas (2011) have establish the dependency of the lunisolar correction on lunar changes, azimuth, on prime vertical and meridian (figures 21)

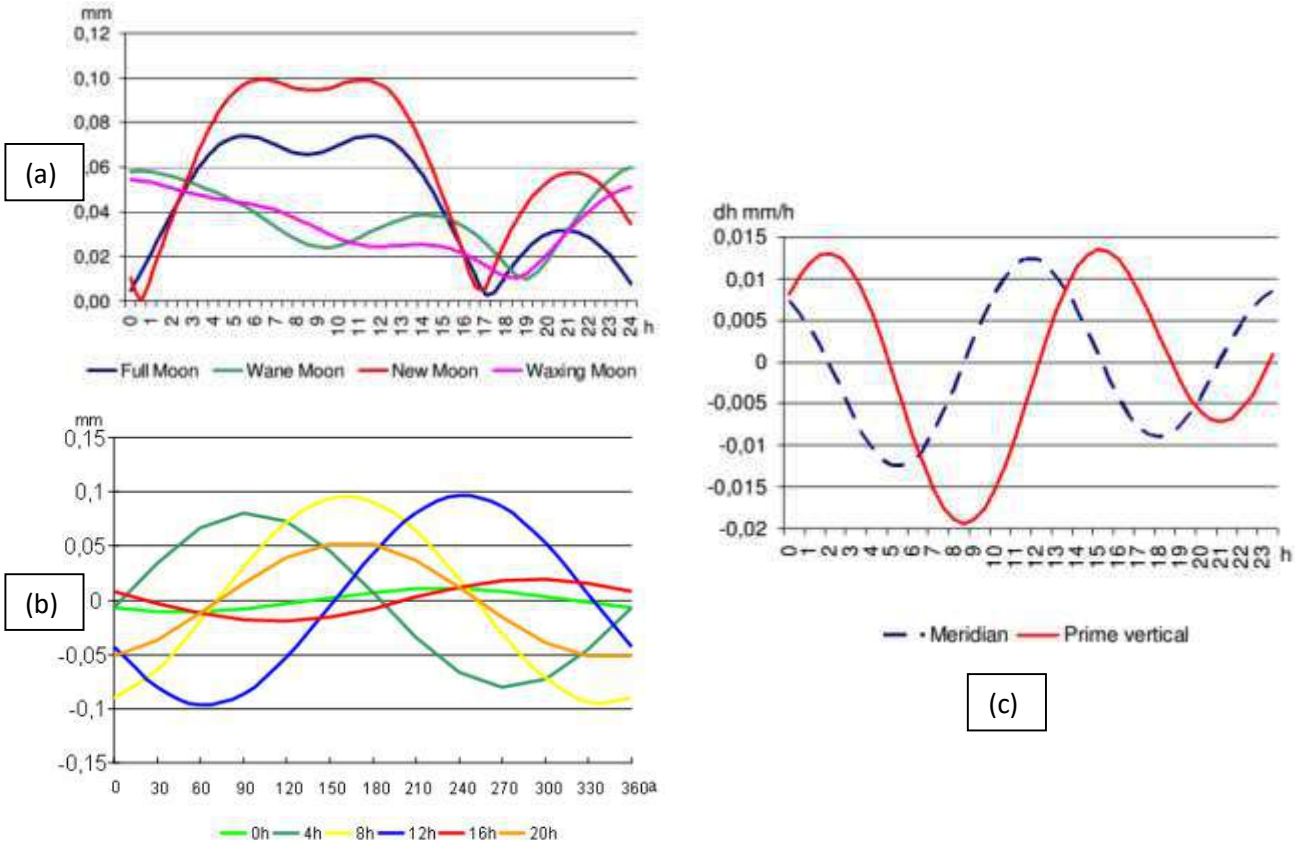

Figure 21: Lunisolar correction dependency factors: (a) Daily change of lunisolar correction at different Moon phase (b) Correction dependency on azimuth change at different time moments (c) Rate of change of lunisolar correction in prime vertical and meridian (Darious Popovas, 2011).

The main objective of gravity observations and gravity corrections is the analysis and interpretation of subsurface structures underlying the measurements sites. These interpretations are done thru the deciphering of the differences between observed gravity data and expected gravity data at a given point. These differences are expressed in terms of gravity anomalies. There are categorized according to the type(s) of correction applied. We have the free-air anomaly which results from the application of free-air correction (equation 3) and the bouguer anomaly which results from the application of free-air, lunisolar, latitude, terrain and bouguer corrections (equations 3, 6, 9 and 12).

$$A_A = (g_{obs} - g_{ref}) + C_F \tag{3.13}$$

$$A_B = (g_{obs} - g_{ref}) \pm 6 corrections \tag{3.14}$$

1.. Correction for instrumental drift

2.. Free air correction $C_F = 0.3086h \quad mgal$

3.. Latitude correction $C_\phi = 8.1669\times10^{-4}.l.\sin 2\phi \quad [mgal] \quad (N \to S)$

4.. Plateau correction $C_p = -0.04191\rho_B h \quad mgal \quad (h \succ 0)$

5.. Terrain correction C_T

6.. Lunisolar correction C_L

1.2. Evaluation of Gravity reductions

In table 1, we present some values of the measured gravity data at stations with the corresponding five corrections applied.

Table 1: Gravity Reductions.

Stations	Measured gravity	Free-air Correction	Plateau correction	Latitude Correction	Terrain Correction	Lunisolar Correction
1	978019.2577	2.1602	-0.7832979	0.0732	0.0720	0.1117
2	978015.6103	7.0978	-2.5736931	0.0717	0.0731	0.102
3	978014.0008	7.4064	-2.6855928	0.0726	0.074	0.0918
4	978014.9688	4.0118	-1.4546961	0.0726	0.072	0.0814
5	978015.3402	4.3204	-1.5665958	0.0726	0.0726	0.0707
6	978016.248	6.7892	-2.4617934	0.072	0.0726	0.0543
7	978013.2966	8.9494	-3.2450913	0.074	0.0726	0.0433
8	978020.0299	3.3946	-1.2308967	0.0731	0.0717	0.0324
9	978017.6795	5.5548	-2.0141946	0.072	.0732	0.0215

In order to better evaluate the impact of various gravity reductions on the raw data, the observed gravity field data was evaluated at each point. This value was represented with respect to the measurements points. The measurement points represent two main profiles in our study area; the Kribi-Campo profile oriented North-South, that constitutes the first 120 values and the

Campo-Ma'an-Nyabessan profile, oriented West-East, which constitutes the remaining 55 points (figure 22). The highest values of G are observed in the first profile (the Kribi-Campo profile). On this profile, there is not a very large variation of the measured gravity, values range around $9.7802x10^5$ mGal. In the second profile, there is a progressive decrease of the measured value until around station 150 (figure 23). A sudden increase is observed at this point which moves from to $9.7801x10^5$ mGal afterwards the value falls back. It is observed that there are more changes in the observed gravity values of the second profile (Campo-Ma'an-Nyabessan) than in the first profile, this is an indication that, the effect of non-geological anomaly sources are more pronounced in this area.

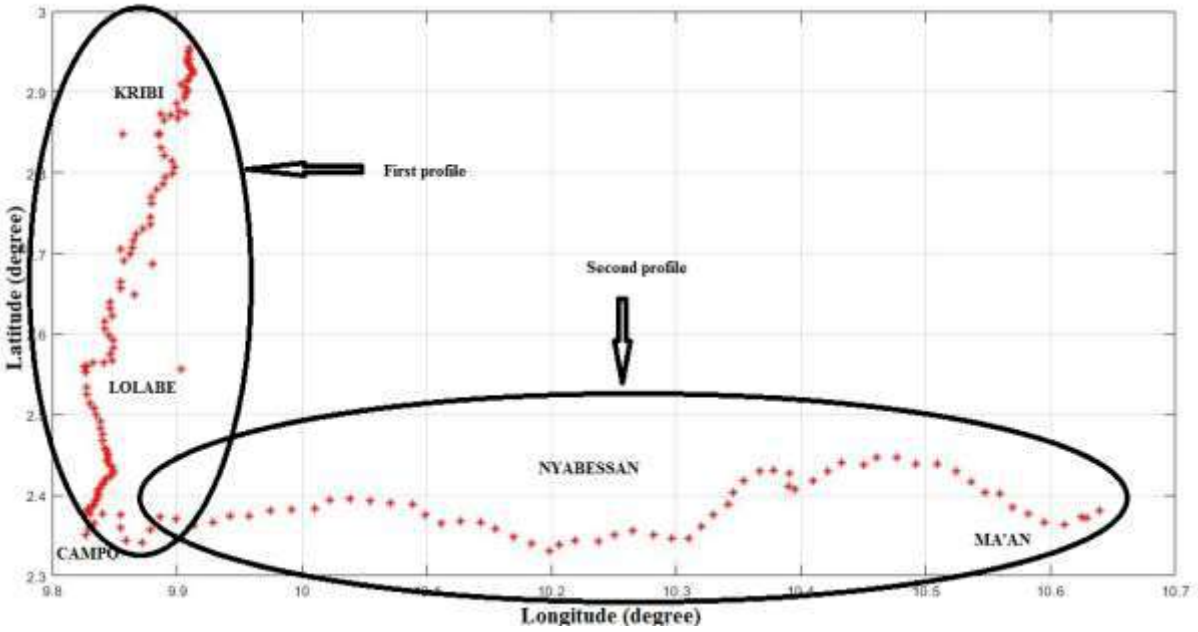

Figure 22 : Gravity Stations.

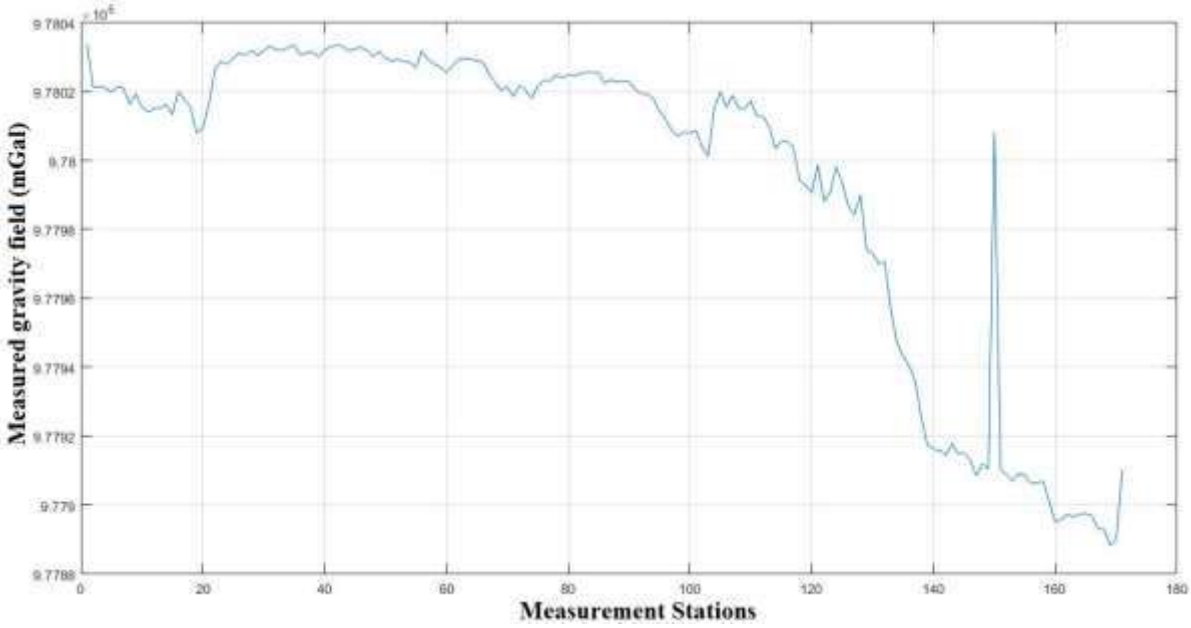

Figure 23: Variation of the measured gravity data along the profiles.

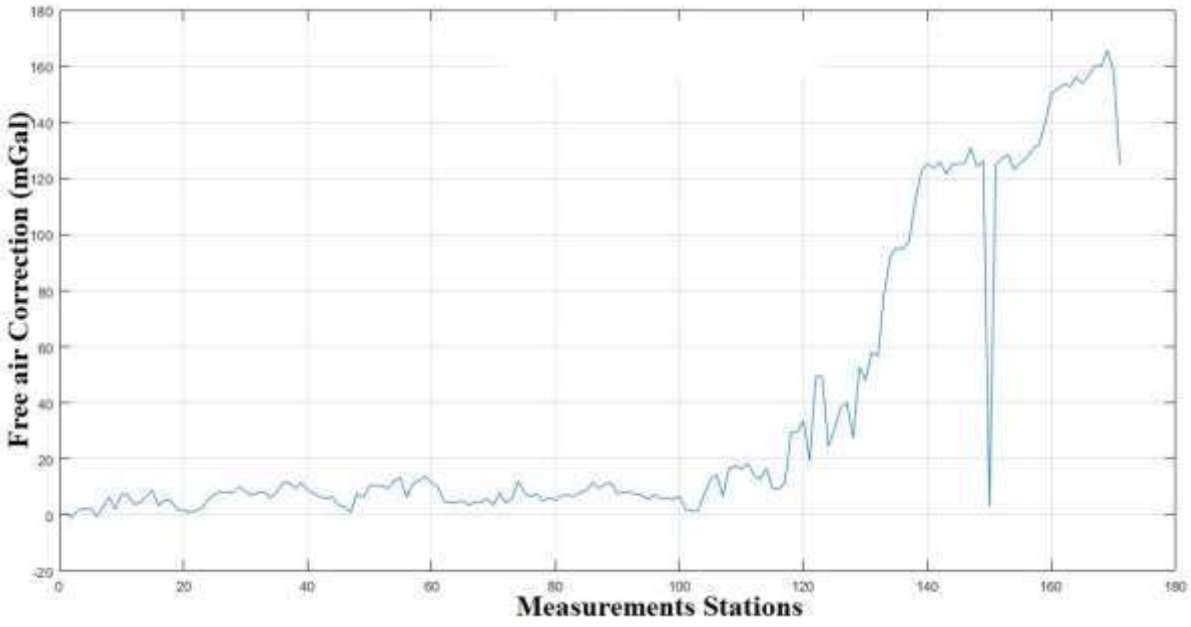

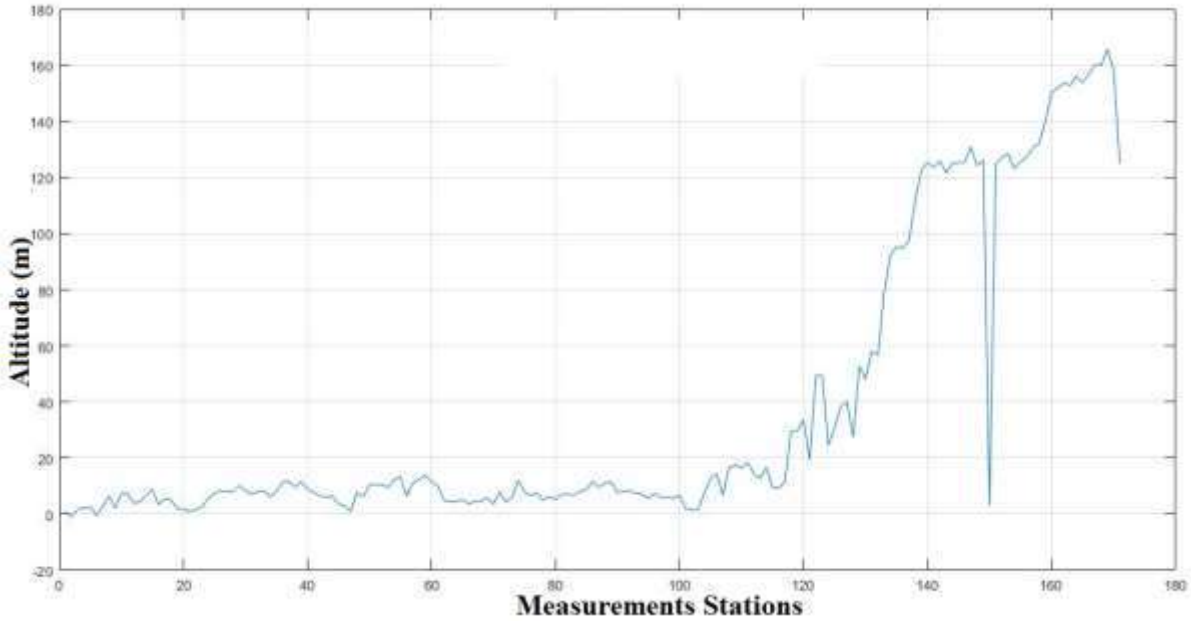

Figure 24: (a) Free air correction variation along the profiles; (b) altitude variation.

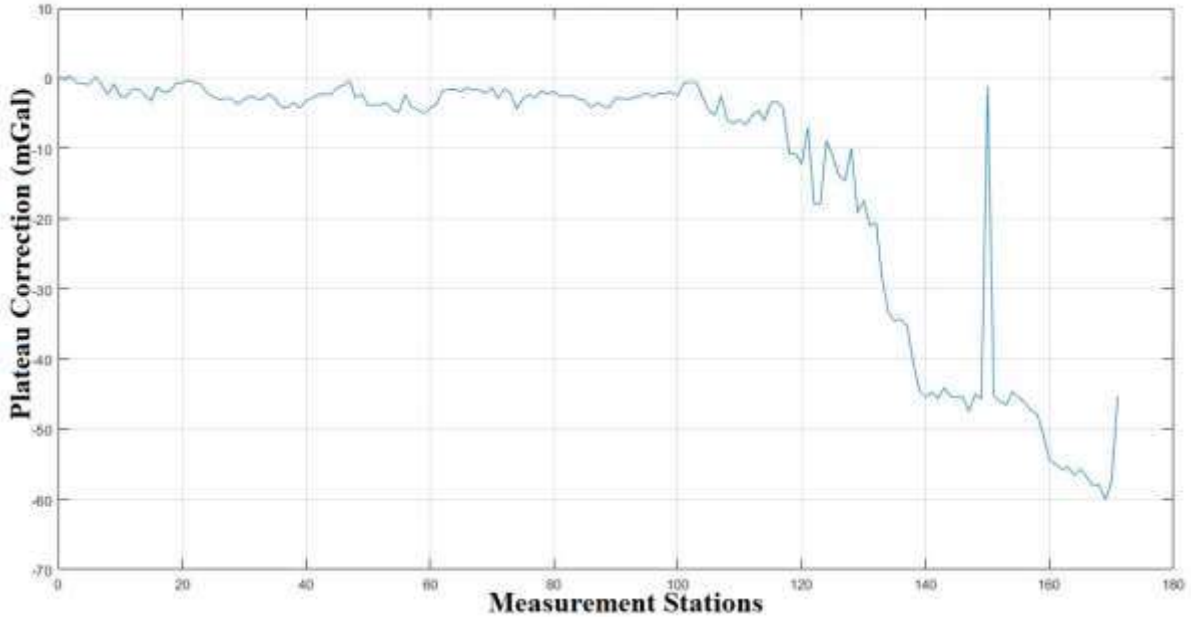

Figure 25 : Plateau correction's variation along the profiles.

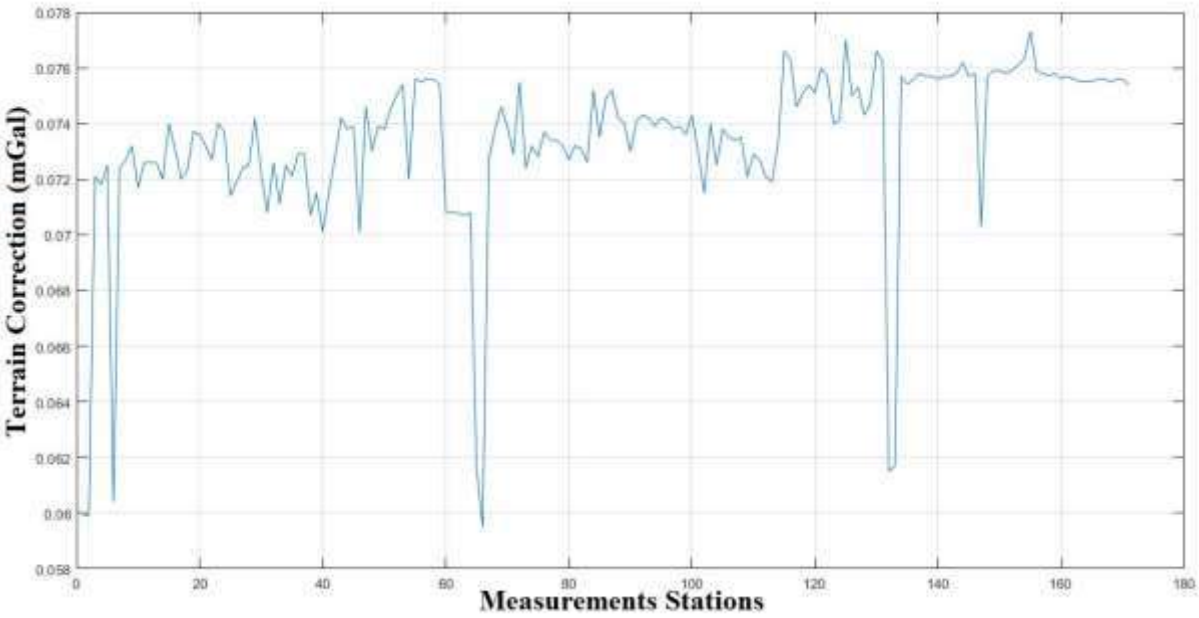

Figure 26: Terrain Correction's variation along the profiles.

A general observation of the variations of various gravity data corrections along our study profiles (figures 24 to 28) suggests major changes in the second profile and minor variations in the first profile. It should be noted that the first profile crosses the Atlantic coast from Kribi to Campo via Lolabe. The measurements were taken a few meters away from the coast. The altitudes on this profile were very low. This can explain the low values of the free air correction observed along the profile. The second profile, oriented eastward, moved from Campo, which is close to the Atlantic Ocean, to Ma'an thru Nyabessan which many kilometers are far away from the coast. The altitude variations are quite important in the zone; this can explain the reason for the high free-air correction values along this profile (figure 24). Observing figure 24(a) and (b) it can be seen clearly that the two curves, one representing the free-air correction and the other representing the variation of the altitude, have the same pace, which is justified by the close relationship which exists between these two parameters.

The terrain correction takes into account the effects of topographic elevations and deficits of masses, this correction's values are insignificant (ranging from 0.06 to 0.078 mGal, figure 10), compared to the value of g (ranging from about 9.7788×10^5 to about 9.7804×10^5 mGal, figure 23) in the study area. This can be explained by the fact, a greater part of our study zone being on a coastal area, topographic elevation and deficits can be under looked on a

broader scale. This correction is usually important when the study area is of regional scale with major topographic variations.

The bouguer slab is obviously thicker under the second profile than under the first given that we are at seashore and the datum plane is shorter. This can be observed on the plateau correction representation (figure 25)

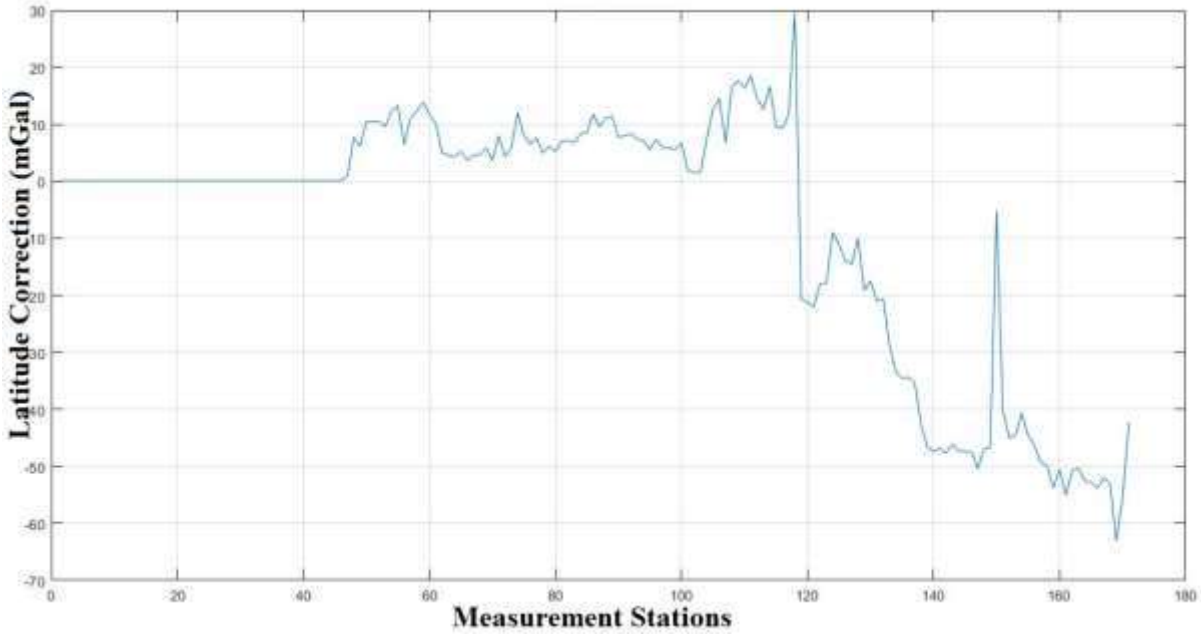

Figure 27: Latitude correction's variation along the profiles.

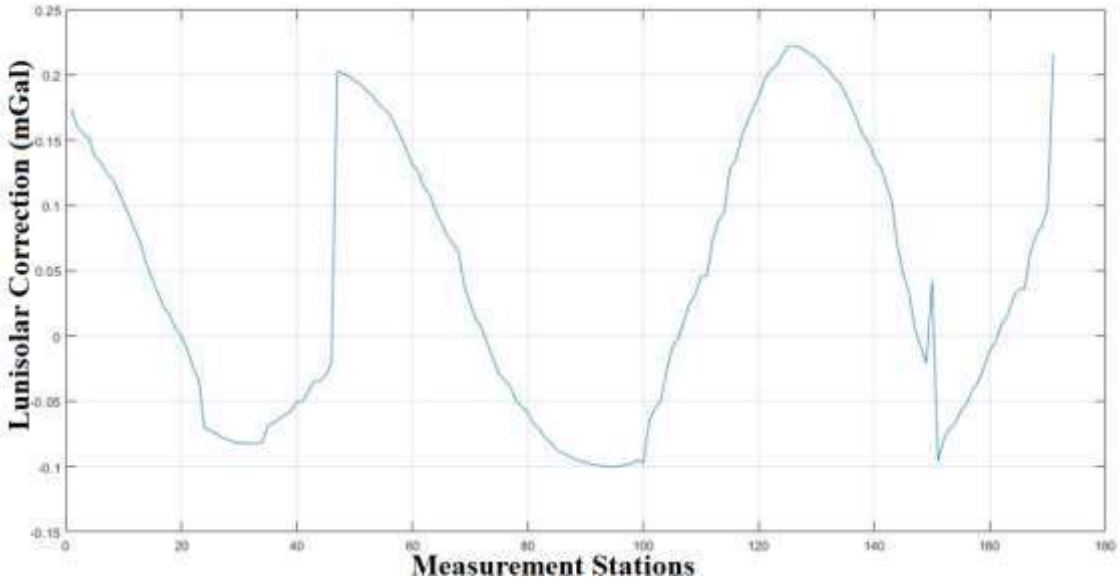

Figure 28: Lunisolar Correction's variation along the profiles.

The variation of latitude caused by the rotation of earth, which is considered in calculating the latitude correction, is almost constant along the first profile given that, the measurement points in this profile are located on the same parallel. This justifies small range of variation of the latitude correction along this profile. On the second profile, their values decrease importantly as we move away from the Greenwich meridian (figure 27). However, these changes are considered very small compared to the measured values of g in the area. Their impact therefore small.

The variation of the Lunisolar correction along the studied profiles is the most regular, the sinusoidal shape of the representing curves (figure 28) is an indication of the regular fluctuations of the values in time and space eventually. As established by Darius Popovas in 2011, this correction can depend of many factors, namely the daily change of Lunisolar correction at different Moon phase, the Correction dependency on azimuth change at different time moments, the rate of change of Lunisolar correction in prime vertical and meridian.

1.3. Graphical representation of reduction effects

In this section, we compared the observed gravity data curves with the corrected gravity data curves in order to decipher the magnitude of changes and their location, therefore better understand the impact of this correction on the raw data.

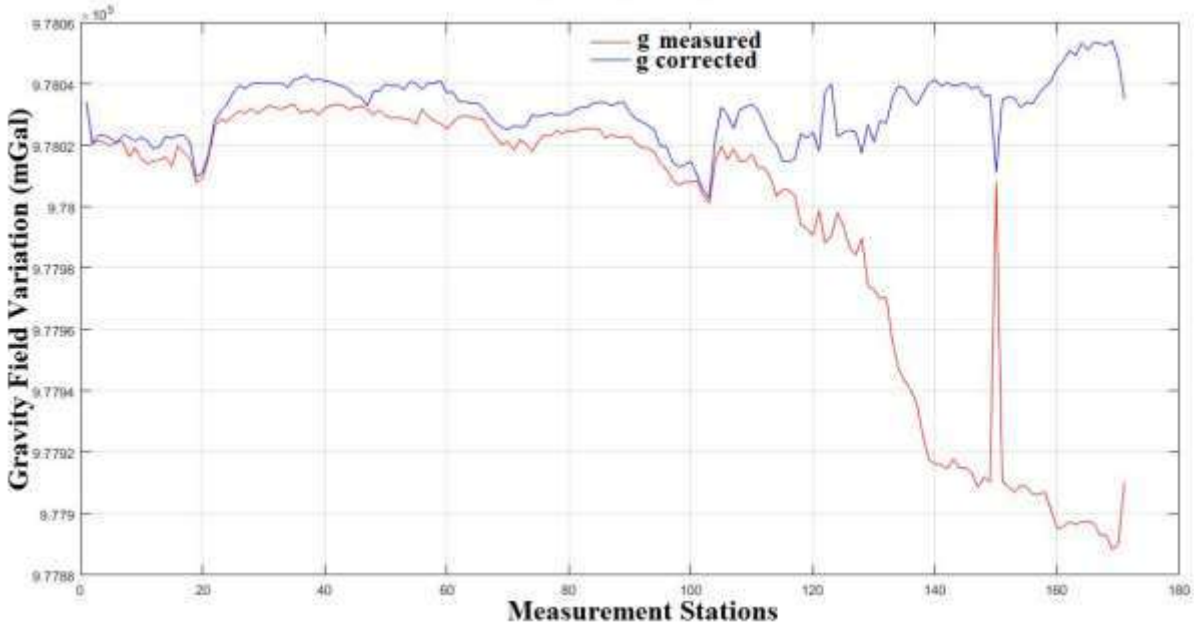

Figure 29: The effect of free-air correction on raw data.

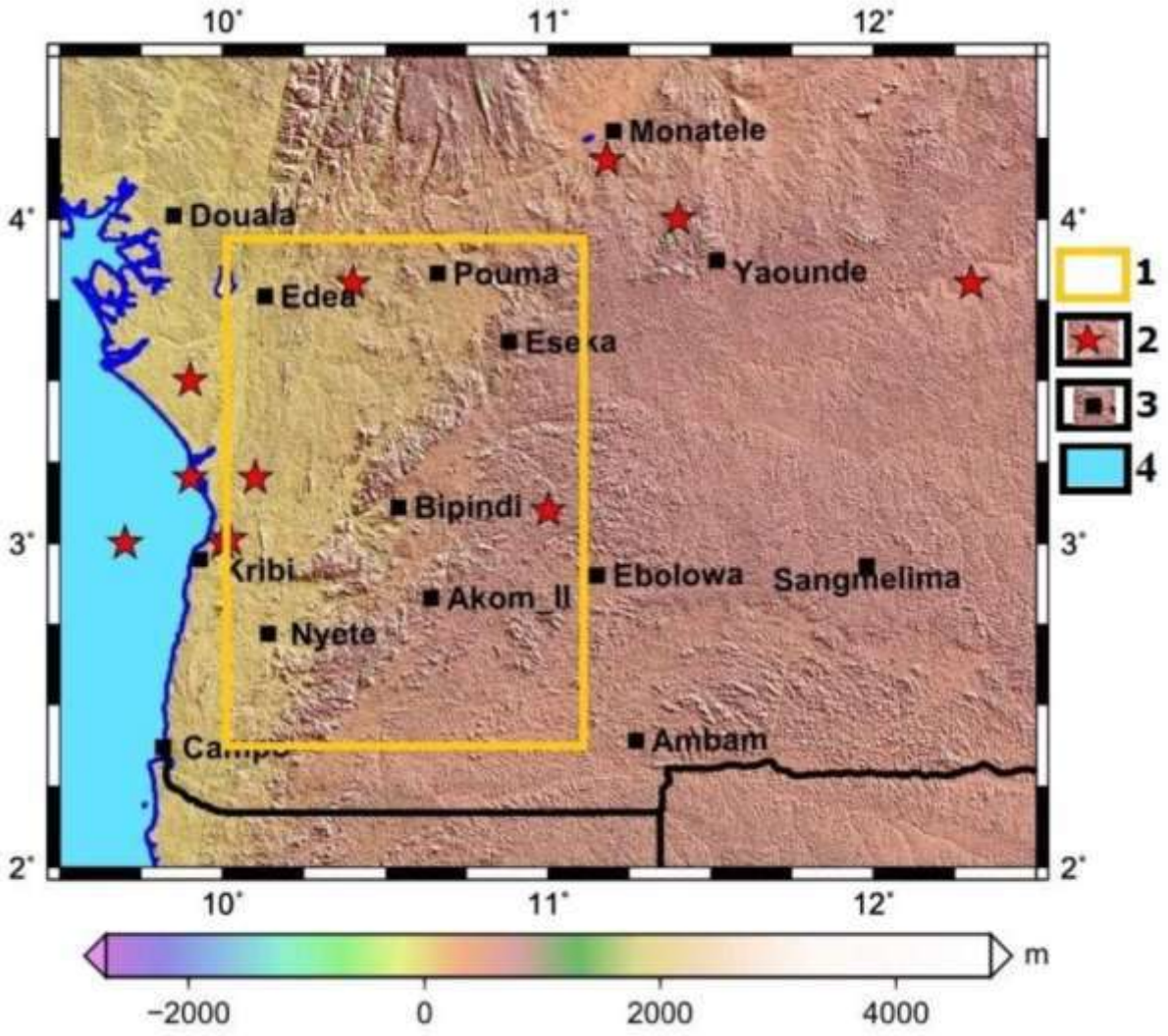

Figure 29b: topographic map of the region showing (1) altitude variation area; (2) areas with seismic activities; (3) localities; (4) Atlantic Ocean.

In figure 29a, we superposed the curves showing the measured value of g along the profiles and the same values after the application of the free-air correction. We can observe that, in the first hundred stations (first profile), the two curves are closed one to the other with a similar evolution. Comparing figures 29a and 29b, it is obvious that the measurement stations with the lowest free air effect correspond to the low elevation values in the profile. The proximity of the measurement stations to the sea implied the proximity of the station altitudes to the sea level. As we peruse along the second profile, the gap between the two curves increases. This is a confirmation of the increasing values of the altitude as we move from the

coast to the continent (along the second profile). At station 150, there is a considerable tightness between the two values. This change is observed at a major depression in the study area around the Lokoundje River.

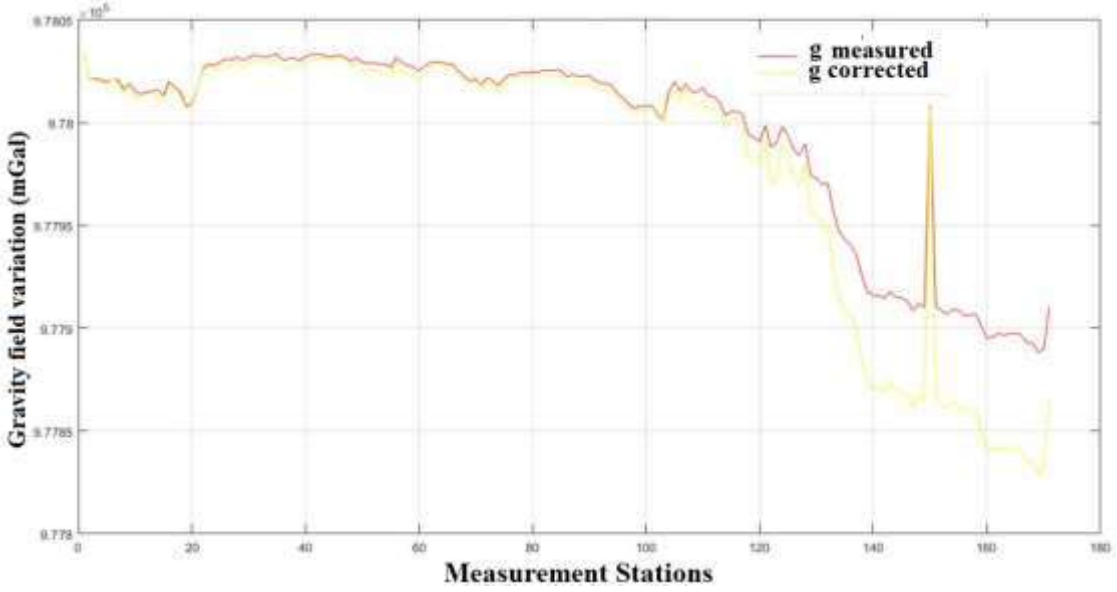

Figure 30: The effect of Plateau Correction on raw data.

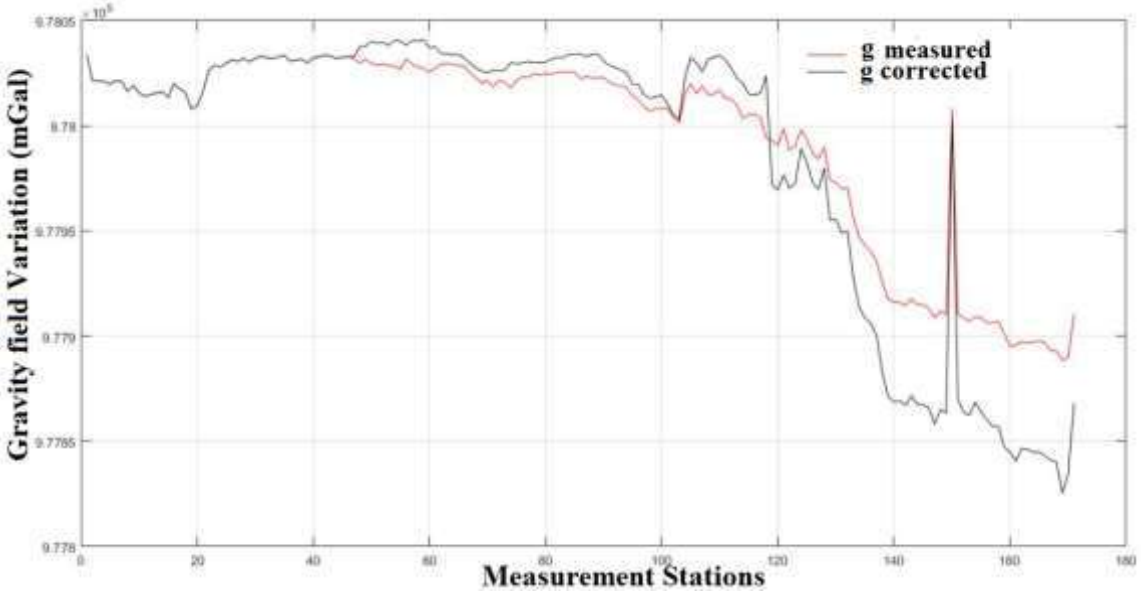

Figure 31: The effect of Latitude Correction on raw data.

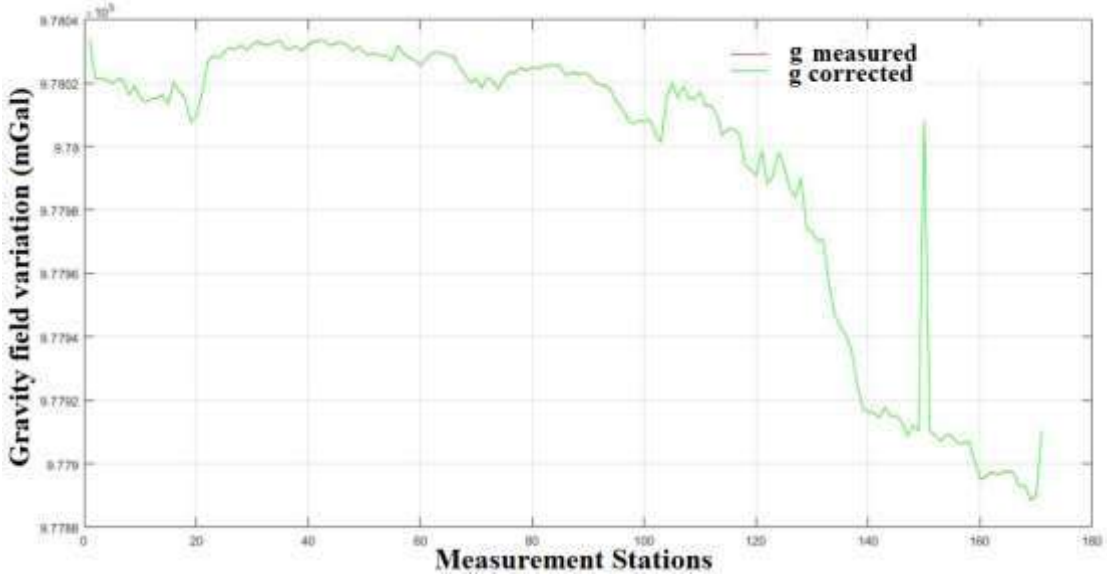

Figure 32: The effect of Terrain Correction on raw data.

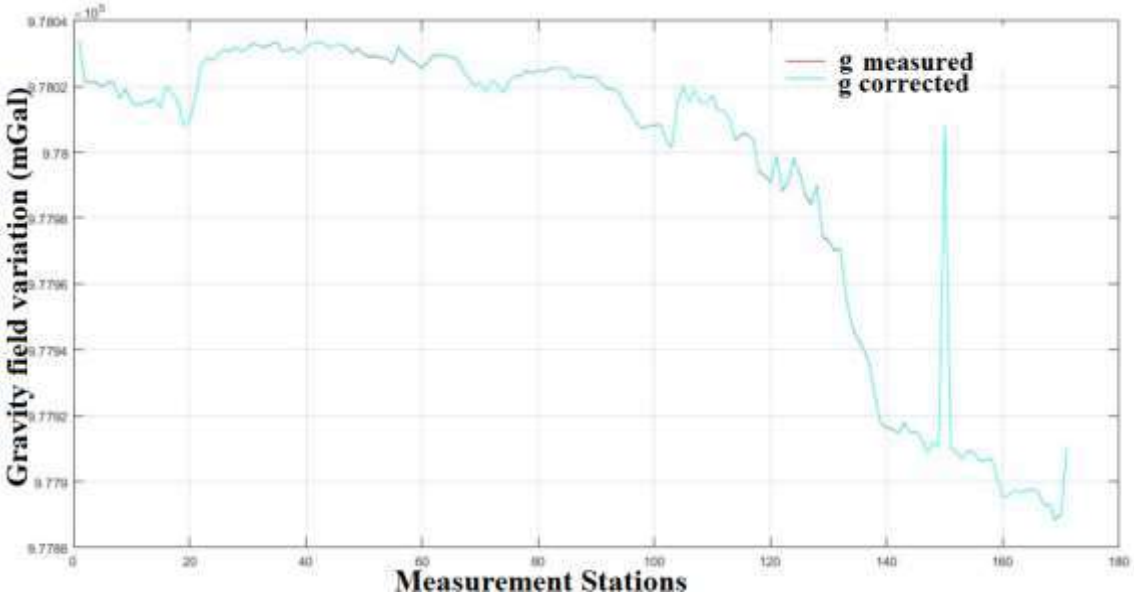

Figure 33: The effect of Lunisolar Correction on raw data.

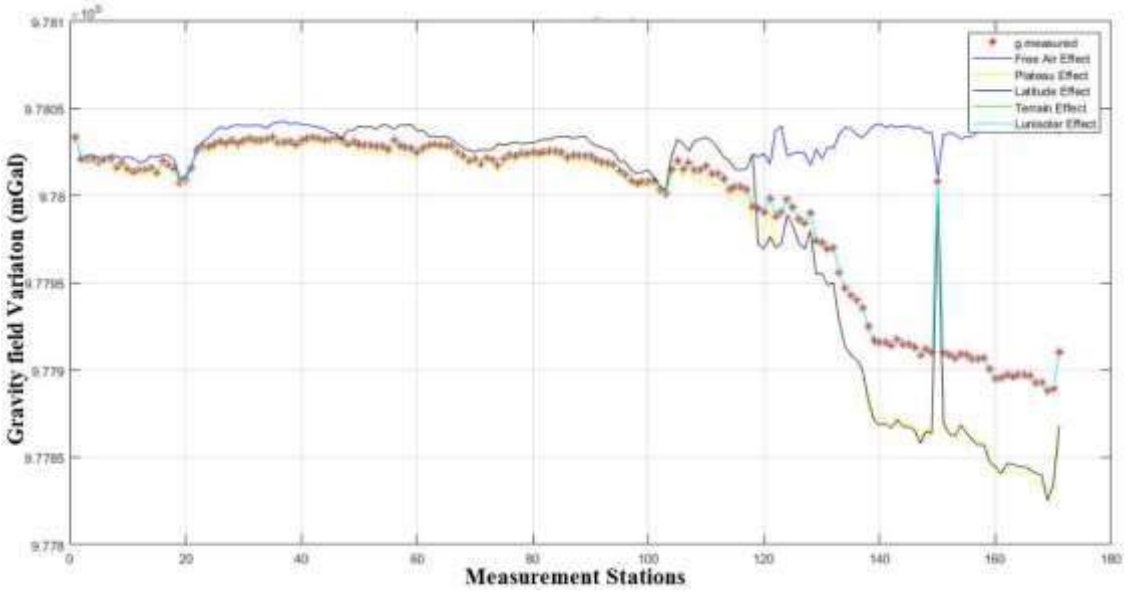

Figure 34: Comparison of all effects.

On the figures 29 to 33, we present the effects of the five gravity corrections applied on the raw data.

The effect of the plateau and latitude corrections on the raw data (figure 30 and 31 respectively) are quite similar as their curves have similar paces. They are less pronounced in the first profile and get increased we progress along the second profile. The effect of the terrain correction and the Lunisolar correction on raw data (figures 32 and 33 respectively) are equally very similar as their curves have similar paces. The terrain correction seems to have no effect on the observed data given that the red curve representing the measured values of g and the blue curves representing the corrected values of g, are almost perfectly superposed. This is the result of the smallness of the correction values compared to the observed values. The Lunisolar correction effect figure on the other and exposes slide differences between the two curves as we can observe parts of the red curve in some stations along the profile

Figure 34 is a recapitulation of the former figures and outlines the corrections that have the most impact on raw data and their location along the profiles. It can be observed that, for the first hundred points (first profile), most of the corrections, especially terrain correction, latitude correction and Lunisolar correction have little impact on gravity data while on the second profile, the impact are more obvious and consistent.

1.4. Implications and discussions

The free-air correction calculated in this study appears to be the one with the most impact on measured gravity data. Their values vary less along the first profile where the altitudes are low, while along the second profile located in the continent with multiple altitude variation, we observe more important values.

The plateau correction and the latitude correction have approximate variations. Given that the bouguer slab is a function of the masses located between the base datum and the reference, these masses are thinner at the coast and thicker in the continent. In the Kribi locality, the plateau correction was subject to major change in value. This station appears to be at the earthquake epicenter observed in 2002 in this region (Tokam et al. 2010). The importance of the latitude correction is a function of the distance between the given station and the origin meridian. For the first profile, this distance is quasi-constant because it this parallel meridian. The distance increase slightly for the stations in the second profile. This is the reason for the more pronounced differences between observed and corrected data in this profile.

If there is a correction to be neglected in the reduction of gravity data in this region, it should be the terrain correction because value are too inferior to the observed ones. However, this correction is important as it adds accuracy to the studied data. The values of the terrain correction equally indicate that there is a good isostatic compensation of masses in the subsurface (Telford, 1976)

One of the most important corrections to be considered in this study is the Lunisolar correction because the increasing accuracy of the measurements requires more precise evaluation of the Lunisolar correction. Therefore, the more detailed analysis of algorithms is required. Mostly the Lunisolar correction is calculated assuming that levelling proceeds at constant speed and in the same azimuth between benchmarks (Jensen, 1949 and Agnew, 2007). This correction is almost always important regardless of time and space.

1.5. Conclusion

In as much as the corrections applied on raw gravity data help to eliminate the non-geological sources of anomalies affecting the measured data, they equally reveal information related to the reparation of masses in the subsurface, areas with the highest gravity noise and how this noise is related to the geographical, geological and geophysical configuration of a study area (Telford, 1976).

The well-known relationship between the altitude and the free-air correction was emphasized in this study. A perfect superposition signifies that the correction is negligible. The more gap between the curves, the more important the correction.

The second profile of data in our study area has revealed the presence of more non-geological sources than the first, indicating a considerable gravity noise.

SECTION 2: DETERMINATION OF STRUCTURAL AND GEOMETRICAL PARAMETERS OF THE KRIBI-CAMPO SEDIMENTARY SUB-BASIN.

2.1. Introduction

The gravity anomaly maps generally superpose the effects of deep, shallow, local and extended gravity contrasts. The effects of a local or shallow structure are of- ten hidden in the signatures of regional structures. We carried out regional-residual separation using the polynomial fitting method with the aim of isolating the anomalies caused by deep and extended sources (long-wavelength anomalies) from those caused by local and shallow density contrasts (short wavelength anomalies). The residual field (figure 36) is obtained by estimating the regional gravity field and removing it from the observed field which is the Bouguer anomaly (figure 35). In effect, the order of the regional field n is assimilated to a polynomial of n degree. When n is small, the regional anomaly possesses values which are relatively more different from those of the Bouguer anomaly. In this case, the thickness of the part of the crust causing the corresponding residual anomalies is relatively large. This thickness decreases when n increases. In fact, the wavelength of the residual anomaly decreases when the degree of the polynomial increases thereby revealing geological structures which appear closest to the surface (Koumetio et al. 2012)

In this work, we have used a polynomial of degree '1', for spectral analysis, Horizontal gradient and Euler deconvolution, so as to have a better chance of locating the major contacts.

2.2. First order residual map analysis

The first order residual map (figure 4) reveals several local anomalies. The positive ones to the west at Kribi (A1), north-east of Kribi (A2), south-west of Kribi (A3), Lolabe (A4), Campo (A5) south-east of Lolabe (A6) and north of Kribi (A7) which indicate basement uplift and lateral differences in density from causative rocks. The Kribi positive anomaly is caused by an intrusive igneous body (gneiss, granidiorite) with a density estimated at about 2.74 g/cm^3. The Lolabe and Campo anomalies could also be the results of dense rocks intrusion oriented N-S and buried under the sedimentary cover. The main negative anomalies are observed in the northeast, central south and southeast parts of the study area trending NW-SE (A8), SW-NE at Nyabessan (A9) NW-SE (A10) at Ma'an and the nearly circular anomaly to the east of Bipindi

(A11). Koumetio and al. (2014) suggested that the nearly circular anomaly of Bipindi was caused by a low density intrusive block having a density contrast of −0.095 g/cm^3.

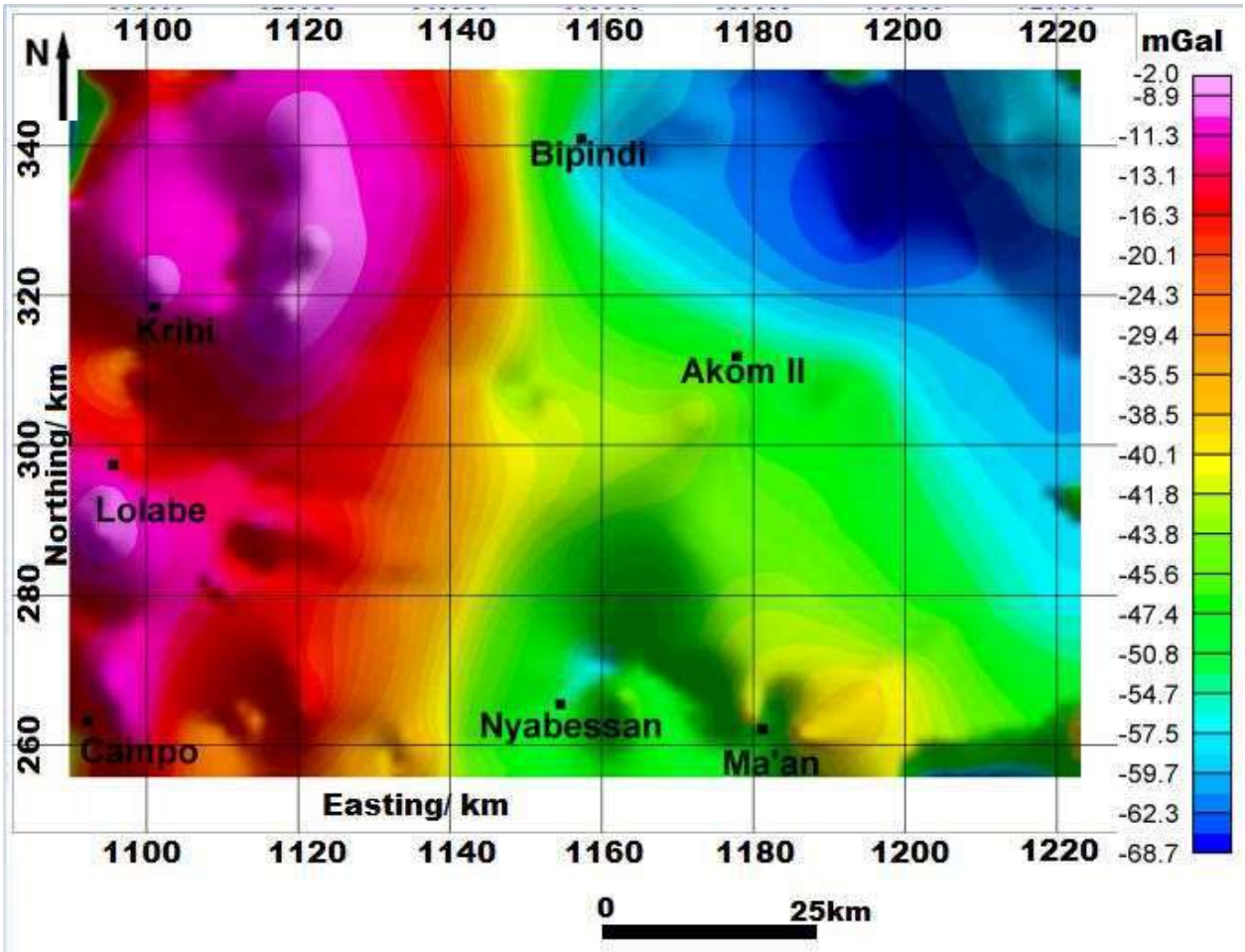

Figure 35: Bouguer anomaly map of the study area.

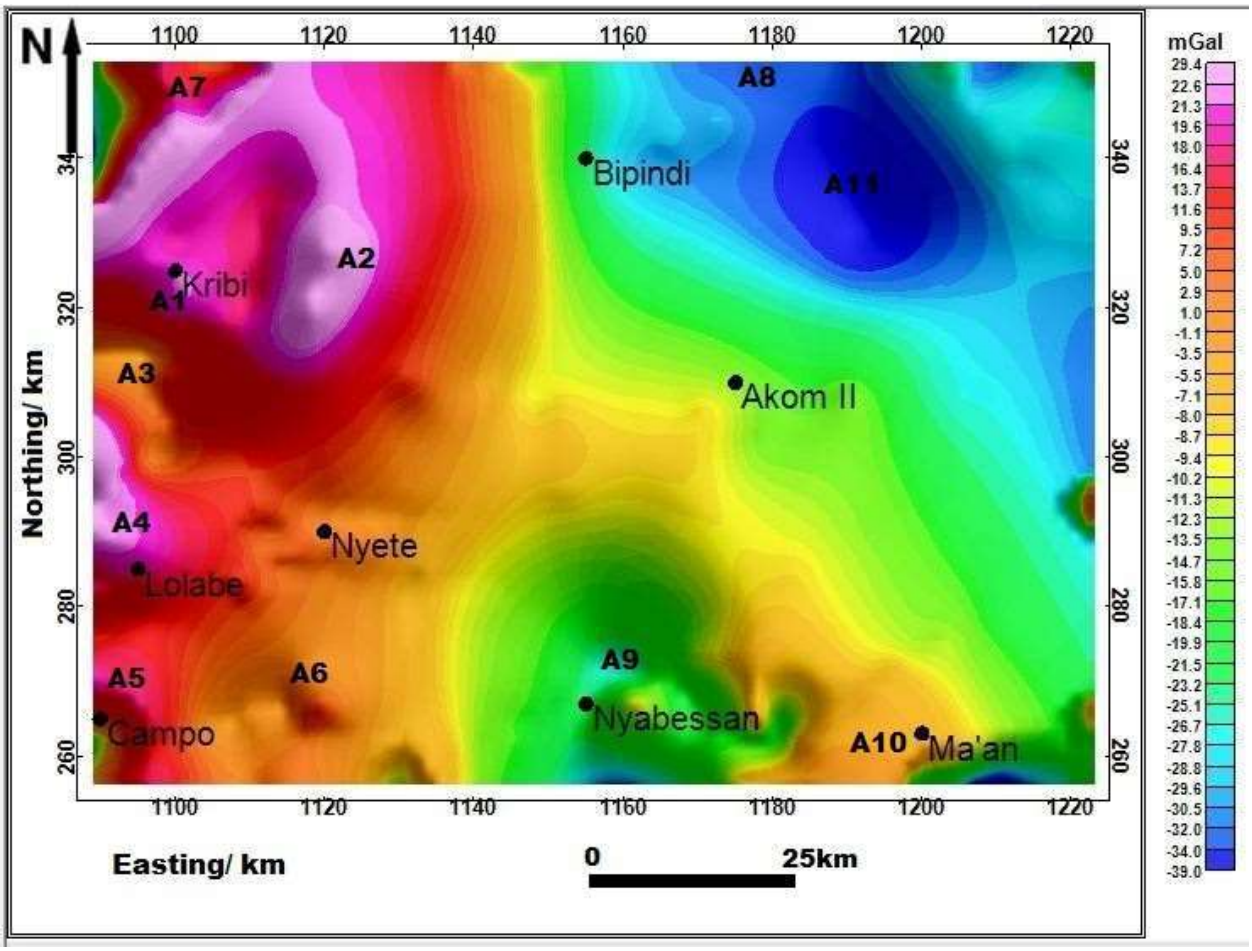

Figure 36: First order residual anomaly map of the study area.

2.3. Estimation of the thickness of the Basin

We applied a 2D spectral analysis on grids centered on positive anomalies in the basin situated on the western area of the map (A1, A2, A3, A4, A5, A6, and A7), which enabled us to determine the depths. The power spectrum has been obtained from the energy values which derive from the anomaly values. The given values are presented in Table 2.

Figure 37 presents a sample of the power spectrum curves obtained for the various anomaly grids. The line segment on this curve can be identified and plotted by a least square fitting on the data points. This curve is obtained from the anomaly values of grid A2. The same calculation was carried out for A1, A3, A4, A5, A6 and A7. The mean depth of density contrast plane may be interpreted as an inter-basement density variation associated with the depth to basement (Mouzong et al., 2014). This mean depth, highlighting the discontinuities observed for the positive anomalies has been calculated and presented in Table 3. The first observation

that can be made from this table is that, the sedimentary infill thickness decreases as we move from the west to the east of the area. The depths to basement vary from 0.60 km to about 3.93 km. We also observe that there is a relatively high accumulation of sediments in the basin (>0.6 km). The areas with the highest depth to basement or highest sedimentary thickness (~4 km) are the most promising regions for oil and gas exploration. The zone situated between Kribi and Lolabe and the Campo area are well indicated for further prospections. These results are therefore important for the selection of new exploration areas.

Table 2: Anomaly Values, Power Spectrum and wavenumber values for the anomaly grid A2.

Anomaly Values/ mGal	Power Spectrum	Log (Power Spectrum	Wavenumber/ km^{-1}
−50.00	**87.44**	**1.95**	**0.02**
−12.60	**2.06**	**0.33**	**0.07**
−4.19	**0.40**	**−0.40**	**0.09**
−7.58	**0.11**	**−0.95**	**0.11**
−9.22	**0.04**	**−1.40**	**0.15**

Table 3: Depths to basement obtained from power spectrum of gravity data.

Anomaly ID	Depth To Basement/km
A1	**2.62**
A2	**2.84**
A3	**3.48**
A4	**0.97**
A5	**3.93**
A6	**0.60**
A7	**1.19**

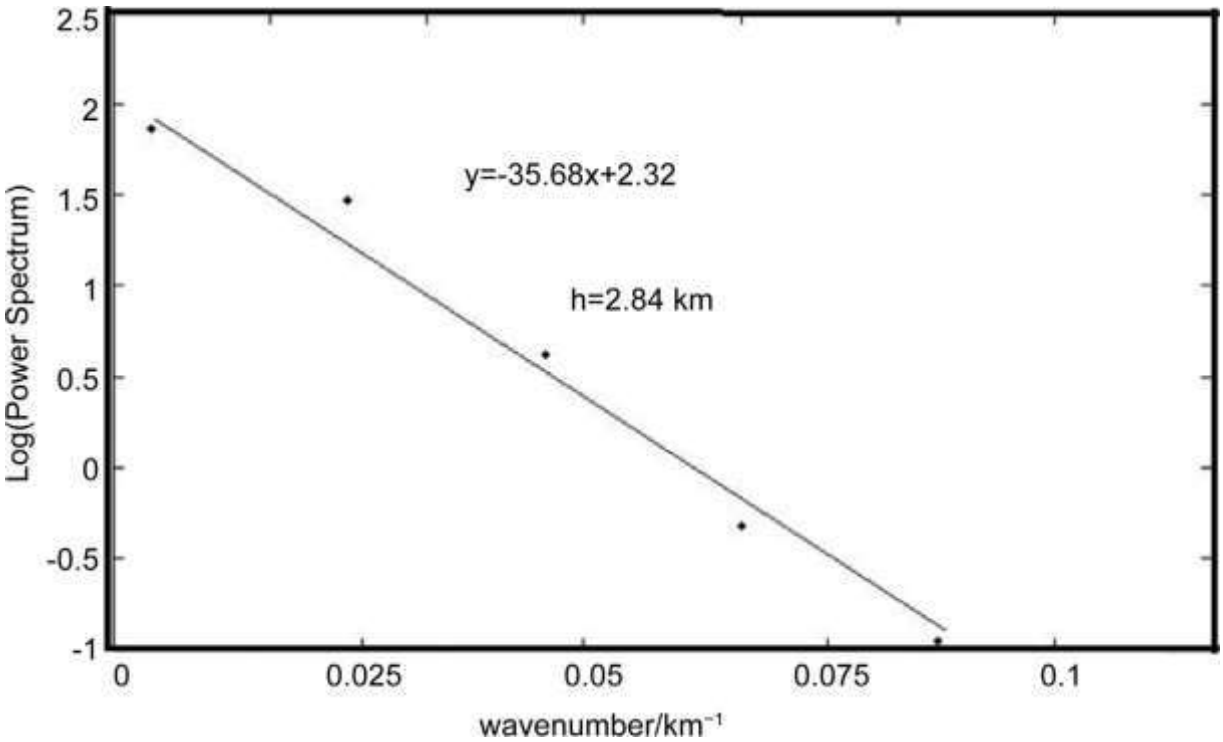

Figure 36: Power spectrum of the gravity data. The linear segment corresponds to the density layer used to compute depth.

2.4. Structural Map of the Basin

- **Horizontal Gradient Method**

We used the Oasis montaj 8.0 software to calculate the amplitude of the horizontal gradient of the residual data of the study area (Figure 38). We can clearly observe on this map the regions with high gradient amplitude indicating high density variation between contacts. The two major lineament that are interpreted from this map are striking in the direction NW-SE from Kribi right to Nyabessan and from Lolabe to the south east of Campo. The east of Bipindi is also characterized by high gradient variation. This could mark the huge change in density between the Bipindi intrusive block and metamorphic formations surrounding it. Due to the broad nature of the high gradients, we suggest that the boundaries of density contacts in the Kribi-Campo basin are probably not necessarily vertical and relatively deep or produced by several boundaries.

- **Euler Solutions**

For the Euler method, the following parameters have been used to compute the Euler solutions: structural Index N = 0.5, maximum % of tolerance of 5 and a window size of 5 km × 5 km. Figure 7 shows the results of the Euler method from the first order residual gravity data. This map presents the structural layout of the area showing the different faults affecting the subsurface. The computed depths vary between 2.0 km and 20.4 km for the entire region and between 2.0 km and 7.0 km for the western zone which makes up the basin. It is observed that the faults and contacts highlighted here get deeper as we move to the east. The shallowest are those located in the basin area at the extreme west and in the extreme south zone of the map. We present in the first column of Table 4 the various faults delineated using the Euler deconvolution approach, the orientations of these faults are given in the second column; it is observed that the SW-NE is the main fault direction in the basin. This information can be helpful in the determination of fluid flow direction in the basin. The last column of Table 4 gives the depth range of faults, the shallowest identified from 2 km and the deepest at about 12 km of depth. The different faults detected in the basin area can be interpreted as a result of local tectonic movements coupled with the setting up of intrusive rocks (granodiorites and gneisses) into the sedimentary and metamorphic formations.

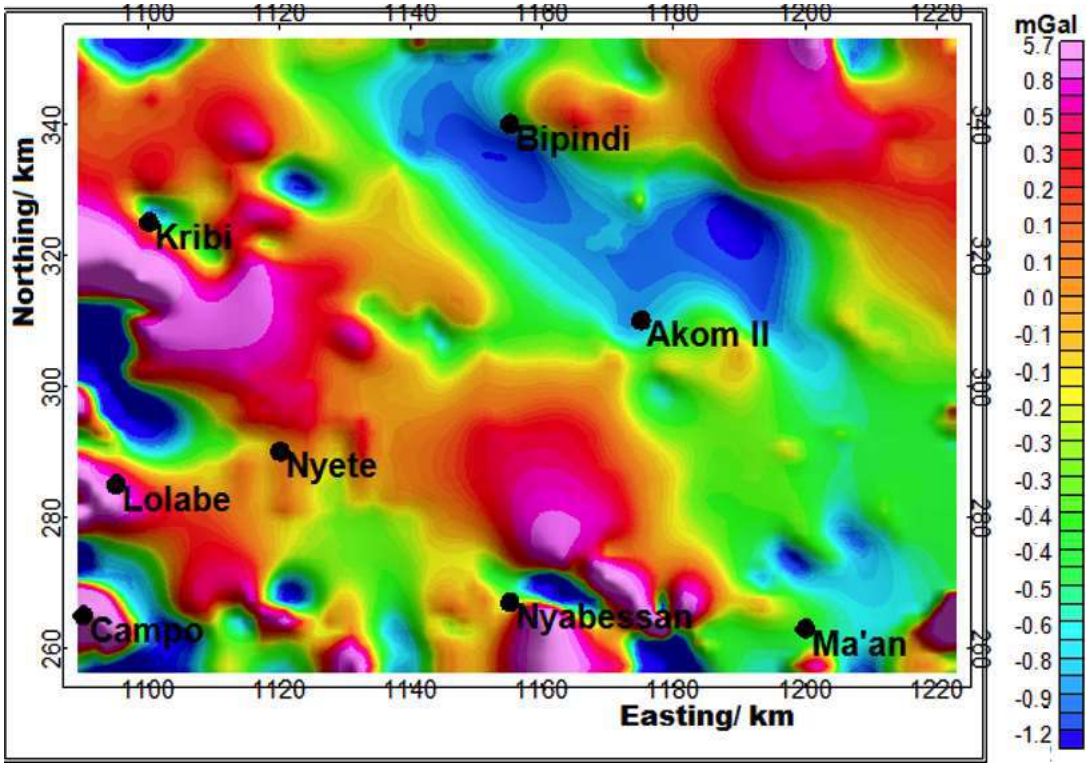

Figure 38: Horizontal gradient map of the study area.

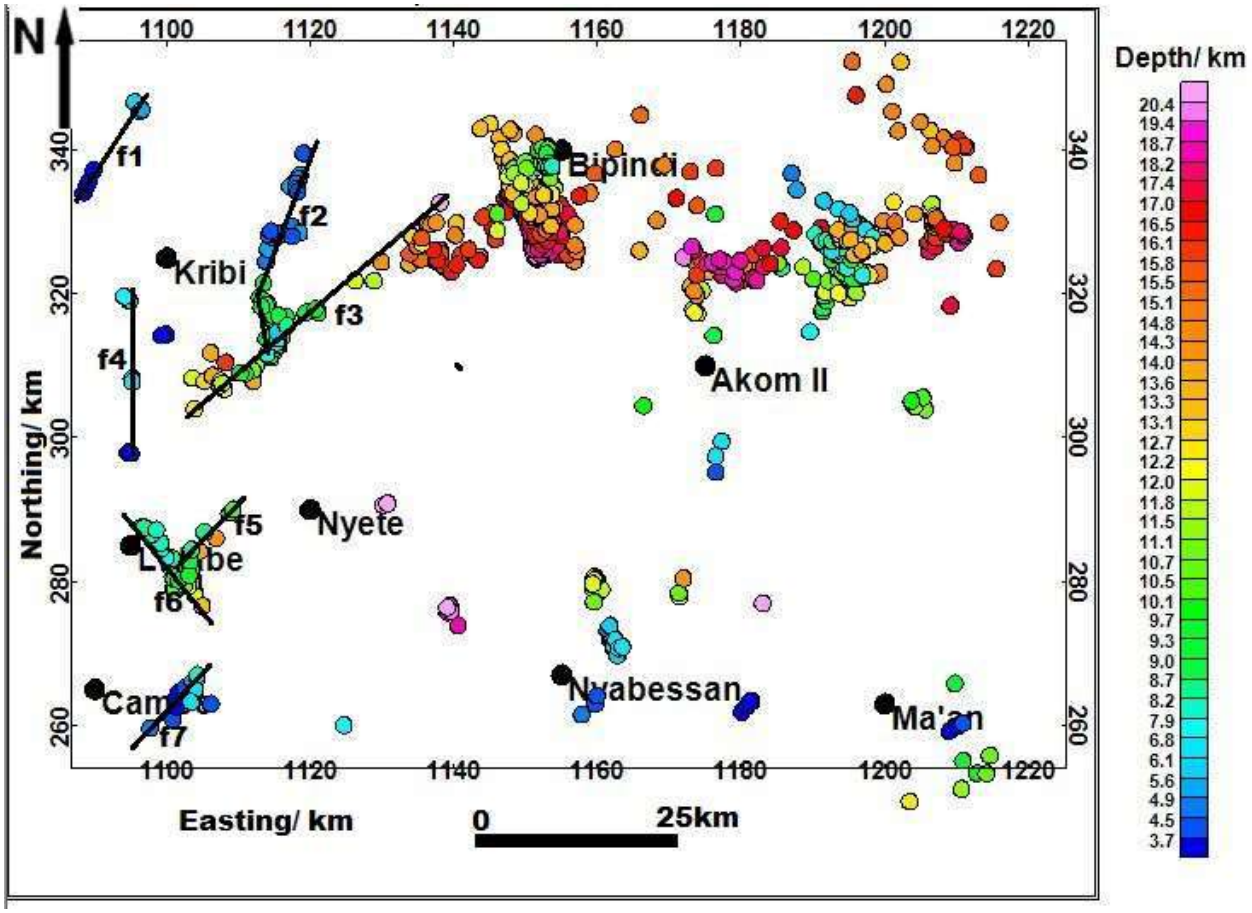

Figure 39: Structural interpretation of Euler Solutions for N = 0.5. The black lines represent the highlighted faults.

Table 4: Direction and Depth range of Faults in the basin.

Fault	Direction	Depth range/ km
f1	SW-NE	2-5
f2	SSW-NNE	2-4
f3	SW-NE	7-13
f4	NS	2-5
f5	SW-NE	2-6
f6	NNW-SSE	6-12
f7	SW-NE	2-8

- **Structural Map**

The combination of the above described results, namely the spectral analysis, horizontal gradient and Euler solutions have enabled us to propose a structural map of the Kribi-Campo sedimentary basin (Figure 40). This map shows quasi-linear contacts (numbered 1 to 12) which can describe faults and quasi-linear contacts (denoted C_1, C_2 and C_3) corresponding to horizontal limits of intrusive bodies.

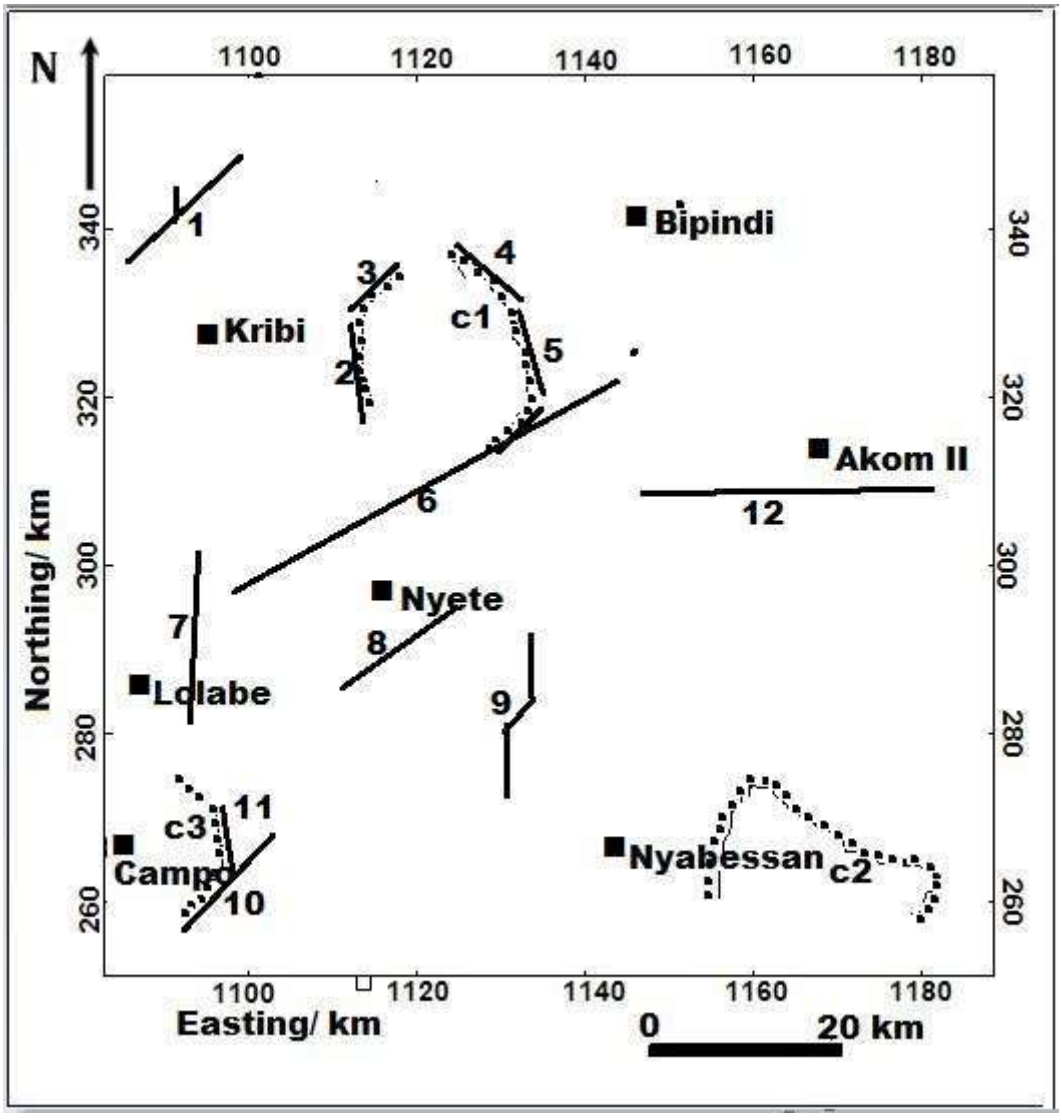

Figure 40: Interpreted structural Map of the Kribi Campo basin. (1) to (12) are interpreted linear contacts; (C_1), (C_2) and (C_3) are interpreted boundaries of intrusions.

2.5. Discussion

The results presented in the above sections are in accordance with the fact that the Kribi-Campo basin formations are relatively shallow compared to the Douala and Garoua basins. The general disposition of anomalies on the first order residual anomaly map (Figure 36) shows a west-to east diminution in the anomaly values which indicates the same variation of density values. The Kribi zone is intruded by a 4.5 km thick block of body composed of gneiss and granidiorites. This intrusion has considerably influenced the sedimentary cover in the area. From the results of the sedimentary thickness obtained by spectral analysis, it can be seen that as we move from the North to the South of the study area, the sedimentary layer varies following a sinusoidal trend. This variation of the sediment thickness could be explained by the presence of high tectonic activities in the area (Owona et al., 2011) leading either to an uprising or to a subsidence of the basement. The horizontal gradient map shows that the boundaries of density contacts in the Kribi-Campo basin are not vertical and are relatively deep or produced by several boundaries because of the broad nature of the high gradients. From Figure 40 it has been shown that the discontinuities and contacts in the Kribi-Campo basin are relatively shallow. These contacts get deeper as we move into the continent. Seven (7) major faults have been delineated (from f1 to f7) each with its direction and depth range. The analysis of the structural map of the basin highlights the presence of: (1) contacts and faults trending mainly SW-NE, N-S, SSW-NNE and NNW-SSE which confirms the results of (Owona et al. 2013 and 2016) giving the same approximate directions to major lineaments in the region and (2) three circular contacts C_1, C_3 and C_3 representing rocks intrusions. This study also suggests that given the high sedimentary thickness, the area situated between Kribi and Lolabe and the Campo locality are of high potential in mining and/or hydrocarbon resources. This suggestion is supported by the fact that the presence of oil and gas in a basin might be due to two factors: in-situ generation and migration of fluids into the basin (Mouzong et al. 2014). The subsurface pressure which is a function of the sediment thickness (*i.e.*, the sediment weight) is one of the environmental conditions needed for oil and gas formation in a basin. The understanding of the fluid flow formation in the region could be elucidated by Euler solutions,the structural map and gradient maps analysis.

2.6. Conclusion

The aim of this chapter was to provide new insights on the structural setting and the geometrical characteristics of the Kribi-Campo basin. We used the polynomial fitting method

to carry out the separation of the residual and regional components of the gravity field. We observed that the positive residual anomalies in the area are the effect of both high-density rocks intrusions and sedimentary infill. The spectral analysis enabled to estimate the depth to basement on various parts of the Kribi-Campo basin which gives the sedimentary thickness. This thickness varies from 0.60 km to 3.93 km with the highest values obtained in some specific localities of the study area namely Campo and the area between Kribi and Lolabe. From the residual anomaly map and spectral analysis, it can be deduced that the sedimentary infill presents a discontinued nord-south variation and also decreases from the west towards the east as we move from the coast into the continent. We applied the horizontal gradient analysis to the residual component. The residual structural setting of the zone from the Euler method is characterized by major faults and contacts mainly oriented SW-NE with the shallowest in the west (from 2 to 7 km deep) and the deepest in the east (right down to 20 km deep) of the region. The use of spectral analysis and Euler solutions is very advantageous in the geometrical and structural characterization of gravity anomalies in the sense that they help not just to determine depths to basement of causative structures but also to evaluate their dip and their evolution in the longitudinal and transversal directions. The structural map of the basin provides the most relevant structural information in the area. This map can help in identifying the direction of fluid flow in the subsurface. The interpretation of the sedimentary thickness values can serve to identify areas with the highest mineral and hydrocarbon production potentials which correspond to areas with the highest sedimentary thickness.

SECTION 3: QUANTITATIVE INTERPRETATION AND 2.5D MODELLING: STRUCTURAL IMPLICATIONS

3.1. Introduction

The regional structure and distribution of fault zones within the deeply buried Precambrian basement in southeastern Cameroon has been the subject of many investigations. Owona et al., (2013) on delineating lineaments in the region, highlighted a series of deep and shallow faults traversing the area with a SW-NE dominating orientation. Owona et al. (2016) suggested the presence of high-density intrusions in the subsurface of this study area from the analysis and interpretation of the maxima of horizontal gradient of the Bouguer anomalies. In presenting the interpreted structural map of the Kribi-Campo basin, we highlighted in the previous chapter circular contacts indicating boundaries of intrusions in the Lolabe-Campo zone. In order to provide more detailed information on the nature and the characteristics of this intrusion, after a brief analysis and interpretation of the gravity anomaly map for the study area, this work consists of combining the indirect method (spectral analysis), the inverse method (ideal body solution) and the direct method (2.5D modelling) to analyze and interpret the new gravity data collected in this region. The main aim is to present the extensional and longitudinal dimensions of the Lolabe-Campo subsurface structure in general and to locate the gravity intrusion identified in the area.

3.2. Results

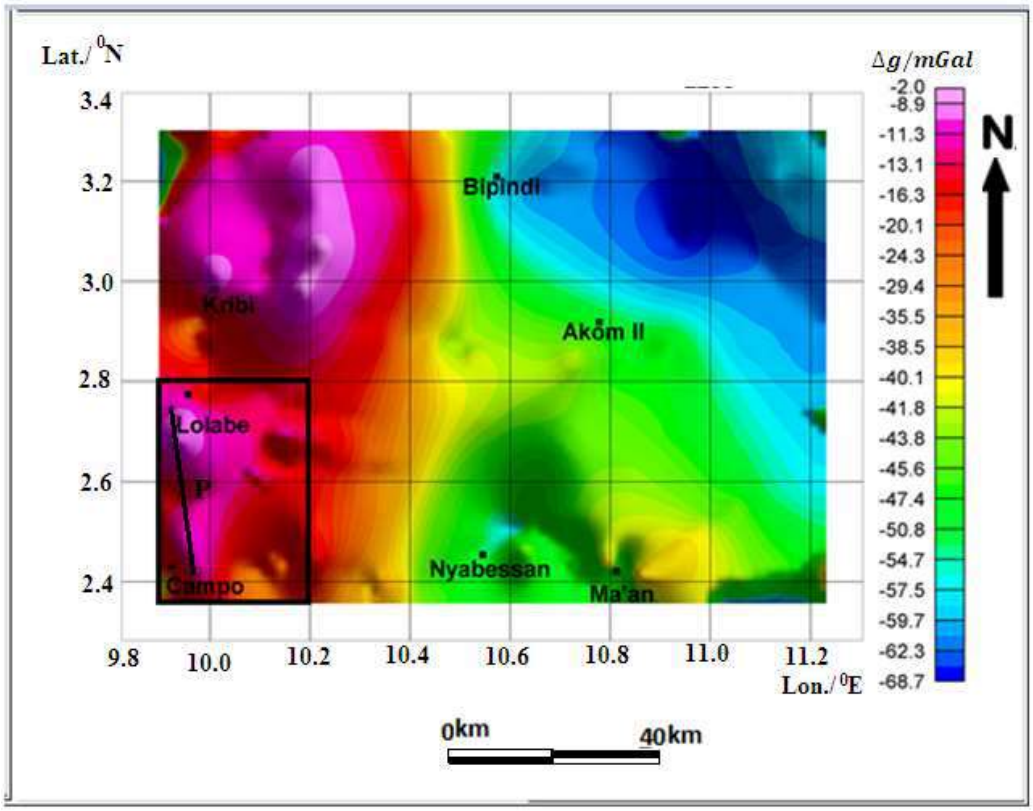

Figure 41: Bouguer gravity anomaly map of the study area.

3.2.1. Bouguer anomaly Map

The Bouguer anomaly map was obtained by an automatic computer drawing using the Geosoft Package software v.8. From the established grids using a contour interval of 3 mGal (figure 41). The area of interest is dominated by a relatively broad gravity high extending southwestward from Lolabe to Campo. The entire western part of the map is dominated by high gravity anomalies with the broader part in the north while the eastern part shows relatively lows values. This indicates a strong gradient of anomalies between the east and the west which is probably linked to the Kribi-Campo fault oriented NE-SW.The northwestern and southwestern high circular shaped anomalies are caused by intrusive dense bodies in the subsurface of the region. The gravity modelling will situate these intrusions into the subsurface.

3.2.2. Depths of anomaly sources from spectral analysis

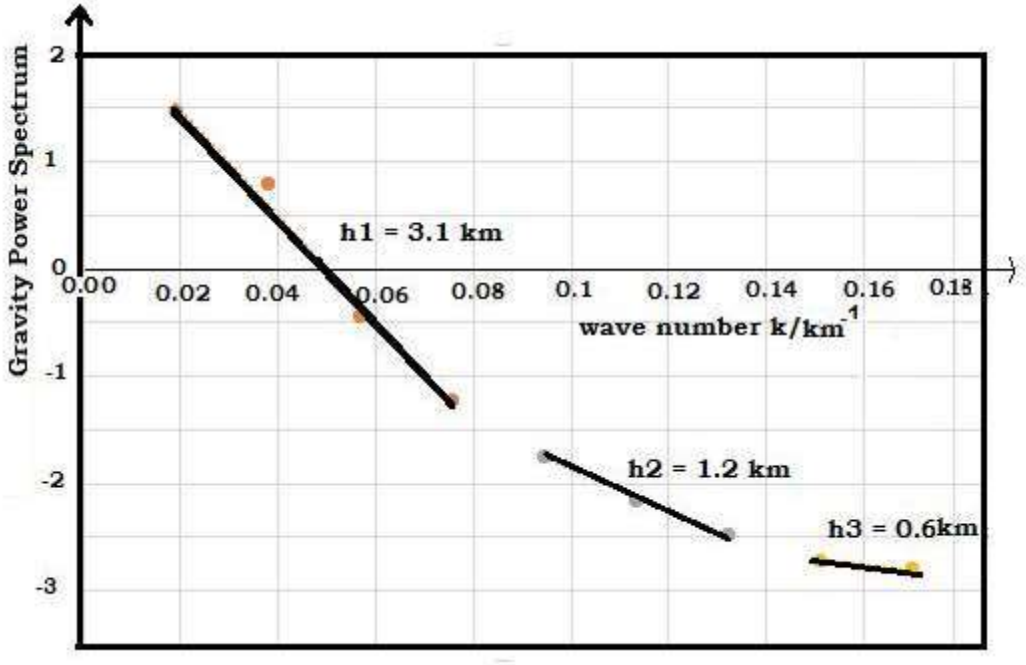

Figure 42: The power spectrum of profile P of the Bouguer anomalies showing depths (h_1, h_2 and h_3) of interfaces.

Figure 42 shows a representation of the gravity power spectrum with respect to the wave number for the profile P. Three different lines can be observed on this graph, which lines have been used to determine the average depth h_1 = 3.1 km, h_2 = 1.2 km and h_3 = 0.6 km corresponding to the interfaces of low, average and high frequencies respectively. These results show that the depth of the form of the intrusion is not uniform. h_1 represents the depth to the base of the body, h_3 the depth to the top while h_2 is the depth to a particular section of the intrusive body.

3.2.3. Ideal body solution

In order to determine the ideal body for the investigated anomaly, we used the IDB2 Fortran Program (Huestis and Ander 1983) which calculates Parker's ideal body using the simplex algorithm for the linear programming. The solution of the ideal body is calculated along the 40 km profile AB (figure 41) and the characteristics of the initial model for data inversion are as follow:

- horizontal length of prisms: Δx = 1 km;
- vertical length of prisms Δz = 0.5 km;

- number of prisms following the horizontal nx = 20;
- number of prisms following the vertical nz = 10;
- error on the value of anomaly: 1 mGal.

Figure 6 presents the solution of the ideal body in which is represented the anomalous bodies responsible for the observed anomaly in the region. The ideal body gives an idea on the distribution of these responsible masses and their apparent geometry. On the right, we have a the bigger block located between at 0.5 km and 3 km, and a smaller block on the left situated 0.5 km and 1.5 km. These two masses, with a density contrast of 0.13 g.cm^{-3} compared to the surrounding rocks, are relatively located in the Northern side of our selected profile.

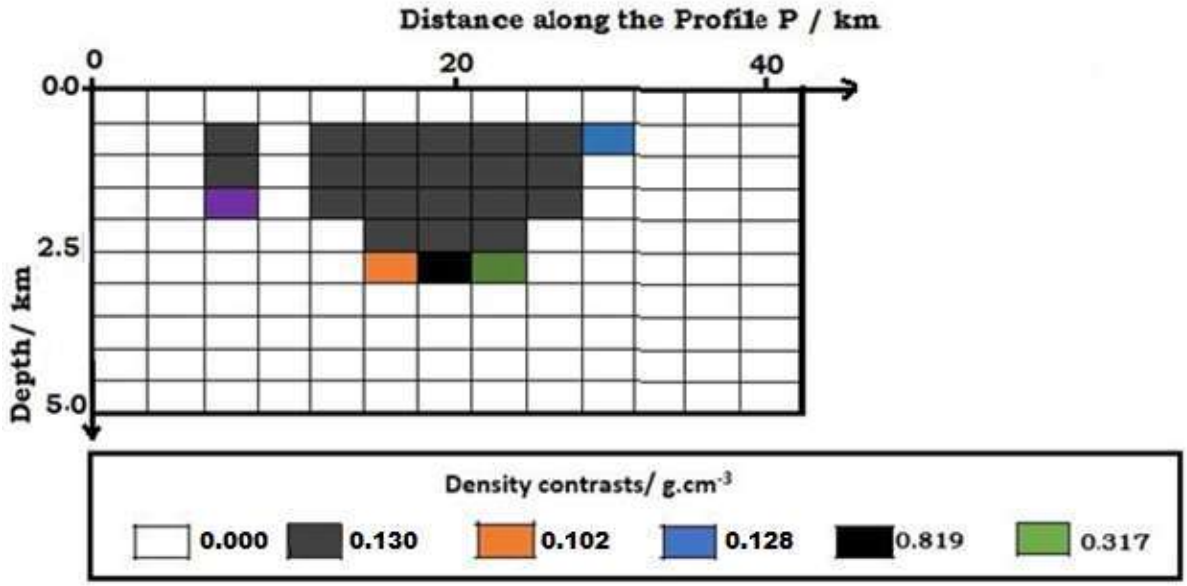

Figure 43: The Ideal Body Solution.

3.2.4. 2.5D Gravity model

The model presented in figure 44 consists of various bodies which are responsible for the observed anomalies along the profile. We used the computer program Grav2dc (Cooper, 1998) to carry out this modelling. This interactive software allows one to design a geological model in the form of the polygon, whose gravity signature is in accordance with the observed anomalies. It takes as initial values the density contrast and the lateral extension of any given body. Three main parameters were used to constrain this model, namely: the value of the

density contrast (0.13 g.cm^{-3}) obtained from the ideal body solution (figure 43); the depths of the intrusions obtained from the spectral analysis calculations (depth to the top 0.6 km and depth to the base of 3.1 km for the main body to the right and 1.2 km for the small block to the left) and the known geological information in the region (region mainly covered by sedimentary and metamorphic formations and other intrusions). The obtained model (figure 44) shows a structure of two blocks which seem to have resulted from the dislocation of a single block interpreted to be a dense intrusive rock surrounded by metamorphic and sedimentary formations. The first block, which is the smaller one is confined at depths of 0.6 km and 2 km approximately, it is located in the northern edge of the subsurface of the profile. An observation of the shape of this block, suggests that it initially formed a single block with the larger one situated on its right. The larger block to the right, with a wider extend than the first is confined at depths of 0.6 km and 3.2 km approximately and occupies mainly the middle portion of the profile. The dislocation of the two blocks could be as a result of the geo-tectonic activities observed in the region which gave rise to various faulting systems (Regnould 1986, Owona et al., 2016)

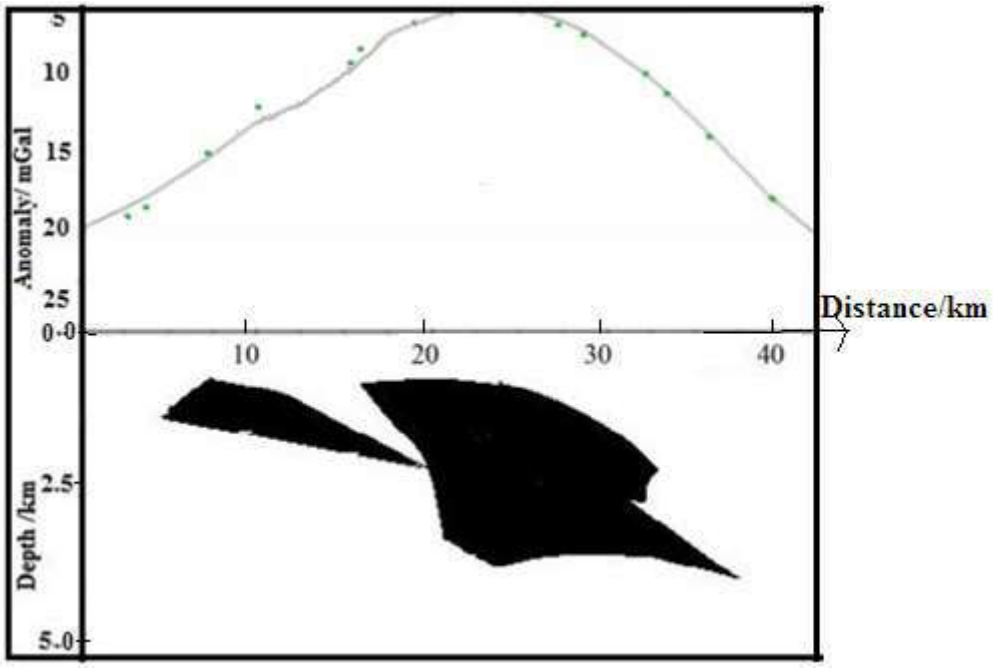

Figure 44: 2.5D model from profile P. The upper section represents the experimental anomaly and the theoretical curve. The green asterisks represent the observed gravity anomaly while the curve represents the calculated anomaly. The lower section shows the modelled blocks.

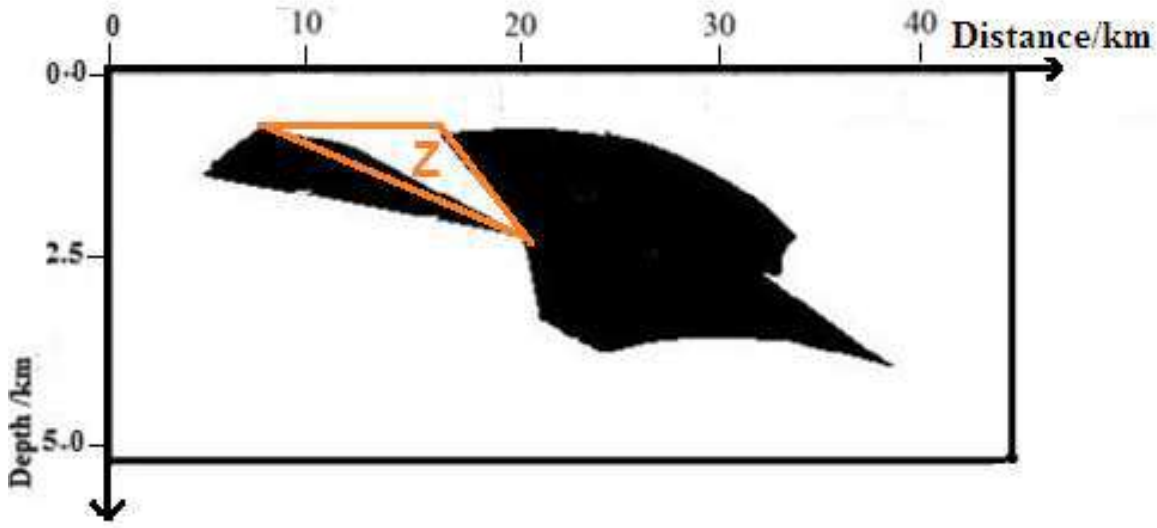

Figure 45: 2.5D model with potential trap zone represented.

3.3. Discussion

The high gravity anomaly values observed in the Lolabe-Campo area seem to have been caused by the presence of two high density rocks within the subsurface. From the results of the ideal body solution, the density contrast of these rocks is about 0.13 g.cm^{-3} compared to the surrounding rocks, which are mainly metamorphic and sedimentary in nature. The model is characterized by a depth to the top of 0.6 km for the two blocks, with a depth to the base of 1 km for the first block, depth to particular sections of the second block of 2.5 km, while the depth to the base of this second block is about 3.5 km. Although these characteristics are in close agreement with the results of spectral analysis, they are slightly different from the results of the ideal body solution, in which the two blocks are vertically separated with no contact between them. The two blocks as observed on the ideal body solution have a top-to-top separation of about 7.0 km and a base-to-middle separation of about 0.4 km. The model obtained highlights discontinuities between interfaces of contrasting densities at depths between 0.6 km, 2.5 km and 3.5 km. A closer look at figure 44 shows that the tectonic events responsible for the emplacement, breaking up and separation of the intrusive igneous body into two blocks could first of all have been as a result of an upward vertical translational tectonic movement followed by an anticlockwise rotational faulting tectonic movement. This in agreement with the results of Regnoult (1986), which indicate that the relief of the study area generally conserves the imprints of the phenomena of faulting tectonics. Popoff (1988) also mentioned the occurrence in the region of a strong extensional tectonic event that dates back to the Cretaceous. Owona et al. (2016) on delineating the lineaments in south Cameroon

obtained a structural map which shows that major tectonic events are responsible for the structural layout of this study zone. Considering that the average density of the metamorphic formations in the study area is equal to 2.67 $g.cm^{-3}$ and given that the density contrast of the intrusive igneous body is 0.13 $g.cm^{-3}$, the density of this body can be estimated at about 2.80 $g.cm^{-3}$. Table 1 below presents the density ranges of the various intrusive rocks in the region (Telford et al., 1976), from which it can be deduced that the intrusive body obtained in this study by the 2.5D gravity modelling could be composed principally of gabbro.

Table 5 : Density values of intrusive rocks in the Lolabe-Lolabe area.

Rock name	gneiss	alkaline syenite	nepheline syenite	granodiorite	dolerite	gabbro	peridotites
Density range/ $g.cm^{-3}$	2.60-2.90	2.60-2.95	2.53-2.70	2.67-2.79	2.70-3.50	2.50-3.10	2.78-3.37
Mean density value/ $g.cm^{-3}$	2.75	2.78	2.61	2.73	3.10	2.8	3.08

Dolerites (micro-gabbro) are intrusive igneous rocks that occur as dikes and sills and contain minerals such as olivine, plagioclase and feldspar. This suggestion about gabbro is based on the fact that the study area forms the onshore portion of the Kribi-Campo sedimentary sub-basin found around the Atlantic Ocean. The open zone (Z) between the two blocks (figure 45) obtained in this modelling, which is apparently triangular in shape could be favorable for the accumulation of hydrocarbons or minerals and should constitute a subject for more detailed studies to be carried out in the area may be using microgravity survey or other reliable geophysical prospecting methods. This fracture Zone resulting from a major tectonic movement can equally provide more detailed information on the fluid flow direction in the area.

3.4. Conclusion

The purpose of this section was to provide more information on the nature and the characteristics of the intrusive body in the Lolabe-Campo Area as proposed in the previous chapter. The analysis of the gravity map, the interpretation of the gravity anomalies by spectral analysis, ideal body solution and by 2.5D modelling reveal high gravity discontinuities between rocks of different densities and the presence of two high density blocks of rocks in the subsurface of Lolabe-Campo. The emplacement, breaking up and separation of the intrusive igneous body resulting to these two blocks have been interpreted as deriving from two tectonic events corresponding first of all to an upward vertical translational tectonic movement followed by an anticlockwise rotational faulting tectonic movement. The isolated intrusive igneous blocks whose density has been estimated at 2.8 $g.cm^{-3}$ based on an average density of 2.67 $g.cm^{-3}$ for the local rocks and a density contrast of 0.13 $g.cm^{-3}$, are completely surrounded by both sedimentary and metamorphic formations. A comparison of this high density value with

that of other intrusive rocks in the study area and also the location of this area around the Atlantic Ocean has led to the conclusion that the two intrusive blocks may be composed principally of dolerites. The disposition and shape of the open zone (Z) highlighted by the resulting separation of the intrusive blocks is suggestive of a very good trap for the accumulation of hydrocarbons and mineral resources. This conclusion however paves the way for more detailed studies to be carried out in the area using either microgravity survey or other more reliable geophysical prospecting methods.

SECTION 4: THREE-DIMENSIONAL MODELLING OF THE INTRUSIVE BODY IN THE NORTHERN PART OF THE SUB-BASIN

4.1. Analysis and Interpretation of Gravity Data

4.1.1. Analysis of Bouguer Anomaly Map

The Bouguer anomaly map presented in Figure 46 was obtained after an interpolation using a kriging gridding algorithm implemented in Oasis Montaj software. The highlight shows the most prominent anomalies within the study area. An overview of the map reveals three gravity domains:

The first domain which covers the western part of the map is characterized by high values of gravity anomalies. The form of these anomalies suggests that it marks the limit of a large structure to the left of the study area. In the field, this area corresponds to low altitudes and its position near the Atlantic Ocean shows that this anomaly has it source from highly dense rocks. This domain, with anomaly values ranging between −40.1 mGal and −2.0 mGal presents four prominent peaks, one at the Lolabe locality, another one in Kribi and the last two to the east of Kribi. All these peaks can be interpreted as high density or basic intrusive bodies within the main formation. The two peaks observable to the east of Kribi may be considered as a unique, very high-value anomaly, which according to Owona et al. (2016) corresponds to a ring complex affected by a nearly N-S trending discontinuity.

The second domain, located at the northeastern side of the map displays two apparent ring shapes, characterized by very low amplitude anomalies trending NW-SE from Bipindi to the eastern part of Akom II, these anomaly values range from −68.7 to −54.7 mGal. There are interpreted as due to the presence of intrusive low-density bodies in the subsurface.

The third domain which is situated in the middle of the map, from Bipindi to Nyabessan, consists of average anomaly values ranging from −50.9 mGal to −40.9 mGal and is separated from the two other domains by high gradients marking discontinuities between two structures in the subsurface. The correlation with surface geology shows that this area is the signature of charnockites and green rock belts of the Ntem Unit.

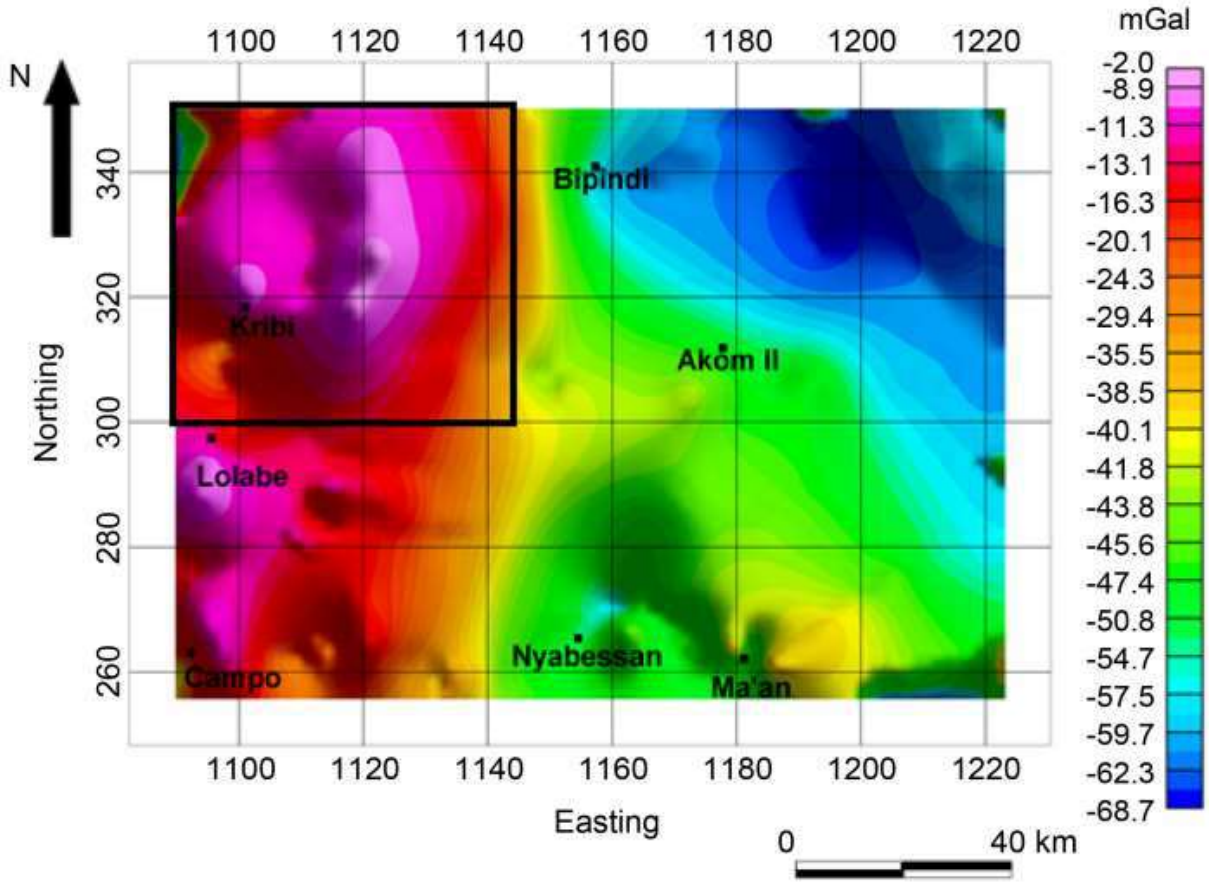

Figure 46: Bouguer anomaly map of the region showing the Kribi anomaly.

4.1.2. Analysis of Residual Anomaly Map

The Bouguer anomalies are the combination of deep and shallow sources, a separation of these anomalies into regional (deep sources) and residual (shallow sources) components was carried out in order to clearly identify the anomaly sources. This separation was performed using the polynomial fitting method. The procedure computes the mathematical surface, which gives the best fit to the gravity field within specific limits (Radhakrishna and Krishnamacharyulu, 1990)

This surface is considered to be the regional gravity anomaly. The residual is obtained by subtracting the regional field from Bouguer anomaly. The residual map of the study area presents characteristics similar to the Bouguer anomaly map. However, the high gravity ascribed to dense or basic intrusive bodies within the main formation and the low gravity ascribed to low densities intrusion are visibly more distinct on this residual gravity map. On the third order residual map shown in Figure 47, the three anomalous peaks observed around the Kribi area are seen to have merged to form a single oval peak indicating

the prominence of the dense intrusive body at depth. At depth the characteristics of the structure surrounding this intrusive body extend southeastwards from Kribi to Akom II and become more pronounced again between Nyabessan and Ma'an. Since the effects of the mantle and lower crust are not of interest in this work, a third order residual anomaly is used for modelling in order to have a better chance of locating the depth to bottom of the dense intrusive body.

In order to determine the nature and shape of the Kribi intrusive body, the residual field obtained here will be studied using three methods namely: the multi-scale analysis of gradients method, which is usually employed for the analysis of the multi-scale residual anomalies; the spectral analysis method and the 3D modelling.

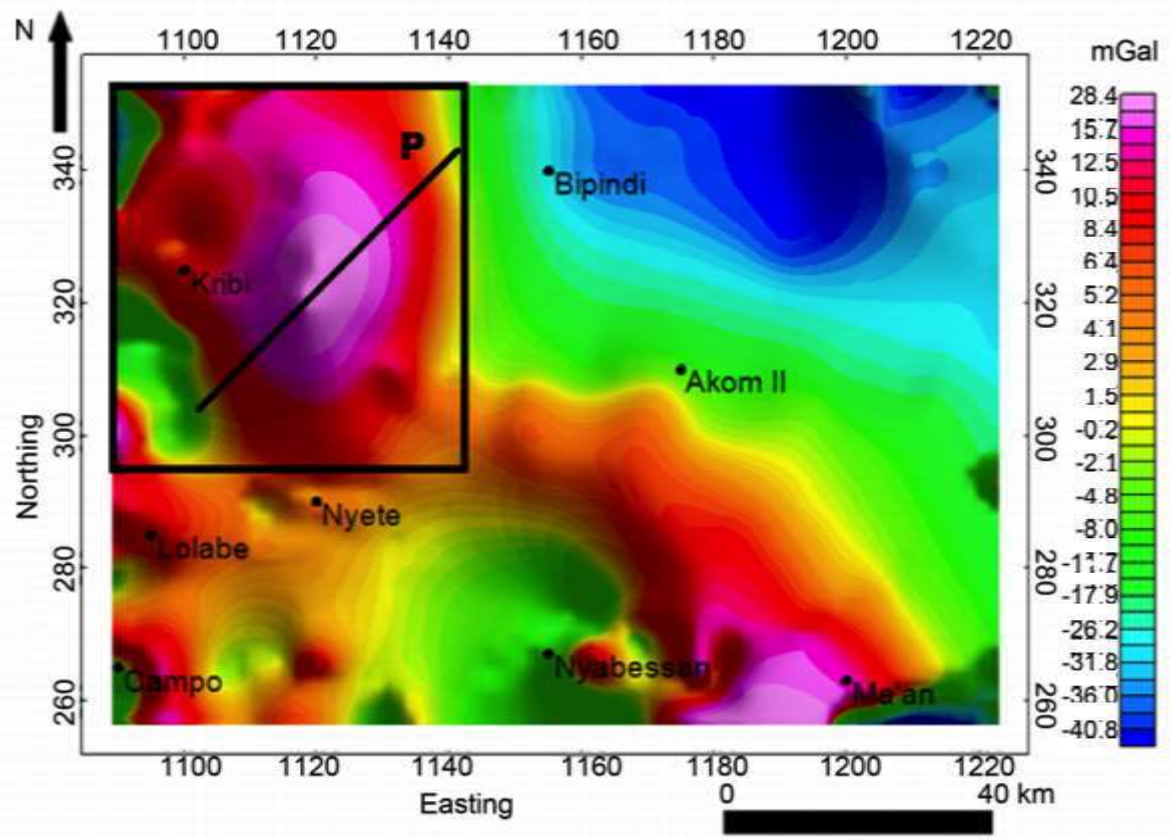

Figure 47: Third order residual anomaly map of the region showing the Kribi anomaly.

4.1.3. The Local Maxima Map of the Horizontal Gradient of the Residual Anomaly

After computing the horizontal gradient of the third order residual anomaly, the resulting map is upward continued at 0 km, 1 km, 2 km, 3 km, 4 km and 10 km. The local

maxima are then calculated and superimposed. The choice of the high of the upward continuation is determined by the types and depth of the structures that we intend to highlight. Given that, the higher we upward continue, the deeper the structures are highlighted. In our study, we intend to model a shallow formation. The maxima of the gradient of the residual anomaly upward continued could be observed on the map until the depth of 10 km. after 10 km, no effect of the anomaly featured on the map. That is why we choosed to stop at 10 km. The Maxima of the horizontal gradient of the third order residual anomaly map upward continued to 0 km, 1 km, 2 km, 3 km, 4 km and 10 km as presented in Figure 48 shows lines and quasi-circular contacts corresponding to horizontal limit of lineaments and intrusive bodies respectively. The depth of a lineament or an intrusive body is determined by the continued presence of the local maxima for increasingly high altitudes of upward continuation. This study will be focused on the continued presence of a quasi-circular contact noted (B1) in the Kribi area in the analyzed maxima of the horizontal gradient of the residual anomaly map upward continued to 0 km, 1 km, 2 km, 3 km, 4 km and 10 km.

The vertical limits of such an intrusive body can be predicted by the method developed by Koumetio et al. (2012), in which the depth of the top of the anomaly sources obtained after an upward continuation at the height h is greater than or equal to h/2, because the upward continuation at the height h eliminates the effect of the sources situated above the depth h/2. This implies in Figure 48 that the effects of the sources situated above the depth 0.5 km, 1 km, 1.5 km, 2 km and 5 km have been eliminated for the upward continuation to 1 km, 2 km, 3 km, 3 km, 4 km, and 10 km respectively. The presence of green, red, yellow, blue and black contact on the western side of the intrusive body B1 indicates that the depth to bottom is between 2 and 5 km. Also, the presence of green, red and yellow with the absence of black maxima on the eastern side of the contact indicates the depth to bottom here is between 1.5 and 2 km. The results obtained from the analysis of the maxima map will be used to constrain the modelling of B1.

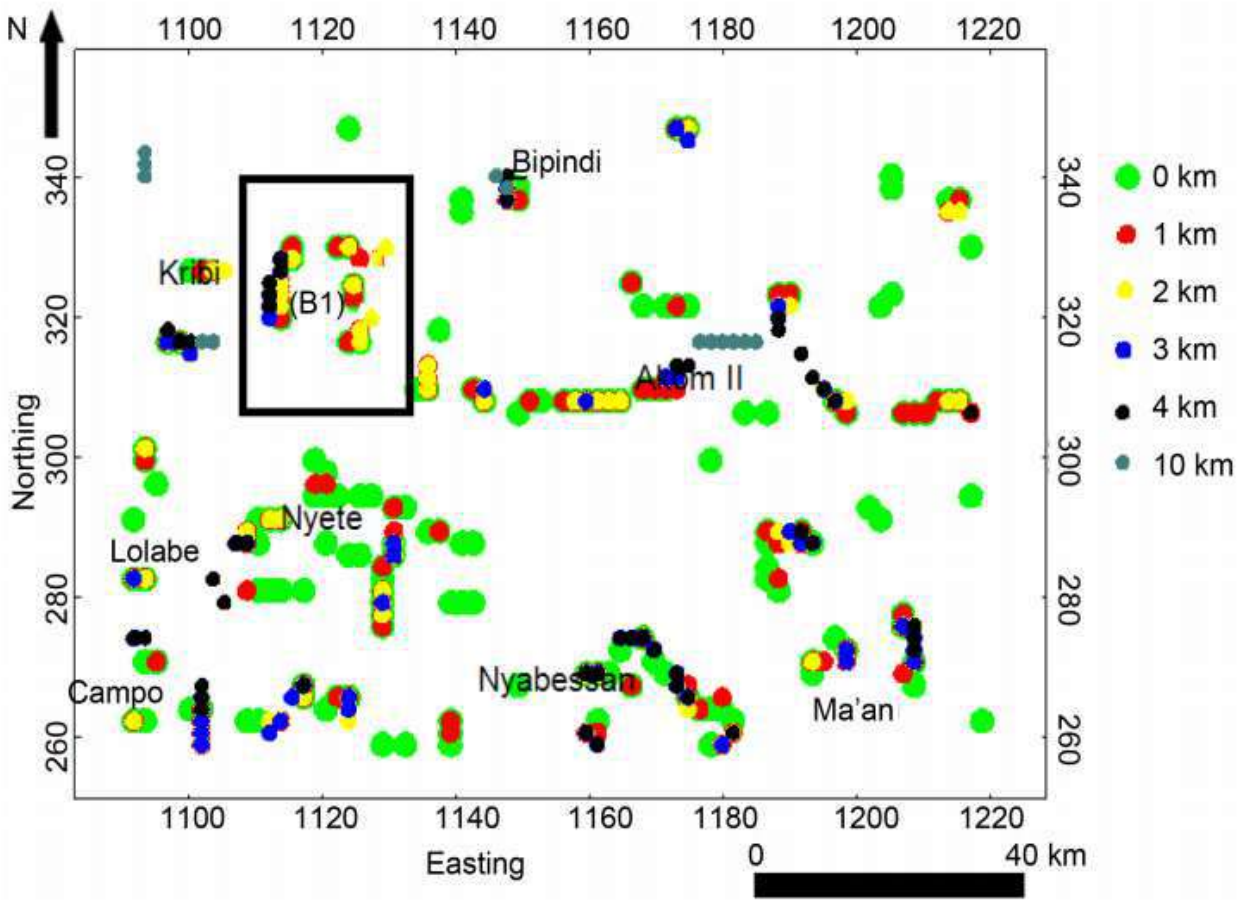

Figure 48: Superposition of the maxima of the gradients computed at various heights of upward continuation. Maxima are represented by small colored circles. The green, red, yellow, black and gray colors represent the maxima of the gradients upward continued at the heights of 0 km, 1 km, 2 km, 3 km 4 km and 10 km respectively. The located anomalous body source in the black frame.

4.1.4. Source Depth Estimation Using Spectral Analysis

A profile (P) was chosen and drawn on the third order residual gravity map. The data used to carry out the spectral analysis were from this profile shown by the black line crossing the main positive anomaly (Figure 47)

This profile was drawn with a NE-SW orientation and traversing through the suspected area of the intrusion.

Figure 49 shows the representation of the logarithm of the gravity power spectrum (energy E) with respect to wave number (spatial frequency) for the profile

P. The curve obtained from this representation, made up of 9 points is observed to have three (3) slopes represented by the 3 colored lines fitted into the figure, each of which is obtained

from 3 points. The depths obtained from the slope of the curve represent the average depths of the top of the anomalous source. This spectral graph presents three gradients that are used in determining the average depths h1 = 3.6 km, h2 = 1.6 km and h3 = 0.5 km of interfaces of low, average and high spatial frequencies respectively. The resulted values observed on the graph suggest that the depth to the upper surface of the intrusive body B1 is not uniform. It is believed that h1 presents the average depth of the bottom of B1, while h2 and h3 are depths to particular sections of the roof of the intrusion. These values obtained using spectral analysis will serve as constraints for the modelling of the body.

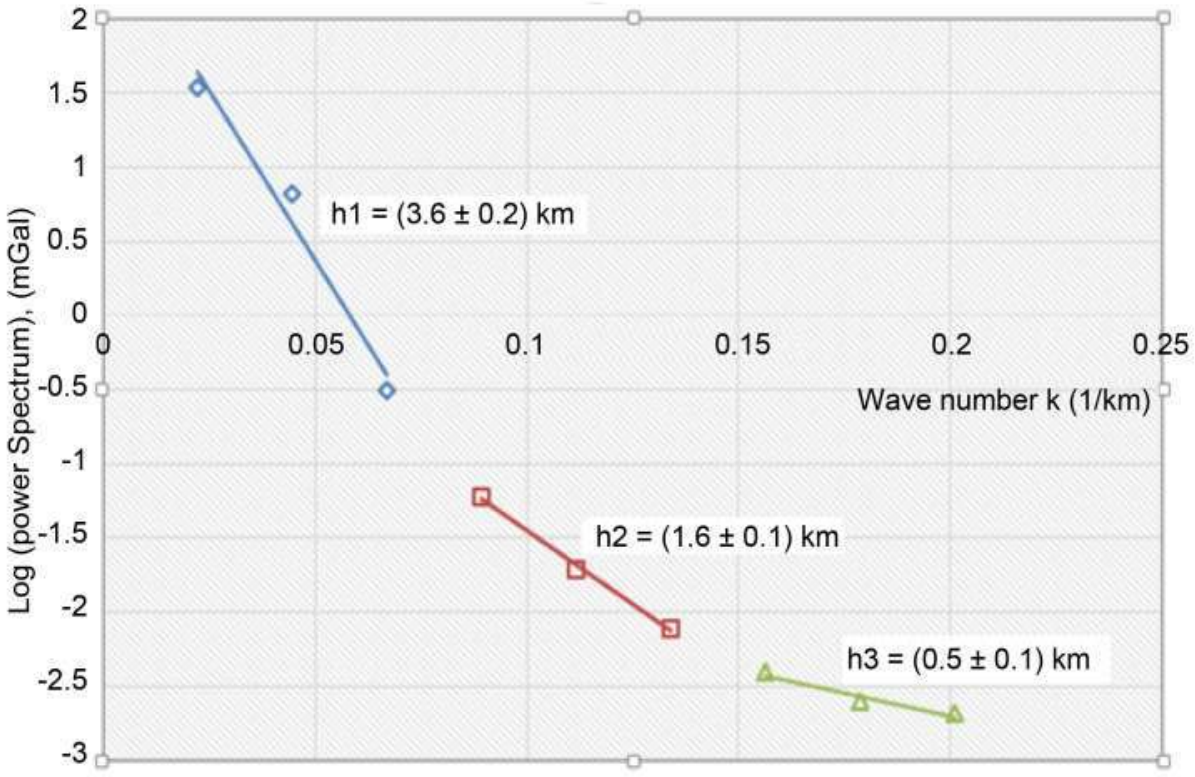

Figure 49: Logarithm of gravity power spectrum of profile *P* of the third order residual anomalies plotted versus the wave number *k*.

4.1.5. Direct Modelling

3D modelling was carried out using GRAV3D software on the residual field with the aim of delineating and characterizing the dense intrusive body responsible for the observed gravity anomalies in the study area. The GRAV3D library consists of three major programs and one utility. The facilities include: GM-DATA- VIEWER: this utility was used for viewing the observed gravity data, error distributions, and for comparing observed to

predicted data directly or as difference maps; MESHTOOLS3d: this utility was used for displaying resulting 3D models as volume renderings.

The modelling process of the intrusive body consists of constructing the body block by block in a predefined mesh. Every block is a combination of cubeoids of the same volume. Every block, with a constant density is defined along a vertical axis and along a horizontal axis. The coordinates of the blocks have been given taking as origin the point O (1095, 300, 0) bring latitude, longitude and altitude respectively all in kilometers. The body was constructed taking into account all the results provided by the multi-scale analysis of the maxima of gradients and spectral analysis. The statistics of the constructed model are given in table 6.

Table 6: Input Model Parameters

Block number	1	2	3	4	5	6	7	8	9
X_Coordinates (km)	1130 - 1135	1145 - 1150	1145 - 1150	1140-1145	1140-1145	1135-1145	1135 - 1140	1130-1135	1120-1130
Y_Coordinates (km)	324-360	344-348	340-344	336-340	332-336	328-332	324-328	320-324	320-324
Z_Coordinates (km)	5.1	4.8	4.8	4.8	4.8	4.8	4.8	4.8	4.8
Block number	10	11	12	13	14	15	16	17	
X_Coordinates (km)	1135 - 1140	1140 - 1145	1115 - 1125	1125-1130	1125-1130	1125-1130	1115 - 1145	1120-1125	
Y_Coordinates (km)	328-356	336-352	324-328	328-348	356-336	336-344	320-324	328-340	
Z_Coordinates (km)	4.8	4.8	5.1	4.8	5.1	4.8	4.8	4.8	

Table 6 presents the geometrical coordinates of the 17 blocks that were used to construct the model body. The x-coordinate representing the lateral extension of every block. The y-

coordinate representing the longitudinal extension of the blocks and the z-coordinate representing their respective depths.

After constructing the body, we used the GRAV3D program to calculate the gravity signature of the body, this signature is presented in the form of a map. This map is then compared with the map obtained from the observed gravity data. The best model is the one for which the two maps can approximately be superposed.

Figure 50 presents the map for the observed gravity data, obtained by plotting 254 data points from the study area using the GM-DATA-VIEWER utility of the GRAV3D software. The experimental residual anomaly map from 244 data points computed by the software is presented in Figure 51 It is observed that the two maps can approximately be superposed.

The intrusive body was depicted to be located between the depths of 0.5 km and 2 km from the surface on its Eastern side and between 0.5 km and 5 km on its Western side. The result provided by the spectral analysis, giving the depth to the top of the Kribi intrusive body was also considered.

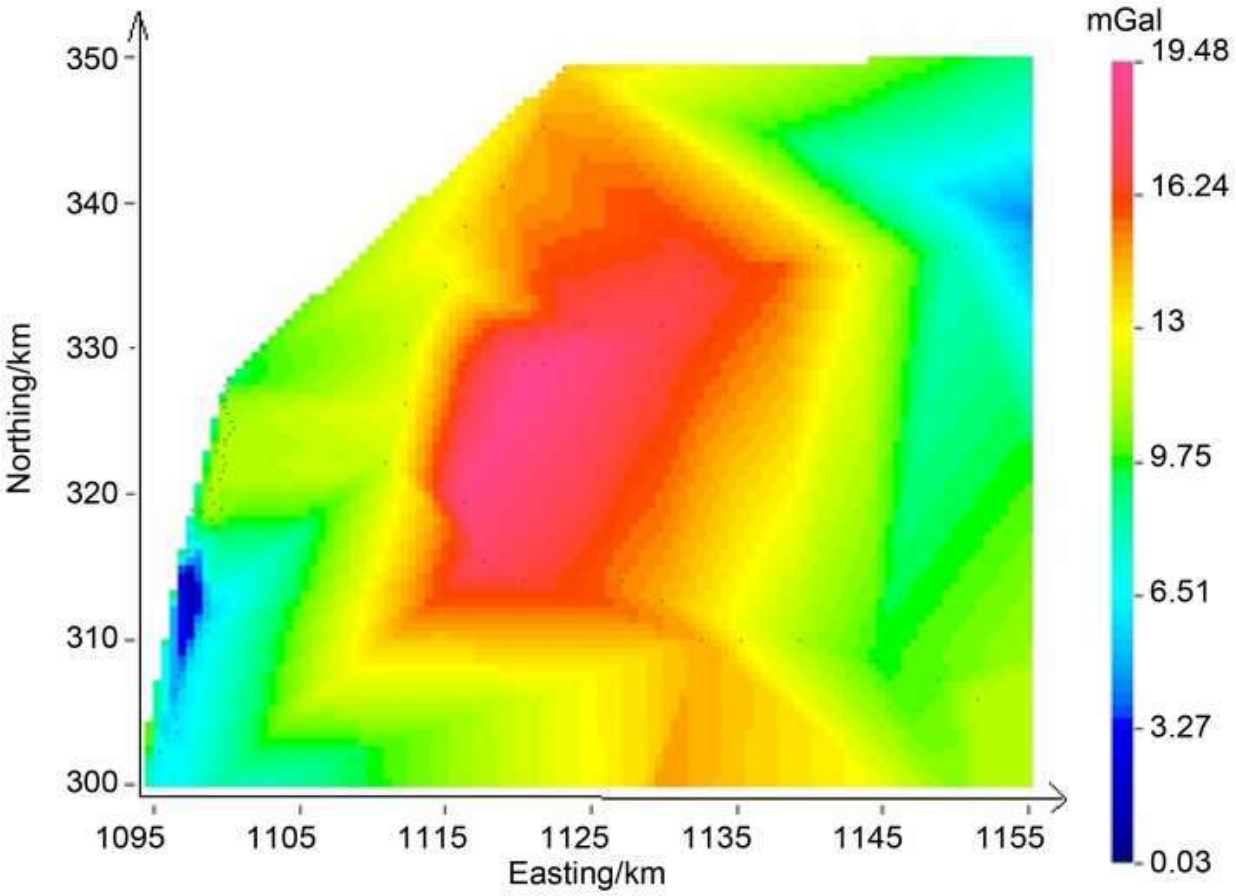

Figure 50: Observed residual anomaly map from 254 data points.

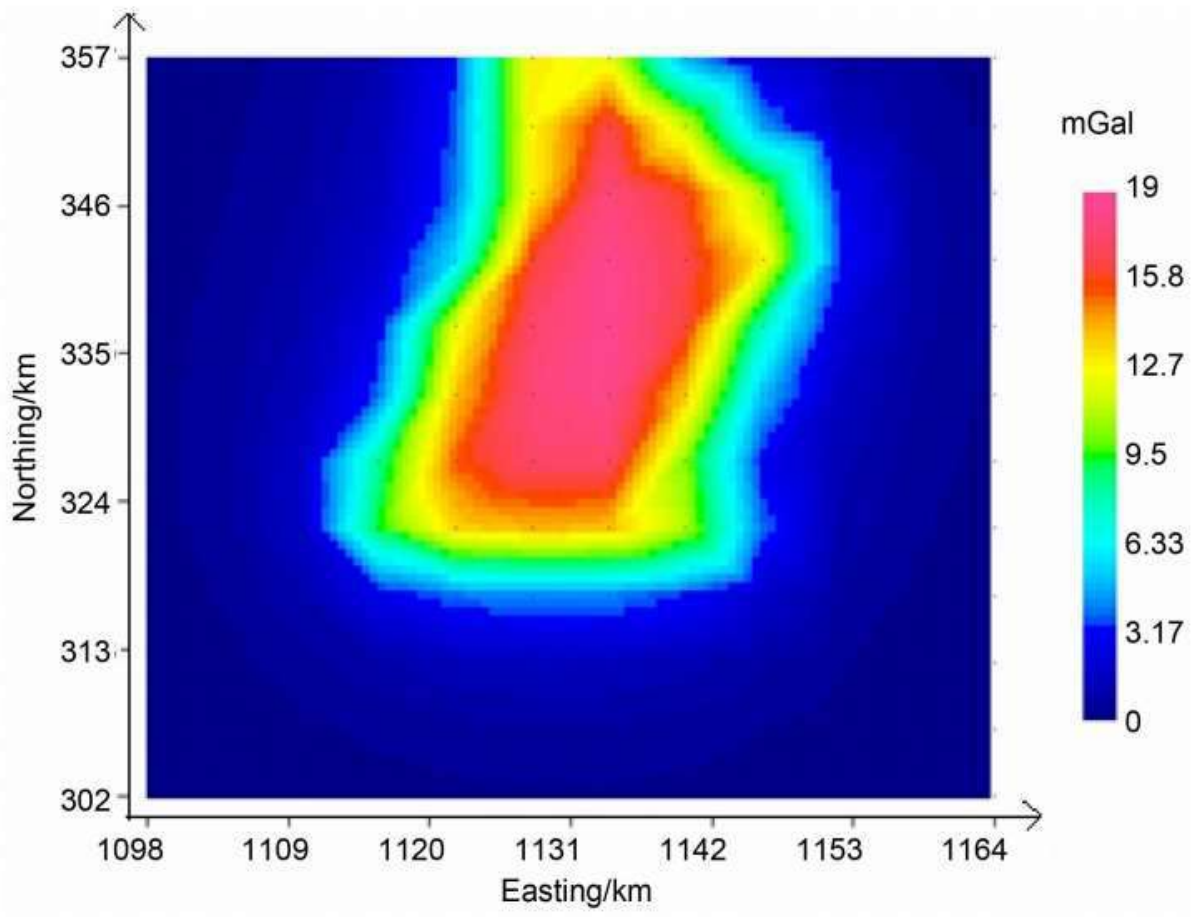

Figure 51: Experimental residual anomaly map from 244 data points.

The various views of the 3D model of the Kribi intrusive body are presented in figures 52 - 57. These models consist of a major block having a density of 2.74 g/cm^3, a depth from the ground surface varying between 0.5 km and 1.5 km. The latitudinal and longitudinal extensions of the body are about 12 km and 30 km respectively. figure 54, figure 56 and figure 57 show that the general base of the body is situated at the depth of 4.8 km from its surface and its middle part extends to about 5.2 km. The upper surface of this modelled body has a trapezoid shape while its other facades are more or less defined.

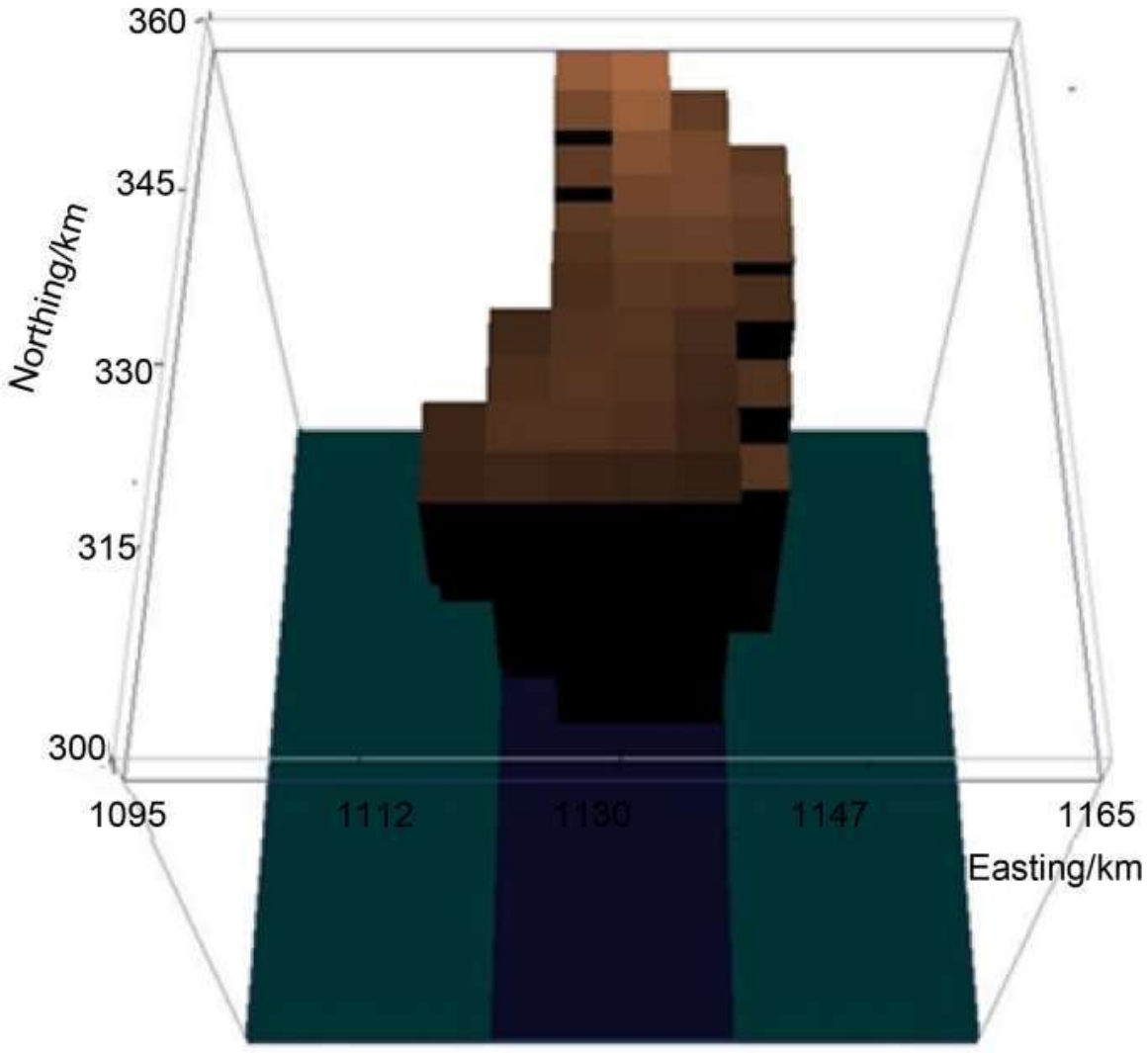

Figure 52: 3D Model of the Kribi dense intrusive body as viewed from above.

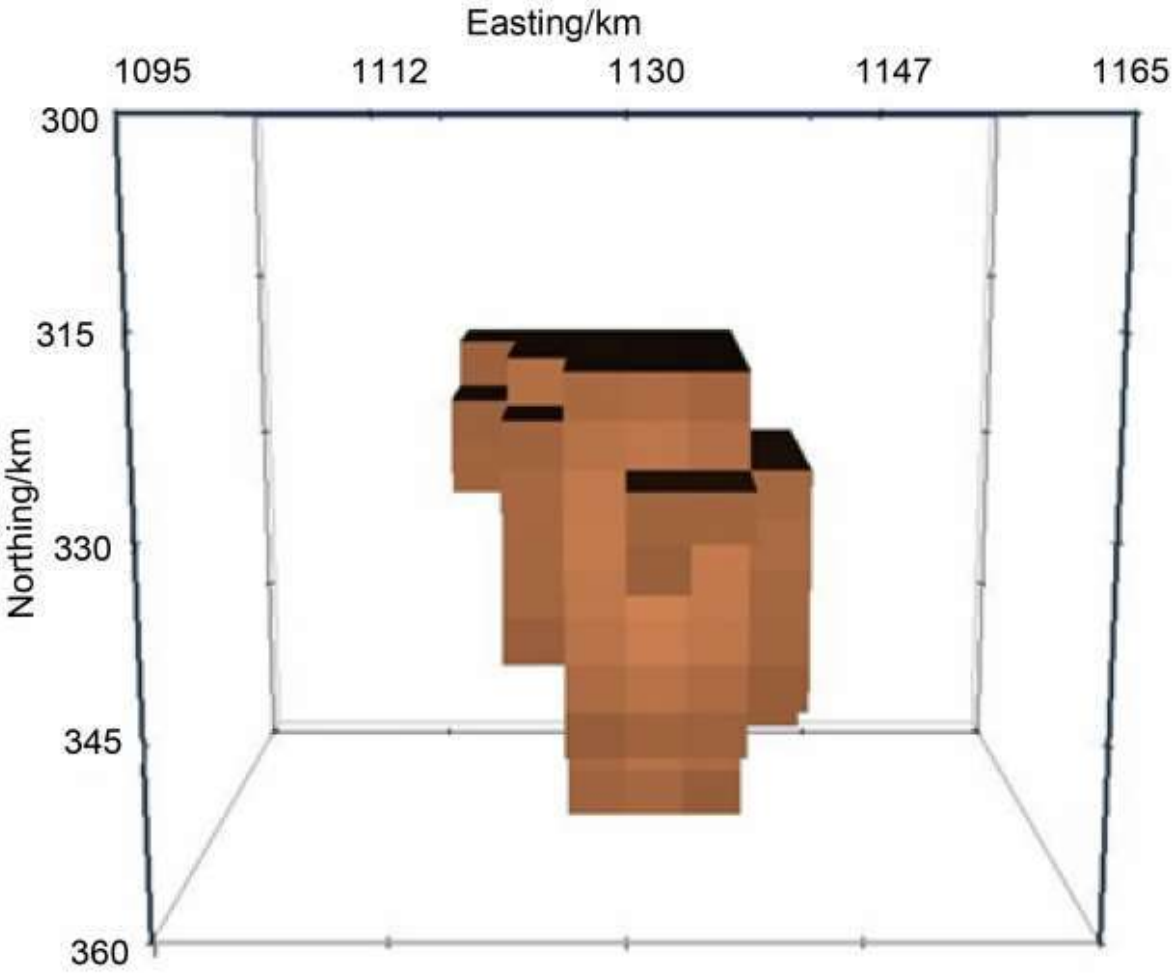

Figure 53: 3D Model of the Kribi dense intrusive body as viewed from below.

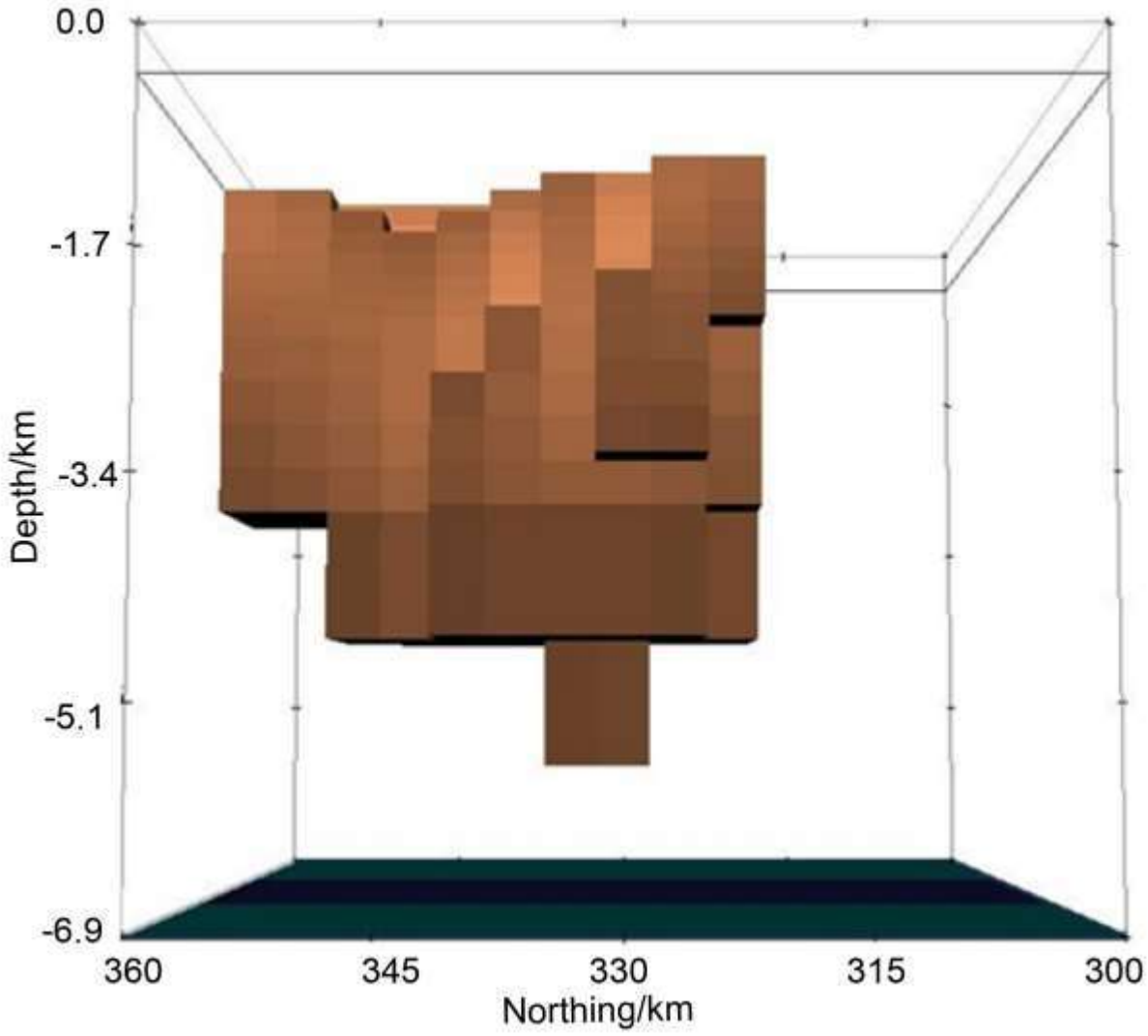

Figure 54: 3D Model of the Kribi dense intrusive body as viewed from the West.

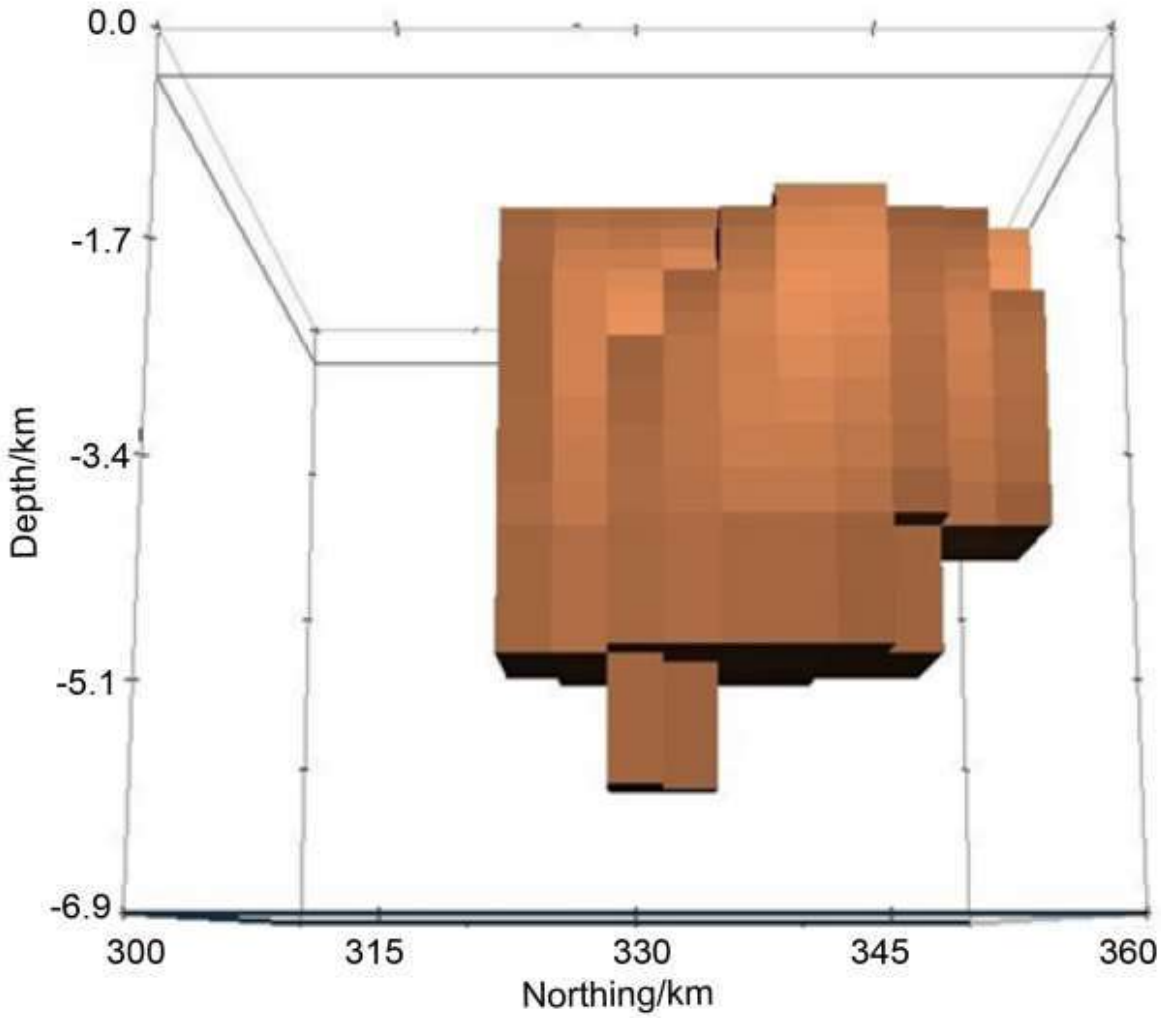

Figure 55: 3D Model of the Kribi dense intrusive body as viewed from the East.

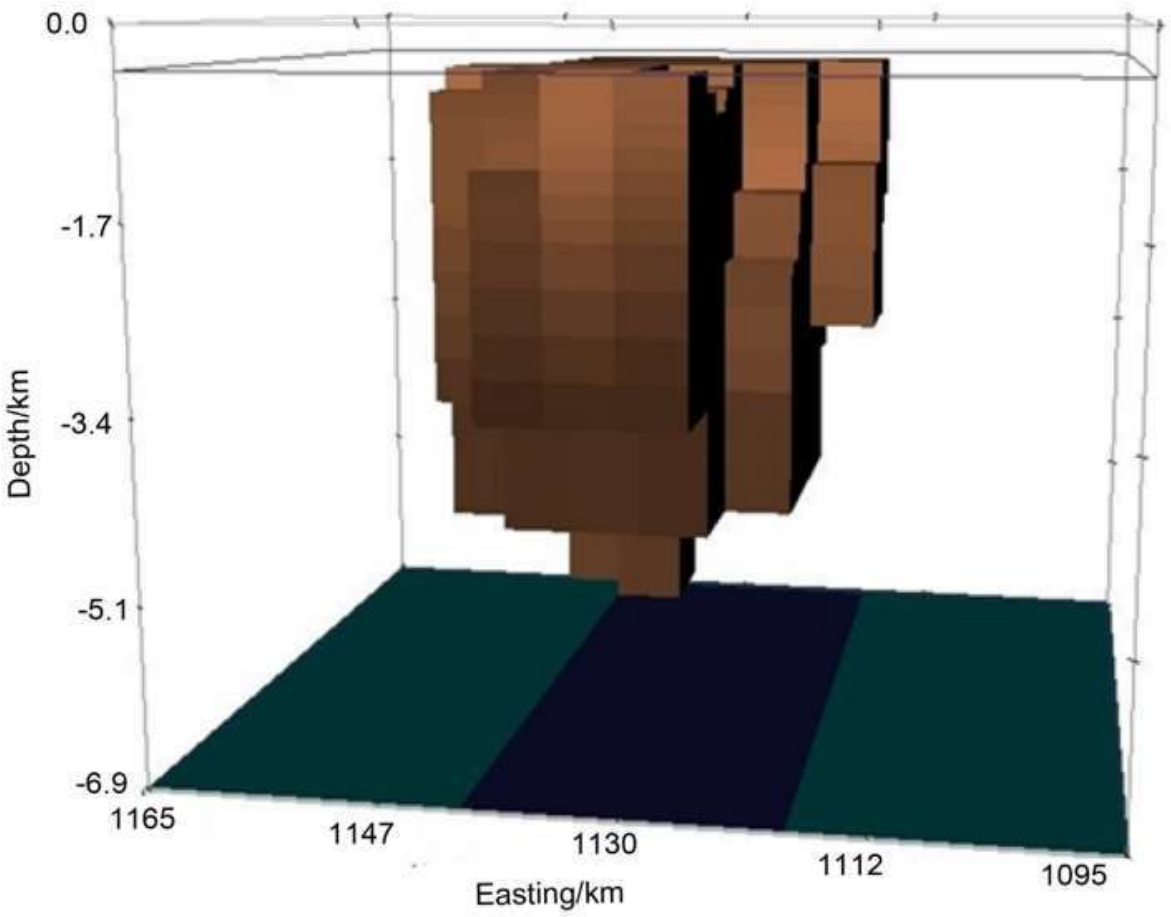

Figure 56: 3D Model of the Kribi dense intrusive body as viewed from the North.

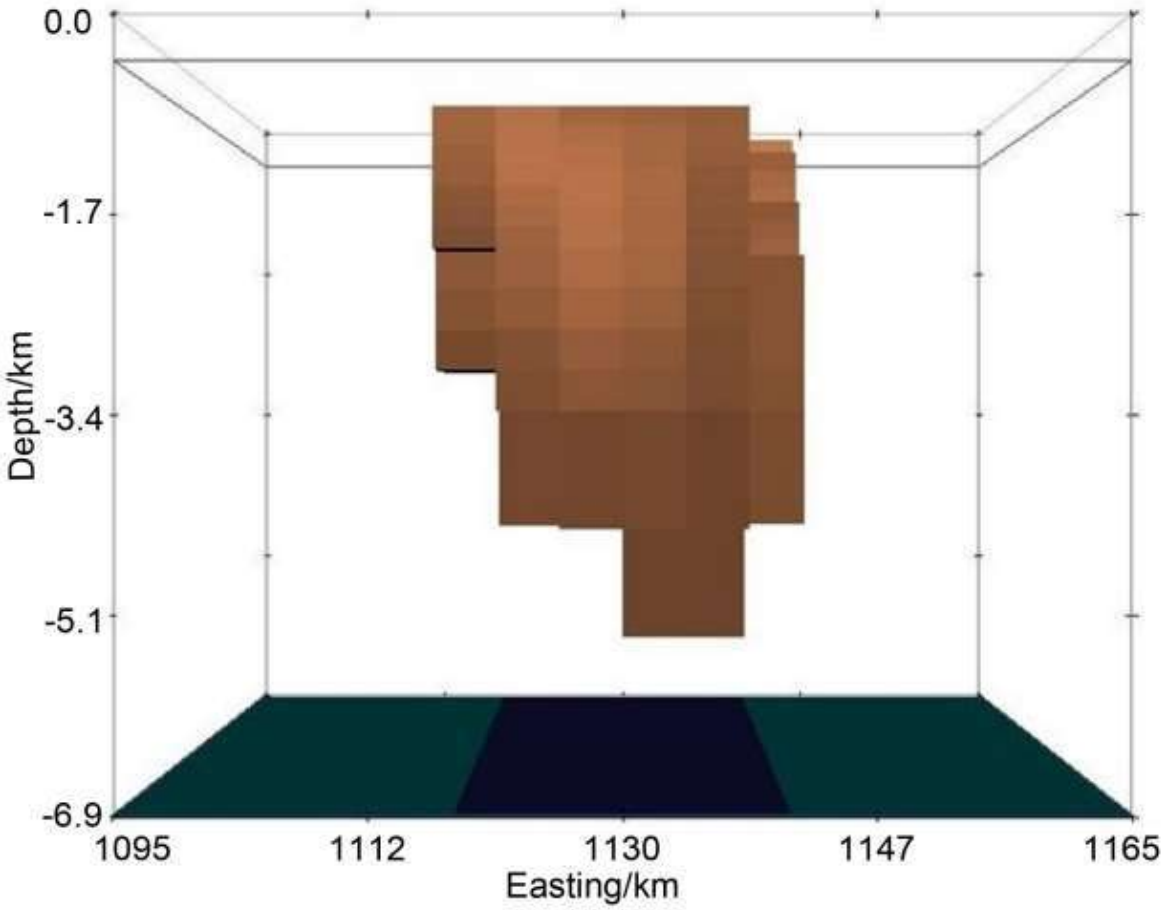

Figure 57: 3D Model of the Kribi dense intrusive body as viewed from the South.

4.1.6. Discussion

The forward modelling of gravity data can have many models developed from an anomaly. In order to obtain a model that best reflects the subsurface structure, one has to consider certain parameters that would limit this uncertainty. As part of the constraints, the multi-scale analysis of the maxima of the horizontal gradient of the third order residual anomaly has been used to locate and determine the depth range of the anomalous body. The spectral analysis has also been used to determine the average depths to the tops and bottoms of the anomalous body. It is observed that the depth varies between 0.5 km and 5 km from the surface of the earth. These constraints give an assurance of the validity of the model. The parameters of the model (depth to the top of 0.5 km and 1.5 for some sections of the body, and depth to the bottom of 4.8 km and 5.2 km for a slide section of the center of the body) are in accordance with the results obtained by Owona et al. (2016) giving the depth range of the anomaly sources of Kribi between 0 and 6 km. They also agree with the results

of the multi-scale analysis of the maxima of gradient which situates the depth of the intrusive body between 0.5 km and 5 km. However, there is a slide shift of the depth of the center of the body that extends to 5.2 km approximately. This value also agrees with the results provided by the spectral analysis method which give the average depth of the intrusive body between 0.5 km and 3.6 km. The depth of 1.6 km obtained for some sections of the body by spectral analysis has been confirmed by the approximately 1.5 km obtained for particular sections of the roof of the body. The density of the body was evaluated to be about 2.74 g/cm^3. A superposition of the residual anomaly map with the geological map and previous studies (Maurizot et al. 1986) indicate that the intrusive rocks in the studied area are mainly gneiss, alkaline syenite, nepheline syenite, granodiorite, dolerite, tonalite and peridotites. Telford et al. (1976) give the average density values for these rocks as presented in table 7

Table 7: Density values of intrusive rocks in the Kribi area.

Rock name	gneiss	Alkaline syenite	Nepheline syenite	granodiorite	dolerite	tonalite	peridotites
Density range/ g/cm^3	2.60 - 2.90	2.60 - 2.95	2.53 - 2.70	2.67 - 2.79	2.70 - 3.50	2.62 - 2.96	2.78 - 3.37
Mean density value/ g/cm^3	2.75	2.78	2.61	2.73	3.10	2.79	3.08

Given all these, the intrusive igneous body obtained by gravity modelling may be composed of gneiss, and granodiorite because their mean density is close to that of the modelled body. Assuming the value of the density of the surrounding metamorphic rocks to the North-East of 2.67 g/cm^3 and the value of the density of the surrounding sedimentary formations to the south-west mainly limestones and sandstones with mean densities of 2.55 g/cm^3 and 2.35 g/cm^3 respectively, the 3D model possibly consist of an intrusive igneous body (gneiss, granodiorite) with a density estimated at about 2.74 g/cm^3 surrounded by other metamorphic formations to the north-east and sedimentary formations to the south-west. The density

contrast between this body and the sorrounding formations varies from 0.07 g/cm^3 to 0.39 g/cm^3.

According to Vicat et al. (1996), the intrusive rocks emplaced in the Nyong Unit were linked to an overstretching phase just before the Panafrican Orogeny. It is therefore possible that this overstretching phase coupled with the high tectonic activity and the regional field stress present in the area (Owona et al. 2013) caused the dislocation of this dense intrusive block from the broader intrusion suspected in the area (Koumetio et al. 2012). The further characterization and modelling of this broader structure will ensure a better understanding of the structural layout of the Cameroon coastal basins made up of the Douala and Kribi-Campo sub-basins.

4.1.7. Conclusion

The analysis of the third order residual anomaly map and the superposition of horizontal gradient maxima from the residual anomaly and its upward continuation at several heights shows quasi-circular disposition of many maxima indicating the presence of a dense intrusive body in the Kribi area. The multi-scale analysis of the maxima of the horizontal gradient of the third order residual anomaly led to the location of this body at a depth to bottom ranging 0.5 km and 5.0 km. The power spectrum method used gave the depth to the top from the surface at 0.5 km and 1.6 km and to a mean depth to the bottom of 3.6 km. The 3D model obtained using the GRAV3D software and taking into account the results provided by the two previous methods, shows a block with part of its top located at 0.5 km and other sections located at about 1.5 km. Its bottom lies at a depth ranging from 4.8 km to 5.2 km. The identified body of density 2.74 g/cm^3 which is surrounded by other lower density metamorphic formations to the north-east and sedimentary formations to the southwest suggests that it is an igneous intrusion. The observation of the shape of this body coupled with the results obtained by (Koumetio et al. 2012) leads to the observation that this body is part of a broader intrusion extending northwards. A further 3D modelling and characterization of this broader structure can lead to a more profound understanding of the tectonic origin and structural layout of the Cameroon coastal basins namely the Douala sub-basin and the Kribi-Campo sub-basin. The interpretation of the 3D model of the Kribi-Campo intrusive body and the discontinuities surrounding it could serve as a guide in the investigation and exploitation of oil, gas and mineral sources in the study area, facilitating the location of points favorable to their existence. This result could also serve as a guide in the identification of risk areas. Apart from this, further studies could be carried out to identify the types of minerals that can be found in this massive and dense igneous intrusion.

GENERAL CONCLUSION AND FURTHER STUDIES

GENERAL CONCLUSION

The geophysical study of the Kribi-Campo sub-sedimentary basin using gravity data has contributed immensely to the understanding of the geodynamics of the region and the structural layout of the basin.

The set objectives at the beginning of this thesis were to enlarge the gravity data base of South Cameroon and especially the Kribi-Campo sub-basin where ground gravity data were not available until the start of this research, to use this data and develop multidimensional modelling of the basins' subsurface that can give the best understanding of the masses distribution, the rocks nature and structure and eventually the mining potential of the given basin which altogether constitute the structural layout of the basin. In order to attain these objectives, we first carried out a gravity data survey in the study region. This survey led to the collection of over 223 data points which were combined to the old existing ones. The obtained data were corrected from multiple sources of gravity noise, namely the free-air correction, the latitude correction, the lunisolar correction, the plateau and the terrain correction. In as much as the corrections applied on raw gravity data help to eliminate the non-geological sources of anomalies affecting the measured data, they equally reveal information related to the repartition of masses in the subsurface, areas with the highest gravity noise and how this noise is related to the geographical, geological and geophysical configuration of a study area. The corrected data were processed, analyzed and transformation operators were applied to them.

The spectral analysis enabled to estimate the depth to basement on various parts of the Kribi-Campo basin which gives the sedimentary thickness. This thickness varies from 0.60 km to 3.93 km with the highest values obtained in some specific localities of the study area namely Campo and the area between Kribi and Lolabe. We applied the horizontal gradient analysis to the residual component. The residual structural setting of the zone from the Euler method is characterized by major faults and contacts mainly oriented SW-NE with the shallowest in the west.

The analysis of the third order residual anomaly map and the superposition of horizontal gradient maxima from the residual anomaly and its upward continuation at several

heights shows quasi-circular disposition of many maxima indicating the presence of a dense intrusive body in the Kribi area. The identified body of density 2.74 g/cm^3 which is surrounded by other lower density metamorphic formations to the north-east and sedimentary formations to the southwest suggests that it is an igneous intrusion to which 3D modelling was applied. The Kribi 3D body with part of its top located at 0.5 km and other sections located at about 1.5 km. has a bottom which lies at a depth ranging from 4.8 km to 5.2 km.

The results of the application of the spectral analysis, ideal body solution applications suggest the presence of two blocks of dense bodies to which 2.5D modelling was applied. The emplacement, breaking up and separation of this intrusive igneous body was the outcome of two tectonic events corresponding to an upward vertical translational tectonic movement followed by an anticlockwise rotational faulting tectonic movement. From a density contrast of 0.13 g.cm^{-3}, the isolated blocks have an estimated density of 2.80 g.cm^{-3} which is comparatively higher than the average density of 2.67 g.cm^{-3} for the autochthonous rocks and are composed principally of gabbro.

The disposition and shape of the open zone (Z) highlighted by the resulting separation of the intrusive blocks is suggestive of a very good trap for the accumulation of hydrocarbons and mineral resources.

The interpretation of the 3D model of the Kribi-Campo intrusive body and the discontinuities surrounding it could serve as a guide in the investigation and exploitation of oil, gas and mineral sources in the study area, facilitating the location of points favorable to their existence. This result could also serve as a guide in the identification of risk areas.

The structural map of the basin provides the most relevant structural information in the area. This map can help in identifying the direction of fluid flow in the subsurface. The interpretation of the sedimentary thickness values can serve to identify areas with the highest mineral and hydrocarbon production potentials which correspond to areas with the highest sedimentary thickness.

FURTHER STUDIES

In this study, we presented the subsurface structure of the Kribi-Campo sub-sedimentary basin in multidimensional gravity models. The models presented helped to understand the origin, the nature and the structure of the formations constituting the basins'.

They equally ease the understanding of the basins' layout, its tectonics and geodynamics. However, it is possible that some extended structures still remain hidden.

The gravity method alone is not enough to carry out a study with the aim of thoroughly deciphering the subsurface with the geological significance of delineated faults and intrusions, it has to be coupled with other methods to have the maximum information on the study and the knowledge of a well-defined geological structure. This study could be completed with future investigations using the magnetic method with the aim of highlighting limits between high-contrast susceptibility structures. We intend in further research to:

- To carry out joint inversion of gravity and seismic data in shallow areas. The seismic method is known for its accuracy in imaging shallow structures. Combining this method with the gravity method could be used to delineate minor faults,
- Perform joint inversion of gravity and magnetic data in deep faulted area,
- Perform joint inversion of gravity and magneto telluric data will permit to attain deeper formations. The magneto telluric current is known to penetrate right to the mantle. Combining it with the gravity method can provide further information on the nature of the geotectonic activities observed in the sub-basin and responsible for the breaking up of the observed intrusions,
- Carry out magnetic studies in order to determine the magnetic susceptibility of rocks and deduce their nature,
- Perform a geochemical study of the Kribi intrusive body to determine its content.

BIBLIOGRAPHY

1. Abdelrahman, E. M., Riad, S., Refai, E. and Amin, Y., 1985. On the least-squares residual anomaly determination, Geophysics, 50, pp. 473-480.
2. Agnew, D. C., 2007. Earth tides Treatise on Geophysics 3(06), pp. 163-195.
3. Ateba, B., Ntepe, N., Ekodeck, G. E., Soba, D. and Fairhead, J. D., 1992. The recent earthquakes of Cameroon and their possible relationship with main geological features of Central Africa, J. Afr. Earth Sci., 4, pp. 365-369.
4. Balmino, G., 1986. La forme de la Terre, Pulsar, Revue de la S.A.P., N° 656, N° 657, pp. 5-15.
5. Bernard, G. and Chouteau M., 2008. Lecture notes on applied geophysics, University of Montreal, 220 p.
6. Bessoles B. et Trompette, R. 1980. Géologie de l'Afrique : La Chaîne Panafricaine, Zone mobile d'Afrique Centrale (partie Sud) et zone Soudanaise". Mémoire BRGM N° 92.
7. Bessoles, B. et Lasserre, M., 1977. « Le complexe de base au Cameroun ». Bull. Soc. Géol. Fr., Vol. 19, No. 7, pp. 1085-1092.
8. Bessoles, B. et Trompette, R., 1980. La chaîne panafricaine « zone mobile d'Afrique centrale (partie Sud) et zone mobile soudanaise ». Mémoire du BRGM, 92, 396 p.
9. Bhattacharyya, B. K., 1966. Continuous spectrum of the total-magnetic-field anomaly due to a rectangular prismatic body, Geophysics, 31, pp. 97-121.
10. Caby, R. and Boesse, J. M., 2001. Pan-African nappe system in southwest Nigeria: the Ife-Ilesha schist belt. Journal of African Earth Sciences 23, pp. 211–225.
11. Champetier De Ribes, G., 1957. Rapport de fin de campagne. Indice de fer. Région de Kribi. "Les Mamelles", Dir. Mines et Géol., Cameroun.
12. Chapin, D. A., 1996. "The theory of the Bouguer gravity anomaly: A tutorial." The Leading Edge, 15(5), pp. 361-363.
13. Clifford, T. N. and Gass, I. G., 1970. African Magmatism and Tectonics. Olivier and Boyd, Edinburgh, 461p.
14. Collignon, F., 1968. Gravimétrie et reconnaissance de la République Fédérale du Cameroun. [Gravimetry and Recognition of the Federal Republic of Cameroon.] ORSTOM, Paris, 35 p.

15. Cornacchia, M. et Dars R., 1983. “Un trait Structural Majeur du Continent Africain. Les Linéaments Centrafricains du Cameroun au Golfe d’Aden, ”Bulletin de la Société Géologique de France, Vol. 25, pp. 101-109.
16. Darius Popovas., 2011. Estimation of lunisolar correction in precise levelling: The 8th International Conference May 19–20, 2011, Vilnius, Lithuania.
17. Dimitriadis, K., Tselentis, G. A. and Thanassoulas, K., 1987. A basic program for 2-D spectral analysis of gravity data and source depth estimation, Computers and Geosciences, 13, pp. 549-560.
18. Dumont, J. F., 1986. Identification par télédétection de l’accident de la Sanaga (Cameroun). Sa position dans le contexte des grands accidents d’Afrique Centrale et de la limite nord du craton congolais. Géodynamique 2(1), pp. 55-68.
19. Florio, G., Fedi, M. and Pasteka, R., 2006. On the application of Euler deconvolution to the analytic signal, Geophysics, 71, pp. 87-93.
20. Gunn, P. J., 1975. Linear transformation of gravity and magnetic fields, Geophysical Prospecting, 23, pp. 300-312.
21. Huestis, S. P. and Ander, M. E., 1983. IDB2—A Fortran program for computing extremal bounds in gravity data interpretation Geophysics, 48, pp. 999–1010.
22. Jensen, H., 1949. Formulas for the astronomical correction to the precise levelling. Danish Geodetic Institute. Publication 23 : pp. 22-27.
23. Koumetio, F., 2017. Investigation géophysique par méthodes gravimétriques dans la région du Sud-ouest Cameroun : implications structurales et tectoniques. Thèse Doctorat/PhD Univ. Yaoundé I, 132 p.
24. Koumetio, F., Njomo, D., Tabod, C. T., Noutchogwe, T. C. and Manguelle-Dicoum, E., 2012. Structural Interpretation of Gravity Anomalies from the Kribi-Edea Zone, South Cameroon: A Case Study. Journal of Environmental & Engineering, 9, pp. 664-673.
25. Koumetio, F., Njomo, D., Tatchum, C. N., Tokam, K. A. P., Tabod, C. T. and Manguelle-Dicoum, E., 2014. Interpretation of Gravity Anomalies by Multi-Scale Evaluation of Maxima of Gradients and 3D Modelling in Bipindi Region (South-West Cameroon). International Journal of Geosciences, 5, pp. 1415-1425.
26. Kröner, A., 1979. Pan-African plate tectonics and its repercussion on the crust of northeast Africa, Geologishe Rundshau, 68, pp. 565-583.
27. Lasserre, M. et Soba, D., 1976. Age Libérien des granodiorites et des gneiss à pyroxènes du Cameroun Méridional. Bulletin BRGM 2 (4), pp. 17-32.

28. Lerouge, C., Cocherie, A., Toteu, S. F., Penaye, J., Milesi, J. P., Tchameni, R., Nsifa, N. E., Fanning, C. M. and Deloule, E., 2006. SHRIMP U/Pb zircon age evidence for paleoproterozoic sedimentation and 2.05 Ga syntectonic plutonism in the Nyong Group, South-western Cameroon: consequences for the eburnean-transamazonian belt of NE Brasil and central Africa. Journal of African Earth Sciences, 44, pp. 413-427.
29. Manguellé-Dicoum, E., 1988. Étude Géophysique des structures superficielles et profondes de la région de Mbalmayo. [Geophysical Study of the Superficial and Deep Structures of the Mbalmayo Region.] PhD Thesis, Université de Yaoundé, Yaoundé, 202 p.
30. Manguellé-Dicoum, E., A. S. Bokossah and T. E. Kwende-Mbanwi, 1992. Geophysical evidence for a major Precambrian shist-granite boundary in southern Cameroon. Tectonophysics, 205, pp. 437-446.
31. Mathews, P. M., Dehant, V. and Gipson, J. M., 1997. Tidal station dispalcements, Journal of Geophysical Research 102(20): pp. 469–477.
32. Maurizot, P., Abossolo, A., Feybesse, A., Johan, J. L. et Lecomte, P., 1986. Etude et prospection minière du Sud-Ouest Cameroun. Synthèse des travaux de 1978 à 1985, Rapport B.R.G.M 85, CMR 066, 274 p.
33. Mbom Abane, S., 1997. Investigations géophysiques en bordure du Craton du Congo et implications structurales, Thèse de doctorat d'Etat, Univ. Yaoundé I, 180 p.
34. Mouzong, M. P., Kamguia, J., Nguiya, S., Shandini, Y. and Manguelle-Dicoum, E., 2014. Geometrical and Structural Characterization of Garoua Sedimentary Basin, Benue Trough, North Cameroon, Using Gravity Data. Journal of Biology and Earth Sciences, 4, pp. 25-33.
35. Nédélec, A., 1990. Late calcalkaline plutonism in the Archaean Ntem unit: the Sangmelima granodioritic suite (South Cameroon). 15th Colloquium on African Geology, Publications Occasionnelle, CIFEG 22, pp. 25-28.
36. Nédélec, A., Macaudière, J., Nzenti, J. P. et Barbey, P., 1986. Evolution structurale et métamorphisme des schistes de Mbalmayo (Cameroun). Informations pour la structure de la zone mobile panafricaine d'Afrique Centrale au contact du craton du Congo, C.R. académie des Sciences de Paris, t. 303, série. II, pp. 75-80.
37. Ngako, V., 1999. Les déformations continentales panafricaines en Afrique Centrale. Résultat d'un poinçonnement de type himalayéen. Thèse Doct. D'État, Univ. Yaoundé I, 241 p.

38. Ngako, V., Affaton, P. and Njonfang, E., 2008. Pan-African tectonics in northwestern Cameroon: Implication for the history of western Gondwana. Gondwana Research 14, pp. 509-522.
39. Ngako, V., Affaton, P., Nnange, J. M. and Njanko, T., 2003. Pan-African tectonic evolution in central and southern Cameroon: transpression and transtension during sinistral shear movements, J. Afr. Earth Sci., 36, pp. 207-214.
40. Ngako, V., Jegouzo, P. et Nzenti, J. P., 1991. Le Cisaillement Centre Camerounais. Rôle structural et géodynamique dans l'orogenèse panafricaine. C. R. Acad. Sci. Paris, t. 313, sér. II, pp. 457-463.
41. Njingti-Nfor, Owona Angue, M. L. C., Kue Petou R. M., Bisso, D. and Piameu, K. J., 2017. Magnetotelluric Investigation of the Geo-Tectonic Stability of Campo-Ma'an Area in South Cameroon. International Journal of Geosciences, 8, pp. 1427-1441.
42. Nsifa, E. N., 2005. Magmatisme et évolution géodynamique de l'Archéen au Protérozoïque de la bordure nord-ouest du craton du Congo (complexe du Ntem) au Sud-Ouest Cameroun. Thèse Doctorat d'Etat, Université de Yaoundé I, Yaoundé, 248 p.
43. Ntamack-Nida, M. J., Bourquin, S., Makong, J. C., Baudin, F., Mpesse, J. E., Itjoko Ngouem, C., Komguem, P. B. and Abolo, G. M., 2010. Sedimentology and sequence stratigraphy from outcrops of the Kribi-Campo sub-basin: Lower Mundeck Formation (Lower Cretaceous, southern Cameroon), J. Afr. Earth Sci.58, pp. 1-18.
44. Ntepe, N., Aka, F. T., Ubangoh, R. U., Ateba, B., Nnange, J. M. and Hell, J. V., 2004. The July 2002 earthquake in the Kribi region: geological context and a preliminary evaluation of seismic risk in southwestern Cameroon. J. Afr. Earth Sci., 40, pp. 163-172.
45. Nzenti, J. P., Barbey, P., Bertrand, J. M. L. et Macaudiere, J., 1994. La chaîne panafricaine au Cameroun: cherchons suture et modèle, In : S.G.F. éd., 15e réunion des Sciences de la Terre, Nancy, France, 99 p.
46. Nzenti, J. P., Barbey, P., Jegouzo, P. et Moreau, C., 1984. Un nouvel exemple de ceinture granulitique dans une chaîne protérozoïque de collision : les migmatites de Yaoundé au Cameroun. Comptes Rendus de l'Académie des Sciences de Paris, 299 : pp. 1197-1199.

47. Nzenti, J. P., Barbey, P., Macaudiere, J. and Soba, D., 1988. Origin and Evolution of the Precambrian high grade Yaounde gneiss (Cameroon). Precambrian Res., 38, pp. 91-109.
48. Owona Angue, M. L. C., 2012. Investigation géophysique de la zone de transition entre le sous-bassin sédimentaire de Kribi-Campo et la bordure nord-ouest du Craton du Congo, Thèse de Doctorat/PhD, Univ. de Yaoundé I, 120 p.
49. Owona Angue, M. L. C., Assembe, S. P., Njingti, N., Ngoh, J. D., Ndougsa Mbarga, T., Kue Petou, R. M. and Bisso, D., 2016. Determination of the Structural Lineaments in the Kribi-Campo-Ma'an Area from a Multi-Scale Analysis of Gravity Data Using the HGM and Euler 3D Deconvolution Approaches. International Journal of Geosciences, 7, pp.1122-1143.
50. Owona Angue, M. L. C., Nguiya, S., Nouayou, R., Tokam Kamga, A. P. and Manguelle-Dicoum, E., 2011. Geophysical Investigation of the Transition Zone between the Congo Craton and the Kribi-Campo Sedimentary Basin (South-West Cameroon). South African Journal of Geology, 114, pp. 145-158.
51. Owona Angue, M. L. C., Tabod, C. T., Nguiya, S., Kenfack, J. V. and Tokam Kamga, A. P., 2013. Delineation of Lineaments in South Cameroon (Central Africa) Using Gravity Data. Open Journal of Geology, 3, pp. 331-339.
52. Parker, R. L., 1974. Best bounds on density and depth from gravity data: Geophysics, v. 39, pp. 644-649.
53. Penaye, J., Toteu, S. F., Van Schmus, W. R. and Nzenti, J. P., 1993. Up-Pb and Sm-Nd preliminary geochronologic data on the Yaounde series, Cameroon: reinterpretation of the granulitic rocks as the suture of a collision in the Central African "belt". Comptes Rendus de l'Académie des Sciences, Paris, 317(II), pp. 789–794.
54. Petroškevičius, P. and Popovas, D., 2008. Dangaus kūnų poveikio sunkio laukui įvertinimas, Geodesy and Cartography [Geodezija ir kartografija] 34(1): pp. 19-22.
55. Poidevin, J. L., 1983. La tectonique Panafricaine à la bordure Nord du craton du Congo. L'orogenèse des oubanguides, 12th coll. Afr. Geol. Bruxelles, 75 p.
56. Popoff, M., 1988. Du Gondwana à l'Atlantique Sud: les connexions du ` fossé de la Bénoué avec les bassins du NE brésilien jusqu'à l'ouverture du golfe de Guinée au Crétacé inférieur. Journal of African. Earth Science. (7) pp. 409–31.
57. Pouclet, A., Tchameni, R., Mezger, K., Vidal, M., Nsifa, E. N., Shang, C. and Penaye J., 2007. Archaean crustal accretion at the Northern border of Congo Craton

(South Cameroon): The charnockite-TTG ling. Bulletin Société Géologique France, 178, pp. 331-342.

58. Poudjom- Djomani, Y. H., Nnange, J. M., Diament, M., Ebinger, C. J. and Fairhead, J. D., 1995. Effective elastic thickness and crustal thickness variation in West Central Africa inferred from gravity data. Journal of Geophysical Research, 22, pp. 47–70.

59. Radhakrishna, I. V. and Krishnamacharyulu, S. K. G., 1990. Polyfit: A Fortran 77 Program to Fit a Polynomial of Any Order to Potential Field Anomalies. Journal of the Association of Exploration Geophysicists, 11, pp. 99-105.

60. Regnoult, J. M., 1986. Synthèse géologique du Cameroun. Dir des Mines et de la Géol, Cameroun, 119 p.

61. Rocci, G., 1965. Essai d'interprétation des mesures géochronologiques. La structure de l'Ouest Africain. Science de la Terre France 10, pp. 461-479.

62. Spector, A. and Grant, F. S., 1970. Statistical Models for Interpretation Aeromagnetic Data. Geophysics, 35, pp. 293-302.

63. Tabod, C. T., 1991. Seismological studies of the Cameroon Volcanic line in West Africa, PhD Thesis, Univ. Leeds, England, 242p.

64. Tabod, C. T., Fairhead, J. D., Stuart, G. W., Ateba, B. and Ntepe, N., 1992. Seismicity of the Cameroon Volcanic Line, 1982–1990, Tectonophysics, 212, pp. 303–320.

65. Tadjou, J. M., Manguelle-Dicoum, E., Nguiya, S. et Kamguia, J., 2008. Caractéristiques des anomalies gravimétriques du sous-bassin sédimentaire de Kribi-Campo (Sud Cameroun), Africa Geoscience Review, Special Publication, 112, pp. 39 – 50.

66. Tadjou, J. M., Nouayou, R., Kamguia, J., Kande, H. L. and Manguelle-Dicoum, E., 2009. Gravity Analysis of the Boundary between the Congo Craton and the Pan-African Belt of Cameroon. Austrian Journal of Earth Sciences, 102, pp.71-79.

67. Tchameni, R., 1997. Géochimie et géchronologie des formations de l'Archéen et du Paléoprotérozoïque du Sud Cameroun (Groupe du Ntem, craton du Congo). Thèse de l'Université d'Orléans, France, 356 p.

68. Tchameni, R., Mezger, K., Nsifa, E. N. and Pouclet, A., 2001. Crustal origin of Early Proterozoic Syenites in the Congo Craton (Ntem Complex), South Cameroon. Lithos, 57, pp. 23-42.

69. Tchameni, R., Mezger, K., Nsifa, N.E. and Pouclet, A., 2000. Neoarchaean crustal evolution in the Congo Craton: evidence from K rich granitoids of the Ntem Complex, southern Cameroon. Journal of African Earth Sciences, 30, pp. 133–147.
70. Telford, W. M., Geldart, L. P. and Keys, D. A., 1976. Applied Geophysics. University Press, 4th edition, Cambridge 860 p.
71. Tokam Kamga, A. P., 2010. Crustal Structure beneath Cameroon deduced from the joint inversion of Rayleigh wave group velocities and receiver functions, Thèse de Doctorat/PhD, Univ. de Yaoundé I, 132 p.
72. Tokam, K. A. P., Tabod, C. T., Nyblade, A. A., Julia, J., Wiens, D. A. and Pasyanos, M., 2010 Structure of the Crust beneath Cameroon, West Africa, from the Join Inversion of Rayleigh Wave Group Velocities and Receiver Functions. Geophysical Journal International, 183, pp. 1061-1076.
73. Toteu, S. F., Penaye, J., Van Schmus, W. R., and Michard A., 1994. Preliminary U/Pb and Sm/Nd geochronologic data on the North-Central Cameroon: contribution of an Archaean and Paleoproterozoic crust to the edification of an active domain of the Pan-African orogeny. Comptes Rendus de l'Académie des Sciences Paris, 319, pp. 1519-1524.
74. Toteu, S. F., Michard, A. Bertrand, J. M. and Rocci, G., 1987. U/Pb of Precambrian rock from North-Cameroon, Orogenic evolution and chronology of the Pan-African belt of Central Africa, Precambrian Research, 37, pp. 71-87.
75. Toteu, S. F., Van Schmus, R. W., Penaye, J. and Nyobe, J. B., 1994. U-Pb and Sm-Nd Evidence for Eburnian and Pan-African High-Grade Metamorphism in Cratonic Rocks of Southern Cameroon. Precambrian Research, 67, pp. 321-347.
76. Toteu, S.F., Van Schmus, W. R., Penaye, J. and Michard, A., 2001. New U-Pb and Sm-Nd data from north-central Cameroon and its bearing on the pre-PanAfrican history of Central Africa. Precambrian Research, 108, pp. 45-73.
77. Varga, P., 1989. Love numbers and the inner structure of the Earth, in 6th Inter Symposium Geodesy and Physics of the Earth, Proc Part 1. Veröff ZIPE, 102: pp. 376-396.
78. Vicat, J. P., Leger, J. M., Nsifa, E., Piguet, P., Nzenti, J. P., Tchameni, R. et Pouclet, A., 1996. Distinction au sein du craton congolais du Sud-Ouest du Cameroun, de deux épisodes doléritiques initiant les cycles orogéniques éburnéen (Paléoprotérozoïque) et

PanAfricain (Néoprotérozoïque), Compte Rendu de l'Académie des Sciences, 323, pp. 575–82.

LIST OF PUBLICATIONS ISSUED FROM THIS THESIS

1. **Kue Petou R. M**., Owona Angue. M. L. C., Njingti-Nfor, N., Eloundou E. L. F., Mioumnde A. Negham, M. C., Manguelle-Dicoum, E. and Weiqi Song, 2020. Quantitative Interpretation of New Gravity Anomalies in the Lolabe-Campo Area (South Cameroon) Based on Spectral Analysis and 2.5D Modelling: Structural Implications, *Open Journal of Earthquake Research*, 9, pp. 240-254. https://doi.org/10.4236/ojer.2020.93014
2. **Kue Petou R. M**., Owona Angue. M. L. C., Njingti-Nfor, N., Eloundou E. L. F., Piameu K. J. , Lando T. J. A. , Moupou M. and Manguelle-Dicoum, E., 2019. Evaluation of the Impact of Gravity Corrections on raw gravity Data in South Cameroon: Prospection and tectonic assessments. *European Journal of Scientific Research.* Vol. 153 No 2 June, 2019, pp. 127-144
3. **Kue Petou, R. M**., Owona Angue, M. L, Njingti, N., and Manguelle-Dicoum, E., 2017a. 3D Modelling from New and Existing Gravity Data of an Intrusive Body in the Northern Part of Kribi-Campo Sub-Basin in Cameroon. *International Journal of Geosciences*, 8, pp. 984-1003. https://doi.org/10.4236/ijg.2017.88056
4. **Kue Petou R. M.,** Owona Angue. M. L. C., Njingti-Nfor, N., Ndougsa-Mbarga, T. and Manguelle-Dicoum, E., 2017b. Determination of Structural and Geometrical Parameters of the Kribi-Campo Sedimentary Sub Basin Using Gravity Data. *International Journal of Geosciences*, 8, pp. 1210-1224. https://doi.org/10.4236/ijg.2017.89069

APPENDICES

- Gravity data survey sheet

Date	**Site & description**	**Time GMT**	Long.(deg)	Lat.(deg)	**Altitude. (m)**	g (mGal)
17/03/2015	kribi, customs directorate. Next to the gutter and the electricity poles. 10m from a house without poles.	09:12	9,906666667	2,873472222	2	978033,753
	Lolabe Public School. At the borehole on the right side of the school	10:24	9,857527778	2,690638889	-3	978021,3177
	Lolabe Traditional Chiefery. Measurements taken at about fifty meters from the 3rd degree chieftaincy of Lolabe	10:35	9,862388889	2,698166667	6	978021,3741
	End port of kribi. Measure taken at the sation of an eugin at the end of the fence curling	10:38	9,863972222	2,707	7	978021,0818
	Lolabe's gendarmerie Office. Next to the gendarmerie post of Lolabo. At a secondary entrance to the port	10:58	9,864722222	2,715944444	8	978019,7838
	PK27+400, port entrance	11:07	9,867472222	2,723166667	-2	978021,3576
	PK26+400	11:15	9,873	2,730527778	8	978021,0268
	Apostolic Church	11:22	9,8785	2,735916667	21	978016,2841
	PK23+300	11:30	9,878638889	2,745138889	7	978019,2577
	PK22+200	11:39	9,880416667	2,686444444	23	978015,6103
		11:48	9,879722222	2,762	24	978014,0008

- Printed Publications Resulting from this Thesis

Scientific Research Publishing

Open Journal of Earthquake Research, 2020, 9, 240-254
https://www.scirp.org/journal/ojer
ISSN Online: 2169-9631
ISSN Print: 2169-9623

Quantitative Interpretation of Gravity Anomalies in the Kribi-Campo Sedimentary Basin (South Cameroon) Based on Spectral Analysis and 2.5D Modelling: Structural Implications

Kue Petou Rokis Malquaire[1,2,3*], Owona Angue Marie Louise Clotilde[4,5], Njingti Nfor[1,2], Eloundou Essama Lionel[2,3], Mioumnde Arthur Paterne[6], Kue Negham Martine Clémence[7], Manguelle-Dicoum Eliezer[5], Weiqi Song[1]

[1]Department of Geophysics, School of Geosciences, China University of Petroleum (East China), Qinqdao, China
[2]Postgraduate School of Sciences, Technologies & Geosciences, University of Yaoundé I, Yaoundé, Cameroon
[3]National Institute of Cartography, Yaoundé, Cameroon
[4]Department of Physics, Advanced Teacher Training College, University of Yaoundé I, Yaoundé, Cameroon
[5]Department of Physics, University of Yaoundé I, Yaoundé, Cameroon
[6]Laboratory of Ore Processing, Institute of Geological and Mining Research, Yaoundé, Cameroon
[7]Department of Geography, University of Dschang, Dschang, Cameroon
Email: *rokis.petou@yahoo.fr

How to cite this paper: Malquaire, K.P.R., Clotilde, O.A.M.L., Nfor, N., Lionel, E.E., Paterne, M.A., Clémence, K.N.M., Eliezer, M.-D. and Song, W.Q. (2020) Quantitative Interpretation of Gravity Anomalies in the Kribi-Campo Sedimentary Basin (South Cameroon) Based on Spectral Analysis and 2.5D Modelling: Structural Implications. *Open Journal of Earthquake Research*, **9**, 240-254.
https://doi.org/10.4236/ojer.2020.93014

Received: February 9, 2020
Accepted: April 6, 2020
Published: April 9, 2020

Abstract

Ground gravity survey was recently carried out in the Lolabe-Campo area, which constitutes the southern onshore portion of the Kribi-Campo sub-basin in South Cameroon. The obtained gravity data were processed and interpreted in order to elucidate the subsurface geology of the area in which preliminary studies highlighted the presence of an intrusive igneous body. In order to determine the nature and the characteristics of this body, spectral analysis, ideal body solution and 2.5D modelling methods were applied to the gravity data. The results suggest that the emplacement, breaking up and separation of the intrusive igneous body were the outcome of two tectonic events corresponding to an upward vertical translational tectonic movement followed by an anticlockwise rotational faulting tectonic movement. From a density contrast of 0.13 g·cm^{-3}, the two isolated bodies have an estimated density of 2.80 g·cm^{-3} which is comparatively higher than the average density of 2.67 g·cm^{-3} of the autochthonous rocks. These two blocks are completely surrounded by both sedimentary and metamorphic formations and are confined between the depths of 0.6 km and 3.5 km. The highly dense nature of

the rocks and their location around the Atlantic Ocean led to the conclusion that the two intrusive bodies are composed principally of gabbro. The disposition and shape of the open zone resulting from the separation of the blocks are suggestive of a trap for the accumulation of hydrocarbons and mineral resources.

Keywords

Spectral Analysis, Ideal Body, 2.5D Modelling, Formation Depth, Intrusive Blocks

1. Introduction

The area under study is situated in the southern part of Cameroon (Central Africa), and constitutes part of the onshore domain of the Kribi-Campo sub-basin located between latitudes 2˚20'N and 3˚20'N and longitudes 9˚15'E - 10˚00'E. It is situated at the junction between three main structures: 1) the sedimentary Kribi-Campo sub-basin; 2) the southern edge of the Kribi-Campo fault and 3) the metamorphic cratonic Ntem Complex. This area was affected by a series of tectonic activities due to the collision between the Pan-African belt and the Congo craton that formed the structural features of Southern Cameroon [1] [2]. The collision resulted in the over thrusting of the Pan-African units over the craton to depths of about 50 to 150 km [3] [4] [5] [6]. The Precambrian basement is deeply buried beneath the Pan-African formations across most of the study area. The regional structure and distribution of fault zones within the deeply buried Precambrian basement in southeastern Cameroon have been the subject of many investigations. [7] on delineating lineaments in the region, highlighted a series of deep and shallow faults traversing the area with a SW-NE dominating orientation. [8] [9] suggested the presence of high density intrusions in the subsurface of this study area from the analysis and interpretation of the maxima of horizontal gradient of the Bouguer anomalies. In presenting the interpreted structural map of the Kribi-Campo basin, [10] highlighted circular contacts indicating boundaries of intrusions in the Lolabe-Campo zone. In order to provide more detailed information on the nature and the characteristics of this intrusion, after a brief analysis and interpretation of the gravity anomaly map for the study area, this work consists of combining the indirect method (spectral analysis), the inverse method (ideal body solution) and the direct method (2.5D modelling) to analyze and interpret the new gravity data collected in this region. The main aim is to present the extensional and longitudinal dimensions of the Lolabe-Campo subsurface structure in general and to locate the gravity intrusion identified in the area.

2. Geological and Tectonic Settings

According to geochronologic studies, Cameroon is made up of two principal

structural zones [11]-[15]: 1) the stable Congo Craton in the Southern and Central areas and the 2) Mobile Zone of Central Africa (MZCA) known as the Pan-African belt of Central Africa to the northern area [16]. These structural zones were formed during the Pan-African tectonic events that are related to the Pan-African orogeny (550 ± 100 Ma).

The Congo Craton, which is known as the Ntem Complex in Cameroon [17] constitutes the greater portion of the study area. It consists predominantly of Archean rocks with some reworked and re-sedimented material formed in the Paleoproterozoic era [18] [19]. The Archean period is dominated here by Liberian orogeny (2700 - 2600 Ma), which began with the intrusion of magmatic rocks from which the greenstone belts were derived. Diapiric intrusion of Tonalite-Trondhemite-Granodiorite (TTG) followed the Greenstone belt formations between 2900 and 2800 Ma during the major tectonometamorphic phase [5] [18] [20]. Other intrusions were revealed in the region by [21] (mainly Alkaline Syenite, Nepheline Syenite, granodiorite, dolerite tonalite, peridotites etc.). The main Precambrian boundary between the Ntem Complex and the Pan-African belt consists of meta-sedimentary rocks lying along the northern edge of the Congo Craton [22] [23]. The northern portion of the region of study belongs to the geological unit called "Nyong Unit" composed mainly of gneisses, meta-granidiorites and green rock belts.

In general, the region (see **Figure 1**) has a complex and uneven tectonic structure. This tectonic seems to have given rise to a vertical movement of the basement with subsidence to the North and uplift to the South [24] [25]. This basement movement must have caused irregularities in the formations at depth, given rise to faults, horsts and grabens characteristic of the boundary between the Congo Craton and the Pan-African folds belt [6]. The main faults in the region consist of the Kribi-Campo Fault (KCF) system which is also defined as a continuation of the Sanaga Fault. This fault system is linked with the offshore fault system called the Kribi Fracture Zone. Contacts and faults trending E-W, N-S, NE-SW and NW-SE, which are either deep and/or buried structures and circular features correspond to contacts and intrusive bodies have also been highlighted and characterized in the [8] [9].

3. Gravity Data

3.1. Origin of the Data Used

The ground gravity data used in this study were collected during a geophysical field campaign organized by the geophysics team of the University of Yaoundé 1 in March 2015. Before then, no ground geophysical gravity survey had been carried out in the region. Using a Lacoste & Romberg G-823 gravimeter, 223 gravity data were measured for points. The data consists of irregularly spaced gravitational acceleration values and corresponding geographical coordinates (longitude, latitude and altitude) with a station-spacing varying from 0.5 km to 2.0 km. The coordinates were obtained from a Global Positioning System (GPSMAP 64

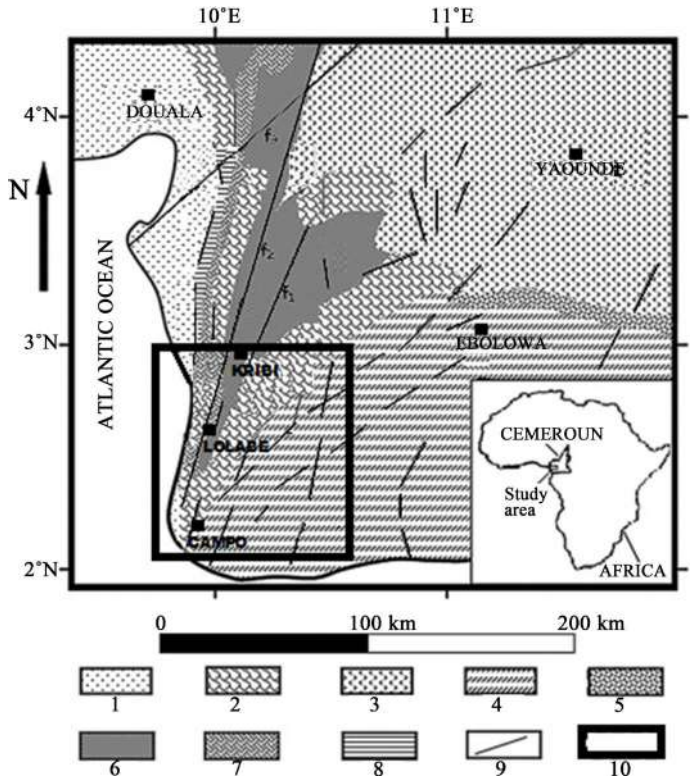

1: sediments; 2: gneiss; 3: Yaounde Group; 4: Ntem Complex; 5: tonalites; 6: green rock belts; 7: metamorphic rocks of the Yaounde Group, 8: metagranodiorite; 9: faults; 10: study area (2, 6, 7 and 8 are geological formations included in a geological unit called "Nyong Unit").

Figure 1. Location and simplified geological map of the region (modified after [3] [26] [27] [28]).

s) receiver of Garmin International Inc. For each station, the Global Positioning System receiver is first used to determine the angular coordinates and the altitude. Then the gravity-meter is used to measure the value of the variation of the gravitational attraction.

Our area of study is located in the dense equatorial forest making access very difficult. A great portion of the area is covered by the Campo-Ma'an national park and the Ntem river flood plains which are very swampy, woody and extremely inaccessible by foot. Data were only collected on open fields and roads.

3.2. Processing of the Data Used

The gravity data were reduced in order to obtain the value of the Bouguer anomaly in each station. Gravity measurements were made with a Lacoste and Romberg Gravimeter having its temperature calibration constant at 50˚C. Observations were made with respect to the base station located in Kribi town. Free air and Bouguer reductions based on mean density of 2.67 g·cm^{-3} were applied to the measured data. The free-air anomaly is calculated by subtracting the latitude correction (theoretical gravity) from the absolute gravity and adding a correction for the station elevation. The latitude correction requires the theoretical gravity at the station location on the earth's spheroid. The formula of free air

anomaly as defined by [29] is given by the formula

$$\Delta_{AL} = ga - \gamma + \left(0.308767763 - 0.000439834\left(\sin\phi\right)^2 - 0.000000072124602 \cdot h_s\right) \cdot h_s \quad (1)$$

where Δ_{AL} is the Free air anomaly in milliGals (mGal); ga absolute gravity; γ latitude correction in degrees; h_s station elevation in metres (m) and ϕ the latitude of the station in degrees. The formula accounts for the non-linearity of the free-air anomaly as function of both latitude and height above the geoids.

The Bouguer anomaly corrects the free air anomaly for the mass of rock that exists between the station elevation and the spheroid. For ground survey (including lake surface survey) the Bouguer anomaly formula is:

$$\Delta_B = \Delta_{AL} - 0.0419088\left[\rho h_s + h_w\left(\rho_w - \rho\right) + h_i\left(\rho_i - \rho_w\right)\right] - \delta_c \quad (2)$$

where, Δ_B is the simple Bouguer anomaly in milligals; Δ_{AL} free air anomaly; ρ Bouguer density of the earth in g·cm^{-3}, ρ_w Bouguer density of water in g·cm^{-3}; ρ_i Bouguer density of ice in g·cm^{-3}; h_s station elevation in metres; hw water depth in metres (including ice); ice thickness in metres; δ_c curvature correction. Terrain correction was also applied on the data and complete Bouguer anomaly derived using the formula:

$$\Delta_{CB} = \Delta_B + \delta_T \quad (3)$$

where Δ_{CB} is the complete Bouguer Anomaly; Δ_B simple Bouguer anomaly and δ_T terrain correction. This equation was used to determine the Bouguer anomaly at each survey station in the area. The resulting Bouguer anomaly data were used to obtain the Bouguer gravity anomaly map of the area (**Figure 3**). We present in **Figure 2** a distribution of the field data points.

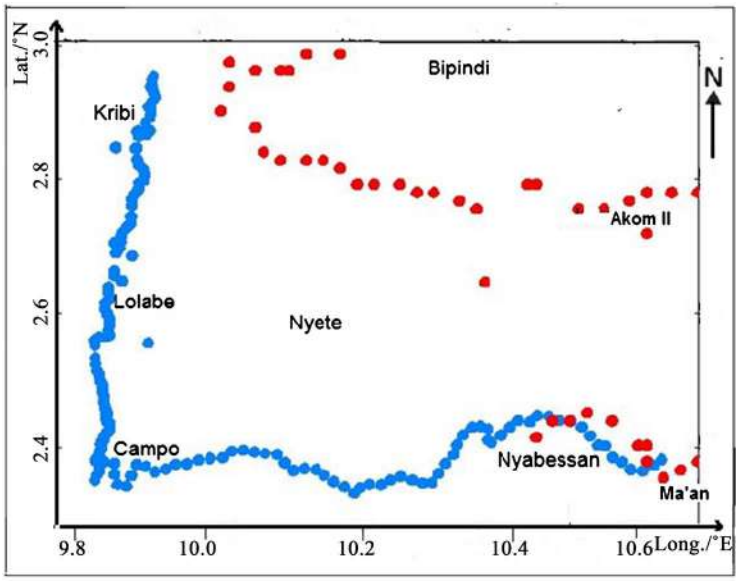

Figure 2. Gravity data points distribution map of the study area. The red dots represent the data collected from the ORSTOM geophysical survey (1965) while the blue dots represent the recently collected data of 2015.

4. Materials and Methods

4.1. Spectral Analysis Method

Spectral analysis as described by [30] is an interpretation technique based on the study of power spectrum properties. The gradient of the linear segments of the Fourier power spectrum is related to the depth of the density below the surface of the earth. From the study of logarithmic power spectrum as a function of the spatial frequency, the mean depth to bodies responsible for the observed gravity anomalies can be estimated. The power spectrum is the magnitude of the discrete Fourier transform of the gravity data. It has been used extensively by many authors namely (1975) [31] [32].

The finite discrete Fourier transform is given by the equation:

$$B(\omega) = \sum_{0}^{N-1} b(x) \exp(-i\omega x) \cdot \Delta x \tag{4}$$

where $b(x)$ represents the discrete N data array of gravity data obtained by sampling a continuous profile at evenly spaced intervals Δx. i is the complex operator, $\omega = 2\pi k$ is the spatial frequency and $k = \lambda^{-1}$ is the wavenumber in the x direction.

The expression of the Bouguer Slab Effect is given by the equation:

$$B(k)_{z=0} = 2\pi\Delta\rho G \cdot \exp(-2\pi kt) \cdot F(k)_{z=0} \tag{5}$$

where $B(k)_{z=0}$ is the Fourier transform of the Bouguer anomaly profile $b(x)_{z=0}$ $\Delta\rho$ is the density contrast between two layers; $F(k)$ is the Fourier transform of $f(x)$, the derivation of the interface from the mean depth z; G is the gravitational constant. The mean depth can then be calculated using the following equation:

$$h = \frac{\Delta \log E}{4\pi\Delta k} \tag{6}$$

where E is the power spectrum of $B(k)$.

The square of the Fourier amplitude spectrum is plotted versus the radial frequency. The slope of the relationship between the wave number of the gravity field and the logarithmic power spectrum provides information about the depths of the source bodies.

4.2. Ideal Body Determination

As pointed out by [33], ideal body theory is used to delineate bounds on the spatial extent of the anomaly source with an approximate model. It is important to have an idea of the suspected anomaly source in order to give a good approximation of it. The inverse method developed by Parker allows us, when the anomalies are well individualized, to choose amongst all possible solutions, those that best fit the data. The linear programming technique is used to carry out the calculations. This technique consists of considering a model where the density value ρ is known at certain given positions (X_0, Z_0). The domain under the profile is subdivided into quadrangular cells with dimensions d_x and d_z (d_x is the

dimension of a cell following the profile direction and d_z is the dimension following the vertical axis) centered in (X_0, Z_0) and for which the value of ρ is assumed to be constant (Figure 3). The gravity field at each point denoted i is the sum of the effects of all the cells. It is given by the following formula:

$$g_i = \sum_{j=1}^{N} \sum_{k=1}^{K} G_{ijk} \rho_{jk} + \varepsilon_i \quad (7)$$

where N is the number of cells in the profile direction, K the number of cells in the vertical direction. G_{ijk} is the Green's function associated with the gravimetric effect of the elementary prism (j, k) observed at the point i, ρ_{jk} is the density of prism centered in (x_j, z_k) and ε_i is the error on the value of field observed at the point i.

4.3. Direct Modelling

3D modelling has proven to be the most descriptive in terms of characterizing bodies, given that it allows the observation on the lateral, longitudinal and angular extends. While 2D modelling is applied to structures with infinite extensions, 2.5D modelling allows a good control of the lateral extension of geological structures [34]. In Figure 4, we see that the body causing the anomaly observed on the map could have a southward extension beyond Campo zone. This way, the data do not permit us to carry out 3D modelling. We have therefore chosen to apply the 2.5D modelling.

5. Results

5.1. Bouguer Anomaly Map

The Bouguer anomaly map was elaborated by an automatic computer drawing from the Geosoft Package software v.8. from the established grids using a contour interval of 3 mGal (Figure 4). The area of interest is dominated by a relatively broad gravity high extending southwestward from Lolabe to Campo. The entire western part of the map is dominated by high gravity anomalies with the broader part in the north while the eastern part shows relatively low values. This indicates a strong gradient of anomalies between the east and the west which is

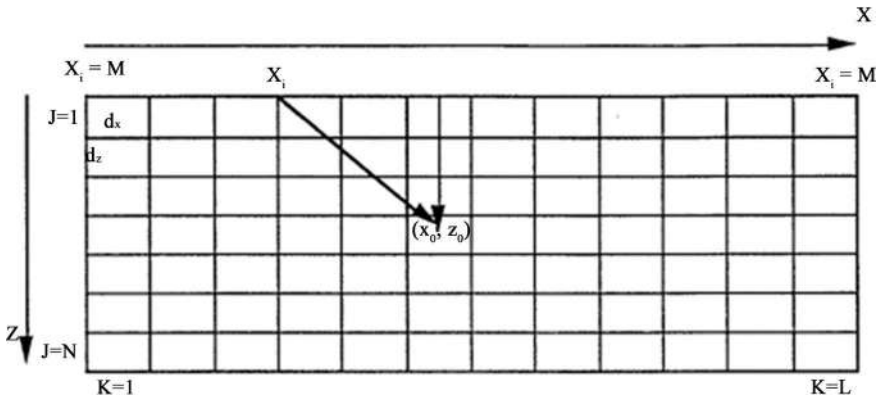

Figure 3. Representation of the prisms in the linear programming technique [2].

probably linked to the Kribi-Campo fault oriented NE-SW and noted f_2 on our geological map (Figure 1). According to [9], the northwestern and southwestern high circular-shaped anomalies are caused by intrusive dense bodies in the sub-surface of the region. The gravity modelling will situate these intrusions into the subsurface.

5.2. Depth of Anomaly Sources from Spectral Analysis

Figure 5 shows a representation of the gravity power spectrum with respect to the wave number for the profile P. Three different lines can be observed on this graph, that has been used to determine the average depths h_1 = 3.1 km, h_2 = 1.2

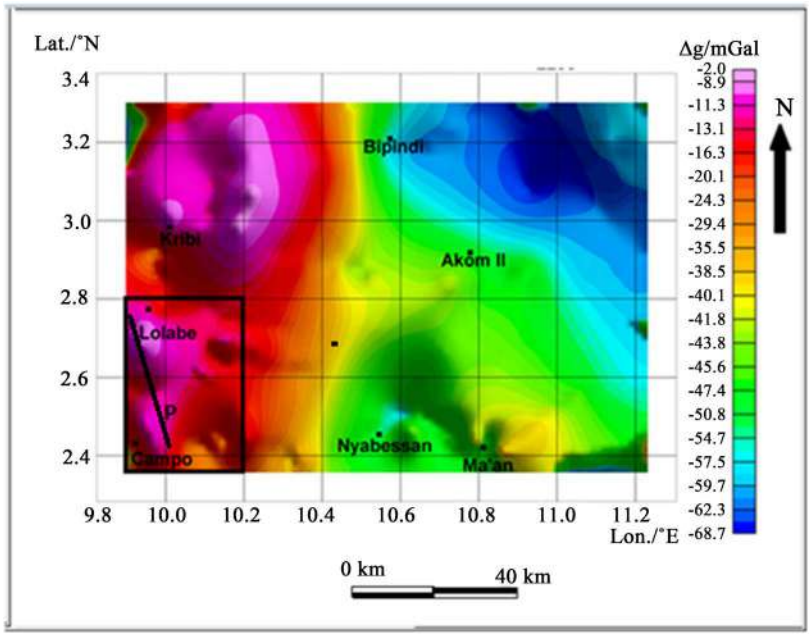

Figure 4. Bouguer gravity anomaly map of the study area.

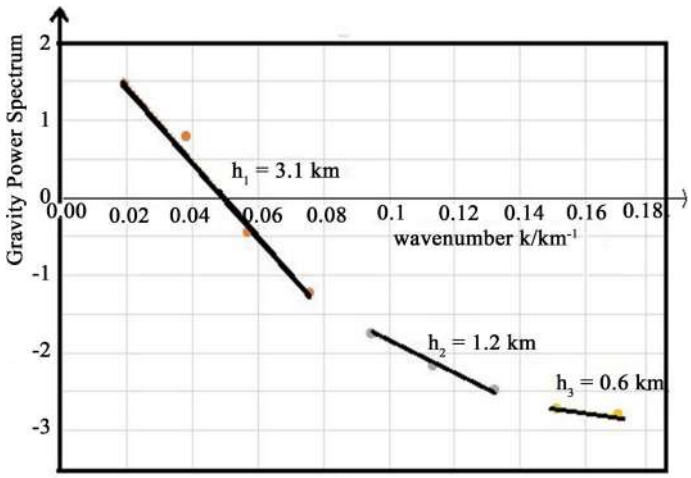

Figure 5. The power spectrum of profile P of the Bouguer anomalies showing depths (h_1, h_2 and h_3) of interfaces.

km and h_3 = 0.6 km corresponding to the interfaces of low, average and high frequencies respectively. These results show that the depth of the form of the intrusion is not uniform. h_1 represents the depth to the base of the body and h_3 the depth to the top, while h_2 is the depth to a particular section of the intrusive body.

5.3. Ideal Body Solution

In order to determine the ideal body for the investigated anomaly, we used the IDB2 Fortran Program [35] which calculates Parker's ideal body using the simplex algorithm for the linear programming. The solution of the ideal body is calculated along the 40 km profile P (**Figure 4**) and the characteristics of the initial model for data inversion are as follow:

- horizontal length of prisms: Δx = 1 km;
- vertical length of prisms Δz = 0.5 km;
- number of prisms following the horizontal nx = 20;
- number of prisms following the vertical nz = 10;
- error on the value of anomaly: 1 mGal.

Figure 6 presents the solution of the ideal body in which are represented the two bodies responsible for the observed anomaly. The ideal body gives an idea on the distribution of these responsible masses and their apparent geometry. On the right, we have the larger block located between at 0.5 km and 3 km, and a smaller block on the left situated between 0.5 km and 1.5 km. These two masses, with a predominant density contrast of 0.13 g·cm^{-3} compared to the surrounding rocks, are relatively located in the northern side of our selected profile.

5.4. 2.5D Model

The model presented in **Figure 7** consists of various bodies which are responsible for the observed anomalies along the profile. We used the computer program Grav2dc [36] to carry out this modelling. This interactive software allows one to design a geological model in the form of the polygon, whose gravity signature is in accordance with the observed anomalies. It takes as initial values the density contrast and the lateral extension of any given body. Three main parameters

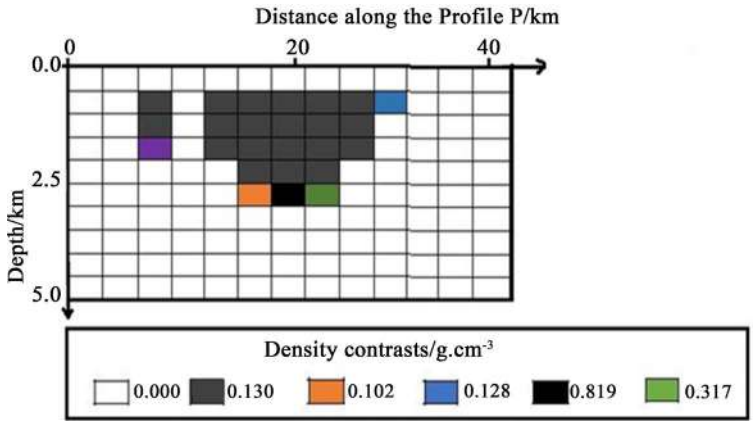

Figure 6. The ideal body solution.

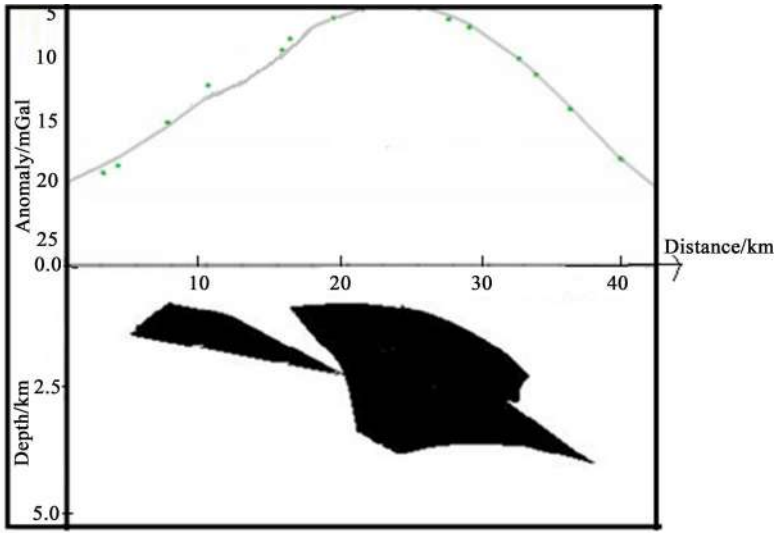

Figure 7. 2.5D model from profile P. The upper section represents the experimental anomaly and the theoretical curve. The green asterisks represent the observed gravity anomaly while the curve represents the calculated anomaly. The lower section shows the modelled bodies with a density contrast of 0.13 g·cm^{-3} each, surrounded by metamorphic and sedimentary formations.

were used to constrain this model, namely: the value of the density contrast (0.13 g·cm^{-3}) obtained from the ideal body solution (**Figure 6**); the depths of the intrusions obtained from the spectral analysis calculations (depth to the top 0.6 km and depth to the base of 3.1 km for the main body to the right and 1.2 km for the small block to the left) and the known geological information in the region (region mainly covered by sedimentary and metamorphic formations and other intrusions). The obtained model (**Figure 7**) shows a structure of two bodies which seem to have resulted from the dislocation of a single body interpreted to be a dense intrusive rock surrounded by metamorphic and sedimentary formations. The first body, which is the smaller one is confined at depths of 0.6 km and 2 km approximately, and it is located in the northern edge of the profile. The geometrical observation and the structural disposition of this body, suggests that it initially formed a single body with the larger one situated on its right. The larger body on to the right, with a wider extend than the first is confined at depths of 0.6 km and 3.2 km approximately and occupies mainly the middle portion of the profile. The dislocation of the two body could be as a result of the geo-tectonic activities observed in the region which gave rise to various faulting systems [8] [9] [10] [37].

6. Discussion

The high gravity anomaly values observed in the Lolabe-Campo area seem to have been caused by the presence of two high density rock bodies within the subsurface. From the results of the ideal body solution, the density contrast of these rock bodies is about 0.13 g·cm^{-3} compared to the surrounding rocks, which are mainly metamorphic and sedimentary in nature. The model is characterized

by a depth to the top of 0.6 km for the two blocks, with a depth to the base of 1 km for the first block, depth to particular sections of the second block of 2.5 km, while the depth to the base of this second body is about 3.5 km. Although these characteristics are in close agreement with the results of spectral analysis, they are slightly different from the results of the ideal body solution, in which the two blocks are vertically separated with no contact between them. The two bodies as observed on the ideal body solution have a top-to-top separation of about 7.0 km and a base-to-middle separation of about 0.4 km. The model obtained highlights discontinuities between interfaces of contrasting densities at depths between 0.6 km, 2.5 km and 3.5 km. A closer look at **Figure 7**, from its geometrical position to its structural disposition coupled with the already known tectonic activities in the region [8] show that the tectonic events responsible for the emplacement, breaking up and separation of the intrusive igneous body into two bodies could first of all have been as a result of an upward vertical translational tectonic movement followed by an anticlockwise rotational faulting tectonic movement. This is in agreement with the results of [37], which indicate that the relief of the study area generally conserves the imprints of the phenomena of faulting tectonics. [38] also mentioned the occurrence in the region of a strong extensional tectonic event that dates back to the Cretaceous. [8] on delineating the lineaments in south Cameroon obtained a structural map which shows that major tectonic events are responsible for the structural layout of this study zone. Furthermore, [9] presented a 3D model of another intrusive body located at about 40 km to the north of these two bodies. Compared to his model, the present study presents a density contrast which indicates the difference in types and densities of rock bodies in the region as one moves from the north towards the south. Considering that the average density of the metamorphic formations in the study area is equal to 2.67 g·cm^{-3} and given that the density contrast of the intrusive igneous body is 0.13 g·cm^{-3}, the density of this body can be estimated at about 2.80 g·cm^{-3}. **Table 1** below presents the density ranges of the various intrusive rocks in the region [21], from which it can be deduced that the intrusive body obtained in this study by the 2.5D gravity modelling could be composed principally of gabbro rocks.

Micro-gabbro and gabbro are intrusive igneous rocks that occur as dikes and sills and contain minerals such as olivine, plagioclase and feldspar. This assurance about dolerite is based on the fact that the study area forms the onshore portion of the Kribi-Campo sedimentary sub-basin found around the Atlantic Ocean.

The open zone (Z) between the two bodies (**Figure 8**) obtained from this

Table 1. Density values of intrusive rocks in the study area.

Rock name	gneiss	Alkaline syenite	Nepheline syenite	granodiorite	dolerite	gabbro	peridotites
Density range/g·cm^{-3}	2.60 - 2.90	2.60 - 2.95	2.53 - 2.70	2.67 - 2.79	2.70 - 3.50	2.50 - 3.10	2.78 - 3.37
Mean density value/g·cm^{-3}	2.75	2.78	2.61	2.73	3.10	2.8	3.08

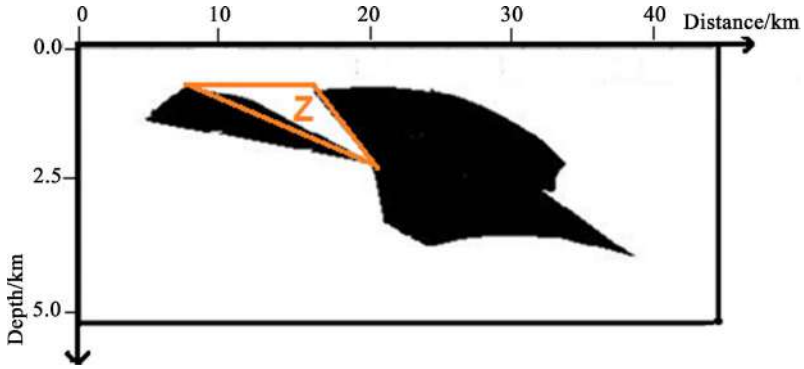

Figure 8. 2.5D model with potential trap zone represented.

modelling, which is apparently triangular in shape could be favorable for the accumulation of hydrocarbons or minerals and should constitute a topic for more detailed studies to be carried out in the area using microgravity survey or other geophysical prospecting methods.

7. Conclusion

The purpose of this study was to provide more information on the nature and the characteristics of the intrusive body in the Lolabe-Campo Area as proposed by [10]. The analysis of the gravity map, the interpretation of the gravity anomalies by spectral analysis, ideal body solution and by 2.5D modelling reveal high gravity discontinuities between rocks of different densities and the presence of two high density bodies of rocks in the subsurface of Lolabe-Campo. The emplacement, breaking up and separation of the intrusive igneous body resulting in these two blocks have been interpreted as deriving from two tectonic events corresponding first of all to an upward vertical translational tectonic movement followed by an anticlockwise rotational faulting tectonic movement. The isolated intrusive igneous blocks whose density has been estimated at 2.80 $g{\cdot}cm^{-3}$ based on an average density of 2.67 $g{\cdot}cm^{-3}$ for the local rocks and a density contrast of 0.13 $g{\cdot}cm^{-3}$, are completely surrounded by both sedimentary and metamorphic formations. A comparison of this high density value with that of other intrusive rocks in the study area and also the location of this area around the Atlantic Ocean has led to the conclusion that the two intrusive bodies may be composed principally of gabbro. The disposition and shape of the open zone (Z) highlighted by the resulting separation of the intrusive blocks is suggestive of a very good trap for the accumulation of hydrocarbons and mineral resources. This conclusion however paves the way for more detailed studies to be carried out in the area using either microgravity survey or other geophysical prospecting methods.

Acknowledgements

This paper will benefit from the fruitful criticism and suggestions of anonymous reviewers, leading to an improvement of the work. They are gratefully ac-

knowledged.

Conflicts of Interest

The authors declare no conflicts of interest regarding the publication of this paper.

References

[1] Abdelsalam, M.G., Liégeios, J.P. and Stern, R.J. (2002) The Sahara Metacraton. *Journal of African Earth Sciences*, **34**, 119-136. https://doi.org/10.1016/S0899-5362(02)00013-1

[2] Toteu, S.F., Fouateu, R.Y., Penaye, J., Tchakounte, J., Mouangue, A.C.S., Van Schmuss, W.R., Deloule, E. and Stendal, H. (2006) U-Pb Dating of Plutonic Rocks Involved in the Nappe Tectonics in Southern Cameroon: Consequence for the Pan African Orogenic Evolution of the Central African Fold Belt. *Journal of African Earth Sciences*, **44**, 479-493. https://doi.org/10.1016/j.jafrearsci.2005.11.015

[3] Nédélec, A., Nsifa, E.N. and Martin, H. (1990) Major and Trace Element Geochemistry of Achaean Ntem Plutonic Complex (South Cameroon) Petrogenesis and Crustal Evolution. *Precambrian Research*, **47**, 35-50. https://doi.org/10.1016/0301-9268(90)90029-P

[4] Manguelle-Dicoum, E., Bokossah, A.S. and Kwende-Mbanwi, T.E. (1992) Geophysical Evidence for a Major Precambrianshist-Granite Boundary in Southern Cameroon. *Tectonophysics*, **205**, 437-446. https://doi.org/10.1016/0040-1951(92)90447-E

[5] Tadjou, J.M., Nouayou, R., Kamguia, J., Kande, H.L. and Manguelle-Dicoum, E. (2009) Gravity Analysis of the Boundary between the Congo Craton and the Pan-African Belt of Cameroon. *Austrian Journal of Earth Sciences*, **102**, 71-79.

[6] Shandini, N.Y., Tadjou, J.M. Tabod, C.T. and Fairhead, J.D. (2010) Gravity Data Interpretation in the Northern Edge of the Congo Craton, South-Cameroon. *Anuário do Instituto de Geociências*, **33**, 73-82.

[7] Owona Angue, M.L.C., Tabod, C.T., Nguiya, S., Kenfack, J.V. and Tokam Kamga, A.P. (2013) Delineation of Lineaments in South Cameroon (Central Africa) Using Gravity Data. *Open Journal of Geology*, **3**, 331-339. https://doi.org/10.4236/ojg.2013.35038

[8] Owona Angue, M.L.C., Assembe, S.P., Njingti, N., Ngoh, J.D., Ndougsa Mbarga, T., Kue Petou, R.M. and Bisso, D. (2016) Determination of the Structural Lineaments in the Kribi-Campo-Ma'an Area from a Multi-Scale Analysis of Gravity Data Using the HGM and Euler 3D Deconvolution Approaches. *International Journal of Geosciences*, **7**, 1122-1143. https://doi.org/10.4236/ijg.2016.79085

[9] Kue Petou, R.M., Owona Angue, M.L, Njingti, N. and Manguelle-Dicoum, E. (2017) 3D Modelling from New and Existing Gravity Data of an Intrusive Body in the Northern Part of Kribi-Campo Sub-Basin in Cameroon. *International Journal of Geosciences*, **8**, 984-1003. https://doi.org/10.4236/ijg.2017.88056

[10] Kue Petou, R.M., Owona Angue, M.L.C., Njingti-Nfor, N., Ndougsa-Mbarga, T. and Manguelle-Dicoum, E. (2017) Determination of Structural and Geometrical Parameters of the Kribi-Campo Sedimentary Sub Basin Using Gravity Data. *International Journal of Geosciences*, **8**, 1210-1224. https://doi.org/10.4236/ijg.2017.89069

[11] Bessoles, B. and Lassere, M. (1977) Le complexe de base du Cameroun. *Bulletin de la Société Géologique de France*, **19**, 1092-1805.

https://doi.org/10.2113/gssgfbull.S7-XIX.5.1085

[12] Bessoles, B. and Trompette, M. (1980) Géologie de l'Afrique: La chaîne Panafricaine, "Zone mobile d'Afrique centrale (partie sud) et Zone mobile soudanaise". *Mémoire du BRGM*, **92**, 19-80.

[13] Penaye, J., Toteu, S.F., Van Schmus, W.R., Tchakounté, J., Ganwa, A.D. and Minyem Nsifa, E.N. (2004) The 2.1-Ga West Central African Belt in Cameroon: Extension and Evolution. *Journal of African Earth Science*, **39**, 159-164. https://doi.org/10.1016/j.jafrearsci.2004.07.053

[14] Shang, C.K., Siebel, W., Satir, M., Chen, F. and Mvondo Ondoua, J. (2004) Zircon Pb-Pb and U-Pb Systematics of TTG Rocks in the Congo Craton: Constraints on Crust Formation, Magmatism, and Pan-African Lead Loss. *Bulletin of Geosciences*, **79**, 205-219.

[15] Ganwa, A.A., Frisch, W., Siebel, W., Ekodeck, E.G., Shang, C.K. and Ngako, V. (2008) Archean Inheritances in the Pyroxene-Amphibole-Bearing Gneiss of the Méiganga Area (Central North Cameroon) Geochemical and 207Pb/206Pb Age Imprints. *Comptes Rendus Geoscience*, **340**, 211-222. https://doi.org/10.1016/j.crte.2007.12.009

[16] Penaye, J., Toteu, S.F., Van Schmus, W.R. and Nzenti, J.P. (1993) Up-Pb and Sm-Nd Preliminary Geochronologic Data on the Yaounde Series, Cameroon: Reinterpretation of the Granulitic Rocks as the Suture of a Collision in the Central African "Belt". *Comptes Rendus de l'Académie des Sciences, Paris*, **317**, 789-794.

[17] Maurizot, P., Abessolo, A., Feybesse, J.L., Johan, V. and Lecomte, P. (1986) Etude et prospection minière du sud-ouest Cameroun. Synthèse des travaux de 1978 à 1985. Rapport, BRGM, 274 p.

[18] Tchameni, R. (2001) Crustal Origin of Early Proterozoic Syenites in the Congo Craton (Ntem Complex), South Cameroon. *Lithosphere*, **57**, 23-42. https://doi.org/10.1016/S0024-4937(00)00072-4

[19] Pouclet, A.K., Tchameni, A., Mezger, M., Vidal, Nsifa, E., Shang, C. and Penaye, J. (2007) Archean Crustal Accretion at the Northern Border of the Congo Craton (South Cameroon). The Charnockite-TTG Link. *Bulletin de la Société Géologique de France*, **178**, 331-342. https://doi.org/10.2113/gssgfbull.178.5.331

[20] Tchameni, R., Mezger, K., Nsifa, E. and Pouclet, A. (2000) Neoarchean Evolution in the Congo Craton: Evidence from K-Rich Granitoids of the Ntem Complex, Southern Cameroon. *Journal of African Earth Science*, **30**, 133-147. https://doi.org/10.1016/S0899-5362(00)00012-9

[21] Telford, W.M., Geldart, L.P. and Keys, D.A. (1976) Applied Geophysics. Cambridge University Press, Cambridge, 860 p.

[22] Mvondo, H., Owona, S., Mvondo-Ondoa, J. and Essono, J. (2007) Tectonic Evolution of the Yaoundé Segment of the Neoproterozoic Central African Orogenic Belt in Southern Cameroon. *Canadian Journal of Earth Science*, **44**, 433-444. https://doi.org/10.1139/e06-107

[23] Mapoka, H., Danguene, E.Y., Prince, J.P., *et al.* (2011) Major Structural Features and the Tectonic Evolution of the Bossangoa Bossembele Basement, North Western Central African Republic. *The Open Geology Journal*, **5**, 21-32. https://doi.org/10.2174/1874262901105010021

[24] Manguelle-Dicoum, E. (1988) Etude Géophysique des structures superficielles et profondes de la region de Mbalmayo. Thèse de Doctorat, Université de Yaoundé I, 202 p.

[25] Shandini, Y. and Tadjou, J.M. (2012) Interpreting Gravity Anomalies in South

Cameroon, Central Africa. *Earth Sciences Research Journal*, **16**, 5-9.

[26] Feybesse, J.L., Johan, V., Triboulet, V., Guerrot, C., Mayaka-Mikolo, F., Bouchot, V. and Eko, N.J. (1998) The West Central African Belt: A Model of 2.5-2.0 Ga Accretion and Two-Phase Orogenic Evolution. *Precambrian Research*, **87**, 161-216. https://doi.org/10.1016/S0301-9268(97)00053-3

[27] Toteu, S.F., Van Schmus, W.R., Penaye, J. and Michard, A. (2001) New U-Pb, and Sm-Nd Data from North-Central Cameroon and Its Bearing on the Pre-Pan-African History of Central Africa. *Precambrian Research*, **108**, 45-73. https://doi.org/10.1016/S0301-9268(00)00149-2

[28] Nsifa, E.N. (2005) Magmatisme et evolution g eodynamique de l'Archeen au Prot erozo ıque de la bordure nord-ouest du craton du Congo (complexe du Ntem) au Sud-Ouest Cameroun. These Doct. d'Etat Univ. Yaounde I, 248.

[29] Heiskanen and Moritz (1967) Physical Geodesy. 373 p.

[30] Spector, A. and Grant, F.S. (1970) Statistical Models for Interpretation Aeromagnetic Data. *Geophysics*, **35**, 293-302. https://doi.org/10.1190/1.1440092

[31] Gerard, A. and Debeglia, N. (1975) Automatic Three-Dimensional Modeling for Interpretation of Gravity or Magnetic Anomalies. *Geophysics*, **40**, 1014-1034. https://doi.org/10.1190/1.1440578

[32] Bhattacharryya, B.K. and Leu, L.-K. (1975) Spectral Analysis of Gravity and Magnetic Anomalies Due to Two-Dimensional Structures. *Geophysics*, **40**, 993-1013. https://doi.org/10.1190/1.1440593

[33] Parker, R.L. (1974) Best Bounds on Density and Depth from Gravity Data. *Geophysics*, **39**, 644-649. https://doi.org/10.1190/1.1440454

[34] Cady, J.W. (1980) Calculation of Gravity and Magnetic Anomalies of Finite-Length Right Polygone Prism. *Geophysical Prospecting*, **45**, 1507-1512. https://doi.org/10.1190/1.1441045

[35] Huestis, S.P. and Ander, M.E. (1983) IDB2—A Fortran Program for Computing Extremal Bounds in Gravity Data Interpretation. *Geophysics*, **48**, 999-1010. https://doi.org/10.1190/1.1441525

[36] Cooper, G.R.J. (1998) GRAV2DC for Windows User's Manual (Version 2.05). Geophysics Department, University of the Witwatersrand, Johannesburg.

[37] Regnoult, J.M. (1986) Synthese géologique du Cameroun Dir. Des Mines et de la Geol., Cameroun, 119.

[38] Popoff, M. (1988) Du Gondwana a l'Atlantique Sud: Les connexions du fosse de la Bénoué avec les bassins du NE brésilien jusqu'à l'ouverture du golfe de Guinee au crétacé inférieur. *Journal of African Earth Science*, **7**, 409-431.

European Journal of Scientific Research
ISSN 1450-216X / 1450-202X Vol. 153 No 2 June, 2019, pp. 127-144
http://www. europeanjournalofscientificresearch.com

Evaluation of the Impact of Gravity Corrections on Raw Gravity Data in South Cameroon: Prospection and Tectonic Assessments

Kue Petou Rokis Malquaire
Department of Geophysics, School of Geosciences
China University of Petroleum (East China), No. 66 West Rd, Qinqdao 266580, China
Postgraduate School of Sciences, Technologies & Geosciences
University of Yaoundé I, P.O. Box 812 Yaoundé, Cameroon
National Institute of Cartography, P.O. Box 157, Yaoundé, Cameroon
E-mail: rokis.petou@yahoo.fr

Owona Angue Marie Louise
Department of Physics, Advanced Teacher Training College
University of Yaoundé I, P.O. Box 47, Yaoundé, Cameroon

Njingti Nfor
Department of Physics, Advanced Teacher Training College
University of Yaoundé I, P.O. Box 47, Yaoundé, Cameroon
Postgraduate School of Sciences, Technologies & Geosciences
University of Yaoundé I, P.O. Box 812, Yaoundé, Cameroon

Mioumnde Arthur Paterne
Laboratory of Ore Processing, Institute of Geological and Mining Research
Yaoundé, Cameroon
Key Laboratory of Deep Oil and Gas
(China University of Petroleum (East China)) Qingdao 266580, P.R. China

Eloundou Essama Lionel
National Institute of Cartography, P.O. Box 157
Yaoundé, Cameroon

Manguelle-Dicoum Eliezer
Department of Physics, University of Yaoundé I, P.O. Box 812
Yaoundé, Cameroon

Song Weiqi
Department of Geophysics, School of Geosciences
China University of Petroleum (East China), No. 66 West Rd, Qinqdao 266580, China

Abstract

Under the effect of non-geological sources such as the altitude of the stations, the effect of the sun and the moon, the effect of the surrounding topography and the instrumental drift, the measured gravity data are subject to changes in time and in space. It

is necessary to evaluate and eliminate these effects in considerable precision in order to have more reliable data that can provide the most information about the subsurface structure in the Kribi-Campo sub-sedimentary basin. This study highlights that, the free-air correction and Lunisolar correction are the most prominent in this area given its geographical position, its topographic variation and the survey configuration. Dependency of the terrain correction with isostatic compensation on one hand, and plateau correction with the established tectonic activities in the survey area were also highlighted. Despite the observed insignificance of terrain correction in local scale areas with little topographic fluctuations, its application contributes however to accuracy of the analyzed data. This analysis could be used to guide the choice of gravity corrections to be applied on raw data and decipher their relationship with gravity noise and tectonic activities.

Keywords: Gravity data, free-air correction, plateau Correction, Latitude Correction, Terrain Correction, Lunisolar Correction

1. Introduction

The purpose of gravity field reduction and correction is to eliminate from the observed gravity data any element that would be observed if we were studying a simple and essentially uniform earth. The remaining components are considered to be anomalous. In other words, anything that is left over is the result of density variation due to local the repartition of geological structures and eventually of local exploration interest. The diagram below is a conceptual flow chart for the gravity correction process, adapted from Chapin (1996), it describes the various steps that need to be followed to carry out obtain Bouguer anomalies from observed gravity data. Given that most gravimeter have instrumental drift incorporated, the first step is usually the subtraction of theoretical gravity which is followed by the subtraction of the free air correction. Free air anomalies are obtained in this case. In land surveys, gravity data are measured above sea level; In order to calculate gravity anomalies, measured values have to be reduced to the sea-level. Anomalies result from subtracting a value for normal gravity on the spheroid.

Diagram 1: Conceptual flow chart of gravity correction process (modified after Chapin, 1996)

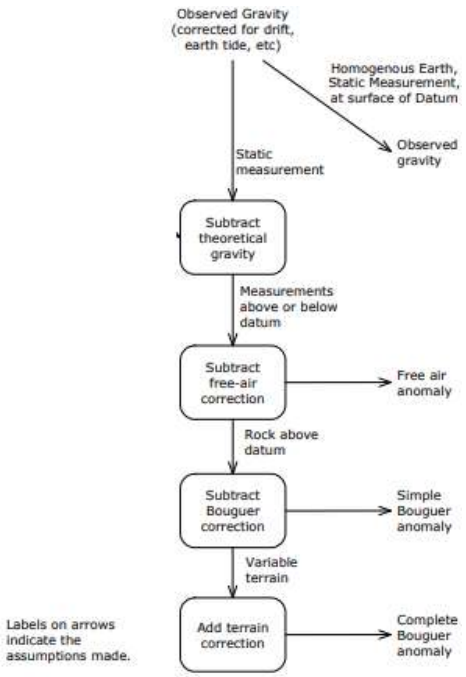

2. Area and Gravity Reductions

2.1. Data Collection Approaches

Two main techniques are generally used in a gravity data acquisition field. There are done in loop were measurements begin at a station and end at the same station. The first approach consists of considering all measurement stations as secondary base stations. Measurements of the relative gravity values are collected at the first station S_1, from S_1 moving to station S_2 to measure and come back to station S_1 and move again to station S_2. Station S_2 becomes at this point the secondary base station from which S_3 can be measured (figure 1). This procedure is repeated until the last station Sn. This technique means that 3 measurements can be done at one station. The loop is close for every consecutive measurement. This approach is costly and time consuming as many measurements are carried in each station, however it reduces substantially the tidal influence on measurements and instrument fatigue **(Telford, 1976).**

The second approach, which is the one we used in this study consists of taking measurements at the base station S_1 , moving to S2, then S3 until Sn and coming back to S1 to close the measurement loop. This approach is more feasible both technically and economically compared to first method because of the good time efficiency and the low cost

In general, the values measured at the beginning and end at the base station are not similar. This difference, called drift, is due partly to the gravity-meter, partly to the lunar tide **(Mathew et al. 1977)**

The measured values are thus hampered by errors since one of their components is derived from the drift and does not reflect a change in the g values due to subsurface heterogeneities.

The Correction is made on the assumption that the drift is linear in time. In our survey in South Cameroon, we used these step by step handling of the Lacoste-Romberg gravimeter to take the measurements at every station:

Using the Gravimeter

1. Level the stool using the bubble in the center. Measure and record the height from the ground to the lip of the stool.
2. Take out instrument and level using the two bubbles figure 1. This is done using the three knobs on the legs at the bottom of the meter and the 2 "bubble" levels at the top. The bubbles of both levels must be at the center of the level for the gravimeter to be level. This is best done by one person adjusting 2 of the legs while watching both levels simultaneously. After the gravimeter is level, turn it on.
3. The meter is read by looking in the eyepiece and turning the "turns indicating" dial until the beam is coincident with the center line of the reticle (cross-hairs). Always approach the center line from the same direction (from the left). To do so, turn the dial clockwise until the beam is on the left. Then turn (slowly) counter-clockwise until you approach the center line. If you overshoot, restart by moving the beam all the way to the left again. The beam takes a second to adjust, so go slowly and wait for the beam to adjust before continuing to turn the dial.
4. Once the beam is aligned with the center line, the dial can be read. The largest two digits of the dial reading (hundreds) are determined from the small number showing through the window indicating how many turns of the dial have been made, the next two digits (ones) are read from the dial with the "0" of the vernier as the reference, and the tenths are read from the vernier. Estimate the errors of the gravity measurements. The number is converted to milligals by multiplying by the dial constant shown on the side of the gravimeter. Note these are relative measurements of gravity. To obtain actual gravity measurements we would have to go to a place where the gravity is known and calibrate the meter.
5. Record the measurement, the time, the geographical coordinate of the station and it's elevation.
6. Make sure to return to the base station before the end of the day!

Figure 1: (A) First approach loop representation: every station is entitled to 3 measurements.Second approach loop representation: (B) measurements are taken around the base station which is the beginning and the ending point of the loop. (C) Measurements are taken along a path, return to base station to close the loop

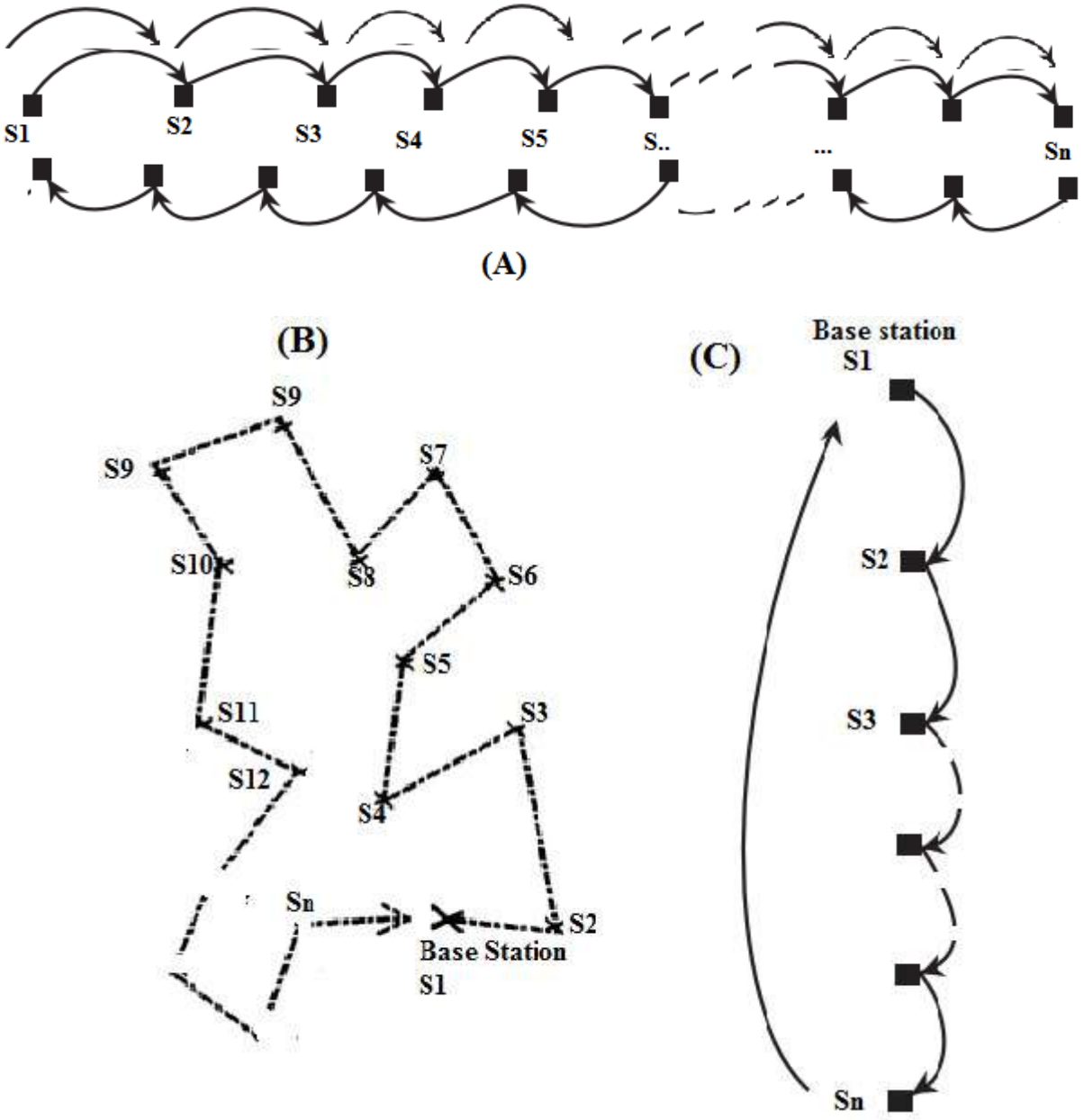

Figure 2: Lacoste-Rombert gravity-meter used for data collection

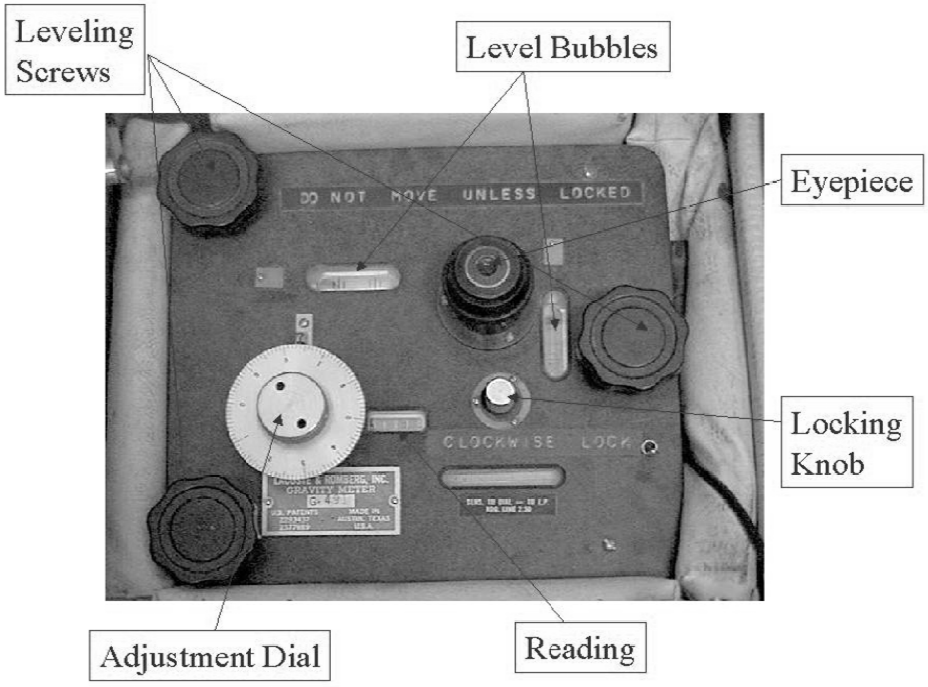

2.2. Correction for Instrumental Drift

This correction attempts to eliminate the influences of tides on the measurements and the fatigue of the instrument. For this purpose, it is necessary to follow a certain path between reading stations. In practice, a series of measurements is made by following a loop path: the series usually starts at a given point and ends at the same point (Figure 1). The starting point of the loop is normally connected to a base station.

2.3. Free Air Correction or Altitude Correction

The measured values of g have variations which are only due to the position of the measuring station and not to the subsurface heterogeneities or the effect for mass between observed point and the datum. In order to eliminate these variations, the altitude or free air correction is applied on the data. The free-air correction accounts for gravity variations caused by elevation differences in the observation locations. For a displacement of h with respect to the reference level, we have (Bernard and Chouteau, 2008)

$$g_h = \frac{Gm}{(r+h)^2} = \frac{Gm}{r^2(1+2(h/r)+(h/r)^2)} \tag{1}$$

Given that $r \gg h$, r is the earth radius , g_h is the value of g at the elevation h, G is the gravitational constant; m the mass of the earth.

The free-air correction is given as

$$C_F = g_h - g_r = -2hg_r / r \tag{2}$$

For stations above the reference level ($h \succ 0$, in meters), C_F is positive and is described by the formula

$$C_F = 0.3086h \qquad (mgal) \tag{3}$$

2.4. Latitude Correction

This correction considers the variations of g with the latitude caused by to the rotation and the flattening of the earth. From world geodesic measurements, we know that the earth is an ellipsoid of almost perfect revolution. On this surface, the gravitational field can be described by the following equation (WGS-84)

$$g_{th}(\phi) = 9.7803253359 \frac{1 + 0.00193185265241 \sin^2 \phi}{\sqrt{1 - 000669437999014 \sin^2 \phi}} \quad (4)$$

Where $g_{th}(\phi)$ is the field value the at the point of geodesic latitude φ. The correction C_ϕ for a displacement l following a meridian is given by

$$C_\phi = \frac{\partial g_{th}}{\partial l}.l \quad \text{with} \quad dl = R(\phi)d\phi \approx R_e d\phi \quad (5)$$

Where R_e is the equatorial radius of the earth (6378, 136 km). For smaller scale studies the expression (with l in meters) can simplified to **(Bernard Giroux and Michel Chouteau, 2008)**

$$C_\phi = 8.1669 \times 10^{-4}.l.\sin 2\phi \quad [mgal] \quad (N \to S) \quad . \quad (6)$$

For the calculations of the latitude correction in this study, given the local nature of the study area and also, the data were taken in an approximate profile line, the distance from the meridian is considered to be constant

2.5. Plateau Correction or Bouguer Slab Correction

The plateau correction is very important as it accounts for the thickness of rocks between the elevation at the current station and the elevation at the base station thus accounts for the excess mass underlying observation points located at altitude higher than the reference elevation (sea level or the geoid). Inversely, it accounts for a mass deficit at points of observation located under the elevation datum (figure 3).

In this paper, we calculated the plateau correction assuming a constant slide value between the observation point and the reference altitude for all the stations.

Figure 3: Bouguer slab representation (Bernard and Chouteau, 2008)

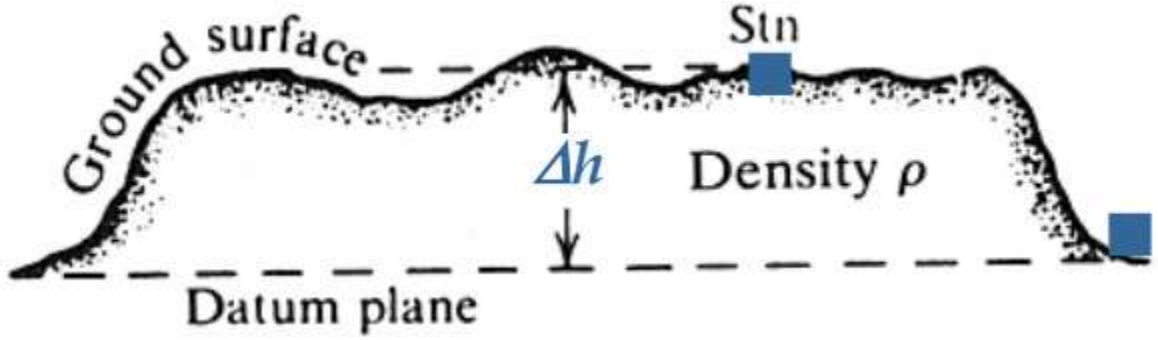

For a slice of height h, the attraction is given by

$$C_p = -0.04191 \rho_B h \quad mgal \qquad (h \succ 0) \quad (7)$$

ρ_B is the presumed density of the mass of the slice (ρ_B = 2.67 g / cm^3 on average). As C_p increases with h, it is subtracted when $h \succ 0$ and therefore

Usually, we the free-air correction and the plateau correction are combined to obtain what is called the Bouguer correction.

$$C_B = (0.3086 - 0.04191\rho_B)h \quad mgal \quad (h \succ 0) \tag{8}$$

For the value of $\rho_B = 2.67$ g / cm^3

$$C_B = 0.1966h \quad mgal \ (h \succ 0) \tag{9}$$

2.6. Terrain Correction

The application of the Bouguer correction removes the attraction of a slice of land of thickness h. If the topographical variations are such that the field cannot be approximated by a uniform slice, it is necessary to integrate numerically on one hand the parts which exceed it and on the other hand the parts which are missing to the slice of Bouguer. Thus the bouguer correction refers to the gravity effect of the intervening plate mass between stations S and the base level B while the terrain correction takes into account the effects of topographic elevations and deficits (Figure 4)

Several approaches have been developed to calculate the terrain correction, amongst which the Hammer approach which uses a reticle that is superposed to topographic maps and tables prepared by Hammer. We also have the of Nettleton approach which consists of representing, on the same figure, a topographic profile and the profiles of the Bouguer anomaly corresponding to it, calculated for several densities. For the terrain correction C_T applied in this paper, we have elaborated a robust matlab code.

Figure 4: Illustration of the Bouguer correction and Terrain correction Indiscrepancies

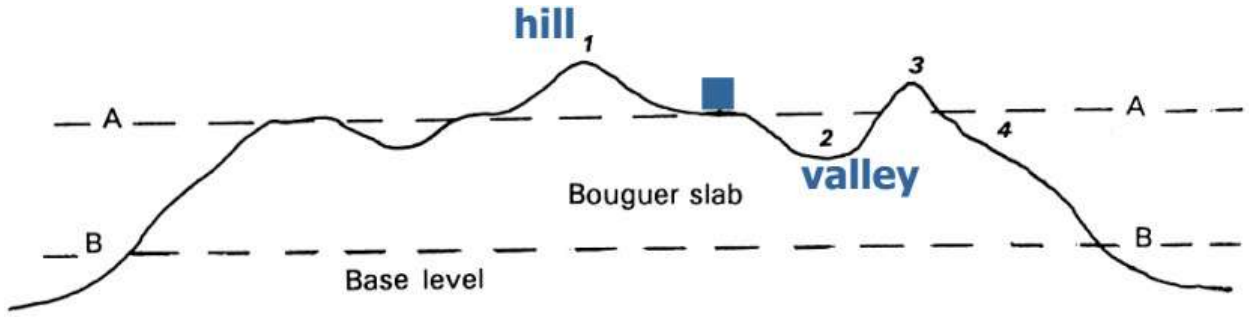

2.7. Luni-solar Correction

The biggest recurring gravity variations are due to effect of nearest to Earth celestial bodies Moon and Sun. Magnitude direction of gravity field vector i.e. vertical direction is varying by changing gravity field. These changes should be taken into account during precise geodetic observations. The influence of the celestial body can be expressed by tide potential. Tide generating potential for non-deformable (rigid) Earth could be defined as spherical function series **(Petroškevičius 2008):**

$$V_T = \frac{Gm}{r}\sum_{n=2}^{\infty}\left(\frac{R}{r}\right)^n P_n(\cos z), \tag{10}$$

where G is the gravitational constant; m the mass of the celestial body; r the geocentric distance to the celestial body; R the geocentric distance of point on Earth surface; z is the geocentric zenith distance of celestial body; $P_n(\cos z)$ –Legendre polynomials.

Darius Popovas (2011) described an algorithm which can be used to analyze the effect of the Moon and the Sun to the levelled height difference, he used the Love numbers h_n and k_n from (Varga 1989) which values depends on the elasticity of the earth.

Therefore the height difference correction for real Earth could be expressed by formulas:

$$\delta h = \sum_{n=2}^{\infty}\gamma_n \delta h_n^{'} \text{ With } \quad \gamma_n = 1 + k_n - h_n \tag{11}$$

Using the Vargas love numbers (h_2 = 0.6053, h_3 = 0.2890; h_4 = 0.1758; k_2 = 0.2993; k_3 = 0.0925; k_4 = 0.0414 (Vargas 1989) the expression was approximated to:

$$C_L = \delta h = \gamma_2 \frac{3GmR}{2gr^3} d\sin 2z\cos(A-a) + \gamma_3 \frac{3GmR^2}{2gr^4} d(4-5\sin^2 z)\sin z\cos(A-a) + \gamma_4 \frac{5GmR^3}{4gr^5} d(4-7\sin^2 z)\sin 2z\cos(A-a) \quad (12)$$

d is the distance between points, A is the azimuth of the deflection of the vertical, a refers to the azimuth of the levelling line.

The change ratio of lunisolar correction is rapidly unstable and uneven. Research have proven that lunisolar corrections in precise levelling can be calculated with more accuracy, considering azimuth changes and levelling rate deficiency. During our data collection survey, we recorded the time and the position at each levelling station which are necessary to accurately assess the impact of celestial bodies. Those values have used in this study to calculate lunisolar correction for each levelling station.

The works of **Darius Popovas (2011)** have establish the dependency of the lunisolar correction on lunar changes, azimuth, on prime vertical and meridian (figures 5).

Figure 5: Lunisolar correction dependency factors: (a) Daily change of lunisolar correction at different Moon phase (b) Correction dependency on azimuth change at different time moments (c) Rate of change of lunisolar correction in prime vertical and meridian (Darious Popovas, 2011)

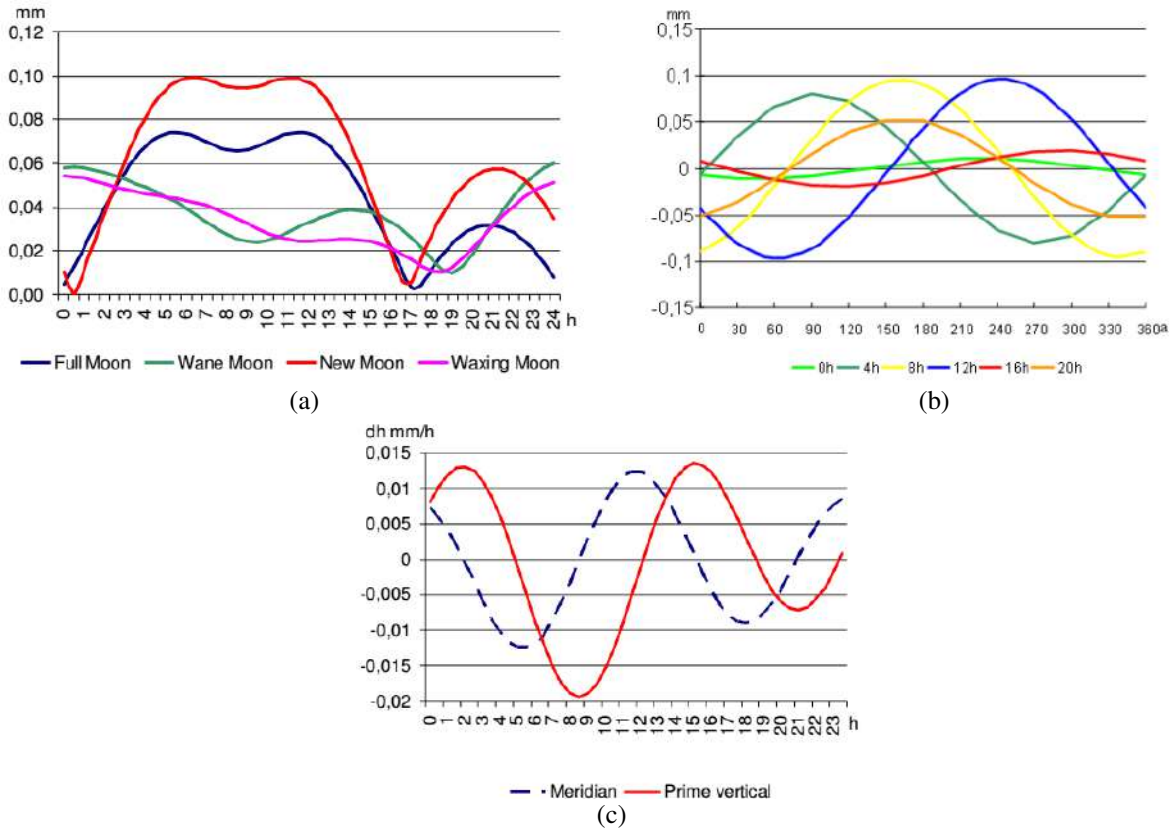

The main objective of gravity observations and gravity corrections is the analysis and interpretation of subsurface structures underlying the measurements sites. These interpretations are done thru the deciphering of the differences between observed gravity data and expected gravity data at a given point. These differences are expressed in terms of gravity anomalies. There are categorized according to the type(s) of correction applied. We have the free-air anomaly which results from the

application of free-air correction (equation 3) and the and the bouguer anomaly which results from the application of free-air, lunisolar, latitude, terrain and bouguer corrections (equations 3, 6, 9 and 12)

$$A_A = (g_{obs} - g_{ref}) + C_F \quad (13)$$

$$A_B = (g_{obs} - g_{ref}) \pm 6 corrections \quad (14)$$

1. Correction for instrumental drift
2. Free air correction $C_F = 0.3086h \ \ mgal$
3. Latitude correction $C_\phi = 8.1669\times10^{-4}.l.\sin 2\phi \ \ [mgal] \ \ (N \to S)$
4. Plateau correction $C_p = -0.04191\rho_B h \ \ mgal \ \ (h \succ 0)$
5. Terrain correction C_T
6. Lunisolar correction C_L

3. Evaluation of Gravity Reductions

In table 1, we present the some values of the measured gravity data at stations with the corresponding five correction applied.

Stations	Measured gravity	Free-air Correction	Plateau correction	Latitude Correction	Terrain Correction	Lunisolar Correction
1	978019.2577	2.1602	-0.7832979	0.0732	0.0720	0.1117
2	978015.6103	7.0978	-2.5736931	0.0717	0.0731	0.102
3	978014.0008	7.4064	-2.6855928	0.0726	0.074	0.0918
4	978014.9688	4.0118	-1.4546961	0.0726	0.072	0.0814
5	978015.3402	4.3204	-1.5665958	0.0726	0.0726	0.0707
6	978016.248	6.7892	-2.4617934	0.072	0.0726	0.0543
7	978013.2966	8.9494	-3.2450913	0.074	0.0726	0.0433
8	978020.0299	3.3946	-1.2308967	0.0731	0.0717	0.0324
9	978017.6795	5.5548	-2.0141946	0.072	.0732	0.0215

In order to better evaluate the impact of various gravity reductions on the raw data, the observed gravity field data was evaluated at each point. This value was represented with respect to the measurements points. The measurement points represent two main profiles in our study area; the Kribi-Campo profile oriented North-South, that constitutes the first 120 values and the Campo-Ma'an-Nyabessan profile, oriented West-East, that constitutes the remaining 55 points (figure 6). The highest values of G are observed in the first profile (the Kribi-Campo profile). On this profile, there is not a very large variation of the measured gravity, values range around $9.7802\text{x}10^5$ mGal. In the second profile, there is a progressive decrease of the measured value until around station 150 (figure 7). A sudden increase is observed at this point which moves from to $9.7801\text{x}10^5$ mGal afterwards the value falls back. It is observed that there are more changes in the observed gravity values of the second profile (Campo-Ma'an-Nyabessan) than in the first profile, this is an indication that, the effect of non-geological anomaly sources are more pronounced in this area.

Figure 6: gravity stations

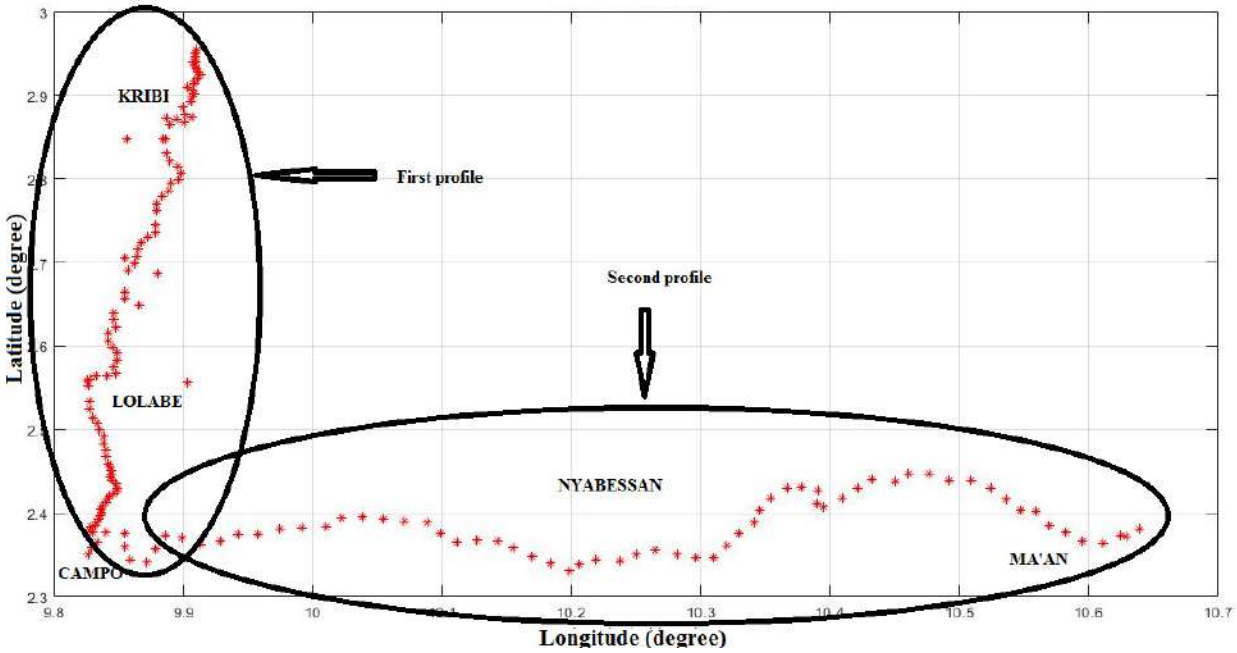

Figure 7: Variation of the measured gravity data along the profiles

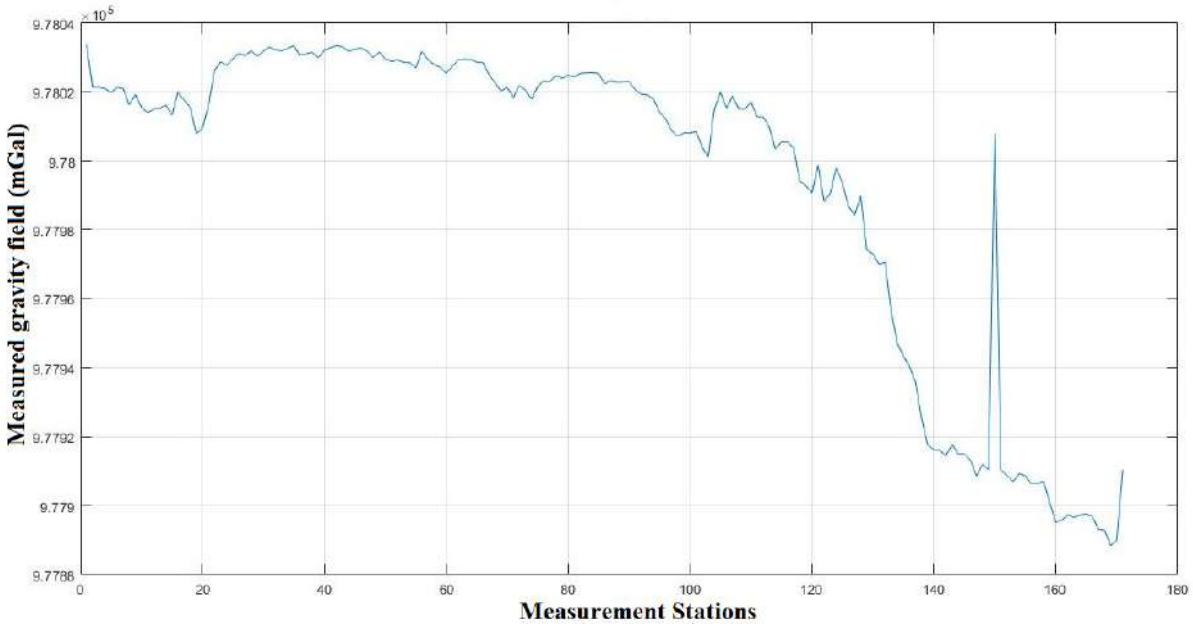

Figure 8: (a) Free air correction variation along the profiles; (b) altitude variation

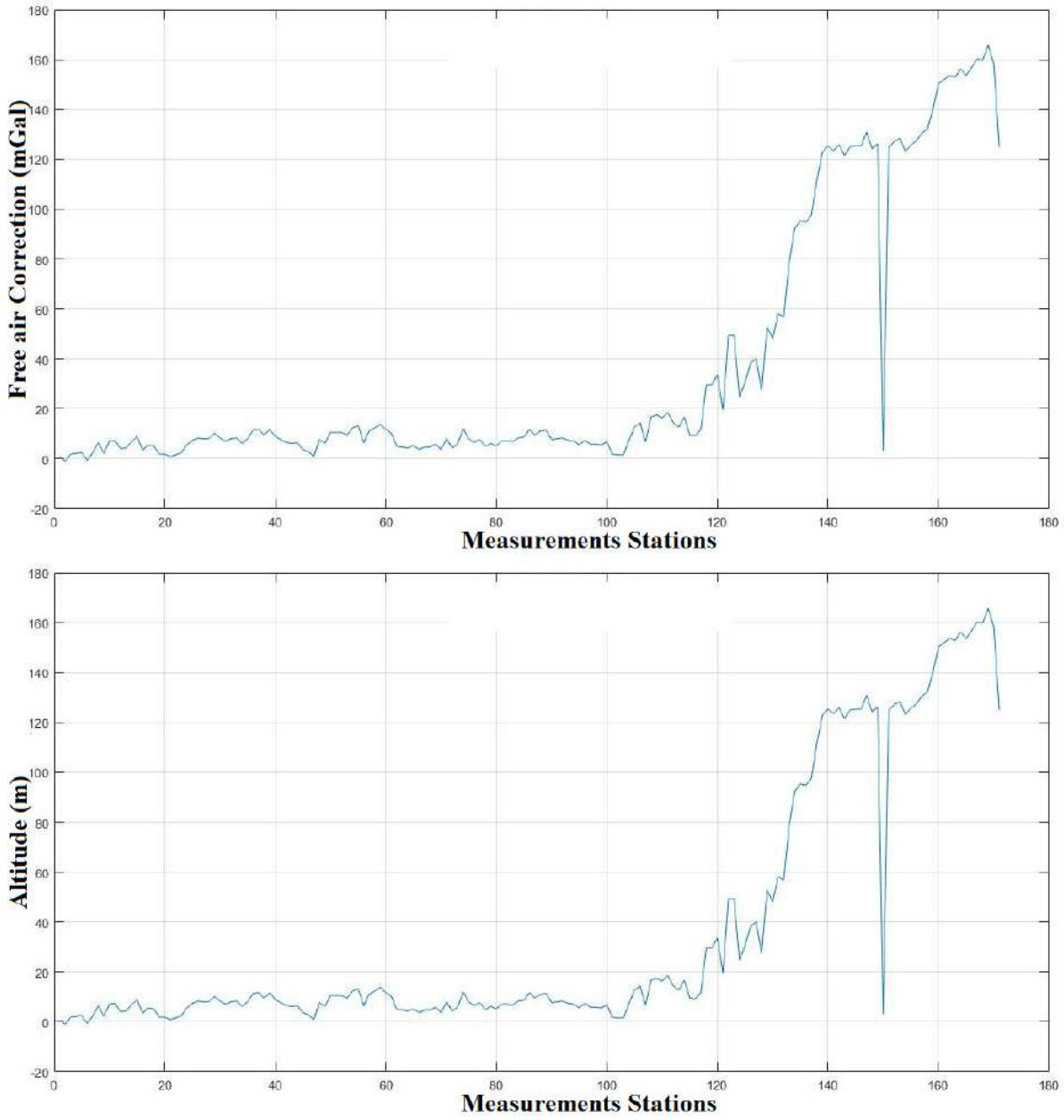

Figure 9: Plateau correction's variation along the profiles

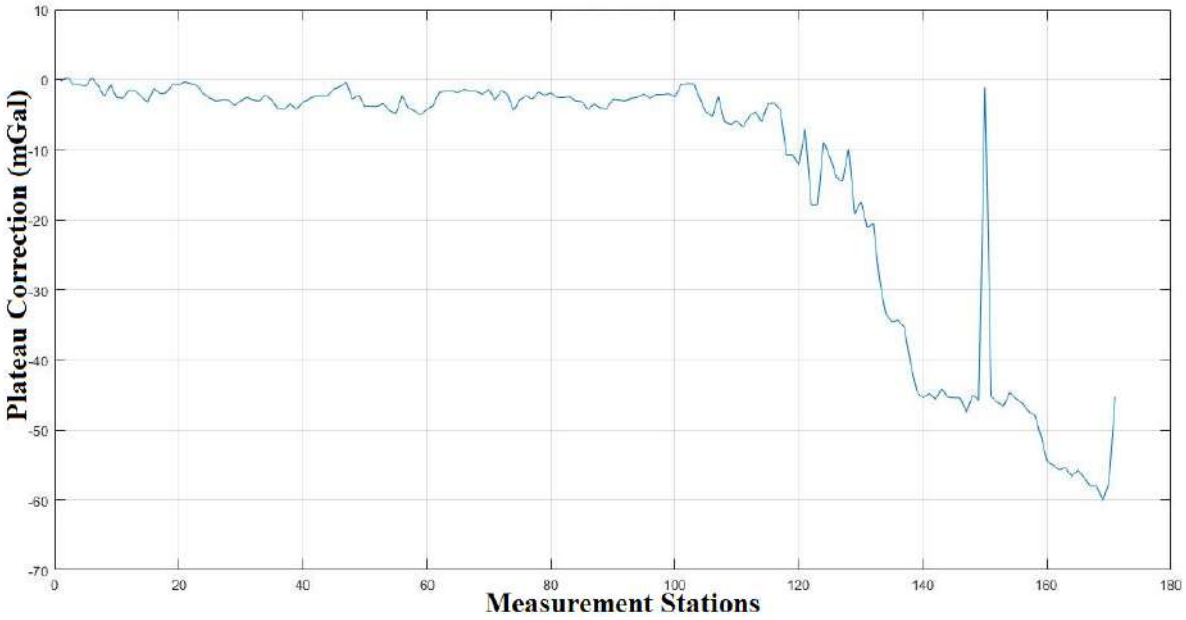

Figure 10: Terrain Correction's variation along the profiles

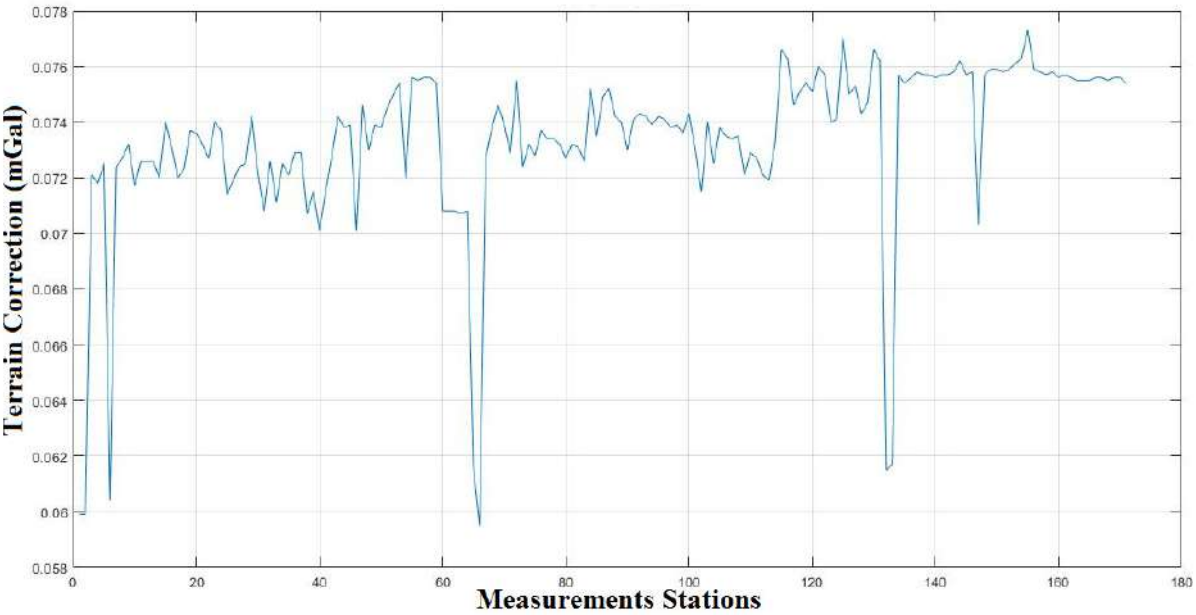

A general observation of the variations of various gravity data corrections along our study profiles (figures 8 to 12) suggests major changes in the second profile and minor variations in the first profile. It should be noted that the first profile crosses the Atlantic coast from Kribi to Campo via Lolabe. The measurements were taken a few meters away from the coast. The altitudes on this profile were very low. This can explain the low values of the free air correction observed along the profile. The second profile, oriented eastward, moved from Campo, which is closed to the Atlantic Ocean, to Ma'an thru Nyabessan which are many kilometers far away from the coast. The altitude variations are quite important in the zone, this can explain the reason for the high free-air correction values along this profile (figure 8). Observing figure 8(a) and (b) it can be seen clearly that the two curves, one

representing the free-air correction and the other representing the variation of the altitude, have the same pace, which is justified by the close relationship which exists between these two parameters..

The terrain correction takes into account the effects of topographic elevations and deficits of masses, this correction's values are insignificant (ranging from 0.06 to 0.078 mGal, Figure 10), compared to the value of g (ranging from about $9.7788x10^5$ to about $9.7804x10^5$ mGal, Figure 7) in the study area. This can explained by the fact, a greater part of our study zone being on a coastal area, topographic elevation and deficits can be under looked on a broader scale. This correction is usually important when the study area is of regional scale with major topographic variations.

The bouguer slab is obviously thicker under the second profile than under the first given that we are at seashore and the datum plane is shorter. This can be observed on the plateau correction representation (figure 9)

Figure 11: Latitude correction's variation along the profiles

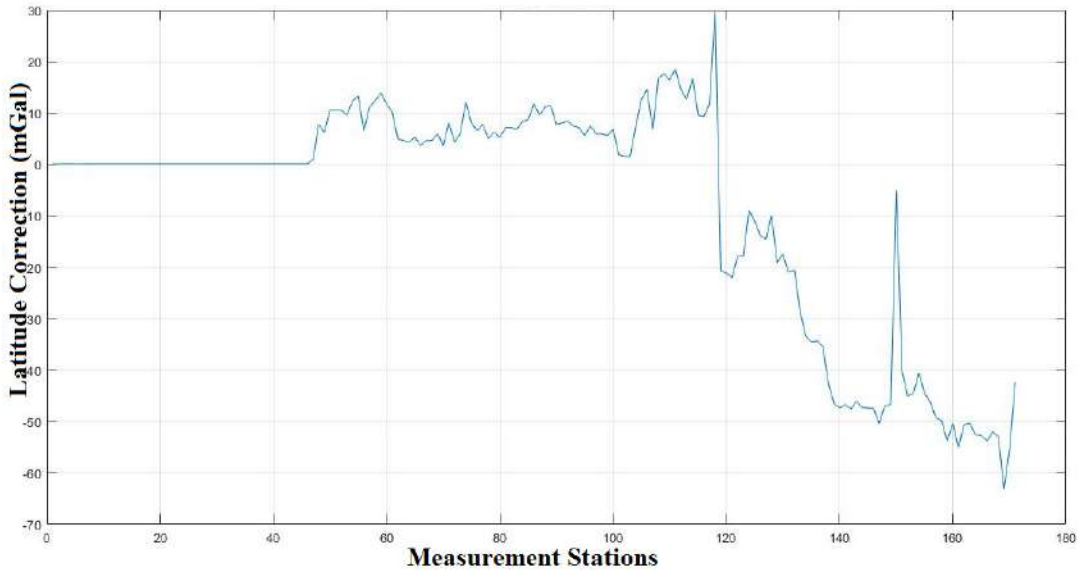

Figure 12: Lunisolar Correction's variation along the profiles

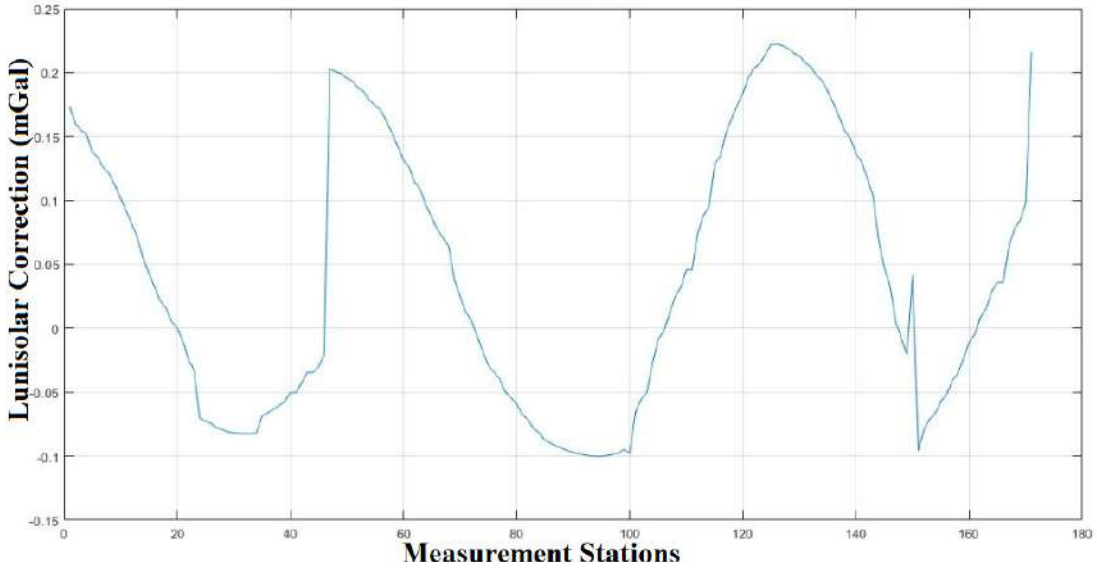

The variation of latitude caused by the rotation of earth, which is considered in calculating the latitude correction is almost constant along the first profile given that, the measurement points in this profile are located on the same parallel. This justifies small range of variation of the latitude correction along this profile. On the second profile, their values decrease importantly as we move away from the Greenwich meridian (figure 11). However, these changes are considered very small compared to the measured values of g in the area. Their impact therefore small.

The variation of the Lunisolar correction along the studied profiles is the most regular, the sinusoidal shape of the representing curves (figure 12) is an indication of the regular fluctuations of the values in time and space eventually. As established by **Darius Popovas in 2011**, this correction can depend of many factors, namely the daily change of Lunisolar correction at different Moon phase, the Correction dependency on azimuth change at different time moments, the rate of change of Lunisolar correction in prime vertical and meridian.

4. Graphical Representation of Reduction Effects

In this section, we compared the observed gravity data curves with the corrected gravity data curves in order to decipher the magnitude of changes and their location, therefore better understand the impact of this correction on the raw data.

Figure 13: The effect of free-air correction on raw data

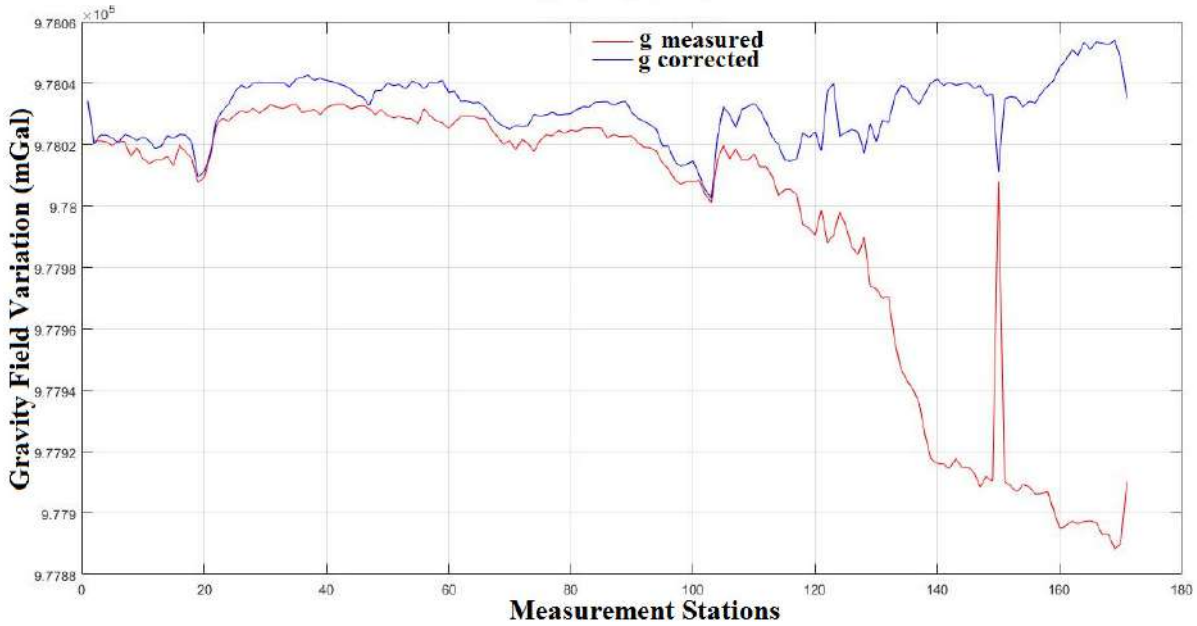

In figure 13, we superposed the curves showing the measured value of g along the profiles and the same values after the application of the free-air correction. We can observe that, in the first hundred stations (first profile), the two curves are closed one to the other with a similar evolution, this is a confirmation of the low elevation values in this profile. The proximity of the measurement stations to the sea implied the proximity of the station altitudes to the sea level. As we peruse along the second profile, the gap between the two curves increases. This is a confirmation of the increasing values of the altitude as we move from the coast to the continent (along the second profile). At station 150, there is a considerable tightness between the two values. This change is observed at a major depression in the study area around the Lokoundje River.

Figure 14: The effect of of Plateau Correction on raw data

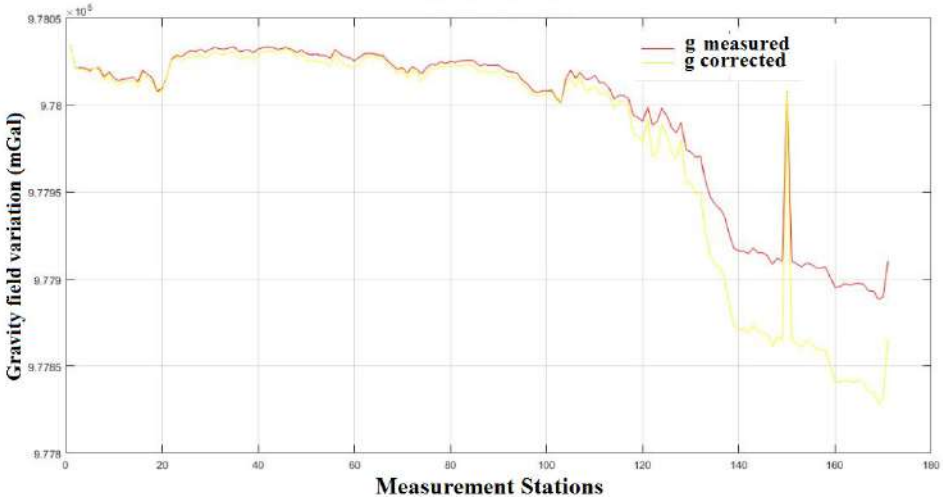

Figure 15: The effect of Latitude Correction on raw data

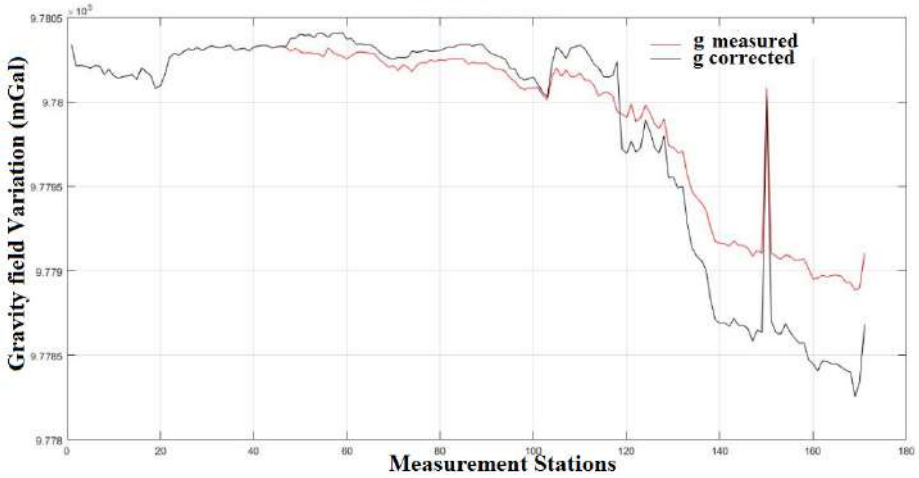

Figure 16: the effect of Terrain Correction on raw data

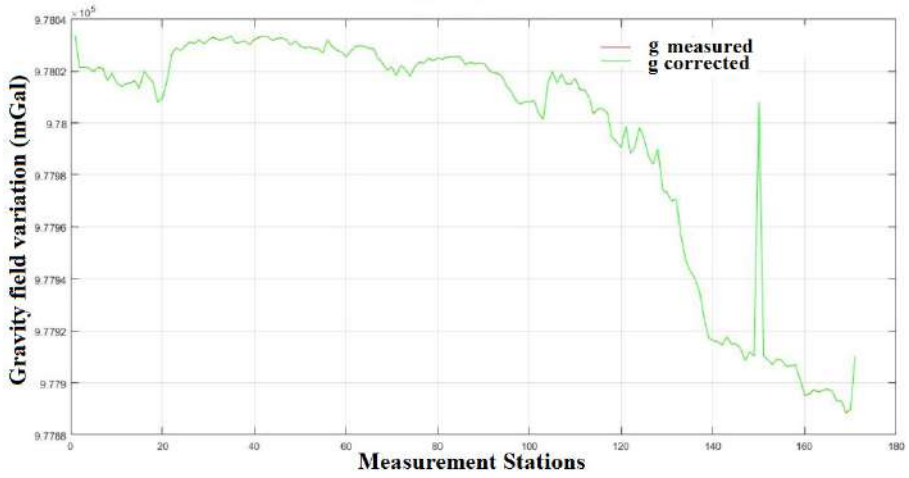

Figure 17: The effect of Lunisolar Correction on raw data

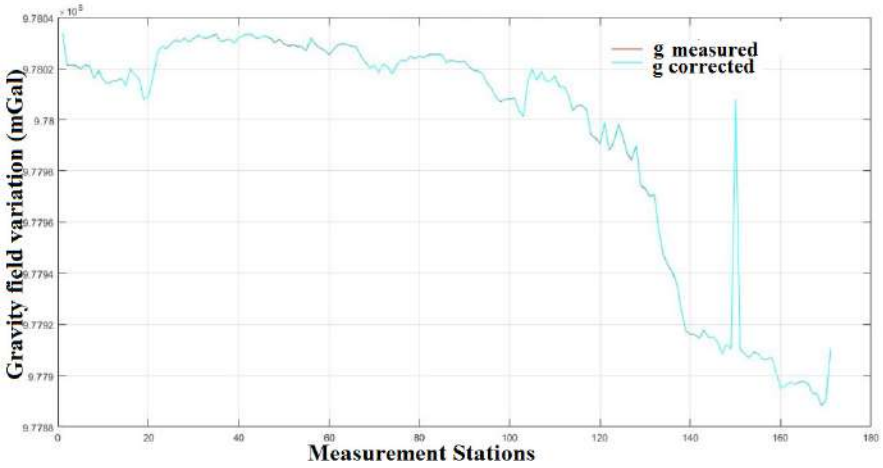

Figure 18: Comparison of all effects

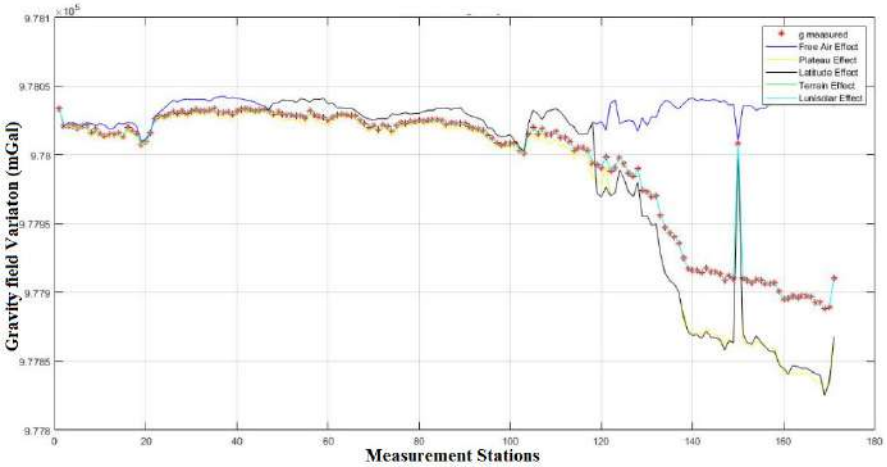

On the figures 13 to 17, we present the effects of the five gravity corrections applied on the raw data.

The effect of the plateau and latitude corrections on the raw data (figure 14 and 15 respectively) are quite similar as their curves have similar paces. They are less pronounced in the first profile and get increased we progress along the second profile. The effect of the terrain correction and the Lunisolar correction on raw data (figures 16 and 17 respectively) are equally very similar as their curves have similar paces. The terrain correction seems to have no effect on the observed data given that the red curve representing the measured values of g and the blue curves representing the corrected values of g, are almost perfectly superposed. This is the result of the smallness of the correction values compared to the observed values. The Lunisolar correction effect figure on the other and exposes slide differences between the two curves as we can observe parts of the red curve in some stations along the profile

Figure 18 is a recapitulation of the former figures and outlines the corrections that have the most impact on raw data and their location along the profiles. It can be observed that, for the first hundred points (first profile), most of the corrections, especially terrain correction, latitude correction and Lunisolar correction have little impact on gravity data while on the second profile, the impact are more obvious and consistent.

5. Implications and Discussions

The free-air correction calculated in this study appears to be the one with the most impact on measured gravity data. Their values vary less along the first profile where the altitudes are low, while along the second profile located in the continent with multiple altitude variation, we observe more important values.

The plateau correction and the latitude correction have approximate variations. Given that the bouguer slab is a function of the masses located between the base datum and the reference, these masses are thinner at the coast and thicker in the continent. In the Kribi locality, the plateau correction was subject to major change in value. This station appears to be at the earthquake epicenter observed in 2002 in this region **(Tokam et al. 2011).** The importance of the latitude correction is a function of the distance between the given station and the origin meridian. For the first profile, this distance is quasi-constant because it this parallel meridian. The distance increase slightly for the stations in the second profile. This is the reason for the more pronounced differences between observed and corrected data in this profile.

If there is a correction to be neglected in the reduction of gravity data in this region, it should be the terrain correction because value are too inferior to the observed ones. However, this correction is important as it adds accuracy to the studied data. The values of the terrain correction equally indicate that there is a good isostatic compensation of masses in the subsurface **(Telford, 1976)**

One of the most important correction to be considered in this study is the Lunisolar correction because the increasing accuracy of the measurements requires more precise evaluation of the Lunisolar correction. Therefore the more detailed analysis of algorithms is required. Mostly the Lunisolar correction is calculated assuming that levelling proceeds at constant speed and in the same azimuth between benchmarks **(Jensen, 1949 and Agnew, 2007).** This correction is almost always important regardless of time and space.

6. Conclusion

In as much as the corrections applied on raw gravity data help to eliminate the non-geological sources of anomalies affecting the measured data, they equally reveal information related to the repartition of masses in the subsurface, areas with the highest gravity noise and how this noise is related to the geographical, geological and geophysical configuration of a study area **(Telford, 1976).**

The well-known relationship between the altitude and the free-air correction was emphasized in this study. A perfect superposition signifies that the correction is negligible. The more gap between the curves, the more important the correction.

The second profile of data in our study area has revealed the presence of more non geological sources than the first, indicating a considerable gravity noise.

References

[1] Agnew, D. C. (2007). Earth tides *Treatise on Geophysics* 3(06): pp. 163–195

[2] Alice, S. Murray, Ray M. Tracey (2001). Best Practice in Gravity Surveying. Geoscience Australia.

[3] Bernard, G. and Chouteau M., (2008). Lecture notes on applied geophysics, University of Montreal

[4] ***Chapin,*** D. A. (***1996***). ”The theory of the Bouguer gravity anomaly: A tutorial.” The Leading Edge, 15(5), pp. 361-363. https://doi.org/10.1190/1.1437341

[5] Darius Popovas, (2011), Estimation of lunisolar correction in precise levelling: The 8th International Conference May 19–20, 2011, Vilnius, Lithuania

[6] Jensen, H. (1949). Formulas for the astronomical correction to the precise levelling. *Danish Geodetic Institute. Publication 23: pp. 22-27*

[7] Mathews, P. M.; Dehant, V.; Gipson, J. M. (1997). Tidal station dispalcements, *Journal of Geophysical Research* 102(20): pp. 469–477.

[8] Petroškevičius, P. Popovas, D. (2008). Dangaus kūnų poveikiosunkio laukui įvertinimas, *Geodesy and Cartography* [*Geodezija ir kartografija*] 34(1): pp. 19–22.

[9] Telford, W.M., Geldart, L.P. and Keys, D.A. (1976) Applied Geophysics. Cambridge University Press, Cambridge, 860 p.

[10] Tokam, K. A. P., Tabod, C. T., Nyblade, A. A., Julia, J., Wiens, D. A. and Pasyanos, M. (2010). Structure of the crust beneath Cameroon, West Africa, from the join inversion of Rayleigh wave group velocities and receiver functions *Geophys. J. Int.* **183:** pp. 1061–76

[11] Varga, P. (1989). Love numbers and the inner structure of the Earth, in 6th Inter Symposium Geodesy and Physics of the Earth, Proc Part 1. Veröff ZIPE, 102: pp. 376–396.

International Journal of Geosciences, 2017, 8, 984-1003
http://www.scirp.org/journal/ijg
ISSN Online: 2156-8367
ISSN Print: 2156-8359

3D Modelling from New and Existing Gravity Data of an Intrusive Body in the Northern Part of Kribi-Campo Sub-Basin in Cameroon

Kue Petou Rokis Malquaire[1,2*], Owona Angue Marie Louise[3,4*], Njingti Nfor[2,3], Manguelle-Dicoum Eliezer[4]

[1]National Institute of Cartography, Yaoundé, Cameroon
[2]Postgraduate School of Sciences, Technologies & Geosciences, University of Yaoundé I, Yaoundé, Cameroon
[3]Department of Physics, Advanced Teacher Training College, University of Yaoundé I, Yaoundé, Cameroon
[4]Department of Physics, Faculty of Science, University of Yaoundé I, Yaoundé, Cameroon
Email: *rokis.petou@yahoo.fr, *mlasseowona@yahoo.fr

How to cite this paper: Malquaire, K.P.R., Louise, O.A.M., Nfor, N. and Eliezer, M.-D. (2017) 3D Modelling from New and Existing Gravity Data of an Intrusive Body in the Northern Part of Kribi-Campo Sub-Basin in Cameroon. *International Journal of Geosciences*, **8**, 984-1003.
https://doi.org/10.4236/ijg.2017.88056

Received: June 23, 2017
Accepted: August 19, 2017
Published: August 22, 2017

Abstract

A new gravity survey was carried out in the northern part of the onshore Kribi-Campo sub-basin in Cameroon. The data were incorporated to the existing ones and then analyzed and modeled in order to elucidate the subsurface structure of the area. The area is characterized in its north-western part by considerably high positive anomalies indicative of the presence of a dense intrusive body. We find, 1) from the analysis of the gravity residual anomaly map, the high positive anomalies observed are the signature of a shallow dense structure; 2) from the multi-scale analysis of the maxima of the horizontal gradient, the structure is confined between depths of 0.5 km and 5 km; 3) from the quantitative interpretation of residual anomalies by spectral analysis, the depth to the upper surface of the intrusive body is not uniform, the average depth of the bottom is h_1 = 3.6 km and the depths to particular sections of the roof of the intrusion are h_2 = 1.6 km and h_3 = 0.5 km; 4) and the 3D modeling gives results that are suggestive of the presence of contacts between rocks of different densities at different depths and a dense intrusive igneous body in the upper crust of the Kribi zone. From the 3D model the dense intrusive igneous block is surrounded by sedimentary formations to the south-west and metamorphic formations to the north-east. Both formations have a density of about 2.74 g/cm^3. The near surface portions of this igneous block lie at a depth range of 0.5 km to 1.5 km while its lower surface has a depth range of 3.6 km to 5.2 km. The shape of the edges and the bottom of the intrusive body are suggestive of the fact that it forms part of a broader structure underlying the Kribi-Campo sub-basin with a great influence on the sedimentary cover.

Keywords

Kribi-Campo Sub-Basin, Gravity Data, 3D Modelling, Spectral Analysis, Residual Anomaly

1. Introduction

According to [1], the Aptian salt basin of Equatorial West Africa is a combination of seven basins among which are the Rio del Rey and the Douala/Kribi-Campo basins. The Doula/Kribi-Campo basin has two sub-basins: the Douala sub-basin to the North and the Kribi-Campo sub-basin to the South. The Kribi-Campo sub-basin is located between 2˚20'N and 3˚20'N, and extends over 6150 km^2 offshore and 45 km^2 in a triangular onshore area [2]. It is limited to the South by the Campo high, to the east by the Precambrian basement, and to the North by a possible Aptian salt and/or the northern end of the Kribi Fracture Zone noted Kribi FZ (**Figure 1**). The western limit of the sub-basin seems to be broadly defined by the Kribi Fracture Zone [2]. The area of study is part of the Precambrian of central and southern Cameroon which shows many geological features of different ages and varying petrographic characteristics [3]. The green rock belts (GRB) and gneiss are part of a geological unit called "Nyong Unit"

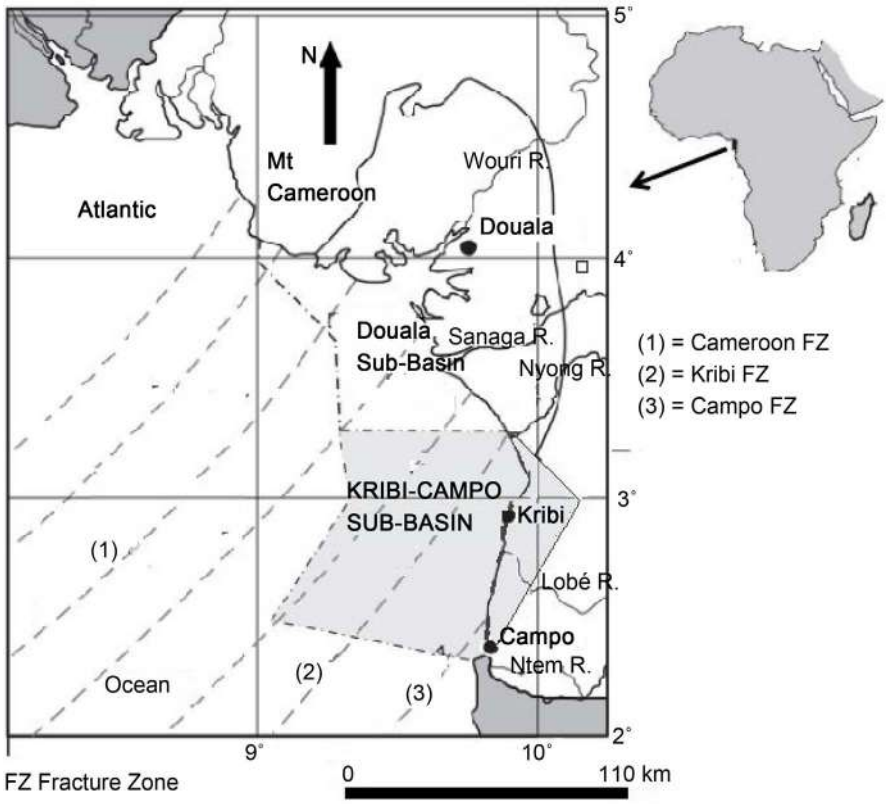

Figure 1. Location of the Kribi-Campo sub-basin in Cameroon (West Africa) between the main fractures of the Cameroon margin (modified after [2]).

which covers a greater part of the study area. The other part of the area is covered by sediments; Metagranodiorite, and Metamorphic rocks of the Yaounde Group, which are part of the Ntem Unit. Until now, oil and gas production and exploration are focused on the offshore portion of the sub-basin. But recent studies are suggesting the possibility of the presence of oil, gas and minerals in the onshore portion [4]. We focus this study on the Kribi-Campo sedimentary basin (especially on the onshore area) to bring more light on the understanding of the basement in that region, and therefore contribute to the identification of potential mining areas of the basin. Gravity investigations conducted by [3] [4] [5] [6], have indicated the presence of dense or basic intrusive bodies within the main formation broadly characterized by the high intensity gravity anomaly observed in the Kribi area. The objective of this study is to conduct a 3D modelling from a combination of new and existing gravity data of an intrusive body responsible for the high anomalies observed in the northern part of Kribi-Campo sub-basin in order to understand its structural layout. From the 3D gravity model derived, new insights of the Kribi-Campo region are provided, along with the structural characterization of this Kribi-Campo intrusive body and the inference of its geometry. The model obtained highlights the mechanism of deep tectonic activity at the transition zone in general and the Kribi-Campo basin in particular, which is related to the setting of the basin.

2. Geological and Tectonic Settings

2.1. Geological Settings

The Kribi-Campo sub-basin, is a sedimentary basin which lies both onshore and offshore on the cost of Cameroon between latitudes 2˚20'N - 3˚20'N and longitudes 9˚15'E - 10˚00'E covering a total surface area of about 6195 km^2 (**Figure 1**). The sub-surface of the Kribi-Campo sub-basin is mostly made up of Archean rocks of the Ntem complex recovered by the Paleoproterozoic rocks of the Nyong Unit [7].

The northern area of the basin is occupied by the Oubanguide Belt which consists of Precambrian rocks that were remobilized by the Panafrican episode (600 to 500 Ma). These rocks are mainly schists and gneisses that have been intruded by granites and diorites [8] [9].

The southern domain of the basin is occupied by the northern edge of the Congo craton, represented by the Ntem complex which consists predominantly of Precambrian rocks of granulite facies formed during the Archean and rejuvenated during the Eburnean orogeny. The Ntem Complex also carries imprints of past magmatic activities, which are characterized by several occurrences of dense rocks such as gabbros [9] [10].

The coastal area of the basin is composed of Cretaceous sediments, mostly sandstones and small amounts of limestone and shales [9]

2.2. Tectonic Settings

Many studies, [3] [5] [9] carried out in the transition zone between the Congo

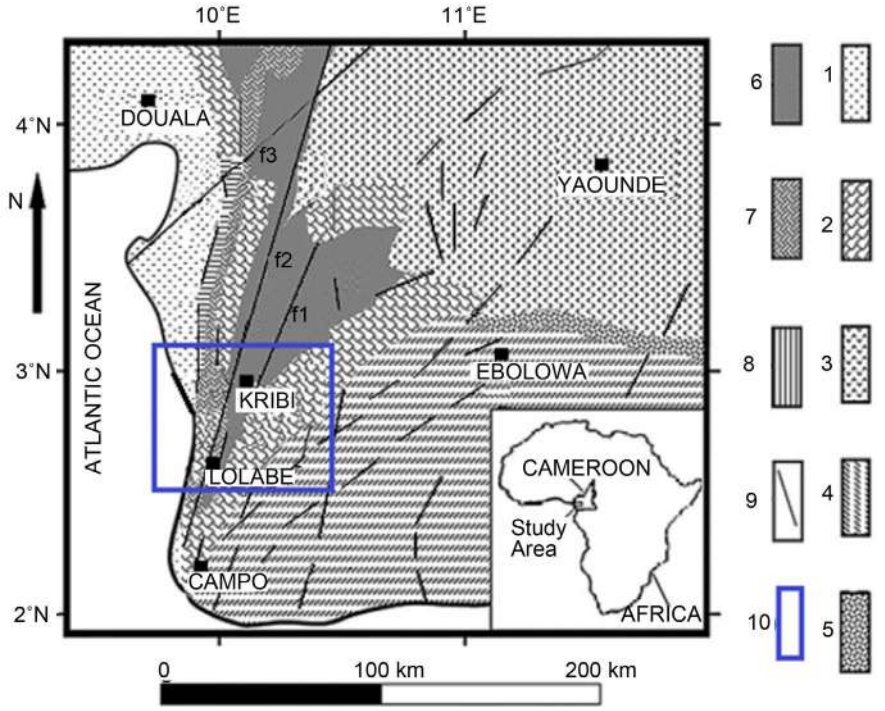

Figure 2. Location and simplified geological map of the region (modified after [18]). 1: sediments; 2: gneiss; 3: Yaounde Group; 4: Ntem Complex; 5: tonalites; 6: green rock belts; 7: metamorphic rocks of the Yaounde Group, 8: metagranodiorite; 9: faults; 10: study area (2, 6, 7 and 8 are geological formations included in a geological unit called "Nyong Unit").

craton and the Oubanguide belt have reported that the northern margin of the Congo Craton resulted from a convergent collision with the Panafrican Mobile Belt (PMB), which has been thrusted southwards onto the Craton. These same studies revealed that the area mainly underwent brittle deformations related to multistage compressional and extensional tectonics that give rise to major faults. These are mainly characterised by the Kribi-Campo Fault (KCF) system which is herein defined as a continuation of the Sanaga Fault [3] [4] [9] [11] [12]. Other studies [13] [14] supported by [15] also link the KCF to an offshore fault system known as the Kribi Fracture Zone inferred as the eastern end of the Ascension Fracture Zone settled during the Cretaceous break-up of Gondwana and the separation of Africa from South America. This gave rise to the development of the Kribi-Campo sub-basin. [16] showed, through joint inversion of Rayleigh waves over the entire Cameroon, that the thickness of the upper crust in the South of Cameroon varies in general between 10 and 20 km.

3. Material and Methods

3.1. Gravity Data

The gravity data used in this work are the combination of new and existing data. The existing data were collected during gravity surveys of central Africa by ORSTOM and referenced in [17]. These data were collected using Worden gra-

vimeters (N˚313 and 600) with a station-spacing of 4 to 5 km. This first dataset is made up of 186 gravity stations. Due to the high station-spacing and the absence of data in some areas, we conducted a gravity campaign in the Kribi-Campo-Ma'an area (this area had not been subject to any ground geophysical survey before this campaign) in March 2015, using a Lacoste & Romberg G-823 gravimeter.The difference of the gravity data distribution from the ORSTOM geophysical survey and our team is induced by the fact that, during the period when ORSTOM survey was carried out (1962) very few roads where available and some areas could not be accessible. Today, with the few progress in roads infrastructures, we have access to more sites even though the zone is located in the dense equatorial forest and the Campo National park where only open field roads are accessible. The survey data constitute 223 gravity data points with a station-spacing of 0.5 to 2 km. Free-air correction, luni-solar tidal correction, Terrain correction and instrumental drift correction were applied on these recent measurements and the Bouguer anomalies were derived.

Putting these new and existing data points together, gives a total of 409 gravity data points.

Free-air and Bouguer reductions based on a mean density of 2.67 g/cm^3 were applied on the data and the simple Bouguer anomalies derived. The resulting Bouguer anomalies as shown in Figure 3 constitute the dataset that is used in

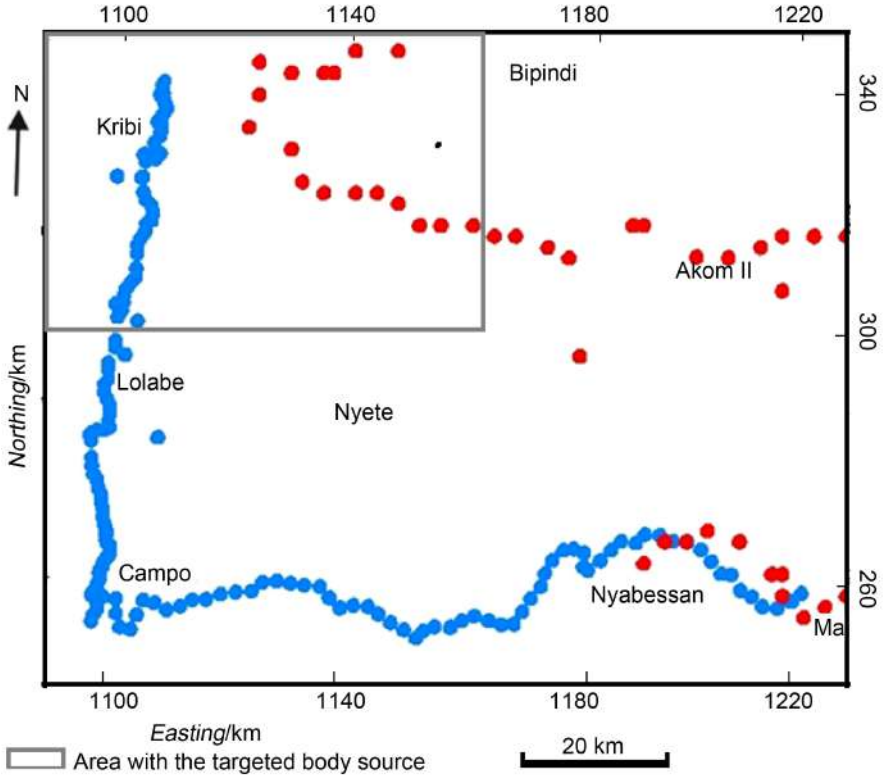

Figure 3. Gravity data distribution map showing the area where the targeted body is located. The red dots represent the data from the ORSTOM geophysical survey (1965) while the blue dots represents the recently collected data in the region by our team.

the context of the present study. The Kriging method was applied on the gravity data for interpolation using kriging gridding algorithm implemented in Oasis Montaj 8.0 software. The maximum value of the Bouguer anomaly in the grid is −68.7 mGal while the minimum value is −2.0 mGal. **Figure 3** shows the distribution of the data points, new and existing ones, in the study area.

3.2. Methodology

In order to delineate the structures of the subsurface in our study area, two main approaches have been used namely:

- the maxima of the horizontal gradient upward continued to locate the anomalous body in the subsurface,
- the spectral analysis to determine the average depth of this body source.

Results of these methods, coupled with previous findings in the area [6] [19] and available geological information confirmed the existence of an anomalous body in the area, to which 3D modelling has been applied.

3.2.1. The Horizontal Gradient and Upward Continuation

According to [20], coupling the horizontal gradient with upward continuation allows to locate the discontinuities and the determination of their dip.

The horizontal gradient is an operation that measures the rate of change of a potential field in the x and y directions [21] in order to image subsurface structures. However, the total horizontal gradient magnitude (HGM) is preferred for its simplicity. The HGM operator is defined by the relation below:

$$HGM(x,y) = \sqrt{\left(\frac{\partial G}{\partial x}\right)^2 + \left(\frac{\partial G}{\partial y}\right)^2} \quad (1)$$

where G is the Bouguer gravity field.

The works of [21] [22] showed that the maxima of the horizontal gradient of gravity anomalies help locate contacts associated with abrupt changes in density, which are interpreted either as faults, geological contacts or intrusions. Faults are expressed by a quasi-linear disposition of at least three maxima and horizontal limits of intrusive bodies are shown by quasi-circular disposition of many maxima. The multi-scale analysis of the horizontal gradient consists in creating a series of analytical upward continuations of gravity data. The horizontal gradient is then computed for every height and its maximum is determined. To determine the direction of dip of the contacts highlighted, it is assumed that the more the gravity data is upward continued, the more the deeper structures are emphasized [4]. In fact, when the contact presents a dip, the maxima of horizontal gradients are displaced progressively down the dip as the height of upward continuation is increased. But in the case of sub-vertical contacts, these maxima remain practically at the aplomb [19].

3.2.2. Spectral Analysis Method

This method is carried out through 2D Fast Fourier Transform which trans-

forms gravity data from the space domain to the wavenumber domain to estimate the depths of the structures responsible for the measured anomaly. It has been used extensively by many authors, namely [23] [24] [25].

The finite discrete Fourier transform is given by the equation:

$$B(\omega) = \sum_{0}^{N-1} b(x) \exp(-i\omega x) \cdot \Delta x \tag{2}$$

where $b(x)$ represents the discrete N data array of gravity data obtained by sampling a continuous profile at evenly spaced intervals Δx. i is the complex operator, $\omega = 2\pi k$ is the spatial frequency and $k = \lambda^{-1}$ is the wavenumber in the x direction.

The expression of the Bouguer Slab Effect is then given by the equation:

$$B(k)_{z=0} = 2\pi\Delta\rho G \cdot \exp(-2\pi kt) \cdot F(k)_{z=0} \tag{3}$$

where $B(k)_{z=0}$ is the Fourier transform of the Bouguer anomaly profile $b(x)_{z=0}$; $\Delta\rho$ is the density contrast between two layers; $F(k)$ is the Fourier transform of $f(x)$, the derivation of the interface from the mean depth z; G is the gravitational constant. The mean depth can then be calculated using the following equation:

$$h = \frac{\Delta \mathrm{Log} E}{4\pi\Delta k} \tag{4}$$

where E is the power spectrum of $B(k)$.

The square of the Fourier amplitude spectrum is plotted versus the radial frequency. The slope of the relationship between the wave number of the gravity field and the logarithmic power spectrum provide information about the depths of the source bodies.

4. Results

4.1. Analysis and Interpretation of Gravity Data

4.1.1. Analysis of Bouguer Anomaly Map

The Bouguer anomaly map presented in **Figure 4** was obtained after an interpolation using a kriging gridding algorithm implemented in Oasis Montaj software. The highlight shows the most prominent anomalies within the study area. An overview of the map reveals three gravity domains:

The first domain which covers the western part of the map is characterized by high values of gravity anomalies. The form of these anomalies suggests that it marks the limit of a large structure to the left of the study area. In the field, this area corresponds to low altitudes and its position near the Atlantic Ocean shows that this anomaly has it source from highly dense rocks. This domain, with anomaly values ranging between −40.1 mGal and −2.0 mGal presents four prominent peaks, one at the Lolabe locality, another one in Kribi and the last two to the east of Kribi. All these peaks can be interpreted as high density or basic intrusive bodies within the main formation. The two peaks observable to the east of Kribi may be considered as a unique, very high-value anomaly, which according to [6] corresponds to a ring complex affected by a nearly N-S trending

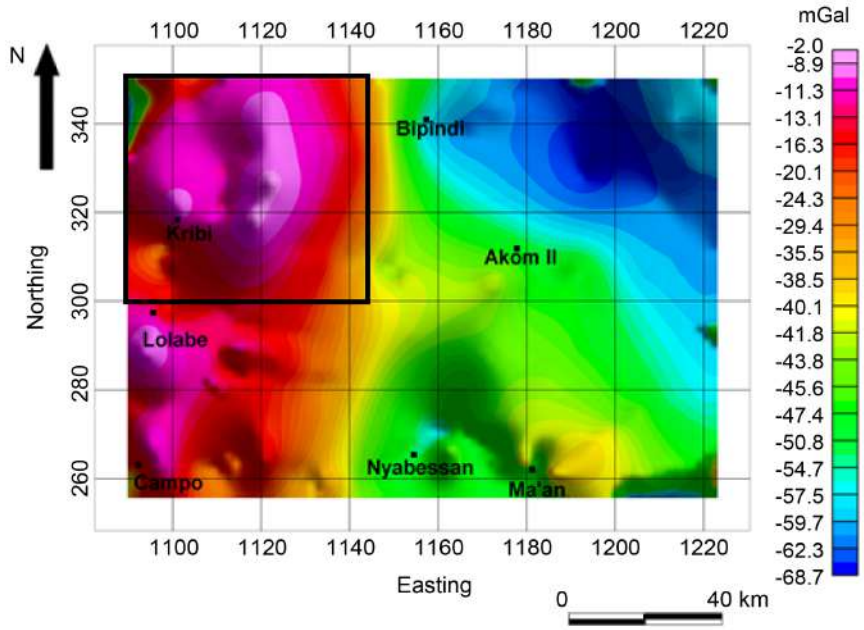

Figure 4. Bouguer anomaly map of the region showing the Kribi anomaly.

discontinuity.

The second domain, located at the northeastern side of the map displays two apparent ring shapes, characterized by very low amplitude anomalies trending NW-SE from Bipindi to the eastern part of Akom II, these anomaly values range from −68.7 to −54.7 mGal. There are interpreted as due to the presence of intrusive low density bodies in the subsurface.

The third domain which is situated in the middle of the map, from Bipindi to Nyabessan, consists of average anomaly values ranging from −50.9 mGal to −40.9 mGal and is separated from the two other domains by high gradients marking discontinuities between two structures in the subsurface. The correlation with surface geology shows that this area is the signature of charnockites and green rock belts of the Ntem Unit.

4.1.2. Analysis of Residual Anomaly Map

The Bouguer anomalies are the combination of deep and shallow sources, a separation of these anomalies into regional (deep sources) and residual (shallow sources) components was carried out in order to clearly identify the anomaly sources. This separation was performed using the polynomial fitting method. The procedure computes the mathematical surface, which gives the best fit to the gravity field within specific limits [26]. This surface is considered to be the regional gravity anomaly. The residual is obtained by subtracting the regional field from Bouguer anomaly. The residual map of the study area presents characteristics similar to the Bouguer anomaly map. However, the high gravity ascribed to dense or basic intrusive bodies within the main formation and the low gravity ascribed to low densities intrusion are visibly more distinct on this residual gravity map. On the third order residual map shown in **Figure 5**, the three anomalous

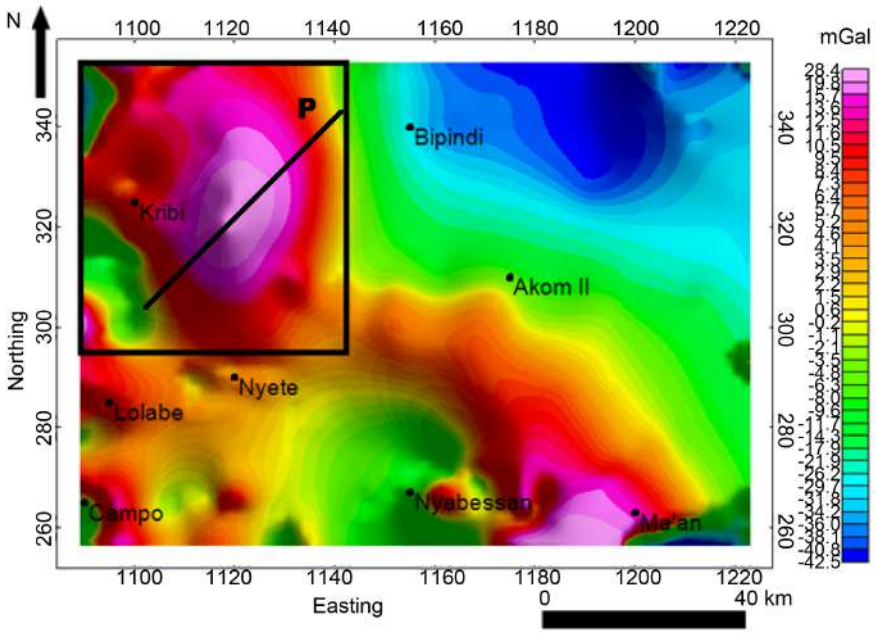

Figure 5. Third order residual anomaly map of the region showing the Kribi anomaly.

peaks observed around the Kribi area are seen to have merged to form a single oval peak indicating the prominence of the dense intrusive body at depth. At depth the characteristics of the structure surrounding this intrusive body extend southeastwards from Kribi to Akom II and become more pronounced again between Nyabessan and Ma'an. Since the effects of the mantle and lower crust are not of interest in this work, a third order residual anomaly is used for modelling in order to have a better chance of locating the depth to bottom of the dense intrusive body.

In order to determine the nature and shape of the Kribi intrusive body, the residual field obtained here will be studied using three methods namely: the multi-scale analysis of gradients method, which is usually employed for the analysis of the multi-scale residual anomalies; the spectral analysis method and the 3D modelling.

4.2. The Local Maxima Map of the Horizontal Gradient of the Residual Anomaly

After computing the horizontal gradient of the third order residual anomaly, the resulting map is upward continued at 0 km, 1 km, 2 km, 3 km, 4 km and 10 km. The local maxima are then calculated and superimposed. The choice of the high of the upward continuation is determined by the types and depth of the structures that we intend to highlight. Given that, the higher we upward continue, the deeper the structures are highlighted. In our study, we intend to model a shallow formation. The maxima of the gradient of the residual anomaly upward continued could be observed on the map until the depth of 10 km. after 10 km, no effect of the anomaly featured on the map. That is why we choosed to stop at 10

km. The Maxima of the horizontal gradient of the third order residual anomaly map upward continued to 0 km, 1 km, 2 km, 3 km, 4 km and 10 km as presented in Figure 6 shows lines and quasi-circular contacts corresponding to horizontal limit of lineaments and intrusive bodies respectively. The depth of a lineament or an intrusive body is determined by the continued presence of the local maxima for increasingly high altitudes of upward continuation. This study will be focused on the continued presence of a quasi-circular contact noted (B1) in the Kribi area in the analyzed maxima of the horizontal gradient of the residual anomaly map upward continued to 0 km, 1 km, 2 km, 3 km, 4 km and 10 km.

The vertical limits of such an intrusive body can be predicted by the method developed by [19], in which the depth of the top of the anomaly sources obtained after an upward continuation at the height h is greater than or equal to h/2, because the upward continuation at the height h eliminates the effect of the sources situated above the depth h/2. This implies in Figure 6 that the effects of the sources situated above the depth 0.5 km, 1 km, 1.5 km, 2 km and 5 km have been eliminated for the upward continuation to 1 km, 2 km, 3 km, 3 km, 4 km, and 10 km respectively. The presence of green, red, yellow, blue and black contact on the western side of the intrusive body B1 indicates that the depth to bottom is between 2 and 5 km. Also, the presence of green, red and yellow with the absence of black maxima on the eastern side of the contact indicates the depth to bottom here is between 1.5 and 2 km. The results obtained from the analysis of the maxima map will be used to constrain the modelling of B1.

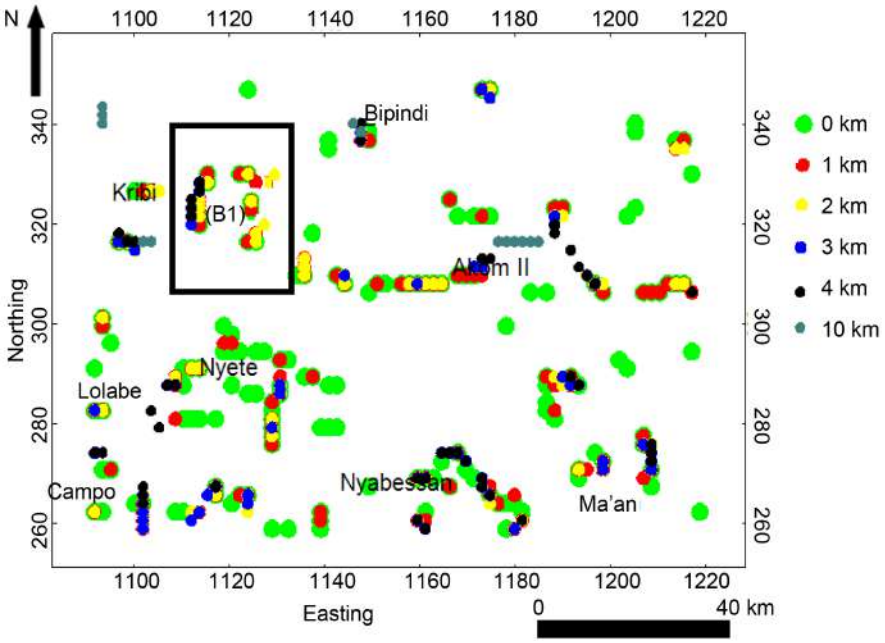

Figure 6. Superposition of the maxima of the gradients computed at various heights of upward continuation. Maxima are represented by small colored circles. The green, red, yellow, black and gray colors represent the maxima of the gradients upward continued at the heights of 0 km, 1 km, 2 km, 3 km 4 km and 10 km respectively. The located anomalous body source in the black frame.

4.3. Source Depth Estimation Using Spectral Analysis

A profile (P) was chosen and drawn on the third order residual gravity map. The data used to carry out the spectral analysis were from this profile shown by the black line crossing the main positive anomaly (Figure 5)

This profile was drawn with a NE-SW orientation and traversing through the suspected area of the intrusion.

Figure 7 shows the representation of the logarithm of the gravity power spectrum (energy E) with respect to wave number (spatial frequency) for the profile P. The curve obtained from this representation, made up of 9 points is observed to have three (3) slopes represented by the 3 colored lines fitted into the figure, each of which is obtained from 3 points. The depths obtained from the slope of the curve represent the average depths of the top of the anomalous source. This spectral graph presents three gradients that are used in determining the average depths h1 = 3.6 km, h2 = 1.6 km and h3 = 0.5 km of interfaces of low, average and high spatial frequencies respectively. The resulted values observed on the graph suggest that the depth to the upper surface of the intrusive body B1 is not uniform. It is believed that h1 presents the average depth of the bottom of B1, while h2 and h3 are depths to particular sections of the roof of the intrusion. These values obtained using spectral analysis will serve as constraints for the modelling of the body.

4.4. Direct Modelling

3D modelling was carried out using GRAV3D software on the residual field with the aim of delineating and caracterizing the dense intrusive body responsible for the observed gravity anomalies in the study area. The GRAV3D library consists of three major programs and one utility. The facilities include: GM-DATA-

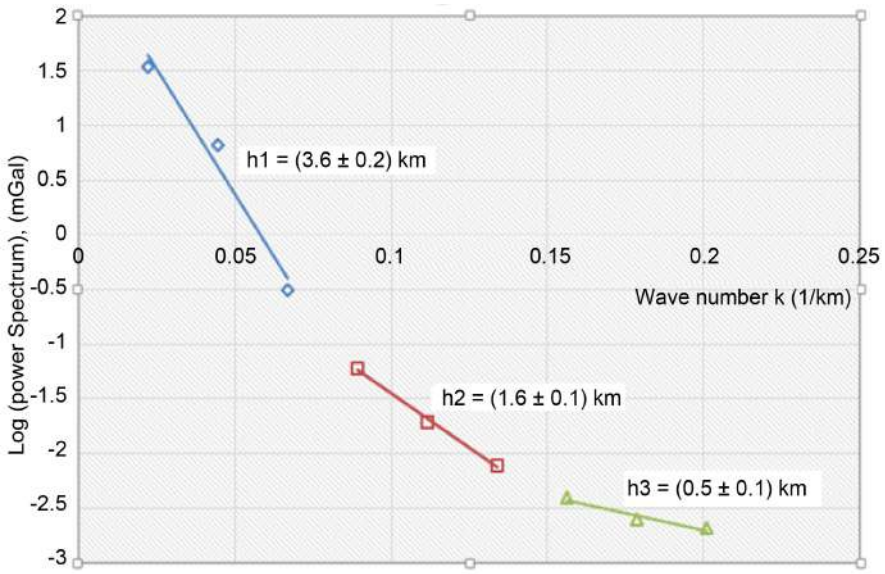

Figure 7. Logarithm of gravity power spectrum of profile *P* of the third order residual anomalies plotted versus the wave number *k*.

VIEWER: this utility was used for viewing the observed gravity data, error distributions, and for comparing observed to predicted data directly or as difference maps; MESHTOOLS3d: this utility was used for displaying resulting 3D models as volume renderings.

The modelling process of the intrusive body consist of constructing the body block by block in a predefined mesh. Every block is a combination of cubeoids of the same volume. Every block, with a constant density is defined along a vertical axis and along a horizontal axis. The coordinates of the blocks have been given taking as origin the point O (1095, 300, 0) bring latitude, longitude and altitude respectively all in kilometers. The body was constructed taking into account all the results provided by the multi-scale analysis of the maxima of gradients and spectral analysis.

After constructing the body, we used the GRAV3D program to calculate the gravity signature of the body, this signature is presented in the form of a map. This map is then compared with the map obtained from the observed gravity data. The best model is the one for which the two maps can approximately be superposed.

Figure 8 presents the map for the observed gravity data, obtained by plotting 254 data points from the study area using the GM-DATA-VIEWER utility of the GRAV3D software. The experimental residual anomaly map from 244 data points computed by the software is presented in Figure 9. It is observed that the two maps can approximately be superposed.

The intrusive body was depicted to be located between the depths of 0.5 km and 2 km from the surface on its Eastern side and between 0.5 km and 5 km on its Western side. The result provided by the spectral analysis, giving the depth to

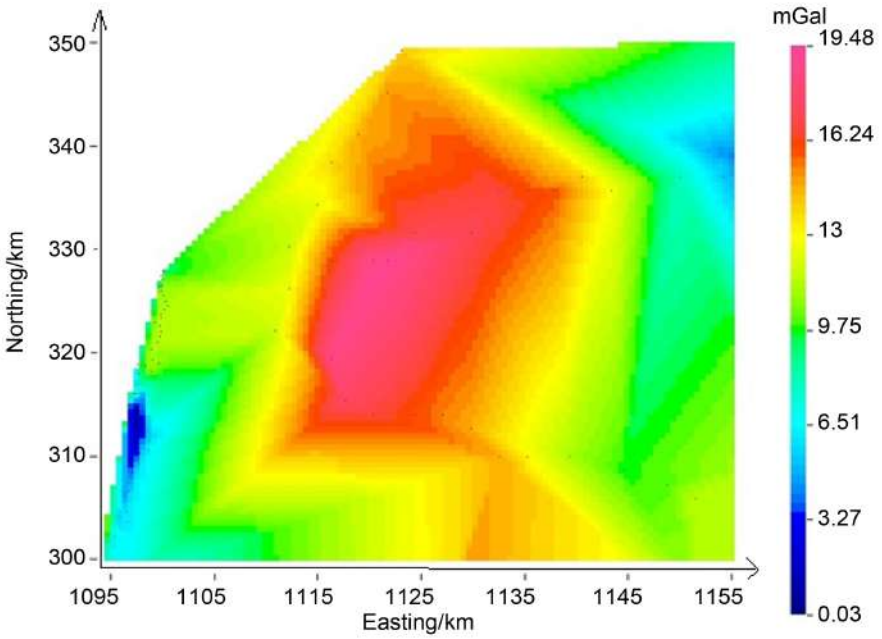

Figure 8. Observed residual anomaly map from 254 data points.

the top of the Kribi intrusive body was also considered.

The various views of the 3D model of the Kribi intrusive body are presented in Figures 10-15. These models consist of a major block having a density of 2.74

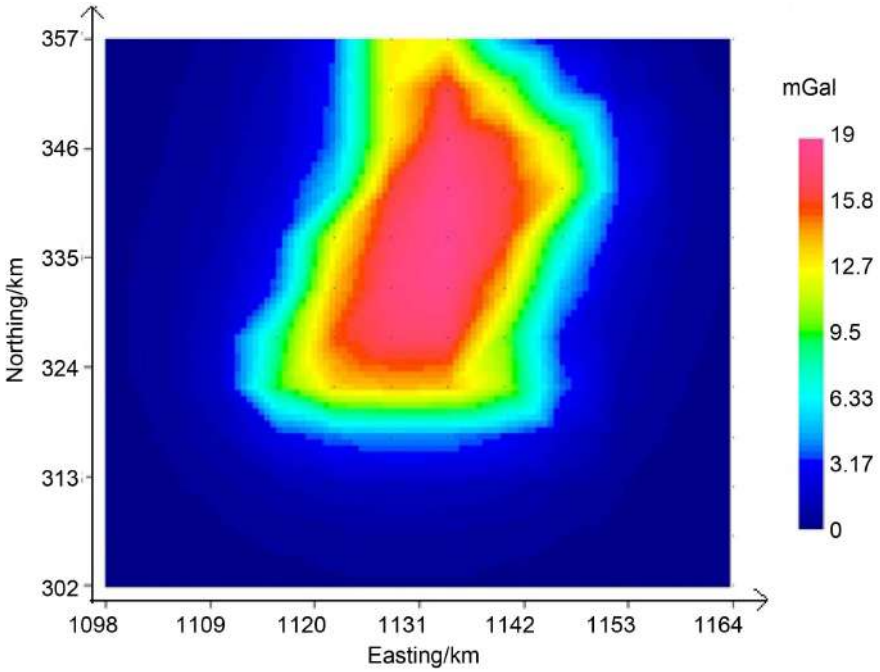

Figure 9. Experimental residual anomaly map from 244 data points.

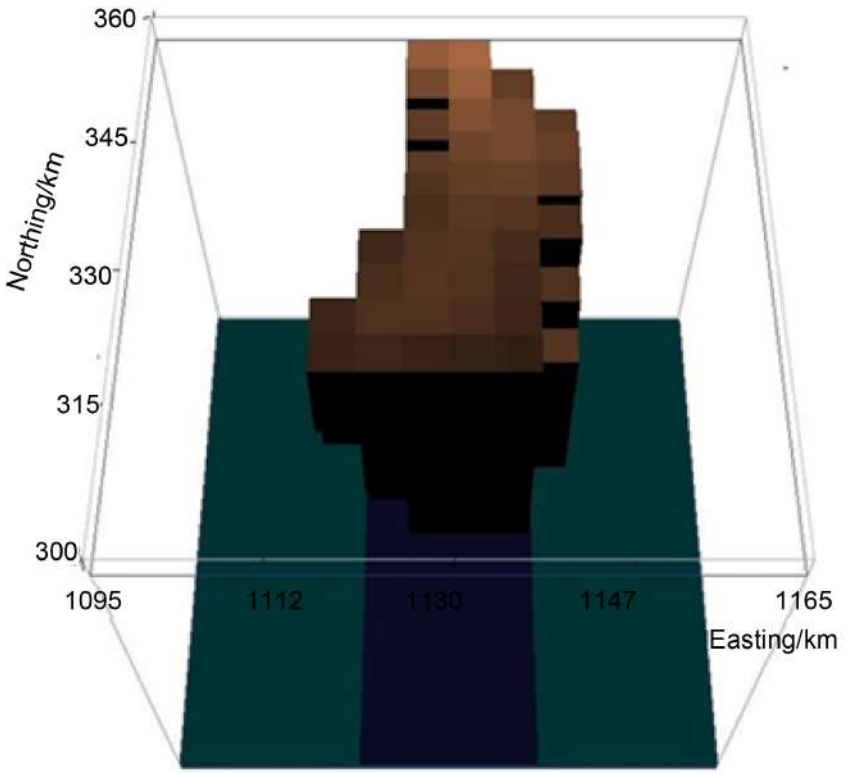

Figure 10. 3D model of the Kribi dense intrusive body as viewed from above.

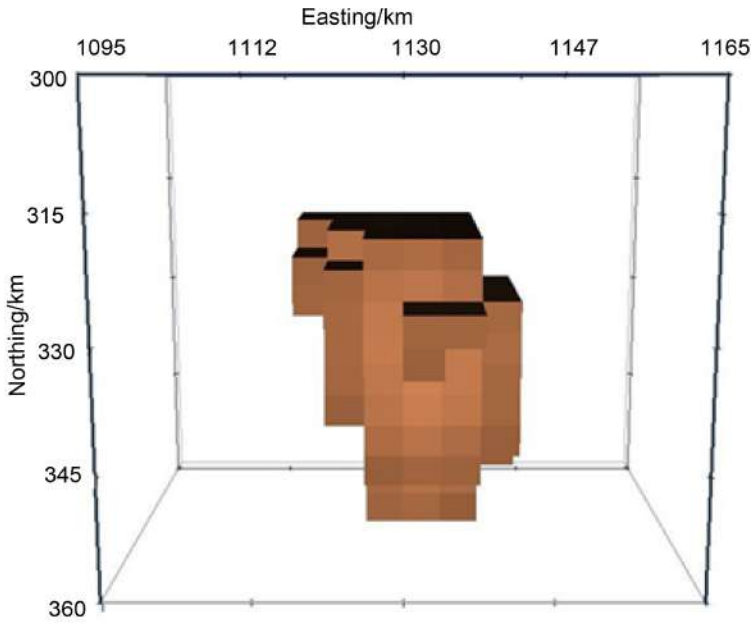

Figure 11. 3D model of the Kribi dense intrusive body as viewed from below.

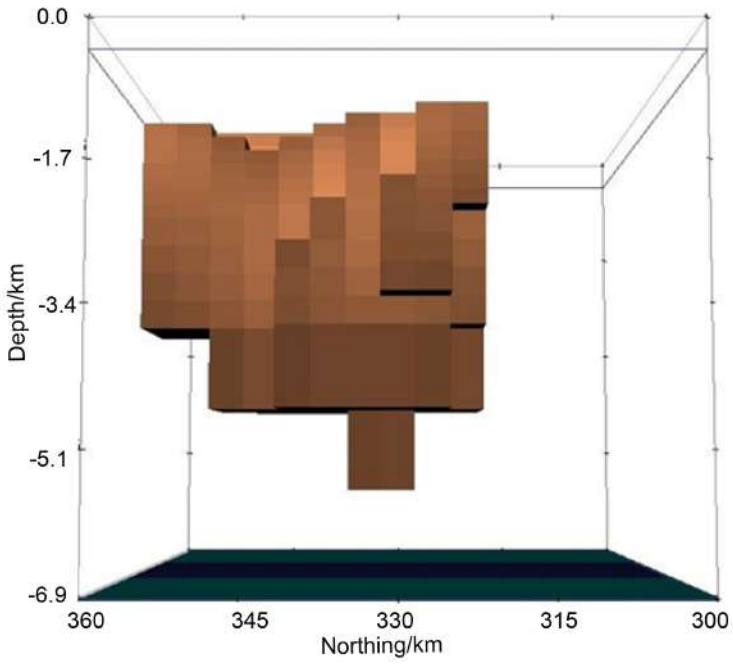

Figure 12. 3D model of the Kribi dense intrusive body as viewed from the West.

g/cm^3, a depth from the ground surface varying between 0.5 km and 1.5 km. The latitudinal and longitudinal extensions of the body are about 12 km and 30 km respectively. **Figure 12**, **Figure 14** and **Figure 15** show that the general base of the body is situated at the depth of 4.8 km from its surface and its middle part extends to about 5.2 km. The upper surface of this modelled body has a trapezoid shape while its other facades are more or less defined.

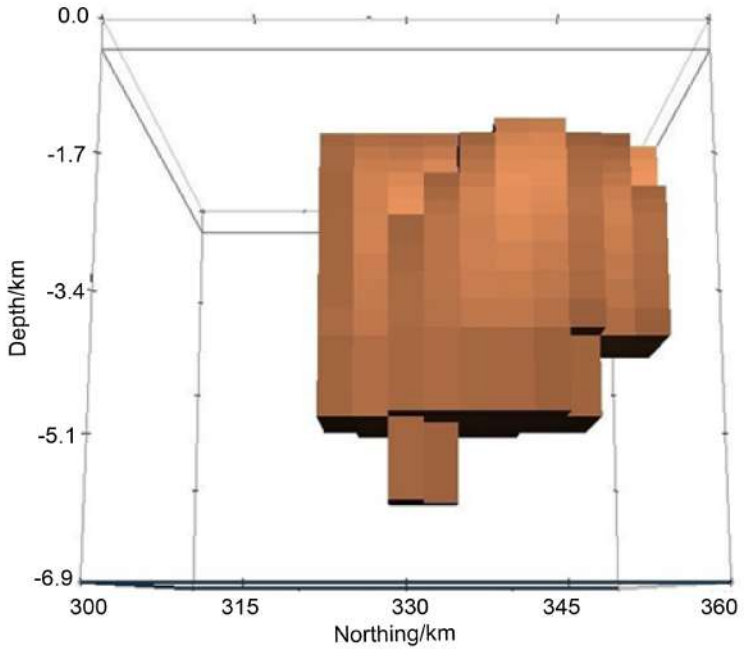

Figure 13. 3D model of the Kribi dense intrusive body as viewed from the East.

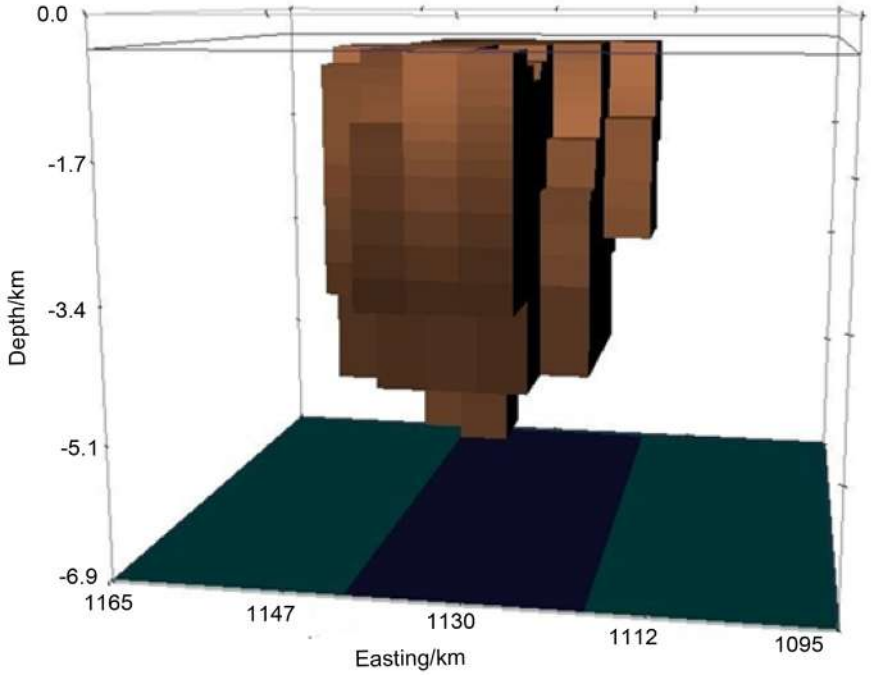

Figure 14. 3D model of the Kribi dense intrusive body as viewed from the North.

5. Discussion

The forward modelling of gravity data can have many models developed from an anomaly. In order to obtain a model that best reflects the subsurface structure, one has to consider certain parameters that would limit this uncertainty. As part of the constraints, the multi-scale analysis of the maxima of the horizontal

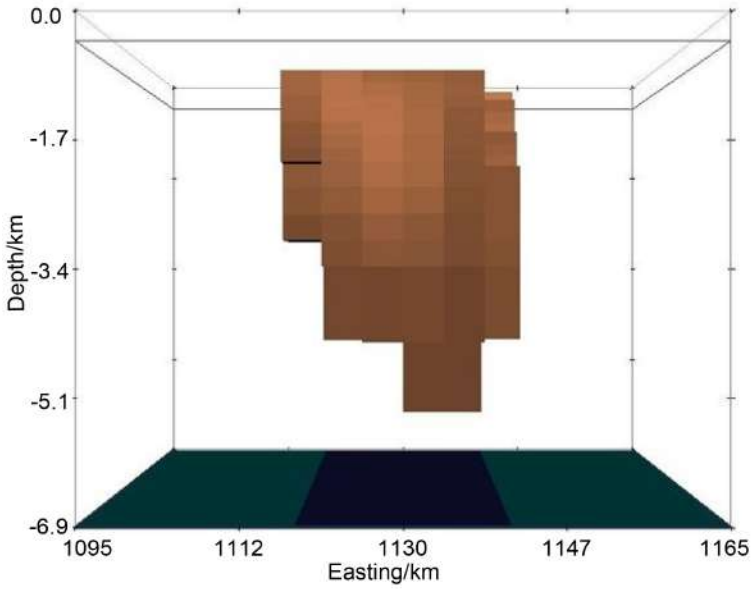

Figure 15. 3D model of the Kribi dense intrusive body as viewed from the South.

gradient of the third order residual anomaly has been used to locate and determine the depth range of the anomalous body. The spectral analysis has also been used to determine the average depths to the tops and bottoms of the anomalous body. It is observed that the depth varies between 0.5 km and 5 km from the surface of the earth. These constraints give an assurance of the validity of the model. The parameters of the model (depth to the top of 0.5 km and 1.5 for some sections of the body, and depth to the bottom of 4.8 km and 5.2 km for a slide section of the center of the body) are in accordance with the results obtained by [6] giving the depth range of the anomaly sources of Kribi between 0 and 6 km. They also agree with the results of the multi-scale analysis of the maxima of gradient which situates the depth of the intrusive body between 0.5 km and 5 km. However, there is a slide shift of the depth of the center of the body that extends to 5.2 km approximately. This value also agrees with the results provided by the spectral analysis method which give the average depth of the intrusive body between 0.5 km and 3.6 km. The depth of 1.6 km obtained for some sections of the body by spectral analysis has been confirmed by the approximately 1.5 km obtained for particular sections of the roof of the body. The density of the body was evaluated to be about 2.74 g/cm^3. A superposition of the residual anomaly map with the geological map and previous studies [27] indicate that the intrusive rocks in the studied area are mainly gneiss, alkaline syenite, nepheline syenite, granodiorite, dolerite, tonalite and peridotites. [28] give the average density values for these rocks as presented in **Table 1**.

Given all these, the intrusive igneous body obtained by gravity modelling may be composed of gneiss, and granodiorite because their mean density is close to that of the modelled body. Assuming the value of the density of the surrounding metamorphic rocks to the North-East of 2.67 g/cm^3 and the value of the density

Table 1. Density values of intrusive rocks in the study area.

Rock name	gneiss	Alkaline syenite	Nepheline syenite	granodiorite	dolerite	tonalite	peridotites
Density range/ g/cm^3	2.60 - 2.90	2.60 - 2.95	2.53 - 2.70	2.67 - 2.79	2.70 - 3.50	2.62 - 2.96	2.78 - 3.37
Mean density value/ g/cm^3	2.75	2.78	2.61	2.73	3.10	2.79	3.08

of the surrounding sedimentary formations to the south-west mainly limestones and sandstones with mean densities of 2.55 g/cm^3 and 2.35 g/cm^3 respectively, the 3D model possibly consist of an intrusive igneous body (gneiss, granodiorite) with a density estimated at about 2.74 g/cm^3 surrounded by other metamorphic formations to the north-east and sedimentary formations to the south-west. The density contrast between this body and the sorrounding formations varies from 0.07 g/cm^3 to 0.39 g/cm^3.

According to [10], the intrusive rocks emplaced in the Nyong Unit were linked to an overstretching phase just before the Panafrican Orogeny. It is therefore possible that this overstretching phase coupled with the high tectonic activity and the regional field stress present in the area [4] caused the dislocation of this dense intrusive block from the broader intrusion suspected in the area [19]. The further characterization and modelling of this broader structure will ensure a better understanding of the structural layout of the Cameroon coastal basins made up of the Douala and Kribi-Campo sub-basins.

6. Conclusion

The analysis of the third order residual anomaly map and the superposition of horizontal gradient maxima from the residual anomaly and its upward continuation at several heights shows quasi-circular disposition of many maxima indicating the presence of a dense intrusive body in the Kribi area. The multi-scale analysis of the maxima of the horizontal gradient of the third order residual anomaly led to the location of this body at a depth to bottom ranging 0.5 km and 5.0 km. The power spectrum method used gave the depth to the top from the surface at 0.5 km and 1.6 km and to a mean depth to the bottom of 3.6 km. The 3D model obtained using the GRAV3D software and taking into account the results provided by the two previous methods, shows a block with part of its top located at 0.5 km and other sections located at about 1.5 km. Its bottom lies at a depth ranging from 4.8 km to 5.2 km. The identified body of density 2.74 g/cm^3 which is surrounded by other lower density metamorphic formations to the north-east and sedimentary formations to the southwest suggests that it is an igneous intrusion. The observation of the shape of this body coupled with the results obtained by [19] leads to the observation that this body is part of a

broader intrusion extending northwards. A further 3D modelling and characterization of this broader structure can lead to a more profound understanding of the tectonic origin and structural layout of the Cameroon coastal basins namely the Douala sub-basin and the Kribi-Campo sub-basin. The interpretation of the 3D model of the Kribi-Campo intrusive body and the discontinuities surrounding it could serve as a guide in the investigation and exploitation of oil, gas and mineral sources in the study area, facilitating the location of points favorable to their existence. This result could also serve as a guide in the identification of risk areas. Apart from this, further studies could be carried out to identify the types of minerals that can be found in this massive and dense igneous intrusion. It is also important to determine in further studies the thickness of this basin in order to know the extent to which this body influences the sedimentary cover and its impact on potential mining resource in the area.

Acknowledgements

We greatly appreciate constructive and insightful comments of reviewers whose remarks and critique have led to a significant improvement of the work. We equally want to thank the team of Geophysicists from the Laboratory of Physics of Earth's Environment of the University of Yaoundé 1 who made the data acquisition campaign possible, Prof. Njandjock Nouck Phillipe, Dr. Evariste Ngatchou and Mr. Abate Marcel are gratefully acknowledged for leading this campaign.

References

[1] Brownfield, M.E. and Charpentier, R.R., (2006) Geology and Total Petroleum Systems of the West-Central Coastal Province (7203), West Africa. *US Geological Survey Bulletin* 2207-B. https://pubs.usgs.gov/bul/2207/B/

[2] Ntamak-Nida, M.J., Bourquin, S., Makong, J.C., Baudin, F., Mpesse, J.E., Ngouem, C.I., Komguem, P.B. and Abolo, G.M., (2010) Sedimentology and Sequence Stratigraphy from Outcrops of the Kribi-Campo Sub-Basin: Lower Mundeck Formation (Lower Cretaceous, Southern Cameroon). *Journal of African Earth Sciences*, **58**, 1-18. https://doi.org/10.1016/j.jafrearsci.2010.01.004

[3] Tadjou, J.M., Nouayou, R., Kamguia, J., Kande, H.L., Manguelle-Dicoum, E. (2009) Gravity Analysis of the Boundary between the Congo Craton and the Pan-African Belt of Cameroon. *Austrian Journal of Earth Sciences*, **102**, 71-79.

[4] Owona Angue, M.L.C., Tabod, C.T., Nguiya, S., Kenfack, J.V. and Tokam Kamga, A.P. (2013) Delineation of Lineaments in South Cameroon (Central Africa) Using Gravity Data. *Open Journal of Geology*, **3**, 331-339. https://doi.org/10.4236/ojg.2013.35038

[5] Manguellé-Dicoum, E., Bokosah, A.S. and Kwende-Mbanwi, T.E. (1992) Geophysical Evidence for a Major Precambrian Schist-Granite Boundary in Southern Cameroon. *Tectonophysics*, **205**, 437-446. https://doi.org/10.1016/0040-1951(92)90447-E

[6] OwonaAngue, M.L.C., Assembe, S.P., Njingti, N., Ngoh, J.D., NdougsaMbarga, T., Kue Petou, R.M. and Bisso, D. (2016) Determination of the Structural Lineaments in the Kribi-Campo-Ma'an Area from a Multi-Scale Analysis of Gravity Data Using the HGM and Euler 3D Deconvolution Approaches. *International Journal of Geos-*

ciences, **7**, 1122-1143. https://doi.org/10.4236/ijg.2016.79085

[7] Minyem, D. and Nedelec, A. (1990) Origin and Evolution of the Eseka Gneisses (Cameroon). Archean TTG Reworked in the Panafrican Mobile Belt. 15*th Colloquium of African Geology*, **2**, 21-24.

[8] Toteu, S.F., Penaye, J. and Poudjom Djomani, Y.H., (2004) Geodynamic Evolution of the Pan-African Belt in Central Africa with Special Reference to Cameroon. *Canadian Journal of Earth Sciences,* **41**, 73-85. https://doi.org/10.1139/e03-079

[9] Owona Angue, M.L.C., Nguiya, S., Nouayou, R., Tokam Kamga, A.P. and Manguelle-Dicoum, E. (2011) Geophysical Investigation of the Transition Zone between the Congo Craton and the Kribi-Campo Sedimentary Basin (South-West Cameroon). *South African Journal of Geology*, **114**, 145-158. https://doi.org/10.2113/gssajg.114.2.145

[10] Vicat, J.P., Leger, J.M., Nsifa, E., Piguet, P., Nzenti, J.P., Tchameni, R. and Pouclet, A. (1996) Distinction au Sein du craton congolais du Sud-Ouest du Cameroun, de deux épisodes doléritiques initiant les cycles Orogéniques éburnéen (Paléoprotérozoïque) et Pan-Africain (Néoprotérozoïque). *Compte Rendu de l'Académie des Sciences*, **323**, 575-582.

[11] Ngoumou, P.C., Ndougsa Mbarga, T., Assembe, S.P. and Kofane, T.C. (2014) Evidence of Iron Mineralization Channels in the Messondo Area (Centre Cameroon) Using Geoelectrical (DC & IP) Methods: A Case Study. *International Journal of Geosciences*, **5**, 346-361. https://doi.org/10.4236/ijg.2014.53034

[12] Tchameni, R., Mezger, K., Nsifa, E.N. and Pouclet, A. (2001) Crustal origin of Early Proterozoic Syenites in the Congo Craton (Ntem Complex), South Cameroon. *Lithos,* **57**, 23-42. https://doi.org/10.1016/S0024-4937(00)00072-4

[13] Rosendahl, B.R. and Groschel-Becker, H. (1999) Deep Seismic Structure of the Continental Margin in the Gulf of Guinea: A Summary Report. In: Cameron, N.R., Bate, R.H. and Clure, V.S., Eds., *The Oil and Gas Habitats of the South Atlantic*, *Geological Society*, London, **153**, 75-83. https://doi.org/10.1144/GSL.SP.1999.153.01.05

[14] Burke, K. (1969) Seismic Areas of the Guinea Coast Where Atlantic Fracture Zone Reach Africa. *Nature*, **222**, 655-657. https://doi.org/10.1038/222655b0

[15] Perez-Diaz, L. and Eagles, G. (2014) Constraining South Atlantic Growth with Seafloor Spreading Data. *Tectonics*, **33**, 1848-1873. https://doi.org/10.1002/2014TC003644

[16] Tokam, K.A.P., Tabod, C.T., Nyblade, A.A., Julia, J., Wiens, D.A. and Pasyanos, M. (2010) Structure of the Crust beneath Cameroon, West Africa, from the Join Inversion of Rayleigh Wave Group Velocities and Receiver Functions. *Geophysical Journal International*, **183**, 1061-1076. https://doi.org/10.1111/j.1365-246X.2010.04776.x

[17] Collignon, F. (1968) Gravimétrie et reconnaissance de la République Fédérale du Cameroun. ORSTOM, Paris, 35 p.

[18] Nsifa, E.N. (2005) Magmatisme et évolution géodynamique de l'Archéen au Protérozoïque de la bordure nord-ouest du craton du Congo (complexe du Ntem) au Sud-Ouest Cameroun. Thèse Doctorat d'Etat, Université de Yaoundé I, Yaoundé, 248 p.

[19] Koumetio, F., Njomo, D., Tabod, C.T., Noutchogwe T.C. and Manguelle-Dicoum, E. (2012) Structural Interpretation of Gravity Anomalies from the Kribi-Edea Zone, South Cameroon: A Case Study. *Journal of Environmental & Engineering*, **9**, 664-673. https://doi.org/10.1088/1742-2132/9/6/664

[20] Archibald, N.J., Gow, P. and Boschetti, F. (1999) Multiscale Edge Analysis of Poten-

tial Field Data Exploration. *Geophysics*, **30**, 38-44.

[21] Cordell, L. and Grauch, V.J.S. (1985) Mapping Basement Magnetization Zones from Aeromagnetic Data in the San Juan Basin, New Mexico. In: Hinze, W. J., Ed., *The Utility of Regional Gravity and Magnetic Anomaly Maps*, Society of Exploration Geophysicists, 181-197. https://doi.org/10.1190/1.0931830346.ch16

[22] Cordell, L. (1979) Gravimetric Expression of Graben Faulting in Santa Fe Country and the Espanola Basin, New Mexico. In: Ingersoll, R.V., Ed., *Guidebook to Santa Fe Country*, New Mexico Geological Society, Socorro, 59-64.

[23] Spector, A. and Grant, F.S. (1970) Statistical Models for Interpretation Aeromagnetic Data. *Geophysics*, **35**, 293-302. https://doi.org/10.1190/1.1440092

[24] Gerard, A. and Debeglia N. (1975) Automatic Three-Dimensional Modeling for Interpretation of Gravity or Magnetic Anomalies. *Geophysics,* **40**, 1014-1034. https://doi.org/10.1190/1.1440578

[25] Bhattacharryya B.K. and Leu, L.-K. (1975) Spectral Analysis of Gravity and Magnetic Anomalies Due to Two-Dimensional Structures. *Geophysics*, **40**, 993-1013. https://doi.org/10.1190/1.1440593

[26] Radhakrishna, I.V. and Krishnamacharyulu, S.K.G., (1990) Polyfit: A Fortran 77 Program to Fit a Polynomial of Any Order to Potential Field Anomalies. *Journal of the Association of Exploration Geophysicists,* **11**, 99-105.

[27] Maurizot, P., Abessolo, A., Feybesse, J.L., Johan, V. and Lecomte, P., (1986) Etude et prospection minière du sud- ouest Cameroun. Synthèse des travaux de 1978 à 1985. Rapport, BRGM, 274 p.

[28] Telford, W.M., Geldart, L.P. and Keys, D.A. (1976) Applied Geophysics. Cambridge University Press, Cambridge, 860 p.

International Journal of Geosciences, 2017, 8, 1210-1224
http://www.scirp.org/journal/ijg
ISSN Online: 2156-8367
ISSN Print: 2156-8359

Determination of Structural and Geometrical Parameters of the Kribi-Campo Sedimentary Sub-Basin Using Gravity Data

Kue Petou Rokis Malquaire[1,2,3*], Owona Angue Marie Louise Clotilde[3,4], Njingti Nfor[3,4], Ndougsa-Mbarga Théophile[3,4], Manguelle-Dicoum Eliezer[5]

[1]National Institute of Cartography, Yaoundé, Cameroon
[2]School of Geosciences, China University of Petroleum, Qingdao, China
[3]Postgraduate School of Sciences, Technologies & Geosciences, University of Yaoundé I, Yaoundé, Cameroon
[4]Department of Physics, Advanced Teacher Training College, University of Yaoundé I, Yaoundé, Cameroon
[5]Department of Physics, Faculty of Science, University of Yaoundé I, Yaoundé, Cameroon
Email: *rokis.petou@yahoo.fr

How to cite this paper: Malquaire, K.P.R., Clotilde, O.A.M.L., Nfor, N., Théophile, N.M. and Eliezer, M.D. (2017) Determination of Structural and Geometrical Parameters of the Kribi-Campo Sedimentary Sub-Basin Using Gravity Data. *International Journal of Geosciences*, **8**, 1210-1224.
https://doi.org/10.4236/ijg.2017.89069

Received: August 11, 2017
Accepted: September 27, 2017
Published: September 30, 2017

Abstract

In order to produce a more detailed structural and geometrical information, and determine sediments thickness along the Kribi-Campo sub-basin, statistical spectral analysis and horizontal gradient analysis of residual anomalies coupled with the Euler deconvolution approach were applied on the gravity data in the area. The results obtained from the 2D spectral analysis on anomaly grids gave a depth to the basement rocks of the basin from 0.60 km to 3.93 km. This represents the thickness of the sedimentary formations overlying the basement. The interpretation of the spectral analysis results indicated that the potential hydrocarbon field areas are situated between Kribi and Lolabe and at Campo given that those areas have the highest sedimentary thicknesses values. From the analysis of the horizontal gradient, deep faults mainly striking SW-NE have been traced and a structural map of the area has been produced. By applying the Euler deconvolution method to the gravity data, information about the depth and trend of the main subsurface structures have been obtained.

Keywords

Sediment Thickness, Spectral Analysis, Horizontal Gradient, Structural Map, Kribi-Campo Sub-Basin, Gravity Data

1. Introduction

The Kribi-Campo basin is located at the northern edge of the South Atlantic rift

and is one of a series of divergent passive margin basins along the west coast of Africa. Covering a total area of about 6.2×10^3 km^2, it was formed during the Mesozoic to Tertiary, as a result of the rifting of Africa and South America during the break-up of the Gondwana supercontinent [1]. This basin lies in the South west coast of Cameroun. Abundant oil seeps exist at the basin margins and a number of oil and gas discoveries have been made so far. Many authors, using both gravity and magneto-telluric data, have published on the structure of the subsurface in the entire South Cameroon. One of the most pertinent geophysical studies done in the Kribi-Campo basin is the 3D modelling, using gravity data, of an anomalous body located in the northern part of the basin [2]. The model obtained suggested that the basin's subsurface is intruded by a massive dense block composed of gneiss and granodiorite which has a thickness of about 4.5 km. The authors also suggested that this high density intrusive body is surrounded by sediments and metamorphic formations. [3] [4] also provided valuable information in the area by delineating some major discontinuities traversing the subsurface. In this paper, we are proposing the use of statistical spectral analysis, horizontal gradient and Euler deconvolution approaches to determine the structural and the geometrical characteristics (the majors and minor discontinuities, their trend and the thickness of the basin) in order to provide further interpretation of the Kribi-Campo basin subsurface structure and locate the areas with high sedimentary thicknesses which are potential targets in hydrocarbon exploration.

2. Geological and Tectonic Settings

The geological formations of Kribi in South Cameroon belong to four major lithological and structural units [5], the Ntem Archean unit; the Nyong Unit; the Neo-proterozoic cover and sedimentary formations. The study area is situated at northern edge of the Congo craton, at the transition zone between this mega-structure and the Mobile zone. The most relevant geological formations that can help to better describe this area are mainly the lower Nyong Unit formations and the sedimentary formations. The lower Nyong Unit is made up of ancient Archean rocks of the Ntem basement that underwent Eburnean orogenesis, their formation resulted from the collision between the Congo craton and the São Francisco [6] [7]. This unit was subject to high degree Tectonometamorphism dated ± 2050 Ma associated to the charnokites formations dated ±250 Ma confirming the hypothesis that the Nyong Unit is a remobilized portion of the Archean Ntem complex [5]. The rocks in this area are mainly schists, gneisses that have been intruded by granidiorites and sedimentary formations rocks such as limestones and sandstone [8] [9].

In general, the region has a complex and uneven tectonic structure. This tectonic seems to have given rise to a vertical movement of the basement with subsidence to the North and uplift to the South [10] [11]. This basement movement must have provoked irregularities in the formations at depth, giving rise to faults, horsts and grabens characteristic of the boundary between the Congo Craton and the Pan-African folds belt [12]. The main faults in the region consist of the

Kribi-Campo Fault (KCF) system which is also considered as a continuation of the Sanaga Fault. This fault system is linked to the offshore fault system called the Kribi Fracture Zone. Contacts and faults trending E-W, N-S, NE-SW and NW-SE, which are either deep and/or buried structures and circular features which correspond to contacts and intrusive bodies have also been highlighted and characterized in the region [2] [4].

3. Material and Methods

3.1. Data Used

Two dataset have been combined to carry out this work: the existing ORSTOM data and the newly collected ones. In **Figure 2**, we present the distribution of the gravity data alongside with the altitude variation in the study area. The ORSTOM data (collected during the ORSTOM survey in 1968) [13] represented by red triangles have been combined with the new gravity data (collected by the team of geophysicist of the University of Yaoundé 1 in March 2015) represented by the blue squares. The new data constitute over 223 points measured along the basin area with a spacing of 0.5 to 1 km. These data were collected using the Lacoste-Romberg G-823 gravity-meter. The irregularity in the data spacing is due to the inaccessibility of some sites given that the study area is found in the dense equatorial forest and the Campo National park where only open field roads are accessible.

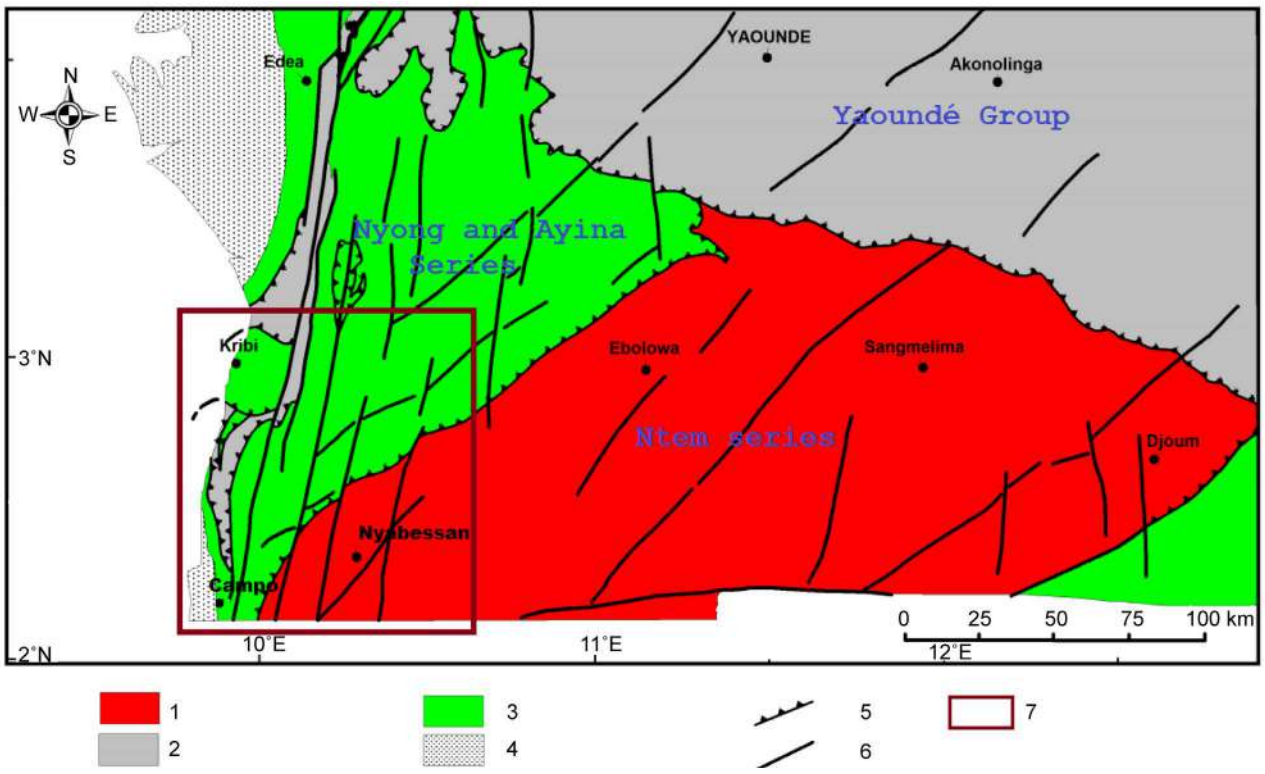

Figure 1. Simplified geological map of the SW-Cameroon [5]. 1: Archaen Basement; 2: Neoproterozoic cover; 3: Neoarchaen-paleoproterozoic cover; 4: Post Panafrican cover; 5: Thrust fault; 6: fault; 7: Study area.

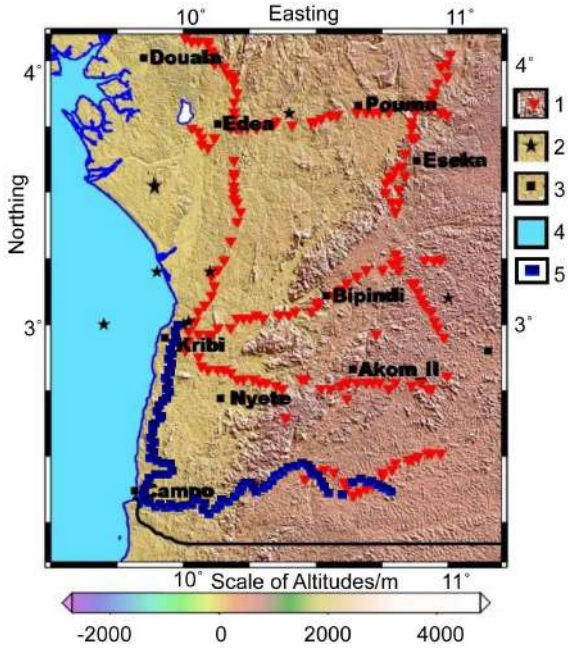

Figure 2. Gravity data distribution map showing the area with altitudes variations. 1: old data points, 2: earthquake epicenters, 3: localities, 4: sea, 5: new gravity data points (March 2015).

3.2. Spectral Analysis

This method is carried out through 2D Fast Fourier Transform which transforms gravity data from the space domain to the wavenumber domain to estimate the depths of the structures responsible for the measured anomaly. It has been used extensively by many authors, namely [14] [15] [16].

The finite discrete Fourier transform is given by the equation:

$$B(\omega)=\sum_{0}^{N-1} b(x)\exp(-i\omega x)\cdot\Delta x \tag{1}$$

where $b(x)$ represents the discrete N data array of gravity data obtained by sampling a continuous profile at evenly spaced intervals Δx. i is the complex operator, $\omega = 2\pi k$ is the spatial frequency and $k = \lambda^{-1}$ is the wavenumber in the x direction.

The expression of the Bouguer Slab Effect is then given by the equation:

$$B(k)_{z=0} = 2\pi\Delta\rho G\cdot\exp(-2\pi kt)\cdot F(k)_{z=0} \tag{2}$$

where $B(k)_{z=0}$ is the Fourier transform of the Bouguer anomaly profile $b(k)_{z=0}$; $\Delta\rho$ is the density contrast between two layers; $F(k)$ is the Fourier transform of $f(x)$, the derivation of the interface from the mean depth z; G is the gravitational constant. The mean depth can then be calculated using the following equation:

$$h=\frac{\Delta LogE}{4\pi\Delta k} \tag{3}$$

where E is the power spectrum of $B(k)$.

When the square of the Fourier amplitude spectrum is plotted against the radial frequency, the slope of the relationship between the wave number of the gravity field and the logarithmic power spectrum provide information about the depths to basement of the anomaly sources.

3.3. Euler Deconvolution

The Euler Method is a technique generally used to locate the apparent depth to the gravity or magnetic anomaly source. Considering a degree of homogeneity, the gravity or magnetic field is related to its gradient component in order to trace the surface of the ground contact. The degree of homogeneity is expressed by the structural index which defines the measure of the fall-off rate of the field with distance from the source. The Euler homogeneity equation is given as:

$$(x-x_0)\frac{\partial T}{\partial x}+(y-y_0)\frac{\partial T}{\partial y}+(z-z_0)\frac{\partial T}{\partial z}=N(B-T) \tag{4}$$

where (x_0, y_0, z_0) is the position of the magnetic or gravity source whose total field (T) is detected at (x, y, z,). B is the regional gravity or magnetic field. N is the measure of the fall-off rate of the gravity field and may be interpreted as the structural index (SI). This value needs to be chosen according to a prior knowledge of the source geometry.

The Euler depth appear wherever there are lithological discontinuities in the geological formations. They represent the structural and/or stratigraphic changes of various geological formations [3].

3.4. The Horizontal Gradient Method

According to [17], the horizontal gradient performed at different heights of the anomaly observation allows for the location of discontinuities and the determination of their dip.

The horizontal gradient is an operation that measures the rate of change of a potential field in the x and y directions [18] in order to image subsurface structures. However, the total horizontal gradient magnitude (HGM) is preferred for its simplicity. The HGM operator is defined by the relation below:

$$HGM(x,y)=\sqrt{\left(\frac{\partial G}{\partial x}\right)^2+\left(\frac{\partial G}{\partial y}\right)^2} \tag{5}$$

where G is the Bouguer gravity field.

The horizontal gradient method is used to locate the boundaries of density contrast from gravity data. These results mark the top edges of gravity or density boundaries. Thus, the maximum value of the horizontal gradient anomalies is placed on top of the sources edges. However, offsets occur when edges are not vertical or when several anomalies are close together. The biggest advantage of the horizontal gradient method is its low sensitivity to the noise in the data, be-

cause it only requires calculations of the two first-order horizontal derivatives (x- and y-directions) of the gravity field [4].

The works of [18] [19] showed that the maxima of the horizontal gradient of gravity anomalies help in locating contacts associated with abrupt changes in density, which are interpreted either as faults, geological contacts or intrusions. Faults are expressed by a quasi-linear disposition of at least three maxima and horizontal limits of intrusive bodies are shown by quasi-circular disposition of many maxima [20].

4. Results and Interpretation

4.1. Gravity Data Analysis

The gravity anomaly maps generally superpose the effects of deep, shallow, local and extended gravity contrasts. The effects of a local or shallow structure are often hidden in the signatures of regional structures. We carried out regional-residual separation using the polynomial fitting method with the aim of isolating the anomalies caused by deep and extended sources (long-wavelength anomalies) from those caused by local and shallow density contrasts (short wavelength anomalies). The residual field is obtained by estimating the regional gravity field and removing it from the observed field which is the Bouguer anomaly (**Figure 3**). In effect, the order of the regional field n is assimilated to a polynomial of n degree. When n is small, the regional anomaly possesses values which are relatively more different from those of the Bouguer anomaly. In this case, the thickness of the part of the crust causing the corresponding residual anomalies is relatively large. This thickness decreases when n increases. In fact,

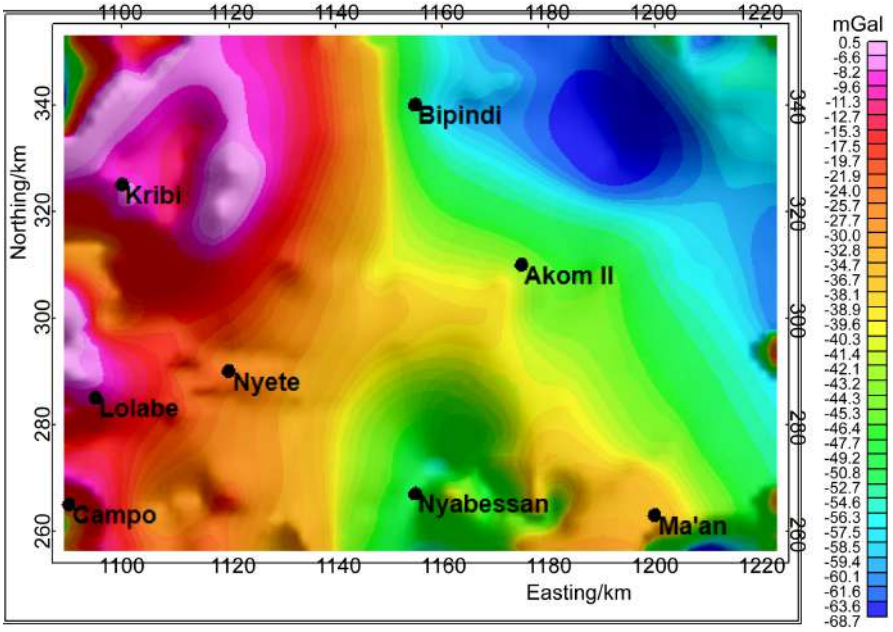

Figure 3. Bouguer anomaly map of the Kribi-Campo sedimentary sub-basin modified after [2].

the wavelength of the residual anomaly decreases when the degree of the polynomial increases thereby revealing geological structures which appear closest to the surface [20].

In this work, we have used a polynomial of degree '1', for spectral analysis, Horizontal gradient and Euler deconvolution, so as to have a better chance of locating the major contacts.

In **Figure 2**, we present the distribution of the gravity data alongside with the altitude variation in the study area. The ORSTOM data (collected during the ORSTOM survey in 1968) [21] represented by red triangles have been combined with the new gravity data (collected by the team of geophysicist of the University of Yaoundé 1 in March 2015) represented by the blue squares. The new data constitute over 223 points measured along the basin area with a spacing of from 0.5 km to 1.0 km. These data were collected using the Lacoste-Romberg G-823 gravity-meter. The irregularity in the data spacing is due to the inaccessibility of some sites given that the study area is found in the dense equatorial forest and the Campo National park where only open fields and roads are accessible.

In **Figure 3**, we present the Bouguer gravity anomalies. This map was obtained by interpolation of gravity data using the kriging gridding algorithm of the Oasis Montaj 8.0 software. As interpreted by [2], the Bouguer map of the area presents three gravity domains: the high gravity anomalies to the west, corresponding to a ring complex affected by a nearly N-S trending discontinuity and basic intrusive bodies within the main formation; the second domain to the north-east corresponding to low density intrusive bodies and the third domain in the middle of the map marking the signatures of charnockites and green rock belts of the Ntem Unit.

The first order residual map **Figure 4** reveals several local anomalies. The positive ones to the west at Kribi (A1), north-east of Kribi (A2), south-west of Kribi (A3), Lolabe (A4), Campo (A5) south-east of Lolabe (A6) and north of Kribi (A7) which indicate basement uplift and lateral differences in density from causative rocks. The Kribi positive anomaly is caused by an intrusive igneous body (gneiss, granidiorite) with a density estimated at about 2.74 g/cm^3 [2]. The Lolabe and Campo anomalies could also be the results of dense rocks intrusion oriented N-S and buried under the sedimentary cover. The main negative anomalies are observed in the northeast, central south and southeast parts of the study area trending NW-SE (A8), SW-NE at Nyabessan (A9) NW-SE (A10) at Ma'an and the nearly circular anomaly to the east of Bipindi (A11). [21] suggested that the nearly circular anomaly of Bipindi was caused by a low density intrusive block having a density contrast of −0.095 g/cm^3.

4.2. Estimation of the Thickness of the Basin

We applied a 2D spectral analysis on grids centered on positive anomalies in the basin situated on the western area of the map (A1, A2, A3, A4, A5, A6, and A7), which enabled us to determine the depths. The power spectrum has been

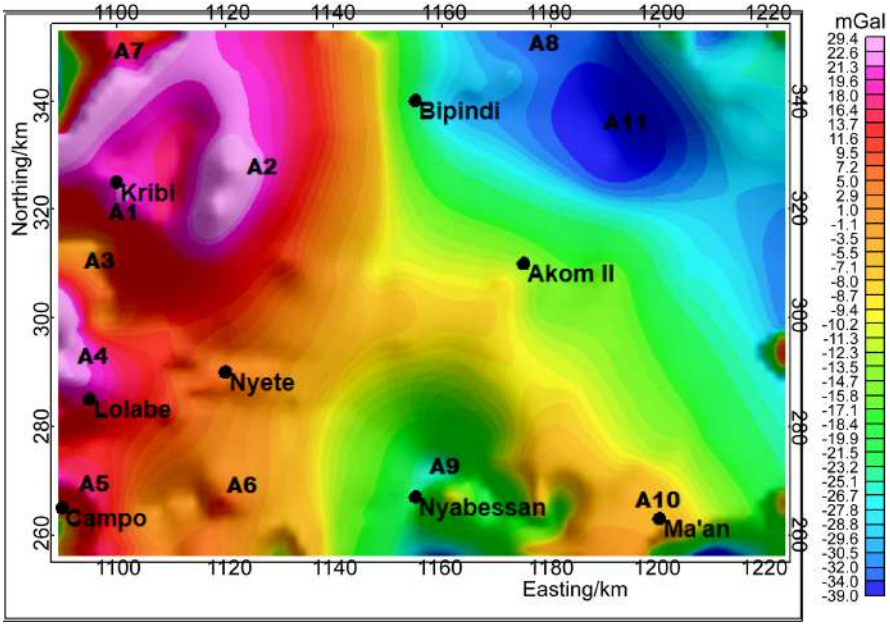

Figure 4. First order residual anomaly map of the study area.

obtained from the energy values which derive from the anomaly values. The given values are presented in Table 1.

Figure 5 presents a sample of the power spectrum curves obtained for the various anomaly grids. The line segment on this curve can be identified and plotted by a least squares fitting on the data points. This curve is obtained from the anomaly values of grid A2. The same calculation were carried out for A1, A3, A4, A5, A6 and A7. The mean depth of density contrast plane may be interpreted as an inter-basement density variation associated with the depth to basement [22]. This mean depth, highlighting the discontinuities observed for the positive anomalies has been calculated and presented in Table 2. The first observation that can be made from this table is that, the sedimentary infill thickness decreases as we move from the west to the east of the area. The depths to basement vary from 0.60 km to about 3.93 km. We also observe that there is a relatively high accumulation of sediments in the basin (>0.6 km). The areas with the highest depth to basement or highest sedimentary thickness (~4 km) are the most promising regions for oil and gas exploration. The zone situated between Kribi and Lolabe and the Campo area are well indicated for further prospections. These results are therefore important for the selection of new exploration areas.

4.3. Structural Parameters of the Basin

4.3.1. Horizontal Gradient Method

We used the Oasis montaj 8.0 software to calculate the amplitude of the horizontal gradient of the residual data of the study area (Figure 6). We can clearly observe on this map the regions with high gradient amplitude indicating high density variation between contacts. The two major lineament that are interpreted from this map are striking in the direction NW-SE from Kribi right

Table 1. Anomaly Values, Power Spectrum and wavenumber values for the anomaly grid A2.

ANOMALY VALUES/ mGal	POWER SPECTRUM	LOG (POWER SPECTRUM)	WAVENUMBER/ km^{-1}
−50.00	87.44	1.95	0.02
−12.60	2.06	0.33	0.07
−4.19	0.40	−0.40	0.09
−7.58	0.11	−0.95	0.11
−9.22	0.04	−1.40	0.15

Table 2. Depths to basement obtained from power spectrum of gravity data.

ANOMALY ID	DEPTH TO BASEMENT/km
A1	2.62
A2	2.84
A3	3.48
A4	0.97
A5	3.93
A6	0.60
A7	1.19

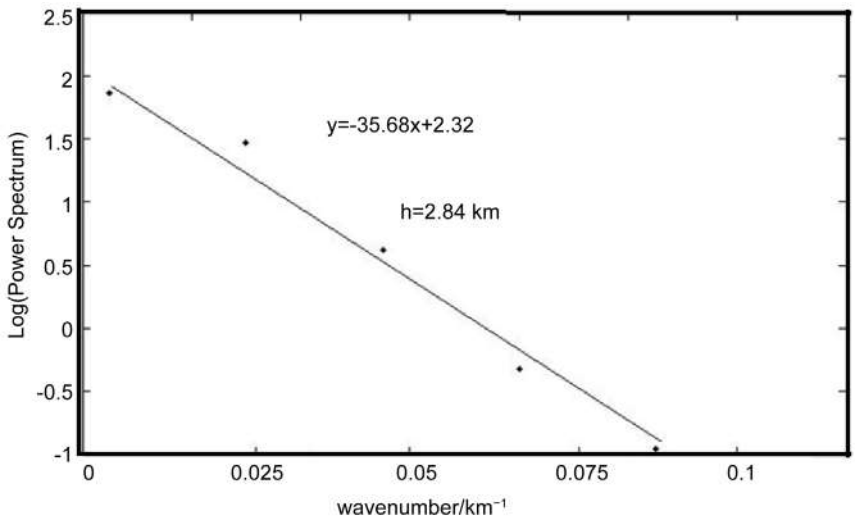

Figure 5. Power spectrum of the gravity data. The linear segment correspond to the density layer used to compute depth.

to Nyabessan and from Lolabe to the south east of Campo. The east of Bipindi is also characterized by high gradient variation. This could mark the huge change in density between the Bipindi intrusive block and metamorphic formations surrounding it. Due to the broad nature of the high gradients, we suggest that the boundaries of density contacts in the Kribi-Campo basin are probably not

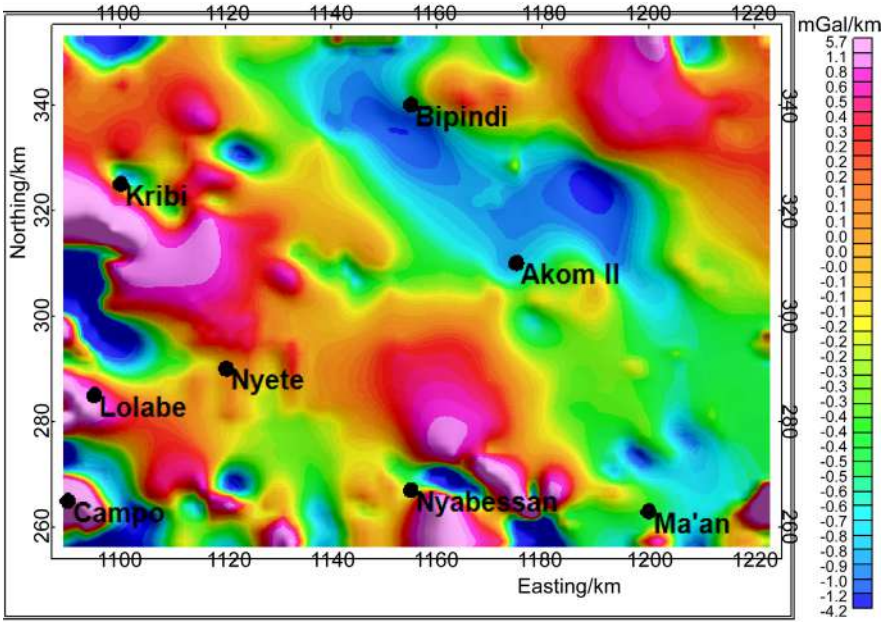

Figure 6. Horizontal gradient map of the study area.

necessarily vertical and relatively deep or produced by several boundaries.

4.3.2. Euler Solutions

For the Euler method, the following parameters have been used to compute the Euler solutions: structural Index N = 0.5, maximum % of tolerance of 5 and a window size of 5 km × 5 km. **Figure 7** shows the results of the Euler method from the first order residual gravity data. This map presents the structural layout of the area showing the different faults affecting the subsurface. The computed depths vary between 2.0 km and 20.4 km for the entire region and between 2.0 km and 7.0 km for the western zone which makes up the basin. It is observed that the faults and contacts highlighted here get deeper as we move to the east. The shallowest are those located in the basin area at the extreme west and in the extreme south zone of the map. We present in the first column of **Table 3** the various faults delineated using the Euler deconvolution approach, the orientations of these faults are given in the second column; it is observed that the SW-NE is the main fault direction in the basin. This information can be helpful in the determination of fluid flow direction in the basin. The last column of **Table 3** gives the depth range of faults, the shallowest identified from 2 km and the deepest at about 12 km of depth. The different faults detected in the basin area can be interpreted as a result of local tectonic movements coupled with the setting up of intrusive rocks (granidiorites and gneisses) into the sedimentary and metamorphic formations.

4.3.3. Structural Map of the Basin

The combination of the above described results, namely the spectral analysis, horizontal gradient and Euler solutions coupled with the results published by [2] have enabled us to propose a structural map of the Kribi-Campo sedimentary

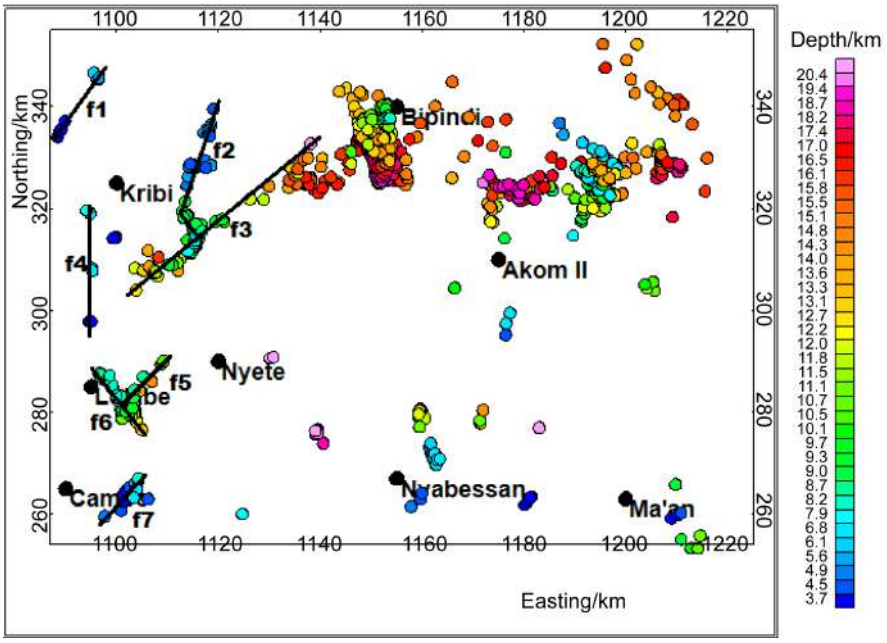

Figure 7. Structural interpretation of Euler Solutions for N = 0.5. The black lines represent the highlighted faults.

Table 3. Direction and Depth range of Faults in the Basin.

FAULT ID	DIRECTION	DEPTH RANGE/km
f1	SW-NE	2 - 5
f2	SSW-NNE	2 - 4
f3	SW-NE	7 - 13
f4	NS	2 - 5
f5	SW-NE	2 - 6
f6	NNW-SSE	6 - 12
f7	SW-NE	2 - 8

basin (**Figure 8**). This map shows quasi-linear contacts (numbered 1 to 12) which can describe faults and quasi-linear contacts (denoted C_1, C_2 and C_3) corresponding to horizontal limits of intrusive bodies.

5. Discussion

The results presented in the above sections are in accordance with the fact that the Kribi-Campo basin formations are relatively shallow compared to the Douala and Garoua basins. The general disposition of anomalies on the first order residual anomaly map (**Figure 4**) shows a west-to east diminution in the anomaly values which indicates the same variation of density values. According to [2], the Kribi zone is intruded by a 4.5 km thick block of body composed of gneiss and granidiorites. This intrusion has considerably influenced the sedimentary cover in the area. From the results of the sedimentary thickness

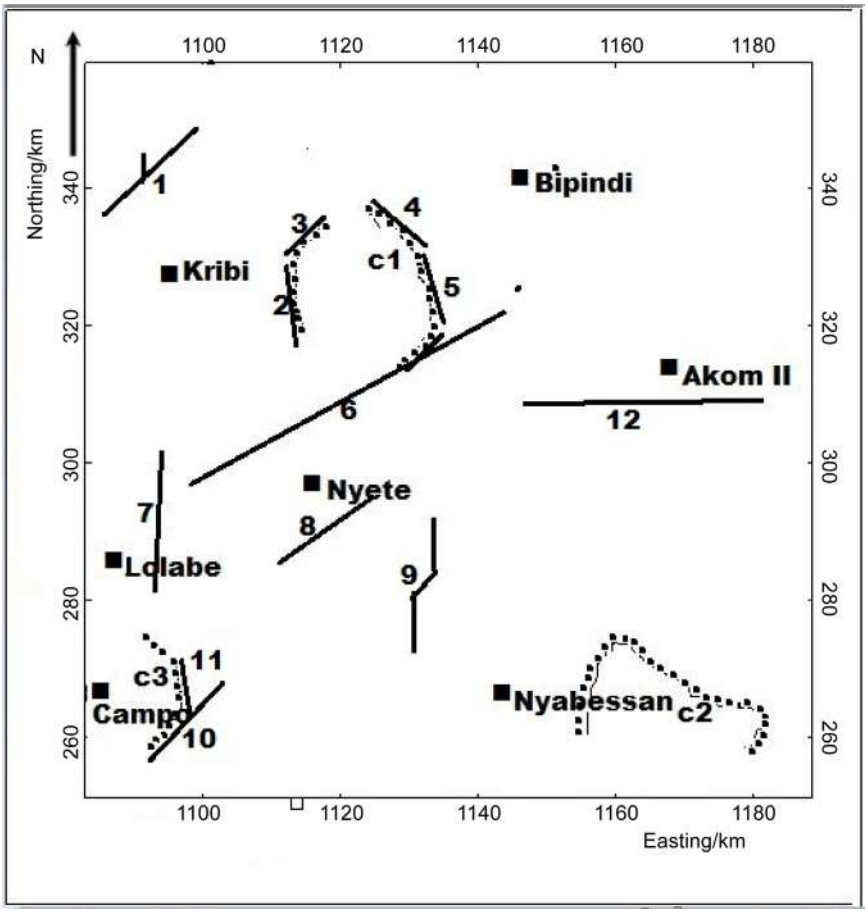

Figure 8. Interpreted structural Map of the Kribi Campo basin. (1) to (12): linear contacts; (C_1), (C_2) and (C_3): circular contacts indicating boundaries of intrusions.

obtained by spectral analysis, it can be seen that as we move from the North to the South of the study area, the sedimentary layer varies following a sinusoidal trend. This variation of the sediment thickness could be explained by the presence of high tectonic activities in the area [9] leading either to an uprising or to a subsidence of the basement. The smallest value of this thickness agrees with the works of [2] which proposed a 3D model of an intrusive body buried in a 0.5 km sediment layer. The horizontal gradient map shows that the boundaries of density contacts in the Kribi-Campo basin are not vertical and are relatively deep or produced by several boundaries because of the broad nature of the high gradients. From **Figure 7** it has been shown that the discontinuities and contacts in the Kribi-Campo basin are relatively shallow. These contacts get deeper as we move into the continent. Seven (7) major faults have been delineated (from f1 to f7) each with its direction and depth range. The analysis of the structural map of the basin highlights the presence of: (1) contacts and faults trending mainly SW-NE, N-S, SSW-NNE and NNW-SSE which confirms the results of [3] [4] giving the same approximate directions to major lineaments in the region and (2) three circular contacts C_1, C_3 and C_3 representing rocks intrusions amongst which one had been characterized and modelled in the works of [2]. This study

also suggests that given the high sedimentary thickness, the area situated between Kribi and Lolabe and the Campo locality are of high potential in mining and/or hydrocarbon resources. This suggestion is supported by the fact that the presence of oil and gas in a basin might be due to two factors: in-situ generation and migration of fluids into the basin [22]. The subsurface pressure which is a function of the sediment thickness (*i.e.*, the sediment weight) is one of the environmental conditions needed for oil and gas formation in a basin. The understanding of the fluid flow formation in the region could be elucidated by Euler solutions,the structural map and gradient maps analysis.

6. Conclusion

The aim of this study was to provide new insights on the structural setting and the geometrical characteristics of the Kribi-Campo basin. We used the polynomial fitting method to carry out the separation of the residual and regional components of the gravity field. We observed that the positive residual anomalies in the area are the effect of both high density rocks intrusions and sedimentary infill. The spectral analysis enabled to estimate the depth to basement on various parts of the Kribi-Campo basin which gives the sedimentary thickness. This thickness varies from 0.60 km to 3.93 km with the highest values obtained in some specific localities of the study area namely Campo and the area between Kribi and Lolabe. From the residual anomaly map and spectral analysis it can be deduced that the sedimentary infill presents a discontinued nord-south variation and also decreases from the west towards the east as we move from the coast into the continent. We applied the horizontal gradient analysis to the residual component. The residual structural setting of the zone from the Euler method is characterized by major faults and contacts mainly oriented SW-NE with the shallowest in the west (from 2 to 7 km deep) and the deepest in the east (right down to 20 km deep) of the region. The use of spectral analysis and euler solutions is very advantageous in the geometrical and structural caracterization of gravity anomalies in the sense that they help not just to determine depths to basement of causative tructures but also to evaluate their dip and their evolution in the longitudinal and transversal directions. The structural map of the basin provides the most relevant structural information in the area. This map can help in identifying the direction of fluid flow in the subsurface. The interpretation of the sedimentary thickness values can serve to identify areas with the highest mineral and hydrocarbon production potentials which correspond to areas with the highest sedimentary thickness.

Acknowledgements

The authors are thankful to the University of Yaoundé 1 and the Ministry of Higher Education for funding the data acquisition campaign. All reviewers of this manuscript are equally acknowledged.

References

[1] Perez-Diaz, L. and Eagles, G. (2014) Constraining South Atlantic Growth with Seafloor Spreading Data. *Tectonics*, **33**, 1848-1873. https://doi.org/10.1002/2014TC003644

[2] Kue Petou, R.M., Owona Angue, M.L, Njingti, N., and Manguelle-Dicoum, E. (2017) 3D Modelling from New and Existing Gravity Data of an Intrusive Body in the Northern Part of Kribi-Campo Sub-Basin in Cameroon. *International Journal of Geosciences*, **8**, 984-1003. https://doi.org/10.4236/ijg.2017.88056

[3] Owona Angue, M.L.C., Tabod, C.T., Nguiya, S., Kenfack, J.V. and Tokam Kamga, A.P. (2013) Delineation of Lineaments in South Cameroon (Central Africa) Using Gravity Data. *Open Journal of Geology*, **3**, 331-339. https://doi.org/10.4236/ojg.2013.35038

[4] Owona Angue, M.L.C., Assembe, S.P., Njingti, N., Ngoh, J.D., Ndougsa Mbarga, T., Kue Petou, R.M. and Bisso, D. (2016) Determination of the Structural Lineaments in the Kribi-Campo-Ma'an Area from a Multi-Scale Analysis of Gravity Data Using the HGM and Euler 3D Deconvolution Approaches. *International Journal of Geosciences*, **7**, 1122-1143. https://doi.org/10.4236/ijg.2016.79085

[5] Maurizot, P., Abessolo, A., Feybesse, J.L., Johan, V. and Lecomte, P. (1986) Etude et prospection minière du sud-ouest Cameroun. Synthèse des travaux de 1978 à 1985. [Study and Mining Prospecting of Southwestern Cameroon. Synthesis of the Work from 1978 to 1985.] Rapport, BRGM, 274 p.

[6] Toteu, S.F., Van Schmus, R.W., Penaye, J. and Nyobe, J.B. (1994) U-Pb and Sm-Nd Evidence for Eburnian and Pan-African High-Grade Metamorphism in Cratonic Rocks of Southern Cameroon. *Precambrian Research*, **67,** 321-347.

[7] Feybesse, J.L., Barbossa Ledru P., Guerrot, C., Johan, V., Triboulet, V., Bouchot, V., Prian, J.P. and Sabate, P. (1995) Paleoproterozoic Tectonic Regime and Markers of the Archean/Proterozoic Boundary in the Congo-Sao Francisco Craton EUG 8, Terra Abstracts P 100.

[8] Toteu, S.F., Penaye, J. and Poudjom Djomani, Y.H. (2004) Geodynamic Evolution of the Pan-African Belt in Central Africa with Special Reference to Cameroon. *Canadian Journal of Earth Sciences*, **41**, 73-85. https://doi.org/10.1139/e03-079

[9] Owona Angue, M.L.C., Nguiya, S., Nouayou, R., Tokam Kamga, A.P. and Manguelle-Dicoum, E. (2011) Geophysical Investigation of the Transition Zone between the Congo Craton and the Kribi-Campo Sedimentary Basin (South-West Cameroon). *South African Journal of Geology*, **114**, 145-158. https://doi.org/10.2113/gssajg.114.2.145

[10] Manguelle-Dicoum, E. (1988) Etude Géophysique des structures superficielles et profondes de la region de Mbalmayo. [Geophysical Study of the Superficial and Deep Structures of the Mbalmayo Region.] PhD Thesis, Université de Yaoundé I, Yaoundé, 202 p.

[11] Shandini, Y. and Tadjou, J.M. (2012) Interpreting Gravity Anomalies in South Cameroon, Central Africa. *Earth Sciences Research Journal*, **16**, 5-9.

[12] Shandini, N.Y., Tadjou, J.M., Tabod, C.T. and Fairhead, J.D. (2010) Gravity Data Interpretation in the Northern Edge of the Congo Craton, South-Cameroon. *Anuário do Instituto de Geociências*, **33**, 73-82.

[13] Collignon, F. (1968) Gravimétrie et reconnaissance de la République Fédérale du Cameroun. [Gravimetry and Recognition of the Federal Republic of Cameroon.] ORSTOM, Paris, 35 p.

[14] Spector, A. and Grant, F.S. (1970) Statistical Models for Interpretation Aeromag-

netic Data. *Geophysics*, **35**, 293-302. https://doi.org/10.1190/1.1440092

[15] Gerard, A. and Debeglia, N. (1975) Automatic Three-Dimensional Modeling for Interpretation of Gravity or Magnetic Anomalies. *Geophysics*, **40**, 1014-1034. https://doi.org/10.1190/1.1440578

[16] Bhattacharryya, B.K. and Leu, L.-K. (1975) Spectral Analysis of Gravity and Magnetic Anomalies Due to Two-Dimensional Structures. *Geophysics*, **40**, 993-1013. https://doi.org/10.1190/1.1440593

[17] Archibald, N.J., Gow, P. and Boschetti, F. (1999) Multiscale Edge Analysis of Potential Field Data Exploration. *Geophysics*, **30**, 38-44.

[18] Cordell, L. and Grauch, V.J.S. (1985) Mapping Basement Magnetization Zones from Aeromagnetic Data in the San Juan Basin, New Mexico. In: Hinze, W.J., Ed., *The Utility of Regional Gravity and Magnetic Anomaly Maps*, Society of Exploration Geophysicists, 181-197. https://doi.org/10.1190/1.0931830346.ch16

[19] Cordell, L. (1979) Gravimetric Expression of Graben Faulting in Santa Fe Country and the Espanola Basin, New Mexico. In: Ingersoll, R.V., Ed., *Guidebook to Santa Fe Country*, New Mexico Geological Society, Socorro, 59-64.

[20] Koumetio, F., Njomo, D., Tabod, C.T., Noutchogwe, T.C. and Manguelle-Dicoum, E. (2012) Structural Interpretation of Gravity Anomalies from the Kribi-Edea Zone, South Cameroon: A Case Study. *Journal of Environmental & Engineering*, **9**, 664-673. https://doi.org/10.1088/1742-2132/9/6/664

[21] Koumetio, F., Njomo, D., Tatchum, C.N., Tokam, K.A.P., Tabod, C.T. and Manguelle-Dicoum, E. (2014) Interpretation of Gravity Anomalies by Multi-Scale Evalution of Maxima of Gradients and 3D Modelling in Bipindi Region (South-West Cameroon). *International Journal of Geosciences*, **5**, 1415-1425. https://doi.org/10.4236/ijg.2014.512115

[22] Mouzong, M.P., Kamguia, J., Nguiya, S., Shandini, Y. and Manguelle-Dicoum, E. (2014) Geometrical and Structural Characterization of Garoua Sedimentary Basin, Benue Trough, North Cameroon, Using Gravity Data. *Journal of Biology and Earth Sciences*, **4**, 25-33.